ACS SYMPOSIUM SERIES 1078

Modern Applications in Membrane Science and Technology

Selective Layer
Support Layer

EDITED BY
Isabel C. Escobar
and Bart Van der Bruggen

Downloaded by 89.163.35.42 on June 17, 2012 | http://pubs.acs.org
Publication Date (Web): October 31, 2011 | doi: 10.1021/bk-2011-1078.fw001

Modern Applications in Membrane Science and Technology

In Modern Applications in Membrane Science and Technology; Escobar, I., et al.;
ACS Symposium Series; American Chemical Society: Washington, DC, 2011.

Downloaded by 89.163.35.42 on June 17, 2012 | http://pubs.acs.org
Publication Date (Web): October 31, 2011 | doi: 10.1021/bk-2011-1078.fw001

ACS SYMPOSIUM SERIES **1078**

Modern Applications in Membrane Science and Technology

Isabel Escobar, Editor
University of Toledo
Toledo, Ohio

Bart Van der Bruggen, Editor
K.U. Leuven
Belgium

Sponsored by the
ACS Division of Environmental Chemistry, Inc.

American Chemical Society, Washington, DC

Distributed in print by Oxford University Press, Inc.

Downloaded by 89.163.35.42 on June 17, 2012 | http://pubs.acs.org
Publication Date (Web): October 31, 2011 | doi: 10.1021/bk-2011-1078.fw001

Downloaded by 89.163.35.42 on June 17, 2012 | http://pubs.acs.org
Publication Date (Web): October 31, 2011 | doi: 10.1021/bk-2011-1078.fw001

Library of Congress Cataloging-in-Publication Data

Library of Congress Cataloging-in-Publication Data

Modern applications in membrane science and technology / Isabel Escobar,
Bart Van der Bruggen, editor[s] ; sponsored by the ACS Division of Environmental
Chemistry, Inc.
p. cm. -- (ACS symposium series ; 1078)
Includes bibliographical references and index.
ISBN 978-0-8412-2618-0
1. Membrane separation--Congresses. 2. Membranes (Technology)--Congresses.
I. Escobar, Isabel. II. Van der Bruggen, Bart. III. American Chemical Society. Division of
Environmental Chemistry.
TP248.25.M46M63 2011
660′.28424--dc23
2011036490

The paper used in this publication meets the minimum requirements of American National Standard for Information Sciences—Permanence of Paper for Printed Library Materials, ANSI Z39.48n1984.

Copyright © 2011 American Chemical Society

Distributed in print by Oxford University Press, Inc.

All Rights Reserved. Reprographic copying beyond that permitted by Sections 107 or 108 of the U.S. Copyright Act is allowed for internal use only, provided that a per-chapter fee of $40.25 plus $0.75 per page is paid to the Copyright Clearance Center, Inc., 222 Rosewood Drive, Danvers, MA 01923, USA. Republication or reproduction for sale of pages in this book is permitted only under license from ACS. Direct these and other permission requests to ACS Copyright Office, Publications Division, 1155 16th Street, N.W., Washington, DC 20036.

The citation of trade names and/or names of manufacturers in this publication is not to be construed as an endorsement or as approval by ACS of the commercial products or services referenced herein; nor should the mere reference herein to any drawing, specification, chemical process, or other data be regarded as a license or as a conveyance of any right or permission to the holder, reader, or any other person or corporation, to manufacture, reproduce, use, or sell any patented invention or copyrighted work that may in any way be related thereto. Registered names, trademarks, etc., used in this publication, even without specific indication thereof, are not to be considered unprotected by law.

PRINTED IN THE UNITED STATES OF AMERICA

Downloaded by 89.163.35.42 on June 17, 2012 | http://pubs.acs.org
Publication Date (Web): October 31, 2011 | doi: 10.1021/bk-2011-1078.fw001

Foreword

The ACS Symposium Series was first published in 1974 to provide a mechanism for publishing symposia quickly in book form. The purpose of the series is to publish timely, comprehensive books developed from the ACS sponsored symposia based on current scientific research. Occasionally, books are developed from symposia sponsored by other organizations when the topic is of keen interest to the chemistry audience.

Before agreeing to publish a book, the proposed table of contents is reviewed for appropriate and comprehensive coverage and for interest to the audience. Some papers may be excluded to better focus the book; others may be added to provide comprehensiveness. When appropriate, overview or introductory chapters are added. Drafts of chapters are peer-reviewed prior to final acceptance or rejection, and manuscripts are prepared in camera-ready format.

As a rule, only original research papers and original review papers are included in the volumes. Verbatim reproductions of previous published papers are not accepted.

ACS Books Department

Downloaded by 89.163.35.42 on June 17, 2012 | http://pubs.acs.org
Publication Date (Web): October 31, 2011 | doi: 10.1021/bk-2011-1078.pr001

Preface

This ACS symposium series book edited by Drs. Isabel C. Escobar and Bart Van der Bruggen, pioneers in membrane technologies, provides a rich collection of emerging topics in the field of membrane science and technology. Consisting of the Introduction and 17 chapters, the book covers modern aspects in the field of membranes with focus on two major themes: membranes for energy, gas separations and CO_2 capture (Part I) and membranes for liquid separations (Part 2). In the Introduction section that follows, the editors explain the importance of the role of membrane technologies on (i) energy production using conventional and alternative approaches, (ii) production and purification of alternative fuels, (iii) purification of chemicals using "green chemistry" alternative routes, (iv) separation of gases, (v) water reuse, treatment, and purification, (vi) separation of fluids in food industry, (vii) purification of pharmaceuticals, (viii) reduction in greenhouse gases, (ix) sustainable and cost effective solutions in various industries, and several other applications. They also emphasize recent developments in the areas of (x) membrane modeling, (xi) biofouling, (xii) membrane synthesis using advances in pore engineering and nanotechnology, (xiii) membrane surface properties, modification and functionalization, (xiv) fundamental aspects of solute transport in new types of membrane, (xv) advanced membrane characterization, (xvi) novel aspects in modern membrane processes like forward reverse osmosis, and other emerging aspects in the field.

The 17 chapters, which are highlighted in the Introduction, are nicely balanced in the two themes, and include topics on (i) membranes for energy, pervaporation, gas separation and CO_2 capture, (ii) development, characterization, and evaluation of novel materials for hydrogen separation, (iii) tailor-synthesis and evaluation of nanotubular polymeric membranes for hydrophobicity-based separations, (iv) pervaporation applications of PDMS membranes modified with hydrophilic zeolites, (v) nanocomposite membranes modified with ionic liquids for CO_2 capture, (vi) synthesis, characterization, and evaluation of ortho-functionalized polyimide membranes for separation of aromatic/aliphatic mixtures by pervaporation, (vii) synthesis and membrane properties for gas separation of triptycene-based polyimide membranes, (viii) simulation studies of the synthesis of hollow fibers by spinning, (ix) membranes in water treatment and purification, (x) role and applications of membranes in the dairy industry, (xi) novel methods for membrane biofilm characterization and control, (xii) permeation properties of magnesium chloride and sodium chloride in highly-charged sulfonated polymeric membranes, (xiii) the role of chemical force microscopy technique to understand interactions of feed solution characteristics (solution chemistry) and ultrafiltration membrane properties (surface properties, morphology, heterogeneity), (xiv) synthesis, characterization, and water permeation and anti-biofouling properties of composite multi-walled carbon nanotube/polyether sulfone membranes, (xv) role of membrane thickness and pore controlling additives on the permeation properties of ultrafiltration polysulfone membranes, (xvi) novel reversible ion exchange-membrane hybrid process for energy efficient desalination of seawater, and (xvii) synthesis, characterization and property evaluation of novel membrane materials for forward reverse osmosis applications.

I am certain that readers interested in forefront developments and latest advances in the field of membrane science and technology, especially in the areas of energy production, removal of greenhouse gases, and separation of liquids will find this book of great value and a nice addition to the scientific literature of the field.

Dionysios (Dion) D. Dionysiou, Ph.D.
Professor of Environmental Engineering
Center of Sustainable Urban Engineering
Drinking Water, Water Supply, Quality, and Treatment,
and Environmental Nanotechnology Laboratories
Environmental Engineering and Science Program
School of Energy, Environmental, Biological, and Medical Engineering (SEEBME)
705 Engineering Research Center
University of Cincinnati
Cincinnati, OH 45221-0012

Downloaded by 89.163.35.42 on June 17, 2012 | http://pubs.acs.org
Publication Date (Web): October 31, 2011 | doi: 10.1021/bk-2011-1078.pr001

Downloaded by 89.163.35.42 on June 17, 2012 | http://pubs.acs.org
Publication Date (Web): October 31, 2011 | doi: 10.1021/bk-2011-1078.ch001

Chapter 1

Introduction

Isabel C. Escobar*,[1] and Bart Van der Bruggen[2]

[1]Chemical and Environmental Engineering Dept., The University of Toledo, Toledo, OH, U.S.A.
[2]Department of Chemical Engineering, K.U.Leuven
***E-mail: isabel.escobar@utoledo.edu**

Energy, water, affordable healthcare and global warming are four major concerns globally resulting from resource depletion, record high oil prices, clean water shortages, high costs of pharmaceuticals, and changing climate conditions. Among many potential solutions, advance in membrane technology is one of the most direct, effective and feasible approaches to solve these sophisticated issues.

Membrane separation technologies are used in diverse applications ranging from production of potable water and wastewater treatment, to tissue repair, power generation, processing of food and beverages, therapeutic procedures and production of pharmaceuticals. The growth in demand can be attributed to the wide adoption by key end-use markets such as wastewater and water treatment and food and beverages industry; replacement of traditional filtration equipment; augmented focus on purity levels of process fluids; and stringent regulations with respect to wastewater and water quality (*1*). The combined U.S. market for membranes used in liquid and gas separations applications is estimated at approximately $1.7 billion in 2010, and is forecast to grow by 2015 to reach $2.3 billion (*2*).

The exponential growth in ‘classical’ applications of membrane technology also catalyzes research on new applications, representing separations that were not yet possible, or that were difficult or costly to achieve. Membranologists are particularly active in finding new ways to separate what seems to be inseparable, and to push reaction and separation systems beyond their limits. Scale-up inevitably takes time, and it might take a decade or even several decades for

In Modern Applications in Membrane Science and Technology; Escobar, I., et al.;
ACS Symposium Series; American Chemical Society: Washington, DC, 2011.

Downloaded by 89.163.35.42 on June 17, 2012 | http://pubs.acs.org
Publication Date (Web): October 31, 2011 | doi: 10.1021/bk-2011-1078.ch001

some challenges to be solved on industrial scale with membranes. Nevertheless, the creativity in imagining membrane-assisted solutions is evident today, and this creativity will translate into tomorrow's practices, in every aspect of human life. Technology and industrial production are at the forefront, but membranes have already found their way in many less obvious areas as well. Perhaps the most important of these is human development. Drinking water production and wastewater treatment have always been core business for membranes; technological progress allows us today to speculate about low-cost membrane filtration systems applied on a massive scale. Alternatively, solutions may be found in high-tech solutions for desalination with efficiencies approaching thermodynamic limits – of course, using membranes. We clearly understand today that this in turn links to the energy challenge: energy is used for separation, but the reverse is possible as well. Few people understood this ten, twenty years ago, while it is plausible today. This is no more than a modest beginning; in ten, twenty years from now we will smile at the state-of-the-art of today and wonder how we could live without using membranes.

New applications of membranes in environmental protection include CO2 separation, which was not of any particular interest in the 1990's, but has now become a critical challenge. Interestingly, the negative motivation for CO2 capture – avoiding or at least decelerate global warming – has now turned into an opportunity. If we can develop systems with sufficient performance, waste CO2 may be used as a source of energy and of chemicals. Again, we push the limits beyond what we could once imagine. Membranes are among the most prominent toys we use to make this happen.

This membrane book is aimed at presenting cutting-edge membrane research and development for water reuse and desalination, energy development including biofuels, CO_2 capture, among others. The proposed two Parts are: membranes for energy, gas separation and CO_2 capture; and membranes for liquid separations.

Part I: Membranes for Energy, Gas Separation, and CO_2 Capture

The book starts with an overview of membranes for energy, gas separations and CO_2 capture (Chapter 2). While several membrane-based gas separations are now mature, during the last decade, membrane gas separations have received a new impulse mainly due to emerging environmental application, and the integration of energy production/consumption with environmental concerns. This resulted in a second wave of innovations on all levels, from membrane development to process engineering.

From this overview, the first Part of the book then proceeds to describe some of the latest advancements in membranes for gas separations. One such is the use of CuPd alloys as a promising materials for future hydrogen separation membranes and membrane reactor applications because of their high hydrogen selectivity and permeability, improved sulfur poisoning resistance and mechanical properties (Chapter 3). In another study, functional nanocomposite network membranes (FNNM) consisting of polymer matrix, nanofiber network and fixed

Downloaded by 89.163.35.42 on June 17, 2012 | http://pubs.acs.org
Publication Date (Web): October 31, 2011 | doi: 10.1021/bk-2011-1078.ch001

carrier molecules, were developed as a platform mixed matrix membrane material and investigated for selective recovery of CO_2 from gas streams (Chapter 6).

The development of a potential new generation of polymer nanopore membranes containing 5 nm long and narrow through-pores with controlled surface chemistry is then described (Chapter 4). Another study shown here focused on tuning of free volume element distributions and sizes in polymer design (using an iptycene-based monomer, i.e., triptycene) to improve fast, selective mass transport (Chapter 8).

On the field of pervaporation, hydrophilic zeolite filled membranes were used to compare fermentation broth pervaporation to ethanol/water pervaporation (Chapter 5). In another study, The performance of a series of soluble aromatic polyimides for the separation of benzene/n-heptane and toluene/n-heptane mixtures by pervaporation is reported (Chapter 7).

Part I of the book ends with an overview and study on membrane fiber spinning, which is used to manufacture hollow fibers for the membrane industry. Simulations of solid fiber and hollow fiber spinning are summarized including both one-dimensional and two-dimensional approaches (Chapter 9).

Part II: Membranes for Liquid Separations

Part II focuses on liquid separations and it starts with two overview chapters. The first one outlines membranes for water treatment applications (Chapter 10). Water purification is a rigorous process, which requires removal of a large number of impurities of varying size, shape and solubility depending on the nature of the water source. Membranes of varying pore size distributions and molecular weight cutoffs (MWCO) are used for this purpose. The second chapter provides a review of all membrane separations used in the dairy industry with suggestions for future processing (Chapter 11).

Chapters then proceed to discuss membrane biofouling and its prevention. Biofouling of membranes is often called membrane cancer, and it has been and will continue to be a problem that must be addressed. Biofouling has been associated to feed spacers, so the effects of using anti-microbial copper charged feed spacers are investigated (Chapter 12). The role of membrane chemical heterogeneities and morphology in biofouling and their effect on solute chemistry using chemical force microscopy as a characterization tool is discussed (Chapter 14).

A chapter focuses on a novel hybrid membrane process that uses reversible ion exchange-membranes (RIX-M) for desalination to eliminate scale formation potentials by changing the chemistry of the feed water through the introduction of a reversible cation exchange step before the membrane based desalination step. The cation exchange step has the potential to reduce the osmotic pressure of the resultant feed solution to the membrane. Thus, the membrane process can operate with high permeate water recovery and enhanced energy efficiency (Chapter 17).

Membrane materials are also the focus of studies shown in Part II. Sulfonated polymers are investigated due to their chlorine tolerance and hydrophilicity, as well as due to their ion exchange ability during desalination to increase sodium chloride rejection (Chapter 13). In a different study, composite membranes were prepared using polyethersulfone (PES) and multi-walled carbon nanotube (MWCNT) to investigate the influence of addition of MWCNT on the morphologies, permeation properties and antifouling (Chapter 15). The next chapter discussed the effects of polysulfone (PSf) dope concentration, membrane thickness and presence/absence of an inorganic additive (i.e. lithium chloride (LiCl)) on the filtration of different salt concentrations (Chapter 16). Lastly, polybenzimidizole nanofiltration membranes were cast and functionalized to investigate their ability to reject monovalent ions for future forward osmosis applications (Chapter 18).

The main goal of this book is to deliver some of the latest breakthroughs and findings in membrane technology and research. These latest research discoveries will hopefully spark new ideas to continue advancements in the field of membrane science.

References

1. Global Industry Analysts, Inc. http://www.StrategyR.com/.
2. http://www.bccresearch.com/report/MST053A.html.

Downloaded by 89.163.35.42 on June 17, 2012 | http://pubs.acs.org
Publication Date (Web): October 31, 2011 | doi: 10.1021/bk-2011-1078.ch001

Downloaded by CORNELL UNIV on June 17, 2012 | http://pubs.acs.org
Publication Date (Web): October 31, 2011 | doi: 10.1021/bk-2011-1078.ch002

Chapter 2

Analysis of the Development of Membrane Technology for Gas Separation and CO_2 Capture

Bart Van der Bruggen,*,[1] Isabel C. Escobar,[2] and Patricia Luis[1]

**[1]K.U.Leuven, Department of Chemical Engineering,
Laboratory of Applied Physical Chemistry and Environmental Technology,
W. de Croylaan 46, B-3001, Leuven, Belgium
[2]The University of Toledo, 2801 W. Bancroft Street, Toledo, OH 43606-3390
*E-mail: bart.vanderbruggen@cit.kuleuven.be. Tel: +32-16-32-23-40. Fax: +32-16-32-29-91.**

Gas separation is an application area for membrane technology with a long history. As a consequence, several membrane-based gas separations are now mature, although there is still a steady improvement in performance of membranes, and membrane functionalities. During the last decade, membrane gas separation had a new impulse mainly due to emerging environmental application, and the integration of energy production/consumption with environmental concerns. This resulted in a second wave of innovations on all levels, from membrane development to process engineering.

This perspective outlines the recent trends in membrane applications related to gas separation, based on the history of scientific research in membrane gas separation, and with reference to competing technologies such as cryogenic distillation, absorption, and adsorption on zeolites or other materials. In addition, the potential of hybrid technologies and newly emerging membrane-based technologies, such as membrane contactors, is probed.

Keywords: Gas separation; CO_2 capture; membrane contactors

Downloaded by CORNELL UNIV on June 17, 2012 | http://pubs.acs.org
Publication Date (Web): October 31, 2011 | doi: 10.1021/bk-2011-1078.ch002

Introduction

Separation of gases poses a specific challenge, and is quite different from liquid separations. Unlike solutes in liquid solution, the number of different gases to be considered is rather limited, and therefore, applications are focused on some specific separations (*1*). These applications, however, are extremely important for more than one reason. Among the most prominent gases to be purified are natural gas, syngas, hydrogen, carbon dioxide, nitrogen, and oxygen. It is evident that this requires dedicated technologies different from those applied in liquid separations. Gas molecules such as those mentioned above are small molecules, which implies that separations should be carried out on molecular level. The enormous progress in meso- and nanoscale technologies during the first decade of this century thus leads to a fast growth in (expertise on) technologies for gas separation. Recent trends in gas separation have a strong focus on membranes. Two factors dominate in this evolution:

(1) The cost related to membranes is decreasing steadily; this is logical from an economical point of view and completely in accordance with the advantages of economy of scale. In addition, research outcomes (mainly those related to improvements in membrane materials) push the membrane market by allowing the same applications with better separation factors and higher fluxes.
(2) During the last decade, new challenges for gas separation emerged, the most visible being those related to carbon dioxide: controlling CO_2 emissions, closing the carbon cycle, CO_2 sequestration and the use of CO_2 as a source material for chemicals production are very high on the research agenda. The original incentive for this was environmental protection, but the insight that there may be additional benefits in other ways as well in doing this has grown steadily since the turn of the centuries.

This chapter gives a general overview of research progress in membrane gas separation, based on a historical review and a comparison with competing technologies, and a perspective on current challenges and trends in this area.

Competing Technologies

Gas separation with membranes is relatively new, but other processes have been developed as well by using more conventional approaches. Three classical processes should be mentioned: absorption in a liquid, adsorption on a solid phase, and cryogenic distillation.

Absorption in a liquid is based on differences in solubility in a solvent, in a closed cycle configuration when the liquid is regenerated. This process is simple and can be applied for many separations, the most straightforward being related with acid gases, e.g., CO_2 and H_2S from methane. Disadvantages are mainly in the low purity of the light product and in the use of solvents that may be harmful. In spite of this, liquid absorption is still important, particularly in

Downloaded by CORNELL UNIV on June 17, 2012 | http://pubs.acs.org
Publication Date (Web): October 31, 2011 | doi: 10.1021/bk-2011-1078.ch002

view of its potential for CO_2 separations. A review published in 2005 by Aaron and Tsouris (*2*) concluded that the most promising current method for CO_2 separation is liquid absorption using monoethanolamine (MEA). However, they remark that the development of ceramic and metallic membranes for membrane diffusion should produce membranes significantly more efficient at separation than liquid absorption. Research on liquid absorption now focuses on the use of ionic liquids is explored for CO_2 absorption (*3*), the use of membrane contactors and the combination with pervaporation (*4*, *5*). Luis et al. (*6*) give an outline of the main limitations of membrane systems based on non-dispersive absorption using porous membranes: avoid membrane wetting, development of long-term stability membranes (or development of cheap membranes that allow a frequent replacement without high expenses, which is still an underdeveloped research line), application of absorption liquids with properties that allow the recovery of CO_2 while minimizing the environmental impact and study of the impact of other compounds in the process efficiency.

Adsorption on a solid phase is of interest today because of the variety of new potential adsorption materials that has been made available. Classical materials include zeolites, activated carbon, molecular sieves, silicagel, and alumina, but a large number of other candidate materials are studied as well, such as metal-organic frameworks (MOFs) (*7*, *8*) and carbon nanotubes (*9*). The scientific interest in these new materials is enormous, although most are still quite far from application. For example, a review on gas separation using MOFs published in 2009 by Li et al. (*40*) was cited 437 times in two years. However, MOFs still need many years of development before they can be actually of use, although the industrial interest is clear (*11*). When a material can be used with sufficient capacity and selectivity, adsorption is a simple process with easy regeneration (temperature swing or pressure swing adsorption). The use of adsorbents is in fact also closely related to membrane technology, because most, if not all, materials proposed for gas adsorption are used as additives in membranes as well (or as the main component). A typical example are zeolites, used in membrane materials for a wide range of separations including gases (*12*). More novel materials, such as MOFs, are also applied as thin films or in membrane structures (*13*). Future applications of adsorbents for gas separation may therefore rather be in a combined adsorption/membrane separation approach.

Cryogenic distillation is based on the same thermodynamic principles as a normal distillation for liquids, with the difference that the process conditions are radically different. In order to create an equilibrium with a liquid phase, extremely low temperatures have to be used: for nitrogen, 77 K, and for helium even 4 K. It can be easily understood that the energy cost related to this approach is huge; on the other hand, distillation is a well-developed process with flexibility towards product purity (depending on the energy input and the number of trays). In general, the cost related to the high purity is very high. Some typical applications include O_2/N_2, CH_4/N_2, CH_4/C_2H_6; these are the applications where condensation is relatively feasible and other technologies – including membrane gas separation – are not operated in optimal conditions. Today, innovation in this approach is scarce, with the energy consumption of cryogenic distillation becoming even a more significant disadvantage. The only research activities that involve cryogenic distillation are based on a hybrid configuration combining cryogenic distillation with membrane separation (e.g., (*14*)).

A Brief History

Early Work

Since Mitchell published *On the penetration of gases* in 1833 (*15*), it has taken a long time for gas separation with membranes to come to maturity. Remarkably, the first scientific publications on gas separation appeared nearly 150 years later only. One of the pioneer publications was published in 1977 by Kamalesh Sirkar (*16*), and marked the start of a new era in which gas separation by membranes became a new trend, slowly at first, but with applications already being developed in the 1980s. An interesting observation is that in the early days, most studies were focusing on nuclear applications, and an unexpected trendsetting journal has been the Journal of Nuclear Science and Technology. These publications had a low impact, in spite of being pioneers for a research area that is now booming. The first abstract that ever appeared under search terms 'membrane gas separation' (*17*) was not cited a single time. Sirkar's paper mentioned above received a disappointing 17 citations, which considerably underestimates the paper's value.

Research on gas separation set off in the 1980s, with basically three distinct directions:

(1) A chemical engineering approach to extend the McCabe-Thiele method to estimate the separation in a distillation column to gas separation using membranes, such as the work of Schulz (*18*). Even though still very relevant today, and not only in gas separation, this work has never received much attention. It is surprising that this topic has faded away, and never made it into reference books on membrane engineering, which rarely take over the chemical engineering approach of cascading in recycled multistage processes but typically describe membrane separations as a once-through system. Membrane gas separations in practice, however, are usually designed as multistage units, which leads to the ambiguous situation that people use cascade designs without the knowledge developed in Schulz' methodology.

(2) Membrane materials development, as in a paper by Kim et al. in 1988 (*19*) – with W. J. Koros as the second author – and several other papers. These studies received more attention, and paved the way towards new and more performant membranes, allowing more challenging separations. Not only classical polymers were suggested at that time for gas separation; ceramic membranes (*20*) and even liquid membranes (*21*) were already suggested.

(3) Feasibility study of several applications, such as nitrogen enriched air (*22*) and other applications that were thought at that time to be of interest and to be feasible with membrane technology. These studies received much attention, and were gradually extended over the years until the applications studied reached industrial maturity. For some applications,

Downloaded by CORNELL UNIV on June 17, 2012 | http://pubs.acs.org
Publication Date (Web): October 31, 2011 | doi: 10.1021/bk-2011-1078.ch002

such as hydrogen separations, this came very fast, even in the early 1980s. Other applications involving more difficult separations, such as oxygen/ nitrogen, took much longer to find industrial relevance. This went hand in hand with the development of new membrane materials, which was the second major research direction.

The 1990s

A fast growth in research on membrane gas separation, and applications, followed in the 1990s. Figure 1 shows the increase in research papers with search term ‘membrane gas separation’ (ISI Web of Science) from 1970 to 2010.

It can be seen that research on membrane gas separation suddenly took off at high speed in 1990, with an almost constant yearly increase in publication volume by ca. 25 papers, arriving at 245 in 2000. Membrane materials remained very high on the research agenda, as can be seen from the review by Stern in 1994 (*23*), which was cited 475 times. This underlines the fast growing interest in membranes for gas separation. Another visionary review was written by Koros and Fleming in 1993 (*24*), and received 422 citations. This paper is a very clear explanation of the insights in gas separation at that time, still useful to read after almost 20 years. The paper starts by stating “An exhaustive treatment of the past decade of intense activity in the membrane-based gas separation field would require an entire book…”, which indeed underlines how dynamic this research area had become. Little did they know at that point on how much would still be added to the body of knowledge on membrane gas separation in the years to come.

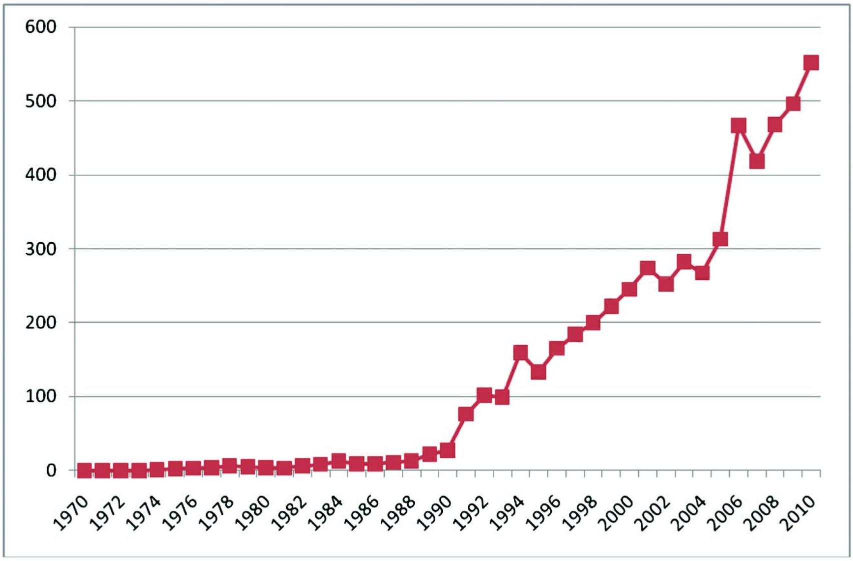

Figure 1. Number of publications in ISI Web of Science on ‘membrane gas separation’ from 1970 to 2010.

Downloaded by CORNELL UNIV on June 17, 2012 | http://pubs.acs.org
Publication Date (Web): October 31, 2011 | doi: 10.1021/bk-2011-1078.ch002

Downloaded by CORNELL UNIV on June 17, 2012 | http://pubs.acs.org
Publication Date (Web): October 31, 2011 | doi: 10.1021/bk-2011-1078.ch002

The most influential papers on membrane gas separation in the 1990s were on new membrane materials. Major efforts in research by eminent experts such as Bakker, Verweij, Tsapatsis, Paul, Koros and several more resulted in a fast increase in the number of membrane materials for use in gas separation (*25–28*). However, also other work appeared in which membrane gas separation was involved; for example, Zaman and Chakma (1994) (*29*) reviewed inorganic membrane reactors, in which ceramic membranes were proposed for application in high-temperature gas-phase reactions. Later, gas phase reactors emerged more, for example in steam reforming of methane (*30*), dry reforming of methane to syngas (*31*) and the water-gas shift reaction (*32*, *33*).

Saracco et al. (*34*) outlined the remaining challenges for membrane reactors: high costs, low permeability, synthesis of defect-free permselective layers, instability of membranes and catalysts, and sealing of membranes into modules. It is worth noticing that most of these challenges, almost two decades later, are still on the wish list for improvement, even though an impressive progress has been made on each of the items mentioned.

In this context, the work of Robeson has been quite remarkable. In 1991, Robeson (*35*) described the upper boundaries in membrane separations, in which fluxes (permeabilities) were related to separation efficiency. From experience, it was clear that the separation factor for gas pairs varies inversely with the permeability of the more permeable gas of the specific pair. Robeson made an analysis of literature data for binary gas mixtures comprising He, H_2, O_2, N_2, CH_4, and CO, and determined an upper bound relationship for these mixtures. The upper boundary was represented in a log-log diagram of separation factor as a function of permeability. This paper has been cited 742 times, and was by far the most cited paper in Journal of Membrane Science in the year of publication (the second paper having less than 200 citations). The work was repeated in 2008 by adding a wealth of new published data on new membranes (*36*). Not long after publication, this paper was already cited 137 times. Robseon concluded that the upper bound position has had only minor shifts in position for many gas pairs. More significant shifts were almost exclusively due to new perfluorinated polymers and involved many of the gas pairs comprising He. The changes observed were mainly due to an upwards shift of the boundary curve (denoted as the front factor k), whereas the slope of the curve remained similar to prior data correlations. It is interesting to note that the 1991 study did not include CO_2, since the relevance of this gas was only minor. In the new study, CO_2/N_2 and N_2/CH_4 separations were included as well.

In 1999, Freeman (*37*) published a fundamental explanation for the permeability/selectivity tradeoff, which completed Robeson's empirical study with a theoretical basis, nowadays widely known and accepted.

The first semi-quantitative prediction of membrane performances in gas separation appeared in 1991 by Jia and Xu (*38*), on the basis of the ratio of molar free volume to molar cohesive energy. The importance of free volume in transport properties was also emphasized by Hensema et al. (*39*), who related an increased permeability to an increased free volume in the polymer. In 1997, Robeson et al. (*40*) proposed a quantitative assessment of the structure/permeability (permselectivity) relationships for polymers of interest for membrane separation

Downloaded by CORNELL UNIV on June 17, 2012 | http://pubs.acs.org
Publication Date (Web): October 31, 2011 | doi: 10.1021/bk-2011-1078.ch002

by making use of a group contribution method. This procedure was shown to allow for. However, physical chemistry studies on gas separation were, at that point, still relatively underdeveloped. Nevertheless, some reference works still of use today appeared in the 1990s. Diffusion through polymeric materials is a core process to understand; however, in spite of the many unknowns related to the effect of the polymer structure and functional properties on permeation, remarkably few studies were made to understand this specifically for gas separation. Solution-diffusion was well-known in general, and clearly explained in a review by Wijmans and Baker in 1995 (*41*). Kerkhof (*42*) described a Maxwell-Stefan approach to model gas transport in membranes. Krishna and Wesselingh (*43*) emphasize the limitations of the use of Fick's law for describing diffusion, and conclude that the Maxwell-Stefan formulation provides the most general and convenient approach for describing mass transport, taking thermodynamic non-idealities and influences of external force fields into account. An early study by Kimmerle et al. (*44*) distinguished flow through three types of composite membranes, which were referred to as pore-flux-type, mixed-flux-type, and nonpore-flux-type composite membranes, and described gas transport by means of simple equations. Kamaruddin and Koros (*45*) considered multicomponent mixtures, and the effect on diffusive permeation. Takaba et al. (*46*) applied molecular dynamics for gas permeation modeling, as one of the few studies in this area.

Engineering of membrane gas separation also never received much attention, probably because this continues on still unresolved mass transfer problems. Worth mentioning is a study made by Thundyil and Koros (*47*), in which for given gas conditions, an algorithm is presented simulating the permeate and residue compositions, and the stage cut, and in which different flow patterns (radial crossflow, countercurrent flow, and concurrent flow) are analyzed for a separation module. Earlier, Krovvidi et al. (*48*) already made in 1992 an analysis of chemical engineering-based methods for estimation of the performance of gas separation units. The cascade approach, developed in the 1980s, was not yet entirely forgotten (*49*, *50*). Engineering issues such as concentration polarization or module configurations were also studied, although sparsely (*51–53*). Furthermore, these papers were generally less cited.

A New Century

A symbolic starting point for research on gas separation in the 21st century is a paper published in 1999 by Gabelman and Hwang (*54*) on hollow fiber membrane contactors. This paper, which has inspired many, gives a general review of hollow fiber membrane contactors, including operating principles, relevant mathematics, and applications. In this review, it is indicated that membrane contactor technology had already been demonstrated in a range of liquid/liquid and gas/liquid applications in fermentation, pharmaceuticals, wastewater treatment, chiral separations, semiconductor manufacturing, carbonation of beverages, metal ion extraction, protein extraction, VOC removal from waste gas, and osmotic distillation (*54*). Nevertheless, the number of publications on membrane contactors in 1999 was no more than 78. In the middle of the next decade, in

Downloaded by CORNELL UNIV on June 17, 2012 | http://pubs.acs.org
Publication Date (Web): October 31, 2011 | doi: 10.1021/bk-2011-1078.ch002

2005, this had increased to 415, and another five years later, in 2010, 1265 articles were published on membrane contactors. None of these papers was cited more often than the reference work by Gabelman and Hwang; in fact, this paper was cited about four times more than the second best cited paper on the same subject.

Later work often focused on the use of contactors for CO_2 absorption. Li and Chen (*55*) mention aqueous solvents, such as solutions of MEA, DEA, NaOH, KOH, LiOH, AMP and 1-propanol-AMP. Kumar et al. (*56*) use aqueous alkanolamines and amino acid salt solutions for CO_2 removal in membrane gas-liquid contactors. Other authors used ionic liquids (*57*). Other gases were studied more recently, such as hydrogen sulfide (*58*), sulfur dioxide (*59*) and acid gas streams (*60*).

Some studies aim at understanding the fundamentals of mass transfer in contactors. Trebouet et al. (*61*) calculate overall mass transfer coefficients using a dynamic model with five dimensionless parameters: one equilibrium, one mass transfer, two volume ratios and one ratio of space times. Al-Marzouqi et al. (*62*) provide a two-dimensional mathematical model based on a laminar parabolic velocity profile for the gas flow at the tube side and Happel's free surface model for the liquid flow at the shell side. Hoff et al. (*63*) used a two-dimensional diffusion-reaction model to explain experimental results on the variation in the flux of the CO_2 absorption rate with the CO_2 partial pressure, liquid CO_2 loading, liquid velocity, and temperature. Dindore et al. (*64*) remark that effect of carbon dioxide and hydrogen sulphide absorption into aqueous solutions through a hollow fiber membrane may not be described using conventional mass transfer models such as the penetration or surface renewal model due to the lack of a well defined liquid phase bulk and the presence of a laminar velocity profile in the mass transfer zone.

However, membrane synthesis and development for gas separation applications continued to dominate the agenda. New hybrid and innovative nanocomposites were developed for many applications including gas separation (for example, (*65–67*)). Lin and Freeman (*68*) provide directions to select the best membrane material, to achieve high CO_2 solubility and CO_2/light gas solubility selectivity specifically by introducing polar groups in polymers. Not long after the turn of the century, Pandey and Chauhan (*69*) review new materials and new preparation techniques developed to produce thinner membranes and/or smaller pore-sized, defect-free membranes, today still important challenges.

Mixed matrix membranes were studied by several authors for application in gas separation. Mahajan and Koros (*70*) state that mixed matrix materials comprising molecular sieve entities embedded in a polymer matrix can economically increase membrane permselectivity, which is a key issue for gas separation. Chung et al. (*71*) also state in their review of mixed matrix membranes that a significant improvement in separation properties with trivial loss in membrane flexibility is expected for the mixed matrix membranes. In addition to a proper choice of materials, Mahajan and Koros (*70*) stress the effect of chemical coupling of the sieve to the polymer, which can lead to better macroscopic adhesion but also to poorer transport properties than in the absence of the adhesion promoter. This is further developed in a follow-up paper (*72*), where membrane formation with a polymer that interacts favorably with the

Downloaded by CORNELL UNIV on June 17, 2012 | http://pubs.acs.org
Publication Date (Web): October 31, 2011 | doi: 10.1021/bk-2011-1078.ch002

sieve is described. It was shown that flexibility during membrane formation can be achieved by formation of films at temperatures close to the glass transition temperature of the polymer.

Numerous other examples of mixed matrix or hybrid membranes can be found. Cornelius and Marand (*73*) develop hybrid silica-polyimide membranes based on 6FDA-6FpDA and 6FDA-6FpDA-DABA polyimides. Gomes et al. (*74*) describe membranes for gas separation based on poly(1-trimethylsilyl-1-propyne)-silica nanocomposites. Jiang et al. (*75*) made Matrimid/polyethersulfone dual-layer hollow fiber membranes. Kim et al. (*76*) synthesize poly(imide siloxane) and carbon nanotube mixed matrix membranes. Some remarkable recent publications include the study of a mixed-matrix membrane containing three components consisting of a solid polymerized room-temperature ionic liquid (poly(RTIL)), a liquid RTIL, and a zeolite material (*77*); the development of mixed matrix membranes combining hollow silicalite-1 spheres with Udel polysulfone and Matrimid polyimide (*78*); the manufacturing of a freestanding foam film as a thin liquid gas separation membrane (*79*); and the development of a mixed-matrix membrane containing submicrometer-sized MOF crystals (*80*). For a more detailed overview, the review of Aroon et al. (*81*) is a good starting point.

In terms of applications, Baker (*82*) emphasized that more than 90% involve the separation of noncondensable gases: nitrogen from air; carbon dioxide from methane; and hydrogen from nitrogen, argon, or methane. According to Baker, a much larger potential market for membrane gas separation lies in separating mixtures containing condensable gases such as the C3+ hydrocarbons from methane or hydrogen, propylene from propane, and n-butane from isobutane. Since then, most attention in gas separation went to hydrogen and carbon dioxide. Bernardo et al. (*83*) recently reviewed the most promising areas of research in gas separation, by considering the materials for membranes, the industrial applications of membrane gas separations, and finally the opportunities for the integration of membrane gas separation units in hybrid systems for the intensification of processes. One of the approaches is membrane gas separation for CO_2 capture from a coal gasification process as a potential solution to reduce greenhouse gas emissions. This is described by e.g., Scholes et al. (*84*). The post-combustion separation is described by e.g., Reijerkerk et al. (*85*), who propose highly hydrophilic, poly(ethylene oxide) based block copolymers for the simultaneous removal of CO_2 and water vapor from a ternary gas simulating a flue gas in a post-combustion capture configuration.

Going even further, Czyperek et al. (*86*) propose a diversified approach for zero-emission fossil power plants. For the pre-combustion process, ceramic microporous membranes that operate at intermediate temperatures (below 400 °C) for H_2/CO_2 separation were developed. For the oxyfuel process, dense ceramic mixed oxygen ionic-electronic conducting membranes that operate at 800−1000 °C were proposed for O_2/N_2 separation. For the post-combustion process, polymeric and organic/inorganic hybrid membranes were developed for CO_2/N_2 separation at temperatures up to 200 °C. A review of all three approaches was also given by Olajire (*87*), in which also the previously mentioned competing technologies (chemical absorption, physical absorption, physical adsorption, cryogenics) are described, and membranes in conjunction with chemical absorption and chemical-looping combustion .

Current Developments and Emerging Challenges: A Bibliometric Analysis

A bibliometric analysis was made of the period 1991−2010, subdivided in four 5-year periods. The increase already shown in Figure 1 clearly appeared again from this analysis. The total number of papers in the area of 'membrane gas separation' in this period is given in Table 1, together with the number of different journals in which articles on this topic appeared. Particularly the latter indicator is remarkable. Table 2 further specifies the journals in which most work on membrane gas separation appeared. Logically, Journal of Membrane Science is the dominant journal. Among other journals, Industrial & Engineering Chemistry Research and Separation and Purification Technology emerge as the most prominent journals. Tendencies in journals are slow, but some observations can be made nevertheless. The strong focus on synthesis of polymeric membranes in the 1990s slowly disappeared in the following decade. In the first period considered (1991−1995), four out of the ten journals publishing the most articles on membrane gas separation were polymer-related journals. In the second period (1996−2000), two were left (with Polymer just outside the range as the third journal). In the third period (2001−2005), this was again two, and in the last period (2006−2010), only one journal on polymers was left, Journal of Applied Polymer Science. The latter journal ranked #2, #2 and #4 in the three first periods, whereas this was #7 in the last period.

Chemical engineering, in spite of the weak focus of membrane gas separation work on engineering aspects, is still visible in the journals that publish on this. Journals like Chemical Engineering Science, AIChE Journal and Industrial & Engineering Chemistry Research are clearly a constant. In contrast, journals on physical chemistry, which could also be expected here, are completely absent. This again underlines a potential need for more in-depth studies on physico-chemical interactions with membrane materials and underlying fundamentals.

The journal categories in this period for publications on 'membrane gas separation' are summarized in Figure 2. The bars denote percentages, and they don't add to 100% because a journal can be in more than one category. The most striking conclusion is the dominance of chemical engineering, and polymer science. The latter, however, is decreasing steadily, which confirms statements made above. Interestingly, the third position is taken by the discipline 'physical chemistry', although it was observed that not many publications in this area appeared. The increasing tendency, however, is encouraging. Chemical engineering, multidisciplinary chemistry, applied chemistry and analytical chemistry remain fairly constant. Among other disciplines, multidisciplinary materials science accounts for the decrease in polymer science, which seems to be

Downloaded by CORNELL UNIV on June 17, 2012 | http://pubs.acs.org
Publication Date (Web): October 31, 2011 | doi: 10.1021/bk-2011-1078.ch002

Downloaded by CORNELL UNIV on June 17, 2012 | http://pubs.acs.org
Publication Date (Web): October 31, 2011 | doi: 10.1021/bk-2011-1078.ch002

due to the development of ceramic membranes, but even more so, hybrid membrane materials. Energy & Fuels has seen a recent growth in interest, whereas the interest for nanoscience & nanotechnology has increased steadily.

Zooming in on the specific topics of articles published in this period, a search term study was made in the same way as above, using ISI Web of Science. The results are shown in Figure 3. Although the choice of search terms is of course arbitrary, some important conclusions can be made that confirm the above observations. It can be seen from Figure 3 that membrane synthesis and preparation, polymeric or ceramic, has a strong dominance in research on gas separation. As indicated above, the emphasis has shifted from pure polymers to other materials, but the objectives of membrane manufacturing remain. The importance of the search terms synthesis/preparation and polymer has even increased during the last decade, even though the findings are less published in polymer related journals, as explained above. Applications, for every gas included in the study, still have the same interest today than 20 years ago, with two exceptions of drastically increased interest: hydrogen and carbon dioxide. Models and simulation are popular, but their use seems to be not quite supported by fundamental or theoretical studies, which underlines the absence of physical chemistry in membrane gas separation studies already mentioned.

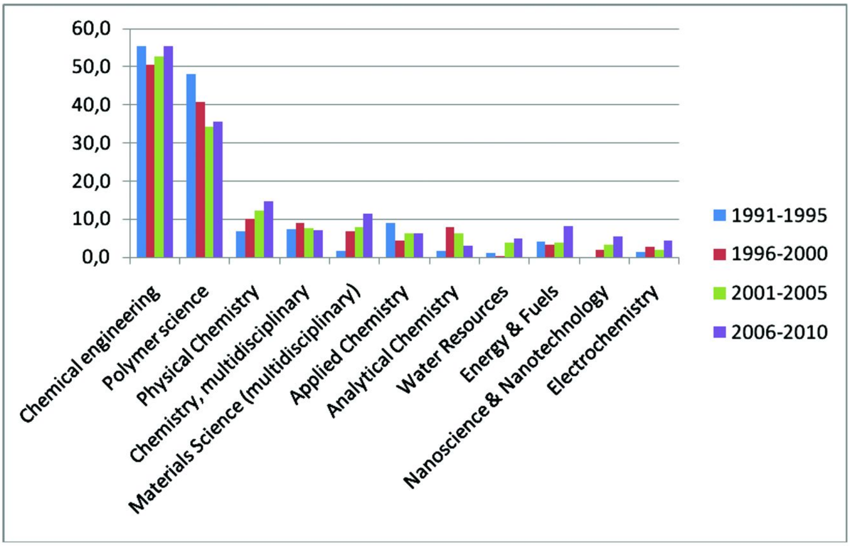

Figure 2. Percentages of publications on 'membrane gas separation', related to a selection of disciplines, from 1991 to 2010 (ISI Web of Science).

Table 1. Articles published in 1991−2010 on 'membrane gas separation', and numbers of journals involved (ISI Web of Science)

Period	*Articles 'membrane gas separation'*	*Number of different journals involved*
1991−1995	506	151
1996−2000	910	287
2001−2005	1225	311
2006−2010	1964	418

Table 2. Journals publishing on membrane gas separation in the period 1991−2010 and their rank in number of publications on membrane gas separation. Numbers between brackets refer to the total number of articles published in a given journal in the five-year period indicated

	1991−1995 rank	*1996−2000 rank*	*2001−2005 rank*	*2006−2010 rank*
Journal of Membrane Science	1 (165)	1 (241)	1 (271)	1 (530)
Industrial & Engineering Chemistry Research	3 (19)	4 (31)	3 (57)	2 (91)
Separation and Purification Technology (Gas Separation and Purification)	5 (11)	8 (16)	2 (71)	3 (90)
Journal of Applied Polymer Science	2 (22)	2 (45)	4 (52)	7 (43)
AIChE Journal		3 (33)	10 (19)	8 (28)
Chemical Engineering Science	10 (8)	6 (21)	8 (23)	10 (25)
Desalination			5 (38)	4 (71)

Continued on next page.

Downloaded by CORNELL UNIV on June 17, 2012 | http://pubs.acs.org
Publication Date (Web): October 31, 2011 | doi: 10.1021/bk-2011-1078.ch002

Downloaded by CORNELL UNIV on June 17, 2012 | http://pubs.acs.org
Publication Date (Web): October 31, 2011 | doi: 10.1021/bk-2011-1078.ch002

Table 2. (Continued). Journals publishing on membrane gas separation in the period 1991−2010 and their rank in number of publications on membrane gas separation. Numbers between brackets refer to the total number of articles published in a given journal in the five-year period indicated

	1991−1995 rank	*1996−2000 rank*	*2001−2005 rank*	*2006−2010 rank*
Microporous and Mesoporous Materials		9 (16)	6 (31)	5 (63)
Separation Science & Technology	4 (17)	5 (25)	9 (22)	9 (27)
Polymer Journal	6 (11)			
Energy Conversion and Management	7 (10)			
Journal of Polymer Science B	8 (9)	7 (18)		
Polymer	9 (9)	11 (10)	7 (25)	
Catalysis Today		10 (13)		
International Journal of Hydrogen Energy				6 (49)

Furthermore, chemical engineering is strikingly absent in these search term hits. Membrane reactors are studied, but not quite as much as membrane development and direct application to separations. Engineering and module design appear to be almost forgotten. Thus, it must be concluded that journals on chemical engineering and applied chemistry publish many (or even most) articles – in this field of study – that are not in the core of their subject. One may wonder whether this is driven by citations, given the fact that engineering publications, as shown before, as less cited. A reinvention of the core engineering discipline would be most welcome.

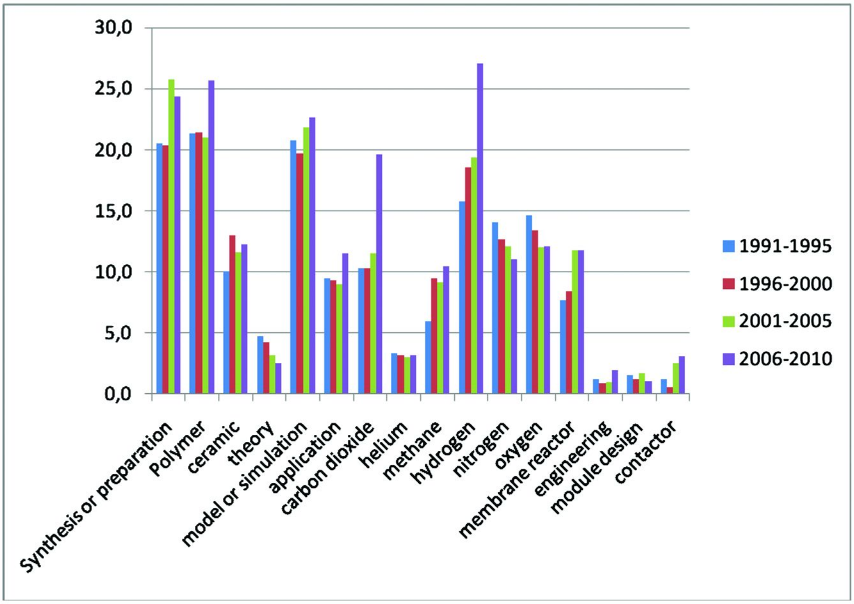

Figure 3. Percentage of publications on 'membrane gas separation' with a selection of search terms. Bars represent the percentage of hits within 'membrane gas separation'.

Conclusions

After the pioneering studies in the 1980s and the steady growth of gas separation with membranes in the 1990s and early 2000, a new era has started in the last five years. The enhanced activities in membrane gas separation are due to emerging challenges directly or indirectly related to energy. Interest in hydrogen separation and purification is booming, but also research on CO_2 separation has set off. Furthermore, it should be noted that this is just a small fraction of the studies that consider CO_2 capture, sequestration and storage using a wide range of technologies, and its further use as feedstock for conversions using renewable energy.

There are no signs that this interest would level off. However, research efforts are concentrated on development of new materials, which has been a constant during the last two decades. Transfer of technologies to industrial implementation may require more intensive work on technology development as well. Therefore, the scientific community is advised to pay substantially more attention to this area. Membrane reactors have a large and still partly unexplored potential. New technologies such as those based on membrane contactors are discovered, but at a slow pace. Furthermore, engineering should be recognized as a front area by leading journals and scientists.

Lastly, fundamental studies on physico-chemical interactions leading to transport and separation are to be encouraged, in order to upgrade existing

Downloaded by CORNELL UNIV on June 17, 2012 | http://pubs.acs.org
Publication Date (Web): October 31, 2011 | doi: 10.1021/bk-2011-1078.ch002

empirical models and simulation tools to be used for performance prediction, comparison, process control and, not in the least, process improvements, which links back to the enormous expertise on membrane materials present in the scientific community.

Acknowledgments

The Research Council of K.U.Leuven is gratefully acknowledged for financial support to P. Luis (F+/10/011).

References

1. Park, H. B.; Lee, Y. M. Polymeric membrane materials and potential use in gas separation. In *Advanced Membrane Technology and Applications*; Li, N. N., Fane, A. G., Ho, W. S., Matsuura, T., Eds.; Wiley: Hoboken, NJ, 2008; pp 633−669.
2. Aaron, D.; Tsouris, C. Separation of CO_2 from flue gas: A review. *Sep. Sci. Technol.* **2005**, *40* (1-3), 321–348.
3. Baltus, R. E.; Counce, R. M.; Culbertson, B. H.; Luo, H. M.; DePaoli, D. W.; Dai, S.; Duckworth, D. C. Examination of the potential of ionic liquids for gas separations. *Sep. Sci. Technol.* **2005**, *40* (1-3), 525–541.
4. Brazinha, C.; Alves, V. D.; Viegas, R. M. C.; Crespo, J. G. Aroma recovery by integration of sweeping gas pervaporation and liquid absorption in membrane contactors. *Sep. Purif. Technol.* **2009**, *70* (1), 103–111.
5. Roizard, D.; Lapicque, F.; Favre, E.; Roizard, C. Potentials of pervaporation to assist VOCs' recovery by liquid absorption. *Chem. Eng. Sci.* **2009**, *64* (9), 1927–1935.
6. Luis, P.; Van der Bruggen, B.; Van Gerven, T. Non-dispersive absorption for CO_2 capture: from the lab to the industry. *J. Chem. Technol. Biotechnol.* **2011** in press.
7. Herm, Z. R.; Swisher, J. A.; Smit, B.; Krishna, R.; Long, J. R. Metal-Organic Frameworks as Adsorbents for Hydrogen Purification and Precombustion Carbon Dioxide Capture. *J. Am. Chem. Soc.* **2011**, *133* (15), 5664–5667.
8. Kizzie, A. C.; Wong-Foy, A. G.; Matzger, A. J. Effect of Humidity on the Performance of Microporous Coordination Polymers as Adsorbents for CO_2 Capture. *Langmuir* **2011**, *27* (10), 6368–6373.
9. Razavi, S. S.; Hashemianzadeh, S. M.; Karimi, H. Modeling the adsorptive selectivity of carbon nanotubes for effective separation of CO_2/N-2 mixtures. *J. Mol. Model.* **2011**, *17* (5), 1163–1172.
10. Li, J. R.; Kuppler, R. J.; Zhou, H. C. Selective gas adsorption and separation in metal-organic frameworks. *Chem. Soc. Rev.* **2009**, *38* (5), 1477–1504.
11. Czaja, A. U.; Trukhan, N.; Müller, U. Industrial applications of metal-organic frameworks. *Chem. Soc. Rev.* **2009**, *38* (5), 1284–1293.
12. Adhikari, S.; Fernando, S. Hydrogen membrane separation techniques. *Ind. Eng. Chem. Res.* **2006**, *45* (3), 875–881.

Downloaded by CORNELL UNIV on June 17, 2012 | http://pubs.acs.org
Publication Date (Web): October 31, 2011 | doi: 10.1021/bk-2011-1078.ch002

13. Shekhah, O.; Liu, J.; Fischer, R. A.; Woll, C. MOF thin films: existing and future applications. *Chem. Soc. Rev.* **2011**, *40* (2), 1081–1106.
14. Wankat, P. C.; Kostroski, K. P. Hybrid Air Separation Processes for Production of Oxygen and Nitrogen. *Sep. Sci. Technol.* **2010**, *45* (9), 1171–1185.
15. Mitchell, J. K. On the penetration of gases. *Am. J. Med. Sci.* **1833**, *12* (25), 100–112.
16. Sirkar, K. K. Separation of gaseous mixtures with asymmetric dense polymeric membranes. *Chem. Eng. Sci.* **1977**, *32* (10), 1137–1145.
17. Dworscha, J. Separation of gas-mixtures with a porous membrane by selective permeation. *Chem. Ing. Tech.* **1974**, *46* (23), 1008.
18. Schulz, G. Gas separation in one-step or 2-step membrane processes. *Chem. Eng. Process.* **1985**, *19* (5), 235–241.
19. Kim, T. H.; Koros, W. J.; Husk, G. R. Advanced gas separation membrane materials – Rigid aromatic polyimides. *Sep. Sci. Technol.* **1988**, *23* (12-13), 1611–1626.
20. Konno, M.; Shindo, M.; Sugawara, S.; Saito, S. A composite palladium and porous aluminum-oxide membrane for hydrogen gas. *J. Membr. Sci.* **1988**, *37* (2), 193–197.
21. Majumdar, S.; Guha, A. K.; Sirkar, K. K. A new liquid membrane technique for gas separation. *AIChE J.* **1988**, *34* (7), 1135–1145.
22. Henwood, N. G.; Krueger, R. T. Membrane separation for the production of nitrogen enriched inert-gas. *J. Oil Colour Chem. Assoc.* **1987**, *70* (10), 286.
23. Stern, S. A. Polymers for gas separations – the next decade. *J. Membr. Sci.* **1994**, *94*, 1–65.
24. Koros, W. J.; Fleming, G. K. Membrane-based gas separation. *J. Membr. Sci.* **1993**, *83* (1), 1–80.
25. Bakker, W. J. W.; Kapteijn, F.; Poppe, J.; Moulijn, J. A. Permeation characteristics of a metal-supported silicalite-1 zeolite membrane. *J. Membr. Sci.* **1996**, *117* (1-2), 57–78.
26. De Vos, R. M.; Verweij, H. High-selectivity, high-flux silica membranes for gas separation. *Science* **1998**, *279* (5357), 1710–1711.
27. Lovallo, M. C.; Tsapatsis, M. Preferentially oriented submicron silicalite membranes. *AIChE J.* **1996**, *42* (11), 3020–3029.
28. Park, J. Y.; Paul, D. R. Correlation and prediction of gas permeability in glassy polymer membrane materials via a modified free volume based group contribution method. *J. Membr. Sci.* **1997**, *125* (1), 23–39.
29. Zaman, J.; Chakma, A. Inorganic membrane reactors. *J. Membr. Sci.* **1994**, *92* (1), 1–28.
30. Oklany, J. S.; Hou, K.; Hughes, R. A simulative comparison of dense and microporous membrane reactors for the steam reforming of methane. *Appl. Catal., A* **1998**, *170*, 13−22.
31. Galuszka, J.; Pandey, R. N.; Ahmed, S. Methane conversion to syngas in a palladium membrane reactor. *Catal. Today* **1998**, *46* (2-3), 83–89.
32. Basile, A.; Drioli, E.; Santella, F.; Violante, V.; Capannelli, G.; Vitulli, G. A study on catalytic membrane reactors for water gas shift reaction. *Gas Sep. Purif.* **1996**, *10* (1), 53–61.

Downloaded by CORNELL UNIV on June 17, 2012 | http://pubs.acs.org
Publication Date (Web): October 31, 2011 | doi: 10.1021/bk-2011-1078.ch002

Downloaded by CORNELL UNIV on June 17, 2012 | http://pubs.acs.org
Publication Date (Web): October 31, 2011 | doi: 10.1021/bk-2011-1078.ch002

33. Xue, E.; Okeeffe, M.; Ross, J. R. H. Water-gas shift conversion using a feed with a low steam to carbon monoxide ratio and containing sulphur. *Catal. Today* **1996**, *30* (1-3), 107–118.
34. Saracco, G.; Versteeg, G. F.; Vanswaaij, J. P. M. Current hurdles to the success of high-temperature membrane reactors. *J. Membr. Sci.* **1994**, *95* (2), 105–123.
35. Robeson, L. M. Correlation of separation factor versus permeability for polymeric membranes. *J. Membr. Sci.* **1991**, *62*, 165–185.
36. Robeson, L. M. The upper bound revisited. *J. Membr. Sci.* **2008**, *320* (1-2), 390–400.
37. Freeman, B. D. Basis of permeability/selectivity tradeoff relations in polymeric gas separation membranes. *Macromolecules* **1999**, *32* (2), 375–380.
38. Jia, L. D.; Xu, J. P. A simple method for prediction of gas-permeability of polymers from their molecular-structure. *Polymer J.* **1991**, *23* (5), 417–425.
39. Hensema, E. R.; Mulder, M. H. V.; Smolders, C. A. On the mechanism of gas-transport in rigid polymer membranes. *J. Appl. Polym. Sci.* **1993**, *49* (12), 2081–2090.
40. Robeson, L. M.; Smith, C. D.; Langsam, M. A group contribution approach to predict permeability and permselectivity of aromatic polymers. *J. Membr. Sci.* **1997**, *132* (1), 33–54.
41. Wijmans, J. G.; Baker, R. W. The solution-diffusion model – A review. *J. Membr. Sci.* **1995**, *107* (1-2), 1–21.
42. Kerkhof, P. J. A. M. A modified Maxwell-Stefan model for transport through inert membranes: The binary friction model. *Chem. Eng. J.* **1996**, *64* (3), 319–343.
43. Krishna, R.; Wesselingh, J. A. Review article number 50 - The Maxwell-Stefan approach to mass transfer. *Chem. Eng. Sci.* **1997**, *52* (6), 861–911.
44. Kimmerle, K.; Hofmann, T.; Strathmann, H. Analysis of gas permeation through composite membranes. *J. Membr. Sci.* **1991**, *61*, 1–17.
45. Kamaruddin, H. D.; Koros, W. J. Some observations about the application of Fick's first law for membrane separation of multicomponent mixtures. *J. Membr. Sci.* **1997**, *135* (2), 147–159.
46. Takaba, H.; Mizukami, K.; Kubo, M.; Fahmi, A.; Miyamoto, A. Permeation dynamics of small molecules through silica membranes: Molecular dynamics study. *AIChE J.* **1998**, *44* (6), 1335–1343.
47. Thundyil, M. J.; Koros, W. J. Mathematical modeling of gas separation permeators - For radial crossflow, countercurrent, and cocurrent hollow fiber membrane modules. *J. Membr. Sci.* **1997**, *125* (2), 275–291.
48. Krovvidi, K. R.; Kovvali, A. S.; Vemury, S.; Khan, A. A. Approximate solutions for gas permeators separating binary-mixtures. *J. Membr. Sci.* **1992**, *66* (2-3), 103–118.
49. Xu, J. G.; Agrawal, R. Gas separation membrane cascades .1. One-compressor cascades with minimal exergy losses due to mixing. *J. Membr. Sci.* **1996**, *112* (2), 115–128.
50. Agrawal, R.; Xu, J. G. Gas separation membrane cascades .2. Two-compressor cascades. *J. Membr. Sci.* **1996**, *112* (2), 129–146.

Downloaded by CORNELL UNIV on June 17, 2012 | http://pubs.acs.org
Publication Date (Web): October 31, 2011 | doi: 10.1021/bk-2011-1078.ch002

51. Ludtke, O.; Behling, R. D.; Ohlrogge, K. Concentration polarization in gas permeation. *J. Membr. Sci.* **1998**, *146* (2), 145–157.
52. Lababidi, H.; AlEnezi, G. A.; Ettouney, H. M. Optimization of module configuration in membrane gas separation. *J. Membr. Sci.* **1996**, *112* (2), 185–197.
53. Qi, R. H.; Henson, M. A. Optimal design of spiral-wound membrane networks for gas separations. *J. Membr. Sci.* **1998**, *148* (1), 71–89.
54. Gabelman, A.; Hwang, S. T. Hollow fiber membrane contactors. *J. Membr. Sci.* **1999**, *159* (1-2), 61–106.
55. Li, J. L.; Chen, B. H. Review of CO_2 absorption using chemical solvents in hollow fiber membrane contactors. *Sep. Purif. Technol.* **2005**, *41* (2), 109–122.
56. Kumar, P. S.; Hogendoorn, J. A.; Feron, P. H. M.; Versteeg, G. F. New absorption liquids for the removal of CO_2 from dilute gas streams using membrane contactors. *Chem. Eng. Sci.* **2002**, *57* (9), 1639–1651.
57. Luis, P.; Garea, A.; Irabien, A. Sulfur dioxide non-dispersive absorption in N,N-dimethylaniline using a ceramic membrane contactor. *J. Chem. Technol. Biotechnol.* **2008**, *83* (11), 1570–1577.
58. Keshavarz, P.; Fathikalajahi, J.; Ayatollahi, S. Mathematical modeling of the simultaneous absorption of carbon dioxide and hydrogen sulfide in a hollow fiber membrane contactor. *Sep. Purif. Technol.* **2008**, *63* (1), 145–155.
59. Luis, P.; Garea, A.; Irabien, A. Zero solvent emission process for sulfur dioxide recovery using a membrane contactor and ionic liquids. *J. Membr. Sci.* **2009**, *330* (1-2), 80–89.
60. Mansourizadeh, A.; Ismail, A. F. Hollow fiber gas-liquid membrane contactors for acid gas capture: A review. *J. Hazard. Mater.* **2009**, *171* (1-3), 38–53.
61. Trebouet, D.; Burgard, M.; Loureiro, J. M. Guidelines for the application of a stationary model in the prediction of the overall mass transfer coefficient in a hollow fiber membrane contactor. *Sep. Purif. Technol.* **2006**, *50* (1), 97–106.
62. Al-Marzouqi, M. H.; El-Naas, M. H.; Marzouk, S. A. M.; Al-Zarooni, M. A.; Abdullatif, N.; Faiz, R. Modeling of CO_2 absorption in membrane contactors. *Sep. Purif. Technol.* **2008**, *59* (3), 286–293.
63. Hoff, K. A.; Juliussen, O.; Falk-Pedersen, O.; Svendsen, H. F. Modeling and experimental study of carbon dioxide absorption in aqueous alkanolamine solutions using a membrane contactor. *Ind. Eng. Chem. Res.* **2004**, *43* (16), 4908–4921.
64. Dindore, V. Y.; Brilman, D. W. F.; Versteeg, G. E. Modelling of cross-flow membrane contactors: Mass transfer with chemical reactions. *J. Membr. Sci.* **2005**, *255* (1-2), 275–289.
65. Merkel, T. C.; Freeman, B. D.; Spontak, R. J.; He, Z.; Pinnau, I.; Meakin, P.; Hill, A. J. Ultrapermeable, reverse-selective nanocomposite membranes. *Science* **2002**, *296* (5567), 519–522.
66. Ismail, A. F.; David, L. I. B. A review on the latest development of carbon membranes for gas separation. *J. Membr. Sci.* **2001**, *193* (1), 1–18.

67. Vu, D. Q.; Koros, W. J.; Miller, S. J. Mixed matrix membranes using carbon molecular sieves - I. Preparation and experimental results. *J. Membr. Sci.* **2003**, *211* (2), 311–334.
68. Lin, H. Q.; Freeman, B. D. Materials selection guidelines for membranes that remove CO_2 from gas mixtures. *J. Molec. Struct.* **2005**, *739* (1-3), 57–74.
69. Pandey, P.; Chauhan, R. S. Membranes for gas separation. *Prog. Polym. Sci.* **2001**, *26* (6), 853–893.
70. Mahajan, R.; Koros, W. J. Mixed matrix membrane materials with glassy polymers. Part 1. *Polym. Eng. Sci.* **2002**, *42* (7), 1420–1431.
71. Chung, T. S.; Jiang, L. Y.; Kulprathipanja, S. Mixed matrix membranes (MMMs) comprising organic polymers with dispersed inorganic fillers for gas separation. *Prog. Polym. Sci.* **2007**, *32* (4), 438–507.
72. Mahajan, R.; Koros, W. J. Mixed matrix membrane materials with glassy polymers. Part 2. *Polym. Eng. Sci.* **2002**, *42* (7), 1432–1441.
73. Cornelius, C. J.; Marand, E. Hybrid silica-polyimide composite membranes: gas transport properties. *J. Membr. Sci.* **2002**, *202* (1-2), 97–118.
74. Gomes, D.; Nunes, S. P.; Peinemann, K. V. Membranes for gas separation based on poly(1-trimethylsilyl-1-propyne)-silica nanocomposites. *J. Membr. Sci.* **2005**, *246* (1), 13–25.
75. Jiang, L. Y.; Chung, T. S.; Li, D. F.; Cao, C.; Kulprathipanja, A. Fabrication of Matrimid/polyethersulfone dual-layer hollow fiber membranes for gas separation. *J. Membr. Sci.* **2004** (1-2), 91–103.
76. Kim, S.; Pechar, T. W.; Marand, E. Poly(imide siloxane) and carbon nanotube mixed matrix membranes for gas separation. *Desalination* **2006**, *192* (1-3), 330–339.
77. Hudiono, Y. C.; Carlisle, T. K.; LaFrate, A. L.; Gin, D. L.; Noble, R. D. Novel mixed matrix membranes based on polymerizable room-temperature ionic liquids and SAPO-34 particles to improve CO_2 separation. *J. Membr. Sci.* **2011**, *370* (1-2), 141–148.
78. Zornoza, B.; Esekhile, O.; Koros, W. J.; Tellez, C.; Coronas, J. Hollow silicalite-1 sphere-polymer mixed matrix membranes for gas separation. *Sep. Purif. Technol.* **2011**, *77* (1), 137–145.
79. Ramanathan, M.; Muller, H. J.; Mohwald, H.; Krastev, R. Foam Films as Thin Liquid Gas Separation Membranes. *ACS Appl. Mater. Interfaces* **2011**, *3* (3), 633–637.
80. Bae, T. H.; Lee, J. S.; Qiu, W. L.; Koros, W. J.; Jones, C. W.; Nair, S. A High-Performance Gas-Separation Membrane Containing Submicrometer-Sized Metal-Organic Framework Crystals. *Angew. Chem., Int. Ed.* **2010**, *49* (51), 9863–9866.
81. Aroon, M. A.; Ismail, A. F.; Matsuura, T.; Montazer-Rahmati, M. M. Performance studies of mixed matrix membranes for gas separation: A review. *Sep. Purif. Technol.* **2010**, *75* (3), 229–242.
82. Baker, R. W. Future directions of membrane gas separation technology. *Ind. Eng. Chem. Res.* **2002**, *41* (6), 1393–1411.
83. Bernardo, P.; Drioli, E.; Golemme, G. Membrane Gas Separation: A Review/State of the Art. *Ind. Eng. Chem. Res.* **2009**, *48* (10), 4638–4663.

Downloaded by CORNELL UNIV on June 17, 2012 | http://pubs.acs.org
Publication Date (Web): October 31, 2011 | doi: 10.1021/bk-2011-1078.ch002

84. Scholes, C. A.; Smith, K. H.; Kentish, S. E.; Stevens, G. W. CO_2 capture from pre-combustion processes-Strategies for membrane gas separation. *Int. J. Greenhouse Gas Control* **2010**, *4* (5), 739–755.
85. Reijerkerk, S. R.; Jordana, R.; Nijmeijer, K.; Wessling, M. Highly hydrophilic, rubbery membranes for CO_2 capture and dehydration of flue gas. *Int. J. Greenhouse Gas Contr.* **2011**, *5* (1), 26–36.
86. Czyperek, M.; Zapp, P.; Bouwmeester, H. J. M.; Modigell, M.; Ebert, K.; Voigt, I.; Meulenberg, W. A.; Singheiser, L.; Stover, D. Gas separation membranes for zero-emission fossil power plants: MEM-BRAIN. *J. Membr. Sci.* **2010**, *359* (1-2), 149–159.
87. Olajire, A. A. CO_2 capture and separation technologies for end-of-pipe applications - A review. *Energy* **2010**, *35* (6), 2610–2628.

Downloaded by CORNELL UNIV on June 17, 2012 | http://pubs.acs.org
Publication Date (Web): October 31, 2011 | doi: 10.1021/bk-2011-1078.ch002

Chapter 3

Accelerated Materials Design for Hydrogen Separation Membranes

R. Hu,[*,1,2] M. C. Gao,[1,2] and Ö. N. Doğan[1]

[1]National Energy Technology Laboratory, 1450 Queen Ave. SW, Albany, OR 97321, U.S.A.
[2]URS Corp., P.O. Box 1959, Albany, OR 97321, U.S.A.
[*]E-mail: rxhu2008@gmail.com

CuPd alloys are among the most promising materials for future hydrogen separation membranes and membrane reactor applications due to their high hydrogen selectivity and permeability, improved sulfur poisoning resistance and mechanical properties. The increased permeability of certain binary CuPd compositions has been attributed to the more open bcc structure. In order to expand the ordered bcc (B2) phase field towards lower Pd contents and higher temperatures, the formation enthalpies of hypothetical B2 $Cu_8Pd_{8-x}M_x$ (x=0-8) ternary alloys were studied using first principles electronic density functional theory (DFT) at the low temperature limit. Based on the present DFT calculations, seven alloying elements were down selected including Ti, Zr, Hf, Y, La, Al and Mg for experimental verification. A total of 14 alloys were selected in order to locate the B2 phase boundaries in the Cu-Pd-M ternary system. The alloys were synthesized via arc melting, and were undergone homogenization and equlibration annealing, and then were characterized using techniques including XRD, SEM, DTA and DSC. The present approach integrates DFT calculations and experiments and allows us to identify the alloying elements that have the most potential in stabilizing the B2 phase much more rapidly compared to traditional trial-and-error experimental approach.

In Modern Applications in Membrane Science and Technology; Escobar, I., et al.;
ACS Symposium Series; American Chemical Society: Washington, DC, 2011.

Introduction

To reduce dependence on oil and emission of greenhouse gases, hydrogen is favored as an energy source for the near future (*1*). One way to produce hydrogen is to separate hydrogen from syngas after coal gasification (*2*). Membranes permeable to hydrogen only are needed to separate hydrogen from other gases. Palladium was identified as a hydrogen separation material since the mid of 1800s due to its high hydrogen permeability and selectivity (*3–8*). However, there are several disadvantages using palladium membrane. Hydrogen atoms occupy the interstitial sites of fcc lattice of Pd, and the interstitial solid solution undergoes a phase separation at temperatures equal to or below 293^{o}C, forming low-hydrogen-concentration (α) and high-hydrogen-concentration (α') solid solution fcc phases. Both phases differ from the parent random solution phase in the lattice parameters and consequently change in molar volumes can lead to internal stress and thus embrittlement (*3*, *9*, *10*). Palladium is also susceptible to contaminants such as H_2S in coal derived syngas and other fossil fuels (*11*). Another disadvantage of Pd is its high cost.

In order to develop affordable hydrogen membrane materials and to improve their H_2S poisoning resistance, alloying elements including but not limited to platinum (*12*, *13*), nickel (*14–16*), silver (*17–23*) and copper (*24–29*) have been extensively studied. Addition of these elements improves the surface resistance of pure Pd against poisoning in exposure to gas components, like CO, H_2S and H_2O (*30*). By alloying palladium with silver, ruthenium, copper, the phase separation of interstitial solid solution fcc phase is suppressed towards lower temperatures and the embrittlement effect can be minimized or avoided; in the mean time, hydrogen permeabilities are comparable to or greater than pure palladium for some specific compositions (*31–34*).

Compared to the extensively studied PdAg alloys, recently PdCu alloys have attracted more attention not only because they are relatively less expensive, but also PdCu alloys exhibit better poisoning resistance to impurities (*25*, *26*, *28*, *29*). High permeability values were obtained for a particular composition, $Pd_{60}Cu_{40}$ (wt%), which has the B2 structure at temperatures below 600°C (*35*, *36*). The higher permeability is assumed due to its bcc structure that is more open than fcc structure. Bcc crystal structure has lower activation energy for hydrogen diffusion (*27*, *37*, *38*) compared to fcc structure.

In order to further lower the cost of the PdCu alloys, an integrated approach that combines first-principles density functional theory (DFT) calculations and key experiments was used in this study to accelerate new CuPdM alloy design that expand the bcc phase field for hydrogen separation in syngas coal gasification.

DFT Calculations

The first principles package of VASP (Vienna *ab initio* simulation package) (*39*, *40*) was used to calculate the total energies using electronic DFT. Projector augmented-wave (PAW) potentials (*41*) were used as supplied with VASP. The Perdew-Burke-Ernzerhof (*42*) gradient approximation to the exchange-correlation functional was used. The Brillouin zone integrations were performed using the Monkhorst–Pack k-point meshes (*43*), and a smearing parameter of 0.2 eV was chosen for the Methfessel–Paxton (*44*) technique. All structures are fully relaxed (both lattice parameters and atomic coordinates) until energies converge to a precision of 1 meV/at. A "high precision" setting is used. The plane-wave energy cutoff is held constant at 500 eV. The semi-core 3p, 4p and 5p electrons of transition metal elements are explicitly treated as valence. To obtain enthalpy of formation values ΔH_f, a composition-weighted average of the pure elemental cohesive energies is subtracted from the cohesive energy of a given composition. The resulting energy is an "enthalpy" because its volume is relaxed at zero pressure. A 2x2x2 supercell was built and individual Pd atom was substituted by the alloying elements. Fig. 1 shows the enthalpy of formation for hypothetical B2 $Cu_8Pd_{8-x}M_x$ (x=0-8) ternary alloys for transition metals and non-transition metals. The results indicate that elements Sc, Ti, Zn, Y, Zr, Hf, La, Al and Mg are strong stabilizers under the assumptions that we ignore the competing phases in the individual ternaries and that we ignore configurational entropy effect and lattice vibration at finite temperatures. Phase stability study for the complete Cu-Pd-M ternaries at finite temperatures are necessary to draw comprehensive conclusions but are beyond the scope of the present work.

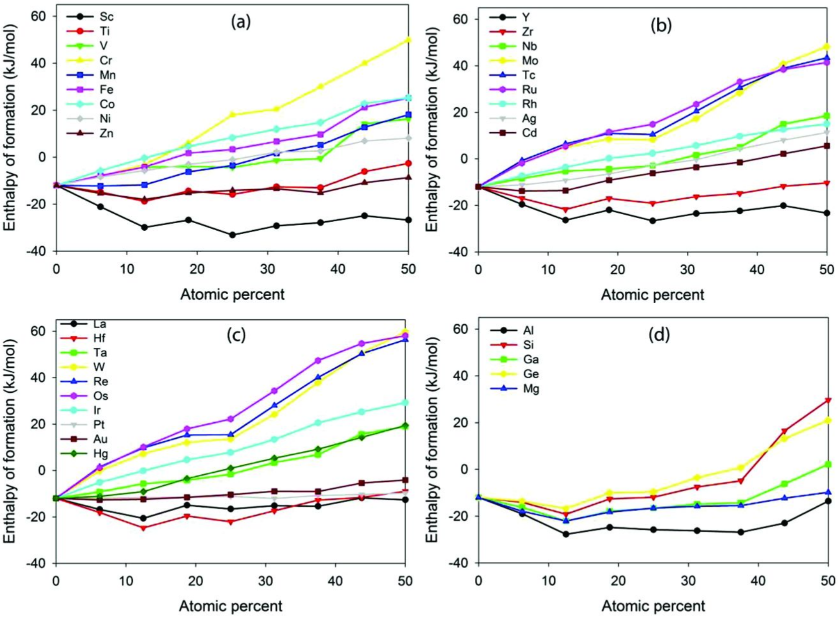

Figure 1. Enthalpy of formation of hypothetical B2 $Cu_8Pd_{8-x}M_x$ (x=0-8) alloys predicted from the present DFT calculations.

Experimental Procedures

Based on the present DFT calculations, we chosen 7 alloying elements (Ti, Zr, Hf, Y, La, Al and Mg) for experimental verification. Accordingly, 14 ternary alloys and two benchmark binary alloys were selected in order to locate the B2 phase field in the Cu-Pd-M ternary system on the M-poor side. The alloy compositions were listed in Table 1.

The starting materials were high purity Cu, Pd, Ti, Zr, Hf, Y, La, Al and Mg elements in pellet or sponge form. The 16 alloys were prepared by melting in a vacuum arc furnace back-filled with high purity argon. Each sample weighted ~40g. After a homogenization at 900°C for 72 hours, the alloys were subjected to an equilibration annealing at 400°C for 21 days.

Wavelength dispersive x-ray fluorescence spectroscopy (WDXRF) (Rigaku, ZSX Primus II) was used for the chemical analysis. Cu-Zn alloys were used for calibrating the WDXRF. The phase identification was done using x-ray diffraction (XRD) (Rigaku, Ultima III with Jade analysis software). Optical microscopy and scanning electron microscopy/energy dispersive spectroscopy (SEM/EDS) (FEI, Inspect F50 scanning electron microscope with Oxford INCA Microanalysis) were used for microstructural characterization and microchemical analysis. The high temperature differential scanning calorimeter (DSC) apparatus (Setaram Setsys16/18) was used to determine the B2↔disordered fcc phase transition temperatures for these alloys. The measurements were conducted between room temperature and 1000°C with a heating and cooling rate of 10K/min in an argon atmosphere.

Experimental Results and Discussions

a. Chemical Analysis

The WDXRF results showed that the impurity in each sample is less than 1 wt.%, listed in Table 2. The relatively large deviation of the Mg atomic percent in one Cu-Pd-Mg sample from the nominal value might be due to the element evaporation since Mg has a lower melting point and high vapor pressure.

b. SEM/EDS and XRD Results

For $Cu_{50}Pd_{43.75}M_{6.25}$ alloys, XRD results showed the presence of the B2 phase for M=Ti, Y, La, Al and Mg, shown in Fig. 2.

All $Pd_{27.75}M_{6.25}Cu_{66}$ alloys showed either Cu_3Pd (Tetragonal, P4/mmm, $L1_0$) or Cu_4Pd (Tetragonal, $P4_2/m$) as the major phase and two alloys (containing Hf and Mg) showed the B2 phase as the minor phase, listed in Table 3. The results show that the B2 phase field does not shift to the Cu-rich side in the Cu-Pd-M ternary for M=Ti, Zr, Y, La, Al, due to the presence of very stable compounds in the Cu-rich Cu-M system (e.g. Al_4Cu_9) or extension of stable Pd-rich Pd-M compounds into the ternary (e.g. YPd_3, $HfPd_3$, $LaPd_5$, $ZrPd_3$). We did not observe the binary Cu_3Pd $L1_2$ phase in these samples.

Table 1. Alloy compositions

High Pd composition (at%)	*Low Pd composition (at%)*
$Pd_{50}Cu_{50}$	$Pd_{34}Cu_{66}$
$Pd_{43.75}Ti_{6.25}Cu_{50}$	$Pd_{27.75}Ti_{6.25}Cu_{66}$
$Pd_{43.75}Zr_{6.25}Cu_{50}$	$Pd_{27.75}Zr_{6.25}Cu_{66}$
$Pd_{43.75}Hf_{6.25}Cu_{50}$	$Pd_{27.75}Hf_{6.25}Cu_{66}$
$Pd_{43.75}Y_{6.25}Cu_{50}$	$Pd_{27.75}Y_{6.25}Cu_{66}$
$Pd_{43.75}La_{6.25}Cu_{50}$	$Pd_{27.75}La_{6.25}Cu_{66}$
$Pd_{43.75}Al_{6.25}Cu_{50}$	$Pd_{27.75}Al_{6.25}Cu_{66}$
$Pd_{43.75}Mg_{6.25}Cu_{50}$	$Pd_{27.75}Mg_{6.25}Cu_{66}$

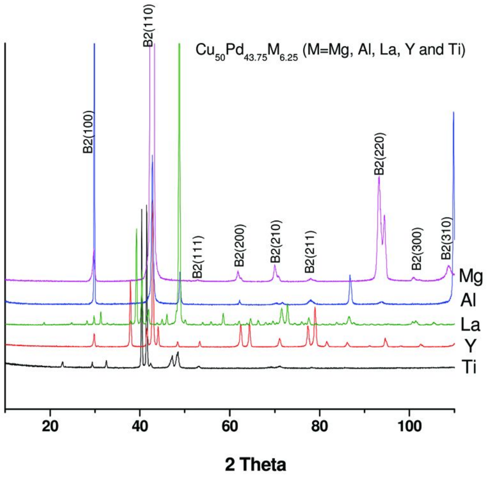

Figure 2. XRD plots for B2-containing $Cu_{50}Pd_{43.75}M_{6.25}$ alloys.

The volume percentage of B2 phase in each sample was estimated from the back-scattered SEM images (e.g. in Fig. 3) using ImageJ software based on the compositional contrast. Listed in Table 4 are the compositions of all phases identified using EDS and XRD as well as the estimated volume percentage of B2 phase where identified. The estimated volume percentage of B2 phase in $Cu_{50}Pd_{43.75}$ $M_{6.25}$ (M=Mg, Al, and Y) is 100%, 75% and 70% at 400°C respectively. The present experiments indicate that Mg is the strongest B2 stabilizer followed by Al and Y.

Table 2. WDXRF Chemical Analysis (wt.%)

Alloy	*Cu*	*Pd*	*Ti*	*Mg*	*Zr*	*Hf*	*Y*	*Al*	*La*
$Pd_{50}Cu_{50}$	38.38	61.52							
$Pd_{34}Cu_{66}$	54.82	45.08							
$Pd_{43.75}Ti_{6.25}Cu_{50}$	40.41	56.49	3.10						
$Pd_{27.75}Ti_{6.25}Cu_{66}$	58.51	38.22	3.26						
$Pd_{43.75}Zr_{6.25}Cu_{50}$	37.53	56.04			6.42				
$Pd_{27.75}Zr_{6.25}Cu_{66}$	56.50	36.34			7.15				
$Pd_{43.75}Hf_{6.25}Cu_{50}$	34.98	51.52				12.81			
$Pd_{27.75}Hf_{6.25}Cu_{66}$	52.81	33.69				13.14			
$Pd_{43.75}Y_{6.25}Cu_{50}$	37.41	56.57					5.61		
$Pd_{27.75}Y_{6.25}Cu_{66}$	55.64	37.70					6.30		
$Pd_{43.75}La_{6.25}Cu_{50}$	37.88	53.26							8.85
$Pd_{27.75}La_{6.25}Cu_{66}$	55.80	36.93							7.23
$Pd_{43.75}Al_{6.25}Cu_{50}$	40.94	56.26						1.81	
$Pd_{27.75}Al_{6.25}Cu_{66}$	57.89	39.07						2.11	
$Pd_{43.75}Mg_{6.25}Cu_{50}$	40.94	57.39		1.67					
$Pd_{27.75}Mg_{6.25}Cu_{66}$	57.92	40.98		0.87					

Table 3. XRD results for $Pd_{27.75}M_{6.25}Cu_{66}$ alloys

Alloys	*Phase 1*	*Phase 2*	*Phase 3*	*Phase 4*
$Pd_{34}Cu_{66}$		(CuPd) _FCC		
$Pd_{27.75}Ti_{6.25}Cu_{66}$	Cu_4Pd_tetra	Cu_3Pd_tetra	Pd_5Ti_3	$TiPd_3$
$Pd_{27.75}Zr_{6.25}Cu_{66}$	Cu_3Pd_tetra	$ZrPd_3$		
$Pd_{27.75}Hf_{6.25}Cu_{66}$	Cu_4Pd_tetra	$HfPd_3$	PdCu_B2	
$Pd_{27.75}Y_{6.25}Cu_{66}$	Cu_3Pd_tetra	YPd_3		
$Pd_{27.75}La_{6.25}Cu_{66}$	Cu_4Pd_tetra	$LaPd_5$		
$Pd_{27.75}Al_{6.25}Cu_{66}$	Cu_3Pd_tetra	$Cu_{0.78}Al_{0.22}$	Al_4Cu_9	$Cu_{5.75}Al_{4.5}$
$Pd_{27.75}Mg_{6.25}Cu_{66}$	Cu_3Pd_tetra	$Cu_{0.7}Pd_{0.3}$	PdCu_B_2	

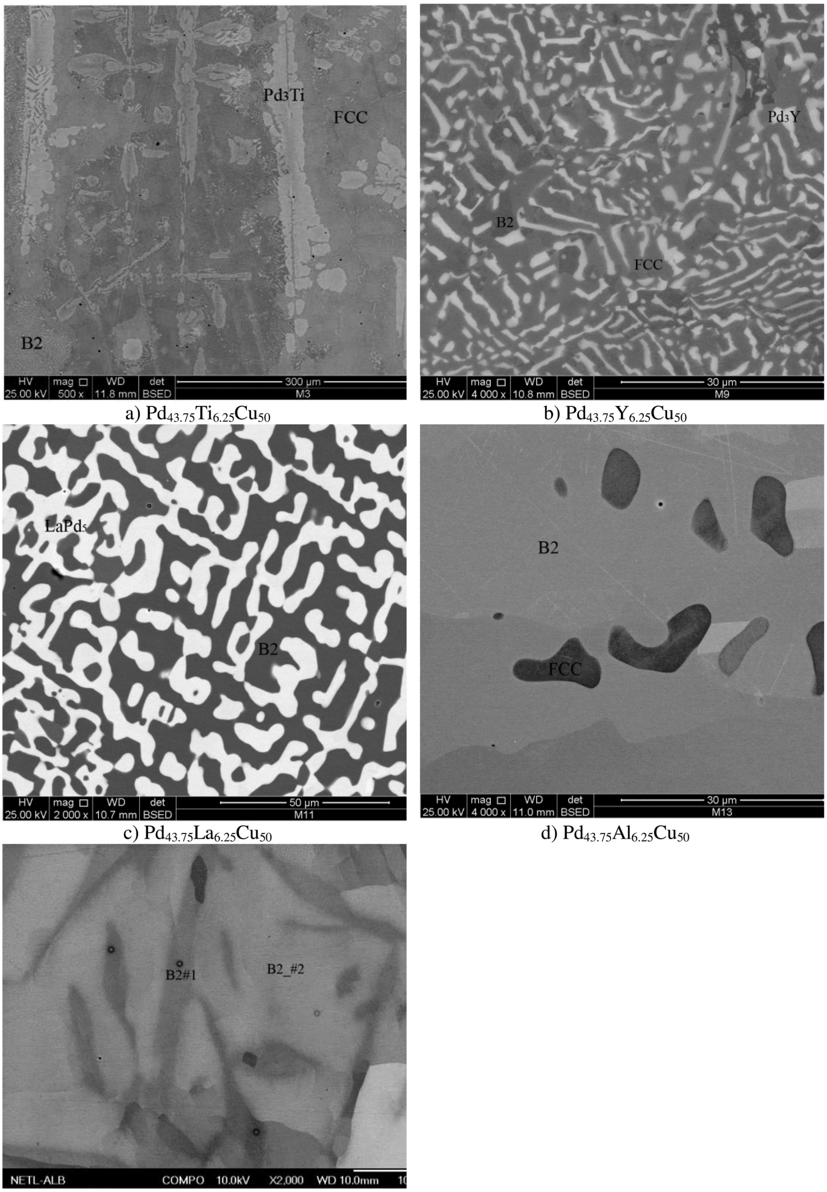
Pd3Ti
FCC
B2
HV 25.00 kV mag 500 x WD 11.8 mm det BSED 300 μm M3
Pd3Y
B2
FCC
HV 25.00 kV mag 4 000 x WD 10.8 mm det BSED 30 μm M9
LaPd5
B2
HV 25.00 kV mag 2 000 x WD 10.7 mm det BSED 50 μm M11
B2
FCC
HV 25.00 kV mag 4 000 x WD 11.0 mm det BSED 30 μm M13
B2#1
B2_#2
NETL-ALB COMPO 10.0kV X2,000 WD 10.0mm

a) $Pd_{43.75}Ti_{6.25}Cu_{50}$ b) $Pd_{43.75}Y_{6.25}Cu_{50}$

c) $Pd_{43.75}La_{6.25}Cu_{50}$ d) $Pd_{43.75}Al_{6.25}Cu_{50}$

e) $Pd_{43.75}Mg_{6.25}Cu_{50}$

Figure 3. SEM back-scattered electron images of B2-containing $Cu_{50}Pd_{43.75}$ $M_{6.25}$ ternary alloys (M=Ti, La, Y, Al and Mg).

Table 4. EDS and XRD results for $Cu_{50}Pd_{43.75}M_{6.25}$ alloys

Alloys	*EDS*			*XRD*	*B2 volume %*
	Cu at%	*Pd at%*	*M at%*		
$Pd_{50}Cu_{50}$	51	49			
$Cu_{50}Pd_{43.75}Ti_{6.25}$	60.91	36.64	2.45	B2	5-10%
	48.94	44.43	6.63	FCC	
	38.82	50.52	10.65	Pd_3Ti	
$Cu_{50}Pd_{43.75}Y_{6.25}$	61.45	38.55	0.00	B2	<70%
	7.33	70.94	21.75	Pd_3Y	
	20.60	61.60	17.80	FCC	
$Cu_{50}Pd_{43.75}La_{6.25}$	65.88	34.12	0.00	B2	5-10%
	22.33	62.08	15.59	$LaPd_5$	
$Cu_{50}Pd_{43.75}Al_{6.25}$	67.10	32.68	0.22	FCC	
	52.21	42.45	5.34	B2	75%
$Cu_{50}Pd_{43.75}Mg_{6.25}$	57.50	40.41	2.09	B2_#1	80%
	46.31	45.15	8.51	B2_#2	20%
$Cu_{50}Pd_{43.75}Zr_{6.25}$	11.80	70.54	17.68	$Pd_{0.845}Zr_{0.155}$	0
	61.05	37.49	1.47	$Cu_{0.54}Pd_{0.46}$_FCC	
$Cu_{50}Pd_{43.75}Hf_{6.25}$	64.01	35.56	0.41	Cu_3Pd_$L1_2$	0
	11.63	69.71	19.20	$HfPd_3$	

c. DSC

In order to examine whether alloying elements M (M=Ti, Y, La, Al and Mg) expand the CuPd B2 phase boundary towards higher temperatures, it is necessary to measure the B2↔fcc transition temperatures of these ternary alloys ($Cu_{50}Pd_{43.75}M_{6.25}$). Several methods are widely used to study the order-disorder transition, such as, electrical resistivity measurement, high temperature XRD, DSC and dilatometric methods.

In this study, DSC was used since it is relatively easier and efficient compared to other methods mentioned above. Fig.4 showed the DSC results for $Cu_{50}Pd_{43.75}M_{6.25}$ (M=Al and Mg) alloys. Due to the sluggishness of the order-disorder process (*45*), the small enthalpy value associated with the order-disorder transition and dynamic characteristic of DSC method, the B2↔fcc transition temperatures were not convincingly detected. For example, there are no peaks detected for $Cu_{50}Pd_{43.75}Al_{6.25}$ during heating and cooling. Although there are two peaks observed during heating for $Cu_{50}Pd_{43.75}Mg_{6.25}$, there is only one peak detected during cooling. Similarly, no phase transitions in the solid state were convincingly detected for $Cu_{50}Pd_{43.75}M_{6.25}$ (M=Ti, Y and La) alloys using DSC. Our conclusion is that DSC is not the ideal tool to measure the B2↔fcc phase transition, Currently, we are using high-temperature XRD to measure the B2↔fcc transition temperatures and the results will be published separately.

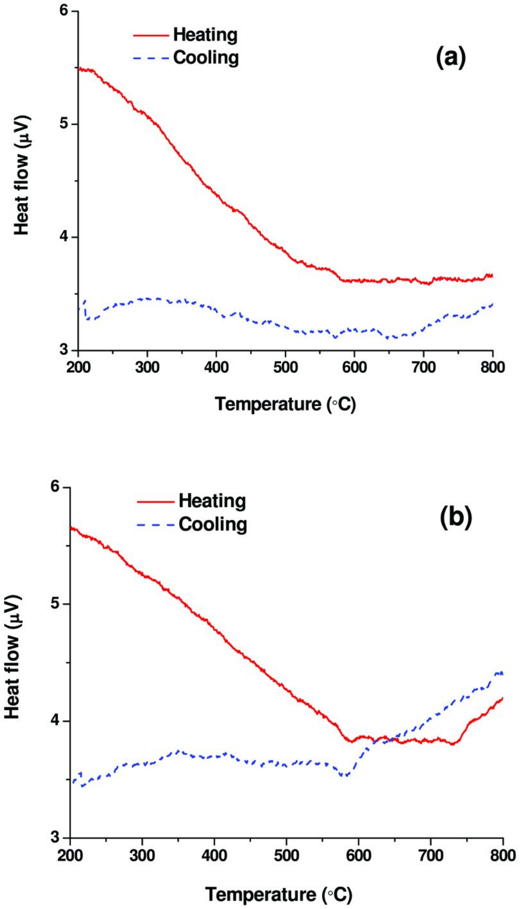

Figure 4. DSC plots for (a) $Cu_{50}Pd_{43.75}Al_{6.25}$ and (b) $Cu_{50}Pd_{43.75}Mg_{6.25}$ alloys.

The present study utilizes predictive DFT calculations to screen for potential alloying elements that can stabilize the CuPd B2 phase field in the Cu-Pd-M ternaries. The screening process was carried out for all transition metals and many non-transition elements without any experimental input. The present DFT calculations are very crude in the sense that we ignore the competing phases against B2 in the individual Cu-Pd-M ternary system and ignore the configurational entropy effect and phonon vibration at finite temperatures. Nonetheless, out of 7 elements recommended for experiments based on our DFT calculations, 5 elements (Mg, Al, Y, Ti, and La) were experimentally verified to expand the phase field of B2 CuPd into the ternary system at 400°C. The present study suggests that utilizing predictive DFT calculations can cut down significantly the number of trial-and-error experiments, and thus accelerates new materials design for hydrogen separation.

Conclusions

This study demonstrated the strategy of designing multi-component alloys by integrating DFT calculations and key experiments. Based on our computational and experimental results, Mg, Al, Y, Ti and La are verified to expand the Cu-Pd B2 phase field into the ternary systems at 400°C.

Acknowledgments

This research was performed in support of the Syngas and Hydrogen Program of the NETL's Strategic Center for Coal under the URS-RES contract DE-FE0004000.

References

1. Office of Fossil Energy, N., *Hydrogen from Coal Program, RD&D Plan, External Draft*; U.S. Dept. of Energy, Editor. September 2008.
2. Stiegel, G. J.; Ramezan, M. *Int. J. Coal Geol.* **2006**, *65*, 173–190.
3. Darling, A. S. The diffusion of hydrogen through palladium. *Platinum Met. Rev.* **1958**, *2* (1), 16.
4. Hunter, J. B. *Surface Area Hydrogen Permeation Cell*; U.S. Patent, Editor. 1960. p 062.
5. DeRosset, A. J. Diffusion of hydrogen through palladium membranes. *Ind. Eng. Chem.* **1960**, *52* (6), 525.
6. Snelling, W. O. *Apparatus for Separating Gases*; U.S. Patent, Editor. 1916. p 631.
7. Grashoff, C. J.; Pilkington, C. E.; Court, C. W. The purification of hydrogen. *Platinum Met. Rev.* **1960**, *4*, 130.
8. Hunter, J. B. Ultra-pure hydrogen by diffusion through palladium. *Abstr. Pap., Am. Chem. Soc.* **1963**, *145*, 12S.
9. Völkl, J.; Alefeld, G. Hydrogen in Metals II. In *Topics in Applied Physics*; Springer-Verlag: New York, 1978; Vol. 29.

10. Völkl, J.; Alefeld, G. Hydrogen in Metals I. Basic Properties. In *Topics in Applied Physics*; Springer-Verlag: New York, 1978; Vol. 28.
11. Musket, R. G. Effects of contamination on the interactions of hydrogen gas with palladium: A review. *J. Less-Common Met.* **1976**, *45*, 173.
12. Dudek, D. Diffusion coefficients of hydrogen in a Pd81Pt19 membrane with time dependent boundary conditions. *J. Alloys Compd.* **2001**, *329* (1-2), 1–7.
13. Kandasamy, K. Influences of self-induced stress on permeation flux and space-time variation of concentration during diffusion of hydrogen in a palladium alloy. *Int. J. Hydrogen Energy* **1995**, *20* (6), 455–463.
14. Huang, L.; et al. Pd-Ni thin films grown on porous Al_2O_3 substrates by metalorganic chemical vapor deposition for hydrogen sensing. *Thin Solid Films* **1999**, *345* (2), 217–221.
15. Nam, S.-E.; Lee, K.-H. A study on the palladium/nickel composite membrane by vacuum electrodeposition. *J. Membr. Sci.* **2000**, *170* (1), 91–99.
16. Meng, G. Y.; et al. Preparation and characterization of Pd and Pd-Ni alloy membranes on porous substrates by MOCVD with mixed metal beta-diketone precursors. *Mater. Res. Bull.* **1997**, *32* (4), 385–395.
17. Fazle Kibria, A. K. M.; Sakamoto, Y. The effect of alloying palladium with silver and rhodium on the hydrogen solubility, miscibility gap and hysteresis. *Int. J. Hydrogen Energy* **2000**, *25* (9), 853–859.
18. Lewis, F. A. Hydrogen in palladium and palladium alloys. *Int. J. Hydrogen Energy* **1996**, *21* (6), 461–464.
19. Keuler, J. N.; Lorenzen, L. Developing a heating procedure to optimise hydrogen permeance through Pd-Ag membranes of thickness less than 2.2 ím. *J. Membr. Sci.* **2002**, *195* (2), 203–213.
20. Amandusson, H.; Ekedahl, L.-G.; Dannetun, H. Hydrogen permeation through surface modified Pd and PdAg membranes. *J. Membr. Sci.* **2001**, *193* (1), 35–47.
21. Lin, Y. S. Microporous and dense inorganic membranes: current status and prospective. *Sep. Purif. Technol.* **2001**, *25* (1-3), 39–55.
22. Tosti, S.; Bettinali, L.; Violante, V. Rolled thin Pd and Pd/Ag membranes for hydrogen separation and production. *Int. J. Hydrogen Energy* **2000**, *25* (4), 319–325.
23. Amandusson, H.; Ekedahl, L.-G.; Dannetun, H. Hydrogen permeation through surface modified Pd and PdAg membranes. *J. Membr. Sci.* **2001**, *193* (1), 35–47.
24. Roa, F.; et al. Preparation and characterization of Pd-Cu composite membranes for hydrogen separation. *Chem. Eng. J.* **2003**, *93* (1), 11–22.
25. Wieland, I. S.; Melin, I. T.; Lamm, I. A. Membrane reactors for hydrogen production. *Chem. Eng. Sci.* **2002**, *57* (9), 1571–1576.
26. Roa, F.; Block, M. J.; Way, J. D. The influence of alloy composition on the H_2 flux of composite Pd-Cu membranes. *Desalination* **2002**, *147* (1-3), 411–416.
27. Howard, B. H.; et al. Hydrogen permeance of palladium–copper alloy membranes over a wide range of temperatures and pressures. *J Membr. Mater.* **2004**, *241*, 207.

28. Han, J.; Kim, I.-S.; Choi, K.-S. High purity hydrogen generator for on-site hydrogen production. *Int. J. Hydrogen Energy* **2002**, *27* (10), 1043–1047.
29. Krueger, C. *Method of improving and optimizing the hydrogen permeability of a palladium-copper membrane and novel membranes manufactured thereby*, U.S. Patent, Editor. 2002. p 363.
30. Gao, H. Y.; et al. Chemical Stability and Its Improvement of Palladium-Based Metallic Membranes. *Ind. Eng. Chem. Res.* **2004**, *43*, 6920.
31. Maeland, A.; Flanagan, T. B. Lattice constants and thermodynamic parameters of the hydrogen-platinum-palladium and deuterium-platinum-palladium systems. *J. Phys. Chem.* **1964**, *68* (6), 1419.
32. Lewis, F. A. Hydrogen interstitial structures in palladium-silver membranes. *Platinum Met. Rev.* **1993**, *37* (4), 220.
33. Cabrera, A. L.; et al. Structural changes induced by hydrogen absorption in palladium and palladium-ruthenium alloys. *Appl. Phys. Lett.* **1995**, *66* (10), 1216.
34. Cabrera, A. L.; et al. Changes in crystallographic orientation of thin foils of palladium and palladium alloys after the absorption of hydrogen. *Catal. Lett.* **1995**, *30*, 11.
35. Lopez, N.; Nørskov, J. K. Synergetic effects in CO adsorption on Cu-Pd (111) alloys. *Surf. Sci.* **2001**, *477* (1), 59–75.
36. Saha, D. K.; Koga, K.; Ohshima, K. I. Short-range order in Cu-Pd alloys. *J. Phys.: Condens. Matter.* **1992**, *4* (49), 10093–10102.
37. Piper , J. Diffusion of hydrogen in copper–palladium alloys. *J. Appl. Phys.* **1966**, *37*, 715.
38. Zetkin, A. S.; et al. Diffusion and penetrability of deuterium in the alloy Pd–53 at.% Cu. *Sov. Phys. Solid State* **1992**, *34*, 83.
39. Kresse, G.; Hafner, J. *Phys. Rev. B* **1993**, *47*, 558.
40. Kresse, G.; Furthmueller, J. *Phys. Rev. B* **1996**, *54*, 11169.
41. Blochl, P. E. *Phys. Rev. B* **1994**, *50* (24), 17953.
42. Perdew, J. P.; Burke, K.; Ernzerhof, M. *Phys. Rev. Lett.* **1996**, *77*, 3865.
43. Monkhorst, H. J.; Pack, J. D. *Phys. Rev. B* **1976**, *13* (12), 5188.
44. Methfessel, M.; Paxton, A. T. *Phys. Rev. B* **1989**, *40* (6), 3616.
45. Harmelin, M.; et al. Study of an order-disorder transition by differential scanning calorimetry. *Thermochim. Acta* **1988**, *125*, 59–78.

Downloaded by STANFORD UNIV GREEN LIBR on June 18, 2012 | http://pubs.acs.org
Publication Date (Web): October 31, 2011 | doi: 10.1021/bk-2011-1078.ch004

Chapter 4

Functional Nanotube Membranes for Hydrophobicity-Based Separations by Initiated Chemical Vapor Deposition (iCVD)

Ayse Asatekin and Karen K. Gleason*

Department of Chemical Engineering, Massachusetts Institute of Technology, 77 Massachusetts Avenue, Cambridge, MA 02139
***E-mail: kkg@mit.edu**

Polymer nanopore membranes, containing long and narrow through-pores with controlled surface chemistry, can be used to perform separations based on specific solute-pore wall interactions. In this study, we describe the manufacture of such membranes with pore diameters as low as 5 nm by a fast, scalable vapor deposition of a fluorinated monomer, and their use for small molecule separations based on hydrophobicity. Increasing selectivity between molecules of similar size but different polarity was observed as pore diameter decreased and as the surface of the pore became more hydrophobic. A maximum selectivity of 83 was achieved. Membranes with small fluorinated pores exhibited an effective cut-off based on the total polar surface area (tPSA) of the molecules, with limited correlation with solute size. This technology could lead to a new generation of membrane separations based on specific interactions.

Introduction

Separation of feed components based on chemical structure is a significant challenge, yet crucial in many applications, including pharmaceutical and biochemical synthesis. These separations are usually performed by chromatography, which is expensive and difficult, especially in the industrial scale (*1*, *2*). Membranes offer a scalable, efficient and easy to operate alternative in many separations (*3*). Most membrane separations, however, are based either

In Modern Applications in Membrane Science and Technology; Escobar, I., et al.;
ACS Symposium Series; American Chemical Society: Washington, DC, 2011.

on size, as in the case of ultrafiltration and microfiltration membranes, or on electrostatics and charge, which is the case for reverse osmosis membranes (*4*). Membranes that can separate small molecules based on their chemical structure and properties, such as hydrophobicity or specific surface interactions, can expand the use of membranes to new applications.

Chemical property-based separations are routinely performed by biological pores in the cell membrane, which can provide inspiration for the design of synthetic membranes with similar function (*5*). Such biological pores consist of through-pores of controlled surface composition, and a diameter that is comparable with the size of the molecules being separated. In such a case, permeation of different solutes is dominated by interaction with pore walls. The solute that interacts more strongly with the wall partitions preferentially into the pore and permeates to the other side. Diffusion through the "bulk" solvent, without wall contact, is severely limited by the small pore diameter. As a result, permeation is regulated based not solely on size but on solute-surface interactions arising from chemical structural properties (*6*). By properly designing the surface, separations can be performed based on properties such as hydrophobicity (*7–10*), charge (*10*, *11*), or even chirality (*12*, *13*). This separation mechanism is strongly related with that of facilitated transport, where molecules are carried on the pore walls rather than through interactions with functional groups distributed throughout the membrane (*6*).

The separation of small molecules by this method requires membranes containing cylindrical pores that are only a few nanometers in diameter with controlled surface chemistry, which is quite difficult to achieve. One method uses atomic layer deposition (ALD) to narrow down the pores of anodized aluminum oxide (AAO) membranes to desired size, then applies silanes for surface functionalization (*14*). This relatively complicated method requires exposure to high temperatures (>200^{o}C), which limits it to inorganic substrates. The diffusion selectivities achieved with these membranes are also low, around 5.5 (*14*). Other researchers have reported taking advantage of the self-assembly of polymers during filtration through track-etched membranes to form 6-9 nm pores (*15*). While this method is simple, it is not possible to alter the pore size or functionality without the synthesis of a new polymer. Furthermore, the resultant pore size is too large for effective separation of small molecules, as indicated by selectivities as low as 3 (*15*).

To date, gold nanotube membranes have been the most common method for the manufacture of nanopore membranes for small molecule separations (*2*, *8*, *9*, *11*, *16–18*). These membranes are prepared by narrowing down the pores of either track-etched or AAO membranes by the electroless deposition of gold, followed by treatment with a functional thiol to form a self-assembled monolayer (SAM) on the pore walls. Gold nanotube membranes have been studied for small-molecule separations based on hydrophobicity (*7–10*), charge (*10*, *11*), chirality (*12*, *13*) and size (*11*, *16*, *19*), and offer selectivities as high as 200 based on chemical structure (*9*). Nevertheless, the manufacture of these membranes is complicated and time consuming. The electroless deposition process consists of three major steps and uses toxic chemicals and heavy metals salts. Only the final plating step can take as long as 20 hours, while SAM formation can add up to 24 hours.

Downloaded by STANFORD UNIV GREEN LIBR on June 18, 2012 | http://pubs.acs.org
Publication Date (Web): October 31, 2011 | doi: 10.1021/bk-2011-1078.ch004

Downloaded by STANFORD UNIV GREEN LIBR on June 18, 2012 | http://pubs.acs.org
Publication Date (Web): October 31, 2011 | doi: 10.1021/bk-2011-1078.ch004

For the wide-spread use of nanopore membranes for small molecule separations, a simpler, faster and cleaner manufacturing method is needed. In this study (*20*), we demonstrate the manufacture of nanopore membranes with hydrophobic pores of controllable diameter down to ~5 nm by a much faster, solvent-free, highly conformal and customizable initiated chemical vapor deposition (iCVD) process, which directly translates free radical polymerization into a chemical vapor deposition (CVD) process (*21–23*). This method allows the customization of pore size through the choice of coating thickness, and the chemical composition of the surface through the choice of monomer. In this study, the effect of pore size and surface hydrophobicity is studied in the context of the separation of molecules of similar size but different chemical structure. We also demonstrate the relative effects of size and hydrophobicity on the selectivity of these membranes.

Experimental Section

Formation of Nanopore Membranes

Nanopore membranes were prepared by iCVD coating of track-etched membranes (Millipore Isopore 0.05 μm) with 50 nm pores and 20 μm in thickness. This process was described in detail elsewhere (*20*). iCVD was performed in a reactor described earlier (*24*), 1H,1H,2H,2H-perfluorodecyl acrylate (PFDA, Alfa Aesar) and divinyl benzene (DVB, VWR) were used as monomers, and *tert*-butyl peroxide (TBPO, Aldrich) was used as initiator. The filament temperature was 250°C. For membranes F5 and F9, PFDA (80°C, 0.4 sccm) and TBPO (1.2 sccm) were delivered to the reactor maintained at 50 mTorr. The substrate stage was held at 40°C. The deposition time was 40-45 min. For membrane X5, DVB (50°C, 1.0 sccm), TBPO (0.7 sccm) and nitrogen gas (0.8 sccm) were fed into the reactor held at 200 mTorr. The overall deposition time was 2-3 hours. The sample stage temperature was 30°C.

Characterization of iCVD Coatings

iCVD coating characterization was performed on films deposited on silicon wafers. Coating thickness was measured using variable angle spectroscopic ellipsometry (VASE, JA Woollam M-2000) at a 65° angle. Chemical characterization of the films was performed using Nexus 870 FTIR (Thermo Nicolet). For contact angle measurements (Rame-Hart, Schott) deionized waster droplets of 2 μL were dropped onto the sample. Advancing contact angle was measured by adding five 2-μL droplets consecutively, measuring the contact angle after each drop. Receding contact angle was measured by removing water from this droplet 2 μL at a time.

Characterization of Membrane Pore Size

Pore sizes of the membranes were estimated from the gas diffusion experiments, as described in literature (*17*). The membrane, 25 mm in diameter,

Downloaded by STANFORD UNIV GREEN LIBR on June 18, 2012 | http://pubs.acs.org
Publication Date (Web): October 31, 2011 | doi: 10.1021/bk-2011-1078.ch004

was placed into an in-line gas filter holder (Cole-Palmer) and secured with a rubber O-ring to prevent leaks. CO_2 gas was fed to the cell at four different pressures 25-40 psi. Flow rate was measured by a bubble flow meter (Aldrich). The slope of the flow rate-pressure plot was used to determine the permeance of the membrane. It was assumed that the narrowed pores remain cylindrical, their number density remains unchanged, and Knudsen flow occurs within the pores. Under such assumptions, the permeance (flux divided by pressure difference) of the membrane is directly proportional with the cube of the pore radius (*17*). Pore size was estimated based on the permeance of the uncoated membrane, assuming its pore size to be 50 nm (*17*, *20*). This assumption was confirmed by scanning electron microscopy (SEM) of the uncoated membrane samples, which were measured to have a mean pore size of 55 nm and median pore size of 48 nm (*20*).

Electron Probe Microanalysis (EPMA)

Membranes were fractured in liquid nitrogen and mounted on a vertical sample holder to expose the cross-section. The samples were sputter-coated with carbon. EPMA was performed on JEOL-JXA-733 Superprobe by Dr. Nilanjan Chatterjee at two spots on the membrane cross-section, one near the top surface and one near the bottom surface.

Diffusion Experiments

Isopropanol, 4-phenylazodiphenylamine (PADPA), alizarin yellow GG (AY), 4-phenylazoaniline (PAA), mesitylene (Mes) and phloroglucinol (Phl) were purchased from VWR. Diffusion of the solutes was measured in a standard diffusion cell. Membranes were sandwiched between two rubber O-rings, and clamped between glass fittings (Kemtech). 25 mL of feed solution (10^{-3} M for PADPA, PAA and AY, 10^{-2} for Mes and Phl, in isopropanol) was placed into the source chamber. 100 mL isopropanol was placed into the sink. 2 mL fractions were removed from the sink at regular intervals, and the test was continued until the sink concentration was significantly above the detection limit for the solute for several data points. Solute concentrations were quantified by UV-visible spectroscopy (Beckman Coulter DU800). Solvent excluded volume and total polar surface area (tPSA) values were calculated using Chem3D Pro 12.0 software.

Results and Discussion

iCVD for the Formation of Nanopore Membranes

iCVD is a process that forms polymer coatings that are conformal, pinhole-free, and of custom thickness and chemical structure (*21–23*, *25*, *26*). Essentially any monomer that undergoes free radical polymerization and of sufficient volatility for CVD can be used. iCVD can also be scaled up for roll-to-roll processing (*27*), which is crucial for the commercial production of novel membranes. As such, iCVD is an ideal method for the formation of nanopore membranes. In the

Downloaded by STANFORD UNIV GREEN LIBR on June 18, 2012 | http://pubs.acs.org
Publication Date (Web): October 31, 2011 | doi: 10.1021/bk-2011-1078.ch004

iCVD process, the substrate (in this case the track-etched membrane) is placed on a chilled stage in a chamber held at low vacuum (Figure 1a). The monomer(s) and a thermally labile initiator are fed into the reactor in the vapor phase. Heated filaments above the substrate cause the initiator to generate free radicals, which adsorb onto the substrate together with the monomer molecules. Free radical polymerization is thus initiated, and a polymer film builds on the membrane. The exceptional capability of iCVD to form conformal coatings (*20*, *25*) allows the gradual narrowing of the cylindrical pores of the membrane to a diameter of a few nm (Figure 1b).

In this study, we focused on separating small molecules by hydrophobicity. For this purpose, polycarbonate (PC) track-etched membranes were used as the base material. The PC membranes were placed into the iCVD reactor on the chilled stage, and either a fluorinated or a hydrocarbon polymer was deposited under conditions that insured good conformality (*20*, *25*, *26*, *28*, *29*). For hydrophobic membranes, a fluorinated polymer, poly(1H,1H,2H,2H-perfluorodecyl acrylate) (pPFDA), was deposited (see Figure 2 for monomer structure) (*20*, *28*, *29*). This process is much faster than alternatives such as electroless deposition of gold. The deposition time for these membranes was only 40-45 minutes, and the whole process, including the loading of the substrate into the reactor and pumping down the vacuum chamber, was usually complete in less than 2 hours. Two fluorinated membrane samples of different pore sizes were prepared, F5 and F9. In this notation, “F” indicates a fluorinated coating, while the numeral is the approximate pore size in nanometers, estimated from gas permeation measurements (*17*, *20*) (see Table 1). pPFDA films had very high contact angles of 118^{o}, which confirm their low surface energy and hydrophobic nature. As the coating thickness measured on the flat silicon substrate increased, the measured pore size became smaller. While this trend was monotonic, it was not linear. This could be due to the polydispersity of the pore sizes of the base PC track-etched membrane, which leads to the narrowing and blocking of smaller pores before others (*20*).

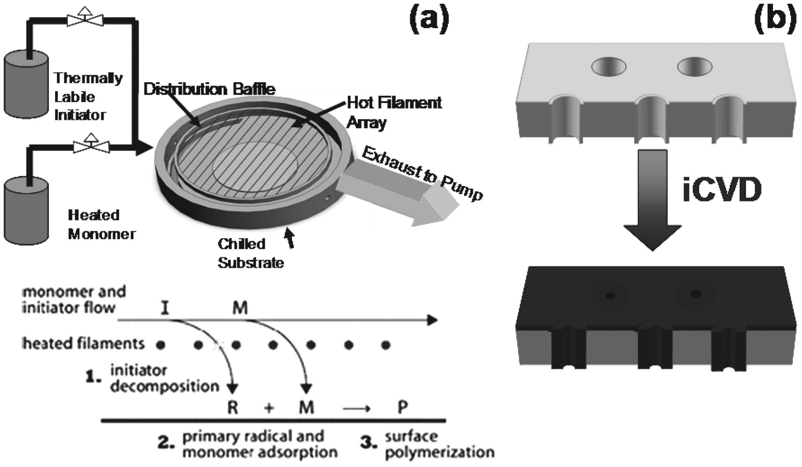
(a)
(b)
Thermally Labile Initiator
Distribution Baffle
Hot Filament Array
Exhaust to Pump
Heated Monomer
Chilled Substrate
monomer and initiator flow
I
M
heated filaments
1. initiator decomposition
R + M ⟶ P
2. primary radical and monomer adsorption
3. surface polymerization
iCVD

Figure 1. (a) A schematic of the iCVD process. (b) Formation of nanopore membranes through the narrowing of pores by iCVD.

Another membrane (labeled X5) was coated with poly(divinyl benzene) (pDVB), a cross-linked polymer, as a control with relatively lower hydrophobicity (*30*). pDVB exhibits a contact angle similar to that of PC, around 80°. Therefore, a pDVB coated membrane would be expected to show a lower hydrophobicity-based selectivity than a pPFDA coated membrane of similar pore size. Since the pore size of the DVB coated membrane X5 was approximately 5 nm (Table 1), its comparison with the F5 membrane would demonstrate the effect of surface energy.

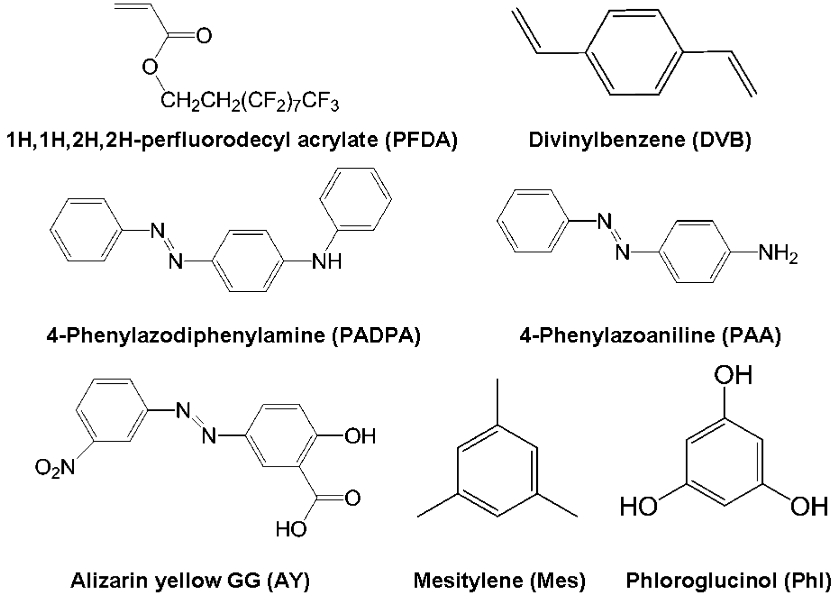

1H,1H,2H,2H-perfluorodecyl acrylate (PFDA) **Divinylbenzene (DVB)**

4-Phenylazodiphenylamine (PADPA) **4-Phenylazoaniline (PAA)**

Alizarin yellow GG (AY) **Mesitylene (Mes)** **Phloroglucinol (Phl)**

Figure 2. Chemical structures of the monomers and solute molecules used in this study.

Table 1. Properties of Membrane Samples. Adapted from (*20*). Copyright 2010 ACS

sam-ple	*mate-rial*	*Film thickness on flat substrate (nm)*	*contact angle with water*			*CO_2 permeance ($L/m^2.h.MPa$)[a]*	*calcu-lated pore size (nm)[b]*
			ses-sile	*advanc-ing*	*reced-ing*		
F9	PFDA	64.3±0.1	118±3	153±2	107±3	1000±20	8.7±0.1
F5	PFDA	69.2±0.2	118±6	152±1	105±3	145±15	4.4±0.1
X5	DVB	105.5±0.1	80±1	84±1	6-±3	222±15	4.6±0.1

[a] CO_2 permeance of the uncoated PC membrane was 2.2 x 10^5 L/m^2.h.MPa. [b] Assuming the pore diameter was 50 nm. This was verified by microscopy in a separate study (*20*).

Downloaded by STANFORD UNIV GREEN LIBR on June 18, 2012 | http://pubs.acs.org
Publication Date (Web): October 31, 2011 | doi: 10.1021/bk-2011-1078.ch004

Downloaded by STANFORD UNIV GREEN LIBR on June 18, 2012 | http://pubs.acs.org
Publication Date (Web): October 31, 2011 | doi: 10.1021/bk-2011-1078.ch004

One challenge in the manufacture of nanopore membranes was to insure conformality of the coatings, especially given the very high aspect ratios of the pores: The base membranes are approximately 20 μm in thickness, and initially the pores are 50 nm in diameter. This indicates a minimum initial aspect ratio of 400. The fact that most pores are not vertical to the membrane surface, and the decrease in pore size during the deposition, results in much higher values throughout the process. It is a great challenge to form conformal coatings under these conditions. However, it is not possible to image such small polymeric pores in cross-section, especially since they are far apart and not vertical. Hence, elemental analysis by Electron Micro-Probe Analysis (EPMA) was used to quantify the fluorine content at the top and bottom regions of the membranes. As a control, uncoated and X5 membranes were also analyzed. No fluorine was detected in these samples. The fluorine content at the bottom of the PFDA coated F5 membrane was measured to be 0.48 ± 0.12 wt%, indicating that the PFDA coating does penetrate to the bottom of the membrane despite the very high aspect ratio. The fluorine content at the top portion of the membrane was measured to be 0.876 ± 0.124 wt%. The fact that this value is higher implies that there is still some non-conformality to the PFDA coating, and the pores that result are of a bottleneck shape, narrower on top and wider at the bottom (*20*). Compared with bottleneck pores, cylindrical through-pores exhibit better separation performance since the distance through which the solutes interact with the walls is longer (*6*). Therefore, achieving better conformality for the deposition of functional coatings by iCVD would improve the performance of nanopore membranes. The conformality of these films and the use of two-layer coatings to get nanopore membranes with cylindrical pores with even higher selectivity is discussed in a separate study (*20*).

Hydrophobicity-Based Diffusion Selectivity

The most important parameter for the performance of a membrane is its separation capability. In this study, we focused on the separation of small molecules based on hydrophobicity rather than size. For this purpose, we performed diffusion experiments with five molecules, the chemical structures of which are given in Figure 2. Two key properties of these molecules, calculated by ChemBioOffice 12.0 software, are listed in Table 2. The solvent excluded volume was selected as the main parameter that defines size. The hydrophilicity/hydrophobicity of the solute was quantified using the total polar surface area (tPSA). This parameter is defined as the total surface are of all polar atoms, and is calculated from the 3D structure of the molecule. It is lower for more hydrophobic molecules. tPSA is documented as one of the best hydrophobicity-based parameters to predict the oral absorption and blood-brain barrier penetration of pharmaceuticals (*31*), and the permeability of chemicals through artificial cell membrane mimics (*32*). As such, it is expected to be a an important parameter in determining the degree of interaction of these molecules with the hydrophobic nanopore walls.

Table 2. Key Chemical Parameters of Solute Molecules and their Diffusion Rates through the Membranes Analyzed

Solute	*Solvent excluded volume (Å³)*	*Total polar surface area (Å²)*	*Diffusion rate/feed concentration (L/h)*			
			PC	*F9*	*F5*	*X5*
PADPA	215.6	36.8	$9.55x10^{-5}$	$6.36x10^{-5}$	$3.42x10^{-5}$	$2.23x10^{-5}$
PAA	156.6	50.74	$6.01x10^{-5}$	$3.78x10^{-5}$	$5.67x10^{-6}$	$3.33x10^{-5}$
AY	197.2	134.1	$2.77x10^{-5}$	$6.28x10^{-6}$	$2.33x10^{-6}$	$6.21x10^{-7}$
Mes	122.1	0	$2.66x10^{-4}$	$1.16x10^{-4}$	$6.92x10^{-5}$	$6.92x10^{-5}$
Phl	90.4	60.7	$6.90x10^{-5}$	$1.33x10^{-5}$	$8.34x10^{-7}$	$7.68x10^{-6}$

Of these molecules, the first three, PADPA, PAA and AY, are dyes. PADPA and AY are of similar size, as indicated by their similar solvent excluded volumes. PADPA is much more hydrophobic than AY, which contains several polar groups such as –OH, COOH and $–NO_2$. This is also evidenced by the difference in tPSA values for these molecules. PAA is a slightly smaller molecule with intermediate hydrophobicity. The last two molecules, Mes and Phl, are almost exactly identical in size. The only difference between these two molecules is the presence of three –OH groups in Phl, which are replaced with three $–CH_3$ groups in Mes.

The diffusion rates of these molecules through the three membranes listed as well as the uncoated PC membrane are given in Table 2. The experiments were performed in isopropanol, as the pores of the PFDA coated membranes were too hydrophobic to be wetted effectively and reproducibly in water. From these values, the diffusion selectivity, defined as the ratio of diffusion rates, was calculated for two pairs of molecules of similar size: PADPA-AY and Mes-Phl. A high diffusion selectivity for these pairs would be a strong indication of a membrane's capability to separate two molecules of a similar size by hydrophobicity. It should be noted that all membranes described in this study, including PC and X5, are hydrophobic to a certain extent, with the PFDA coated samples exhibiting this trait much more strongly. In all cases, the more hydrophobic molecule was shown to diffuse faster than its more hydrophilic counterpart, which confirms that membrane-solute interactions can drive selectivity.

In Figure 3, diffusion selectivities for AY-PADPA and Mes-Phl molecule pairs are plotted versus two key membrane properties, pore size and contact angle (indicating surface energy). This plot demonstrates the strong influence of surface energy as the enabler of hydrophobicity-based separations, especially when two membranes of similar pore diameter, X5 and F5, are compared. While pDVB coated X5 shows quite low selectivities for both molecule pairs, F5 showed the best selectivity among these membranes. In fact, in F5, hydrophobic Mes was shown to diffuse 83 times faster than Phl, a hydrophilic molecule of similar size. X5 showed a selectivity of only 9. It should be noted that pDVB is a relatively hydrophobic material with no polar groups as well, so the stark difference is quite remarkable. A similar trend is observed for PADPA and AY, though the overall

Downloaded by STANFORD UNIV GREEN LIBR on June 18, 2012 | http://pubs.acs.org
Publication Date (Web): October 31, 2011 | doi: 10.1021/bk-2011-1078.ch004

selectivity was lower. This appears to arise from the fact that PADPA, unlike Mes, contains some polar amine groups that partially hinder the passage of this molecule as well as that of AY. This is studied in more detail below as well, where the mechanism of separation is analyzed.

The strong influence of pore size on selectivity can also be observed in Figure 3, especially when the two PFDA coated membranes, F9 and F5, are compared. The membrane with smaller diameter pores, F5, exhibits much higher selectivity than F9 for both molecule pairs. This result conforms to the hypothesis that if the pores are narrow enough, diffusion on the pore walls dominates diffusion through the bulk solvent within the pores. When the pores become smaller, this effect is emphasized further as the amount of bulk solvent that does not interact with the walls decreases further. It should be noted that the track-etched membranes contain a certain munber of double- and triple-pores, which would diminish the separation capability by introducing larger pores even after coating. Therefore, even better separations are possible if membranes with monodisperse pores are used as the substrate.

When the pore size decreases from 9 nm to 5 nm, the change in Mes/Phl selectivity is much more dramatic than that for PADPA/AY, which are larger molecules. This is related with the molecule/pore size ratio: 5 nm pores appear to be small enough to regulate the passage of all molecules. However, while the 9 nm pores are sufficiently small to limit the permeation of the larger hydrophilic molecule AY and show high PADPA/AY selectivity, it is much less capable of constraining the passage of the much smaller hydrophilic molecule Phl. Narrower pores are required for this separation. For the PADPA/AY pair, a sudden increase in selectivity would be expected at a higher nominal pore size, where the pore size/molecular diameter ratio reaches the critical value. All these trends are in agreement with computational models that analyze permeation through nanopore systems (*6*).

Downloaded by STANFORD UNIV GREEN LIBR on June 18, 2012 | http://pubs.acs.org
Publication Date (Web): October 31, 2011 | doi: 10.1021/bk-2011-1078.ch004

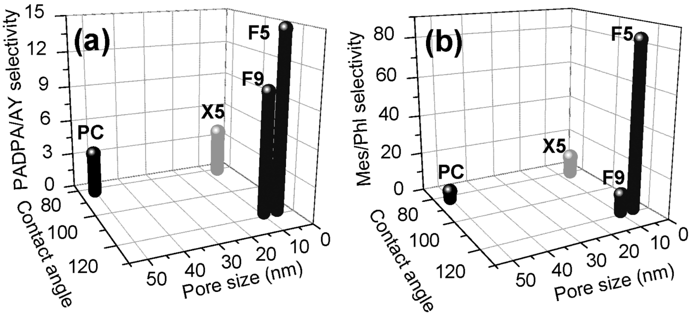

Figure 3. Variation of selectivity between molecules of similar size but contrasting hydrophobicity, PADPA vs. AY (a) and Mes vs. Phl (b), with membrane pore size and contact angle. Black column refers to uncoated PC membrane. pDVB coated X5 is light gray. Single layer pPFDA coated membranes F5 and F9 are dark gray. Adapted from (20), copyright ACS 2010.

Downloaded by STANFORD UNIV GREEN LIBR on June 18, 2012 | http://pubs.acs.org
Publication Date (Web): October 31, 2011 | doi: 10.1021/bk-2011-1078.ch004

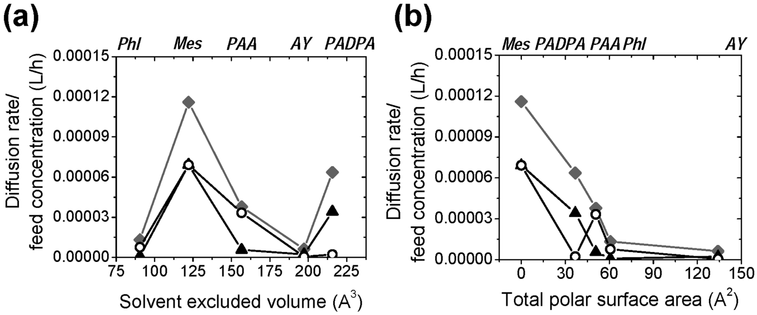

Figure 4. Dependence of diffusion rate normalized by feed concentration through different membranes on (a) solvent excluded volume and (b) total polar surface area (tPSA) of permeant. Permeant names are labeled along top axis. ○: X5, ♦: F9, ▲: F5. Modified from (20), copyright ACS 2010.

Mechanism of Selectivity: Size versus Hydrophobicity

Based on the data we acquired with these solute molecules, we wanted to compare the relative influence of hydrophobicity and size on the diffusion rate of solutes through these nanopore membranes. If we intend to design a membrane that separates based on hydrophobicity, we would ideally like the influence of other factors, including size, to be minimal. However, this is difficult to achieve, as the diffusivity of molecules is strongly influenced by their hydrodynamic diameter. Hence, it is useful to compare the relative influence of size and hydrophobicity on the diffusion rate of different molecules through the nanopore membranes described here, to better understand the mechanisms of permeation and separation.

Figure 4 shows the variation of the diffusion rate normalized by feed concentration for the five molecules through the nanopore membranes, with solute size (Figure 4a) and with hydrophobicity quantified by tPSA (Figure 4b). Diffusion rate does not change monotonously with solute size for any of the membranes, as evidenced by large fluctuations (Figure 4a). This indicates that a competition between size effects, which favor the passage of small molecules, and hydrophobicity effects, which favor hydrophobic molecules, exists even for the less hydrophobic membranes such as X5. These fluctuations are stronger for the PFDA coated membranes.

In comparison, a strong relationship exists between diffusion rate and tPSA (Figure 4b), especially for the pPFDA coated membranes F9 and F5. Diffusivity decreases with tPSA in general for all membranes. For the X5 membrane, this decrease is not monotonous: The diffusion rates of PAA and Phl are higher than that of the more hydrophobic PADPA, as an evidence of size effects. For the other two membranes, F9 and F5, diffusion rates decrease monotonously with increasing tPSA. F5 essentially displays tPSA-based cut-off behavior, as evidenced by very low diffusion rates for molecules with tPSA above a critical value around 40-50 Å^2. F9, on the other hand, allows the passage of even the more hydrophilic molecules to a certain extent due to its larger pore size. These data are especially interesting, as they demonstrate the possibility of decreasing the effects of molecular size on separation performance significantly by proper membrane design (*20*). When the size of the membrane pores is decreased to a level comparable with the size of the targeted molecules, and if the narrow pore region is long enough, the pore wall-molecule interactions overtake size limitations. The existence of a tPSA based cut-off is also significant, since it could be beneficial in predicting selectivity of hydrophobic nanopore membranes for specific applications based on a limited number of permeation experiments.

Downloaded by STANFORD UNIV GREEN LIBR on June 18, 2012 | http://pubs.acs.org
Publication Date (Web): October 31, 2011 | doi: 10.1021/bk-2011-1078.ch004

Conclusions

This study describes the manufacture of polymer nanopore membranes with nominal pore sizes as low as 5 nm and custom surface chemistry, using a simple iCVD process. This method allows the tuning of pore size and chemistry independently, without the use of heavy metals or toxic solvents, through a fast and scalable vapor based process. When the membranes are designed to have fluorinated, highly hydrophobic pores, it is possible to separate small molecules based on hydrophobicity. Selectivity is higher with smaller and more hydrophobic pores. Diffusion selectivities as high as 83 were achieved between small molecules of similar size but varying hydrophobicity. Finally, we have shown that with proper design of the membrane structure and chemistry, it is possible to decrease the influence of molecular size on the diffusion rate through the membranes while emphasizing the effect of specific interactions. This technology could open the way for a new generation of membrane that separate small molecules based on specific interactions.

Acknowledgments

This research was supported by the U.S. Army through the Institute for Soldier Nanotechnologies, under Contract DAAD-19-02-D-0002 with the U.S. Army Research Office. The authors would like to thank Dr. Nilanjan Chatterjee at MIT Department of Earth and Atmospheric Sciences for EPMA analysis, and to the lab of Prof. Kristala Jones Prather at MIT Department of Chemical Engineering for the use of the UV-visible spectrophotometer. This work made use of MRSEC Shared Experimental Facilities supported by the National Science Foundation under Award DMR-0213282.

References

1. van Reis, R.; Zydney, A. *Curr. Opin. Biotechnol.* **2001**, *12*, 208–211.
2. Jirage, K. B.; Martin, C. R. *Trends Biotechnol.* **1999**, *17*, 197–200.
3. Ulbricht, M. *Polymer* **2006**, *47*, 2217–2262.
4. Han, J. Y.; Fu, J. P.; Schoch, R. B. *Lab Chip* **2008**, *8*, 23–33.
5. Jing, P.; Haque, F.; Vonderheide, A. P.; Montemagno, C.; Guo, P. X. *Mol. BioSyst.* **2010**, *6*, 1844–1852.

6. Zilman, A.; Di Talia, S.; Jovanovic-Talisman, T.; Chait, B. T.; Rout, M. P.; Magnasco, M. O. *PLoS Comput. Biol.* **2010**, *6*, e1000804.
7. Huang, S. S.; Yin, Y. F. *Anal. Sci.* **2006**, *22*, 1005–1009.
8. Hulteen, J. C.; Jirage, K. B.; Martin, C. R. *J. Am. Chem. Soc.* **1998**, *120*, 6603–6604.
9. Velleman, L.; Shapter, J. G.; Losic, D. *J. Membr. Sci.* **2009**, *328*, 121–126.
10. Yue, Z. L.; Zhao, G. G.; Huang, S. S.; Fan, X. X.; Shi, W. L.; Zhang, Z. H. *J. Membrane Sci.* **2010**, *356*, 117–122.
11. Martin, C. R.; Nishizawa, M.; Jirage, K.; Kang, M. *J. Phys. Chem. B* **2001**, *105*, 1925–1934.
12. Shao, P.; Ji, G.; Chen, P. *J. Membr. Sci.* **2005**, *255*, 1–11.
13. Lee, S. B.; Mitchell, D. T.; Trofin, L.; Nevanen, T. K.; Soderlund, H.; Martin, C. R. *Science* **2002**, *296*, 2198–2200.
14. Velleman, L.; Triani, G.; Evans, P. J.; Shapter, J. G.; Losic, D. *Microporous Mesoporous Mater.* **2009**, *126*, 87–94.
15. Savariar, E. N.; Krishnamoorthy, K.; Thayumanavan, S. *Nat. Nanotechnol.* **2008**, *3*, 112–117.
16. Jirage, K. B.; Hulteen, J. C.; Martin, C. R. *Science* **1997**, *278*, 655–658.
17. Jirage, K. B.; Hulteen, J. C.; Martin, C. R. *Anal. Chem.* **1999**, *71*, 4913–4918.
18. Wirtz, M.; Parker, M.; Kobayashi, Y.; Martin, C. R. *Chem. Rec.* **2002**, *2*, 259–267.
19. Wirtz, M.; Yu, S. F.; Martin, C. R. *Analyst* **2002**, *127*, 871–879.
20. Asatekin, A.; Gleason, K. K. *Nano Lett.* **2011**, *11*, 677–686.
21. Alf, M. E.; Asatekin, A.; Barr, M. C.; Baxamusa, S. H.; Chelawat, H.; Ozaydin-Ince, G.; Petruczok, C. D.; Sreenivasan, R.; Tenhaeff, W. E.; Trujillo, N. J.; Vaddiraju, S.; Xu, J. J.; Gleason, K. K. *Adv. Mater.* **2010**, *22*, 1993–2027.
22. Asatekin, A.; Barr, M. C.; Baxamusa, S. H.; Lau, K. K. S.; Tenhaeff, W.; Xu, J. J.; Gleason, K. K. *Mater. Today* **2010**, *13*, 26–33.
23. Tenhaeff, W. E.; Gleason, K. K. *Adv. Funct. Mater.* **2008**, *18*, 979–992.
24. Trujillo, N. J.; Baxamusa, S. H.; Gleason, K. K. *Chem. Mater.* **2009**, *21*, 742–750.
25. Baxamusa, S. H.; Gleason, K. K. *Chem. Vap. Deposition* **2008**, *14*, 313–318.
26. Baxamusa, S. H.; Gleason, K. K. *Thin Solid Films* **2009**, *517*, 3536–3538.
27. Gupta, M.; Gleason, K. K. *Thin Solid Films* **2006**, *515*, 1579–1584.
28. Gupta, M.; Gleason, K. K. *Langmuir* **2006**, *22*, 10047–10052.
29. Gupta, M.; Gleason, K. K. *Thin Solid Films* **2009**, *517*, 3547–3550.
30. Ozaydin-Ince, G.; Gleason, K. K. *Chem. Vap. Deposition* **2010**, *16*, 100–105.
31. Kelder, J.; Grootenhuis, P. D. J.; Bayada, D. M.; Delbressine, L. P. C.; Ploemen, J. P. *Pharm. Res.* **1999**, *16*, 1514–1519.
32. Zhu, C. Y.; Jiang, L.; Chen, T. M.; Hwang, K. K. *Eur. J. Med. Chem.* **2002**, *37*, 399–407.

Downloaded by STANFORD UNIV GREEN LIBR on June 18, 2012 | http://pubs.acs.org
Publication Date (Web): October 31, 2011 | doi: 10.1021/bk-2011-1078.ch004

Downloaded by STANFORD UNIV GREEN LIBR on June 19, 2012 | http://pubs.acs.org
Publication Date (Web): October 31, 2011 | doi: 10.1021/bk-2011-1078.ch005

Chapter 5

Comparison of Membrane Performance of PDMS-Based Membranes during Ethanol/Water Pervaporation and Fermentation Broth Pervaporation

S. Chovau,[1] S. Gaykawad,[2] A. J. J. Straathof,[2] and B. Van der Bruggen*,[1]

[1]Department of Chemical Engineering, Laboratory of Applied Physical Chemistry and Environmental Technology, K.U.Leuven, W. de Croylaan 46, B-3001 Leuven, Belgium
[2]Department of Biotechnology, Delft University of Technology, Julianalaan 67, 2628 BC Delft, The Netherlands
***E-mail: Bart.VanderBruggen@cit.kuleuven.be**

In this study, fermentation broth pervaporation is compared to ethanol/water pervaporation. Laboratory unfilled en ZSM-5 filled PDMS membrane samples were used for this purpose. No significant changes were observed for the unfilled membrane, whereas water flux of the zeolite filled membrane was higher during fermentation broth pervaporation, which resulted in a lower permeate ethanol concentration. Subsequently this membrane was subjected to experiments with model ethanol/water mixtures in which the main fermentation by-products were individually added.

It was found that carboxylic acids were responsible for the decreased membrane performance, their concentration rather than the nature of the acid itself determining the extent of membrane deterioration. An explanation was provided by interaction of the carboxylic acids with silanol end-groups of the zeolite surface rendering the membrane more hydrophilic. This was further confirmed by a decrease in water contact angle of the membrane after the experiments with acidic solutions. Membrane fouling could be avoided by increasing the pH to

In Modern Applications in Membrane Science and Technology; Escobar, I., et al.;
ACS Symposium Series; American Chemical Society: Washington, DC, 2011.

more neutral environments since dissociated ions hardly adsorb on zeolite particles.

Introduction

Global warming and depletion of fossil fuels are the main factors which have increased interest research towards more sustainable energy sources (*1*). This is especially true in the transport sector, due to the high contribution of greenhouse gas (GHG) emissions, which is expected to increase even more in the future (*2*, *3*). Bio-ethanol, or ethanol derived from biomass, has been recognized as a potential alternative to petroleum based transportation fossil fuels (*4*, *5*). The main step in the production process of fuel grade bio-ethanol is the fermentation of simple sugars into ethanol (*6*). Since ethanol fermentation is inhibited by the ethanol product itself, rather low ethanol concentrations are reached in the final fermentation broths (*7*, *8*). Lignocellulosic biomass was found to be the most promising feedstock for fermentation processes, due to its availability and low cost (*9*). However, if this feedstock is used final ethanol concentrations in the broths will be significantly lower (< 5 wt. %) than encountered for starch-based feedstocks (*1*, *10*).

So far, distillation is commonly used as the main separation step to purify the ethanol in the fermentation broth to anhydrous ethanol. However, energy requirements increase exponentially when ethanol concentration in the feed solution fall below 5 wt. % (*11*, *12*). Moreover this technique has other disadvantages, such as batch-operation of the fermentor, low glucose-to-ethanol yield and no reuse of salts and microorganisms (*8*). Pervaporation is one of the most promising alternatives, due to the simplicity of operation, the absence of extra chemicals, low energy requirements and hence low operational cost (*7*, *8*, *13–15*). Furthermore, a pervaporation unit coupled to a fermentor will selectively remove ethanol from the broth, hence keeping the ethanol concentration below inhibitory levels for the microorganisms as demonstrated in several studies (*16–19*). This combination could possibly lead to a significant reduction in bio-ethanol cost in the future.

While ethanol and water are the main components in a fermentation broth, often a variety of by-products are encountered, which could hinder the purification. It was found by several authors, that sometimes the membrane performance is strongly affected due to the presence of these by-products, which limits the commercial applicability of a pervaporation system. Hence the aim of this work is to compare fermentation broth pervaporation with general ethanol/water pervaporation, and to clarify the similarities and differences between the two processes.

Downloaded by STANFORD UNIV GREEN LIBR on June 19, 2012 | http://pubs.acs.org
Publication Date (Web): October 31, 2011 | doi: 10.1021/bk-2011-1078.ch005

Downloaded by STANFORD UNIV GREEN LIBR on June 19, 2012 | http://pubs.acs.org
Publication Date (Web): October 31, 2011 | doi: 10.1021/bk-2011-1078.ch005

Materials and Methods

Membranes

In this research, laboratory-made unfilled (M1) and ZSM-5 (CBV 3002) filled (M2) PDMS/PI composite membranes were investigated. The synthesis method of both PDMS-based membranes is described elsewhere (*20*).

Contact Angle Measurements

Contact angle measurements are performed by putting a liquid drop on the top layer of the membrane and examining the contact angle with a special camera (sessile drop method). Contact angles of a water drop were measured and analyzed at room temperature with a Krüss Drop Shape Analysis System (DSA 10 Mk2). Membrane samples were subjected to contact angle measurements before and after experiments to investigate the influence of the feed solution on the hydrophobicity degree. Every time five measurements were done on each membrane sample.

Fermentation

Fermentation medium was prepared in distilled water, which contained only glucose. After autoclaving the glucose solution at 121 °C for 20 min, baker's yeast (Yeast from Saccharomyces cerevisiae, Type II, Sigma-Aldrich) was added. Per liter of pure water, the mixture contained 65 g glucose and 1 g yeast. Ethanol fermentation was carried out at 30°C and homogeneous stirring (500 rpm) until the fermentation broth composition remained constant (~5 days).

Experimental Section

All experiments were carried out with a laboratory cross-flow pervaporation set-up (Lab Test Cell Unit, Sulzer Chemtech) as described by Dotremont et al. (*21*). The feed solution temperature was kept constant at 40°C, while the feed flow rate over the membrane was 250 l/h, resulting in a Reynolds number of approximately 12000 (turbulent flow) (*22*). Prior to analysis, membranes were allowed to equilibrate with feed solution for at least 12h. Every hour permeate was collected in a glass trap cooled in a Dewar flask containing liquid nitrogen. The permeate pressure was maintained below 3 mbar by a two-stage vacuum pump. The active membrane area of the investigated samples was 20 cm. The total amount of permeate was determined gravimetrically using a balance with an accuracy of 10^{-4} g from which the total flux was calculated. Fluxes were normalized by multiplication with the selective layer thickness of the membrane as determined elsewhere (*20*).

Component concentrations were determined by a Shimadzu GC-14A gas chromatograph (column 80/120 Carbopack B/3% SP—1500, FID detector). Ethanol concentration of the fermentation broth was slightly adjusted to obtain exactly 3 wt. %, which allowed direct comparison with other model ethanol/water experiments at the same ethanol concentrations. The membrane selectivity factor, ethanol flux and water flux were calculated to quantify the membrane performance. Based on the relative error of each measurement method (permeate mass, membrane diameter and component analysis), the experimental error of the reported performance factors was estimated to be 4 %.

Results and Discussion

Membrane Characterization and Basic Pervaporation Performance

The contact angle of a water drop on a dry membrane surface sample was found to be 113° and 114° M1 and M2 respectively, which is in good agreement with earlier studies (*20*). Subsequently fermentation broth pervaporation was compared with an ordinary ethanol/water mixture which will serve a reference for further comparison, and results are summarized in Table 1. The main by-products of the fermentation broth were determined to be glycerol (~0.2 wt. %), succinic acid (~0.04 wt. %) and acetic acid (~0.02 wt. %)

From Table 1, it can be seen that no significant differences exist in membrane performance for the unfilled PDMS membrane (M1). However, during fermentation broth pervaporation, water flux of M2 was 11% higher compared to pure ethanol/water pervaporation, while the ethanol flux was more or less similar. This resulted in an 8 % lower permeate ethanol concentration and membrane performance which could not be restored afterwards. Moreover, contact angle of the M2 sample decreased from 114° to a value of 106° whereas no change was observed for M1. Hence the reason for this observed behavior must rely on the presence of by-products and their interaction with the membrane materials.

Influence of By-Products on Pervaporation Performance

Model ethanol/water mixtures were prepared in which each individual by-product was added at double concentration than present in the broth, to investigate their influence on the pervaporation performance. No significant changes in comparison to the reference scenario were observed when M1 was subjected to pervaporation experiments with all of these model mixtures. For M2, no changes were found for the model mixture with glycerol, while similar observations to the fermentation broth pervaporation where found for the carboxylic acid mixtures as presented in Table 2.

Downloaded by STANFORD UNIV GREEN LIBR on June 19, 2012 | http://pubs.acs.org
Publication Date (Web): October 31, 2011 | doi: 10.1021/bk-2011-1078.ch005

Table 1. Comparison between ordinary ethanol/water pervaporation and fermentation broth pervaporation

		M1		*M2*	
Performance parameter		*Pure ethanol /water*	*Fermentation broth*	*Pure ethanol/ water*	*Fermentation broth*
Flux [g/m^2.h]	Total	120	119	150	166
	Ethanol	15.1	14.8	21.9	22.2
	Water	104.9	104.2	128.1	143.8
Permeate EtOH fraction [wt. %]		12.5	12.4	14.6	13.4
Selectivity factor		4.6	4.6	5.5	5.0

Table 2. Membrane performance of the ZSM-5 filled PDMS membrane (M2) during pervaporation experiments with added carboxylic acids

		Additive	
Performance Parameter		*Succinic acid*	*Acetic acid*
Flux [g/m^2.h]	Total	166	167
	Ethanol	22.3	22.1
	Water	143.7	143.9
Permeate EtOH fraction [wt. %]		13.4	13.2
Selectivity factor		5.0	4.9

It was also found that the molar concentration of carboxylic acid determined the extent of decrease in membrane performance rather than the nature of the acid itself, as can be seen in Figure 1.

From this figure it can be seen that the permeate ethanol concentration tends to go to a plateau level at high carboxylic acid concentration, corresponding to a maximum decrease in ethanol concentration of ~25 %. Furthermore, the water contact angle of M2 followed a similar trend, namely a lower value (more hydrophilic membrane) at higher molar concentration of acid in the feed.

Downloaded by STANFORD UNIV GREEN LIBR on June 19, 2012 | http://pubs.acs.org
Publication Date (Web): October 31, 2011 | doi: 10.1021/bk-2011-1078.ch005

Downloaded by STANFORD UNIV GREEN LIBR on June 19, 2012 | http://pubs.acs.org
Publication Date (Web): October 31, 2011 | doi: 10.1021/bk-2011-1078.ch005

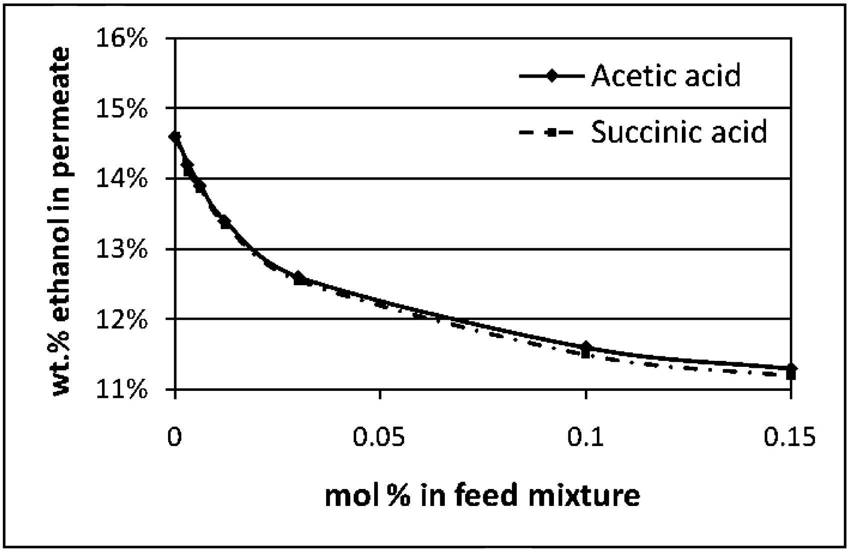

Figure 1. Influence of carboxylic acid concentration on permeate ethanol concentration during pervaporation experiments with M2.

Ikegami et al. (*15*) investigated addition of 0.3 wt. % to a 5 wt. % ethanol in water solution on the membrane performance of silicalite membranes. The authors found a slightly decreased permeate ethanol concentration, which is in agreement with our findings. By immersing silicalite powder in succinic acid and subsequent infrared analysis, stretching vibration peaks of carbonyl and carboxyl groups and deformed hydroxyl groups were observed. From this, the authors suggested that the membranes became more hydrophilic due to adsorption of succinic acid on the silicalite surface. No changes in infrared spectra were observed when a pure silicone rubber material was immersed in the same succinic acid solution, hence no changes for a pure PDMS membrane are expected. Bowen et al. (*13*) did research on stability of zeolite-filled (silicalite-1 and CBV-28014 ZSM-5) PDMS membranes during pervaporation experiments with ethanol/water mixtures. For an unfilled PDMS membrane, no significant changes in membrane performance where observed when 1 wt. % acetic acid was added to a 5 wt. % ethanol in water solution. However an irreversible decrease in selectivity factor was found when the zeolite-filled membranes were subjected to the same feed solution. The authors also explained this by the interaction of acetic acid with silanol (Si-OH) groups end groups of the external surface of the zeolite particle, forming more hydrophilic Si-O-$COCH_3$ bonds.

Not only are the observations of both studies in agreement with our findings, the suggestion of a more hydrophilic surface was confirmed in this research by contact angle measurements. It is thus clear that carboxylic acids render a zeolite-filled membrane more hydrophilic and are responsible for the decrease in membrane performance during fermentation broth pervaporation.

Finally, the influence of pH of the acidic feed solutions on membrane fouling of M2 was investigated. It was found that the decrease in membrane performance diminished by increasing the pH of the solution. At a pH of ~5.5 no change in fluxes was found in comparison to the reference scenario of pure ethanol/water pervaporation. Bowen et al. (*13*) observed similar behavior for a ZSM-5 filled PDMS membrane and explained this by the fact that the dissociated ions of carboxylic acids, which are mainly present above the dissociation constant of the weak acid, adsorb only marginally on zeolite particles. It is hence advisable to increase the pH towards neutral environments during fermentation process to minimize the impact of organic acids on the membrane performance of zeolite-filled membranes.

Downloaded by STANFORD UNIV GREEN LIBR on June 19, 2012 | http://pubs.acs.org
Publication Date (Web): October 31, 2011 | doi: 10.1021/bk-2011-1078.ch005

Conclusion

The aim of this study was to compare fermentation broth pervaporation to ordinary ethanol/water pervaporation. Differences between the two processes were only found for the ZSM-5 filled PDMS membrane, which showed an 11 % higher water flux and 8 % lower permeate ethanol concentration during fermentation broth pervaporation. Furthermore water contact angle decreased from 114° before to106° after the experiments.

Experiments with model mixtures in which the main by-products were individually added revealed that carboxylic acids were responsible for this irreversible membrane fouling, due to interaction of acids with the zeolite surface. The molar concentration of the acid determined the decrease in membrane performance, and maximum decrease in permeate ethanol fraction was estimated to be 25%. Furthermore, the extent of membrane fouling diminished by increasing the pH of the acidic solution to a value above the acid dissociation constants.

Acknowledgments

The work leading to these results has received funding from the European Community's Seventh Framework Programme (FP7/2007-2013) under grant agreement no. NMP3-SL-2009-228631, project DoubleNanoMem.

References

1. Lombardi, L. Life cycle assessment comparison of technical solutions for CO_2 emissions reduction in power generation. *Energy Convers. Manage.* **2003**, *44*, 93–108.
2. Abrahamse, W.; Steg, L.; Gifford, R.; Vlek, C. Factors influencing car use for commuting and the intention to reduce it: A question of self-interest or morality? *Transp. Res., F* **2009**, *12* (4), 317–324.
3. Stichnothe, H.; Azapagic, A. Bioethanol from waste: Life cycle estimation of the greenhouse gas saving potential. *Resour. Conserv. Recycl.* **2009**, *53*, 624–630.
4. Govindaswamy, S.; Vane, L. M. Kinetics of growth and ethanol production on different carbon substrates using genetically engineered xylose-fermenting yeast. *Bioresour. Technol.* **2007**, *98*, 677–85.

5. Wang, M. Q. Greet 1.5—transportation fuel-cycle model, Final Report ANL/ ESD-39. Argonne National Laboratory, USA. (1999)
6. Vane, L. M. A review of pervaporation for product recovery from biomass fermentation processes. *J. Chem. Technol. Biotechnol.* **2005**, *80*, 603–629.
7. Ikegami, T.; Yanagishita, H.; Kitamoto, D.; Haraya, K.; Nakane, T.; Matsuda, H.; Koura, N.; Sano, T. Production of highly concentrated ethanol in a coupled fermentation/ pervaporation process using silicalite membranes. *Biotechnol. Tech.* **1997**, *11* (12), 921–924.
8. Nomura, M.; Bin, T.; Nakao, S.-i. Selective ethanol extraction from fermentation broth using a silicalite membrane. *Sep. Purif. Technol.* **2002**, *27*, 59–66.
9. Kim, S.; Dale, B. E. Global potential bioethanol production from wasted crops and crop residues. *Biomass Bioenergy* **2004**, *26*, 361–375.
10. Hamelinck, C. N.; van Hooijdonk, G.; Faaij, A. P. C. Ethanol from lignocellulosic biomass: techno-economic performance in short-, middle- and long-term. *Biomass Bioenergy* **2005**, *28*, 384–410.
11. Zacchi, G.; Axelsson, A. Economic evaluation of preconcentration in production of ethanol from dilute sugar solutions. *Biotechnol. Bioeng.* **1989**, *34*, 223–233.
12. Madson, P. W.; Lococo, D. B. Recovery of volatile products from dilute high-fouling process streams. *Appl. Biochem. Biotechnol.* **2000**, *84-86*, 1049–1061.
13. Bowen, T. C.; Meier, R. G.; Vane, L. M. Stability of MFI zeolite-filled PDMS membranes during pervaporative ethanol recovery from aqueous mixtures containing acetic acid. *J. Membr. Sci.* **2007**, *298*, 117–125.
14. Fadeev, A. G.; Kelley, S. S.; McMillan, J. D.; Selinskaya, Ya. A.; Khotimsky, V. S.; Volkov, V. V. Effect of yeast fermentation by-products on poly[1-(trimethylsilyl)-1-propyne] pervaporative performance. *J. Membr. Sci.* **2003**, *214*, 229–238.
15. Ikegami, T.; Kitamoto, D.; Negishi, H.; Haraya, K.; Matsuda, H.; Nitanai, Y.; Koura, N.; Sano, T.; Yanagishita, H. Drastic improvement of bioethanol recovery using a pervaporation separation technique employing a silicone rubber-coated silicalite membrane. *J. Chem. Technol. Biotechnol.* **2003**, *78*, 1006–1010.
16. Groot, W. J.; Kraayenbrink, M. R.; van der Lans, R. G. J. M.; Luyben, K. C. H. A. M. Ethanol production in an integrated fermentation/membrane system. Process simulations and economics. *Bioproc. Eng.* **1993**, *8*, 189.
17. O'Brien, D. J.; Roth, L. H.; McAloon, A. J. Ethanol production by continuous fermentation–pervaporation: a preliminary economic analysis. *J. Membr. Sci.* **2000**, *166*, 105.
18. Strathmann, H.; Gudernatsch, W. Continuous removal of ethanol from fermentation broth by pervaporation. In *Extractive Bioconversions*; Mattiasson, B., Ed.; Marcel Dekker, 1990.
19. Kaseno; Miyazawa, I.; Kokuga, T. Effect of product removal by a pervaporation on ethanol fermentation. *J. Ferment. Bioeng.* **1998**, *86* (5), 488–493.

Downloaded by STANFORD UNIV GREEN LIBR on June 19, 2012 | http://pubs.acs.org
Publication Date (Web): October 31, 2011 | doi: 10.1021/bk-2011-1078.ch005

20. Chovau, S.; Dobrak, A.; Figoli, A.; Simone, S.; Galiano, F.; Drioli, E.; Sikdar, S.; Van der Bruggen, B. Pervaporation performance of unfilled and filled PDMS membranes and novel SBS membranes for the removal of toluene from diluted aqueous solutions. *Chem. Eng. J.* **2010**, *159* (1-3), 37–46.
21. Dotremont, C.; Van den Ende, S.; Vandommele, H.; Vandecasteele, C. Concentration polarization and other boundary layer effects in the pervaporation of chlorinated hydrocarbons. *Desalination* **1994**, *95*, 91–113.
22. Bettens, B.; Degrève, J.; Van der Bruggen, B.; Vandecasteele, C. Transport of Binary Mixtures in Pervaporation through a Microporous Silica Membrane: Shortcomings of Fickian Models. *Sep. Sci. Technol.* **2007**, *42* (1), 1–23.

Downloaded by STANFORD UNIV GREEN LIBR on June 19, 2012 | http://pubs.acs.org
Publication Date (Web): October 31, 2011 | doi: 10.1021/bk-2011-1078.ch005

Chapter 6

Development and Characterization of Ionic Liquid-Functionalized Nanocomposite Membranes

Hamid R. Hakimelahi, Pei Li, and Maria R. Coleman[*]

**Department of Chemical & Environmental Engineering,
University of Toledo, 2801 West Bancroft St.,
Toledo, Ohio 43606-3390**
**[*]E-mail: maria.coleman6@utoledo.edu. Tel.: +1 419 530 8091.
Fax: +1 419 530 8086.**

Carbon dioxide (CO_2) capture is important for both energy production and environmental preservation. A key to reducing the cost of hydrogen production is the development of energy efficient separations processes that can provide either preliminary bulk separations or deliver high pressure hydrogen streams by removing CO_2. Functional nanocomposite network membranes (FNNM) consisting of polymer matrix, nanofiber network and fixed carrier molecules, were developed as a platform mixed matrix membrane material and investigated for selective recovery of CO_2 from gas stream. The nanofibers form a highly connected network or mesh, fixed carrier molecules, which are covalently bound to the outer surface of the nanofiber react reversibly with the target species, and polymer matrix provides mechanical stability and processiblity to the resulting composite. Carbon nanofibers (CNF) were functionalized with different ionic liquid (IL) monomers that exhibit affinity for the target gas species, i.e. CO_2 in this case. The permeability of the pure CO_2, H_2, and CH_4 were measured in membranes at loadings up to 30 wt %. There was a decrease in permeability for all gases studied with increases in CO_2/H_2 and CO_2/CH_4 selectivity for IL-based membrane compared to the base PDMS.

In Modern Applications in Membrane Science and Technology; Escobar, I., et al.;
ACS Symposium Series; American Chemical Society: Washington, DC, 2011.

Introduction

Room temperature ionic liquids (RTIL) consisting of organic cations and organic or inorganic anions have attracted considerate attention for a variety of applications in analytical chemistry, separations, electrochemistry and catalyst (*1–8*). RTILs have excellent properties including (*9–12*)*:* 1- specific low melting points (lower than 100 °C or at room temperature such as room temperature ionic liquids); 2- negligible volatility for use in low pressure process; 3- high ionic conductivity for use as electrolytes; 4- nonflammable and chemical stable; 5- good solvents for organic and inorganic chemicals; and 6- easily tuned physical and chemical properties through control of the nature and functionality of the cationic or anionic structures. The tunable solvation properties of RTIL's have resulted in considerable interest in applying them as "green solvents" and in recent years as membranes media.

While the first RTIL, ethanolammonium nitrate (m.p. 52-55 °C), was synthesized by Gabriel and Weiner in 1888 (*13*), these materials did not receive much attention for separation applications until 1999 when Brennecke et al. first reported that CO_2 was highly soluble in ionic liquid, [BMIM] [PF_6], reaching a mole fraction of 0.6 at 8 MPa (*14*). RTILs were first applied to extraction processes with supercritical carbon dioxide (*15*) to take advantage of the high affinity to CO_2. RTILs have been used as the separation medium in supported liquid membrane (SLM) because of their negligible vapor pressure, high thermal stability, adjustable polarity and rheological properties that can be used to produce stable SLM. Supported ionic liquid membranes (SILMs) have been investigated for gas-gas (*16*), gas-liquid or liquid-liquid (*17*) separations. SILMs with bis(trifluoromethanesulfonyl) imide (Tf_2N) as the anion showed high permeability and good selectivity for CO_2/He at temperature up to 125 °C (*18*). The cross membrane pressure was maintained at less than 0.2 MPa to avoid loss of ionic liquid and the selectivity of CO_2/He dropped from 8.7 to 2 when temperature increased from 35 to 125 °C. A low transmembrane pressure will typically result in low permeance and a need for large membrane area. Scovazzo et al. (*2*) studied the humidity effect on gas transport in SILMs. His results showed that for hydrophobic RTILs ([emim] [Tf_2N]) humidity did not affect gas permeability. For hydrophilic RTILs the effect of humidity could not be determined because of the buildup of water that diluted the RTILs and caused the membrane to fail. Quan Gan et al. (*16*) used nanoporous membranes as the support for SILM, which resulted in membranes that were stable at cross membrane pressure up to 0.9 MPa. The selectivity of H_2/CO dropped from 5 to 1.6 and the CO_2/N_2 dropped from 5 to 1.6 and 90 to 5 when pressure increased from 0.3 to 0.9 MPa. Noble et al (*19*) used fluoroalkyl-functionalized room-temperature ionic liquids with different length of fluoroalkyl substituents using supported liquid membranes and showed ideal selectivity for CO_2/N_2 about 27 and the permeability for CO_2 and N_2 around 2.4×10^{-5} and 9.1×10^{-7} m^3 (STP).m/ (m^2.s.Pa), respectively. Jindaratsamee et al. (*20*) investigated the effect of different anions and temperature on permeability of CO_2. Though these SILMs exhibited promising permeation properties, the stability and transport properties at elevated temperatures and pressures must be addressed to apply SILM commercially. For example, reduction in solute flux and membrane selectivity has been reported to occur during operation (*21*, *22*). These effects have been attributed to a loss of solvent from the supporting membrane, either by evaporation or by dissolution/dispersion into the adjacent phases. A possible approach to minimizing instability problems is the adequate design of both the supporting membrane and the contacting phases.

Solid polymeric membranes typically exhibit improved thermal/ mechanical stability relative to SLM. Polymeric Ionic Liquids (PILs) have recently been reported that take advantage of the high solubility of RTILs to certain organic chemicals and improved stabilities of the solid state. Thus far PILs reported in the literature have been made using vinyl chemistry where the resulting polymer has a long hydrocarbon chain with IL-pendant groups. Tang et al. (*23*, *24*) have published results for PIL that exhibited higher solubility and faster sorption/desorption rate for CO_2 than those in corresponding IL monomers. Noble et al. (*25–30*) synthesized PIL that showed good selectivity for CO_2/N_2 (~40) and CO_2/CH_4 (~30) at 0.2 MPa but poor gas permeability (CO_2-3.3 × 10^{-6} m^3 (STP).m/ (m^2.s.Pa), N_2-8.4 × 10^{-8} m^3 (STP).m/ (m^2.s.Pa), CH_4-1.2 × 10^{-7} m^3 (STP).m/ (m^2.s.Pa)). Trevor K. Carlisle et al. (*31*) synthesized three PIL membranes composed of main-chain, poly (imidazolium)s (imidazolium ionenes) that were shown to be selective for CO_2-based separations.

Several research groups have increased the permeability of CO_2 by improving the solubility of CO_2 in the IL. For example, Muldoon et al. (*32*) added fluoroalkyl chains on either the cation or anion, Hong et al. (*33*) tried different anions, Anderson et al (*34*) changed the cation and Camper at el (*35*) investigated the effect of temperature, pressure and different cations and anions. They showed improvement in CO_2 permeability and selectivity of CO_2 relative to N_2.

In order to increase the mechanical stability of IL some researchers have tried to copolymerized the IL with more mechanically stable polymers. For example, Li et al. (*36*) synthesized two diamino room temperature ionic liquids,1,3-di(3-aminopropyl)imidazolium bis [(trifluoromethyl) sulfonyl] imide (monocationic RTIL or mRTIL) and 1,12-di[3-(3- aminopropyl)imidazolium]dodecane bis [(trifluoromethyl) sulfonyl] imide (dicationic RTIL or diRTIL) using a Boc protection method. The two RTILs were incorporated within the polyimide backbones to tune the solubility properties and improve the separation of CO_2 from CH_4. The separation performance of all RTIL based copolyimides followed a trade-off relationship but did not exhibit a significant improvement for CO_2/CH_4 gas pair. The incorporation of RTIL caused a reduction in free volumes and change in free volume distributions of the copolyimides, which resulted in loss in permeability. The RTIL monomers contain more alkyl groups than that of the MDA, which could increase the chain flexibility of the copolyimides. The incorporation of the RTILs in the 6FDA-MDA backbones caused denser packing that resulted in a lower permeability and higher selectivity compared with the pure 6FDA-MDA. For the mRTIL based block copolyimides, the gas permeability and diffusivity (H_2, O_2, N_2, CH_4 and CO_2) decreased and the permeability and diffusivity selectivity for CO_2/CH_4 and O_2/N_2 gas pair increased with the increase in mol% of the mRTILs. The long block copolyimides have a lower permeability/diffusivity and higher permeability selectivity/ diffusivity selectivity than those of the short block copolyimides. The solubilities of gases in the long and short block copolyimides were similar. And the solubilities of O_2, N_2 and CH_4 increased while that of CO_2 decreased with an increase in mRTIL content. For the diRTIL based random copolyimides, the permeability, solubility and diffusivity of the gases decreased with the increase in mol% of the RTIL. The permeability and diffusivity selectivity of CO_2/CH_4 and O_2/N_2 slightly increased while that of N_2/CH_4 decreased. The solubility selectivity of CO_2/CH_4 decreased.

In this study, a novel platform material with high fiber loading is introduced that targets CO_2 separations while providing good mechanical and thermal stability and easy processing. In this case, the ionic liquid molecules were covalently bound to the surface of CNF and incorporated within poly(dimethyl siloxane) (PDMS).

Functional Nanofiber Network Materials

Functional nanofiber network (FNN) composites are novel platform materials, which combine the attractive properties of functionalized nanofillers with the easy formation (processibility) and stability of polymers. Specifically, FNNs consist of a continuous network of high aspect ratio nanofillers, such as carbon nanofibers, with covalently bound functional groups within a matrix polymer as shown in Figure 1.

As shown in Figure 1, the nanofillers serve as the stable network forming core with a highly selective bound molecular or polymer layer that provides a functional annular region at the nanofiller/polymer interface. The ability to select the nanofillers, bound surface group and matrix polymer results in a platform material that can be applied across wide range of systems such as selective membranes. The individual components are described below in detail.

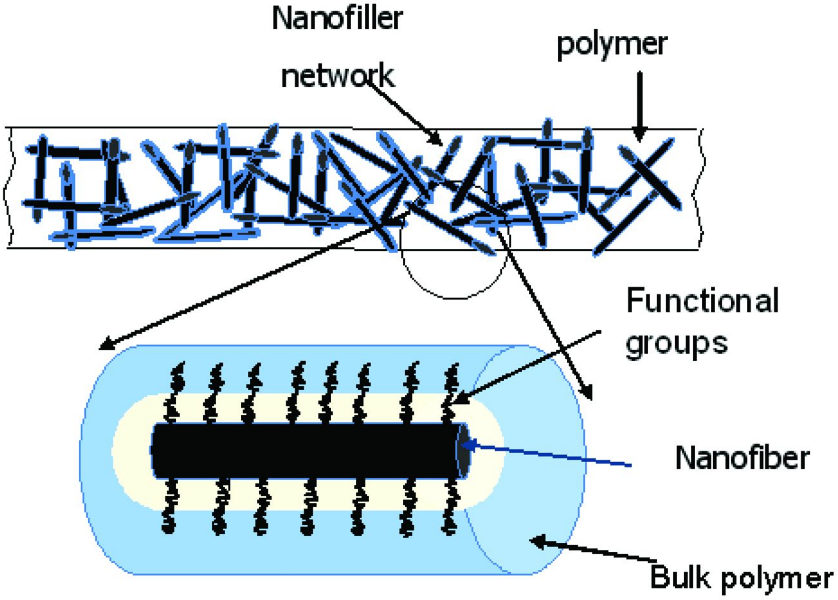

Figure 1. Cartoon depicting functional nanocomposite network material.

In Modern Applications in Membrane Science and Technology; Escobar, I., et al.;
ACS Symposium Series; American Chemical Society: Washington, DC, 2011.

Nanofiber Network

High aspect ratio nonporous nanofillers with surface reactive groups are ideally suited to form a highly connected network within polymer matrices. This network formation is demonstrated by percolation thresholds for conducting nanofibers within polymer at loadings as low as 5 volume %. In addition, the inorganic nanofillers can enhance the thermal-mechanical stability of the resulting composites. Carbon nanofibers were used as the nanofibers for the work reported here.

Functional Molecules in Interfacial Region

Functional groups are covalently bound to the outer surface of the nanofiller to serve to purposes: (i) improve compatibility between nanofiller and matrix polymer and (ii) provide a functional interfacial region with tunable properties, such as, affinity binding for enhanced gas transport or conducting polymers to improve composite conductivity. A copolymer can be used to functionalize nanofiller, in which the first block consists of affinity binding groups, and the second block mimics structure of the polymer matrix to enhance dispersion and network formation. In this study methods to functionalize the oxidized carbon nanofibers (CNF-OX) with molecular ionic liquids shown in Table 2 will be reported.

Table 1. Functional groups

Type	*Functional Groups*
Pristine Carbon Nanofiber (CNF-P)	None
Oxidized Carbon Nanofiber (CNF-OX)	-COOH Carboxyl
Carbon nanofiber Functionalized with Ionic Liquid (CNF- IL [Br])	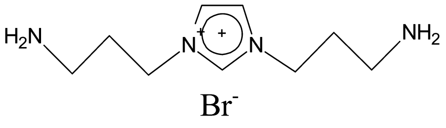 1, 3-di(3-aminopropyl)-imidazolium Bromide [C3-NH_2 C3-NH_2 Im][Br].
Carbon nanofiber Functionalized with Ionic Liquid (CNF- IL [Taurine])	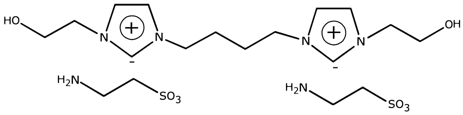 1,4-di[3-ethanol-imidazolium]butane taurate ([C_4[C_2OHim][taurine])

IL [Br] and IL [Taurine] were selected since they have amine groups in their structure (for IL [Br] in cation and for IL [Taurine] in anion), which have affinity for CO_2 and can target CO_2. Besides, the affinity characteristics can be tuned using anion exchange with surface bound ILs to modify the CO_2 separation.

Matrix Polymer

The polymer matrices primarily impart mechanical stability and processiblity to the resulting FNN, however, the structure of the polymer can be modified to enhance properties. For example, poly (dimethylsiloxane) (PDMS) can be processed with high loading carbon nanofiber using a room temperature process. PDMs provides a matrix with very high free volume that is inherently solubility selective, which is advantageous for CO_2/ H_2 separation. As an alternative a low free volume glassy polymer could be used to provide a membrane, in which primary separations mechanism was in the interfacial region between nanofiller and bulk polymer.

The ability to modify the nature of nanofiller, surface groups and matrix in FNN allows design of material with desired transport properties. This paper discusses the formation of FNN systems using IL-functionalized carbon nanofibers within a PDMS matrix at up to 30 wt% loading.

Experimental Section

Materials

Pristine (PR-24-LD-PS) and oxidized carbon nanofiber (PR-24-LD-PS-OX) with diameter of 60~150nm, length of 100,000 nm and density of 1900~1950 kg/m^3 were bought from Pyrograf products, Inc. (Cedarville, OH). Polydimethysiloxane, silanol terminated polydimethylsiloxane (DMS-S21), DI-n-Butyldilauryltin (SND3260), and poly diethoxysiloxane (PSI-021) were purchased from Gelest, Inc. (Morrisville, PA) and used as obtained. N-ethyl-N (-3-dimethylyaminopropyl) carbodimide (EDC, 97% purity), N, N′-Carbonyl diimidazole (CDI, 98% purity), 4-dimethylaminopropyl (DMAP), imidazole sodium, 2-bromoethanol, 1,4-dibromobutane, Amberlite OH exchange resin and taurine and pyridine were obtained from Sigma-Aldrich (Milwaukee, WI) and used without further purification. N, N’-Dimethylacetamide (DMAc) were obtained from Sigma-Aldrich (Milwaukee, WI) and distilled over calcium hydride granules. Di-tert-butyl dicarbonate (BOC group), magnesium sulfurnate, 3-bromopropylamine (hydrobromide), hydrobromic acid, ethyl acetate, 1,4-dibromobutane, 2-bromoethanol, imidazole sodium, taurine, 1-bromobutane, 1-vinylimidiazole, THF, dimethylacetimide (DMAc), triethylamine (TEA), acetic acid (AA) methanol, 1,12-dibromododecane, isopropanol and nitric acid (HNO_3) were purchased from Sigma-Aldrich (Milwaukee, WI).

IL Synthesis

The methods used to synthesize the two RTILs listed in Table 1 were developed in our group and are described below (*36*). The reaction schemes for the IL based diamines and IL based dihydroxyls used in this project are outlined in Schemes 1 and 2, respectively.

Synthesis of 1, 3-Di(3-aminopropyl)-imidazolium Bromide [C3-NH₂ C3-NH₂ Im][Br]

A 0.050 mol sample of di-*tert*-butyl dicarbonate **(2)** was mixed with 0.046 mol of 1-(3-aminopropyl) -imidazole **(1)** in 50ml tetrahydrofuran (THF). The flask was kept in an ice-water bath and stirred for 30 minutes, then warmed to room temperature under constant stirring for 24 h. The THF was removed using vacuum distillation; the product was dissolved in 50ml of ethyl acetate and extracted five times with 10 ml aliquots of Milli-Q water. Ethyl acetate was removed under vacuum and the product **(3)** was placed in a vacuum oven.

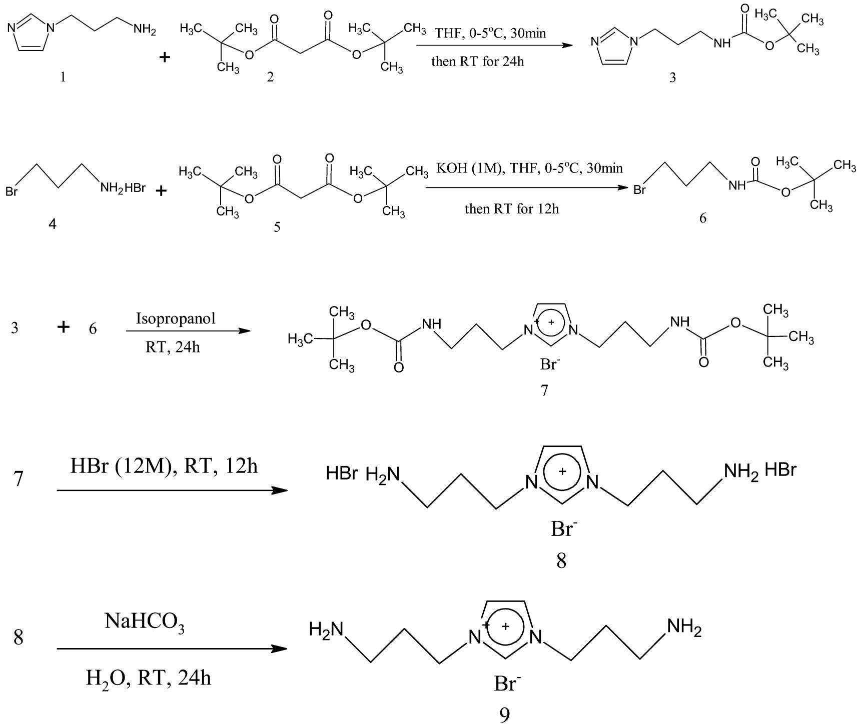
1
2
THF, 0-5°C, 30min
then RT for 24h
3
4
5
KOH (1M), THF, 0-5°C, 30min
then RT for 12h
6
3 + 6
Isopropanol
RT, 24h
7
7
HBr (12M), RT, 12h
HBr H2N
NH2 HBr
Br-
8
8
NaHCO3
H2O, RT, 24h
9

Scheme 1. Synthesis of IL [Br]

A 0.110 mol sample of di-*tert*-butyl dicarbonate **(5)** was dissolved in a mixture of 100 ml THF and 50ml NaOH (1M) aqueous solution, along with 0.099 mol of 3-bromopropylamine hydrobromide **(4)**. The flask was kept in ice-water bath for 30 minute and warmed to room temperature under constant stirring for 24 h. A mixture of 150ml ethyl acetate and 100ml brine was added to the obtained mixture and two layers were formed. The organic layer was recovered and the aqueous layer was washed by ethyl acetate. The two ethyl acetate solutions were mixed together and further extracted five times with 50 ml aliquots of brine, dried with $MgSO_4$, and filtered. Finally, ethyl acetate and THF were removed under vacuum to yield product as a yellowish oil **(6)** in Scheme 1.

A 0.020 mol sample of **3** and 0.019 moles of **6** were dissolved in 50 ml isopropanol and refluxed at 70 °C with stirring for 24 h. Following removal of the solvent, the obtained ionic liquid was dissolved in 15 ml of Milli-Q water to be extracted five times with 10 ml aliquots of ethyl acetate. After purification, the water phase was collected, rotary evaporated and vacuum heated to remove water and obtain **7** as brown oil. **7** was washed with an aqueous solution of HBr (6M) to remove the boc protecting group and produce 1, 3-di(3-aminopropyl hydrobromide)-imidazolium Bromide (**8**). **8** was neutralized with an aqueous solution of $NaHCO_3$. The monocationic IL monomer, 1, 3-di(3-aminopropyl)-imidazolium Bromide **(9)**, was recovered and further dried in a vacuum oven overnight.

Synthesis of 1,4-Di[3-ethanol-imidazolium]butane Taurate ([C_4][C_2OHim][taurine])

A 4.5 g sample of sodium imidazole **(1)** (50 mmol) was dissolved in 50 ml methanol. 5.4 g of 1, 4-dibromobutane **(2)** (25 mmol) was added to the solution dropwise. The mixture was stirred for 24 hours and filtered to recover the white precipitate, NaBr. To the filtered solution or 1,4-di(1,3- imidazole) **(3)**, 6.25 g 2-bromoethanol **(4)** (50 mmol) was added. The reaction mixture was heated at 50 ^{0}C for 2 days and the methanol was vaporized under vacuum. The remainder of the solution was dissolved in 100 ml DI-water and extracted three times with ethyl acetate. The water phase was collected and vacuum distilled to remove the water. A solid brown product 1, 4- di[3-ethanol-imidazolium]butane bromide **(5)** was acquired as shown in Scheme 2.

To obtain the taurate ionic liquid, the 1,4-di [3-ethanol-imidazolim]butane bromide **(5)** was first dissolved in 50 ml DI-water and sent through a column filled with OH-exchange resin to exchange the bromine anion with OH. The pH of the RTIL solution or 1,4-di [3-ethanol-imidazolim]butane hydroxide **(6)** was measured using a titration method. An amount of taurine **(7)** equal to the amount of OH of the RTIL was added to the RTIL solution or 1,4-di [3-ethanol-imidazolim]butane hydroxide **(6)** to neutralize the OH anions. The water of the resulting solution was removed under vacuum and the taurate RTIL, 1,4-di[3-ethanol-imidazolium]butane taurate **(8)** was acquired.

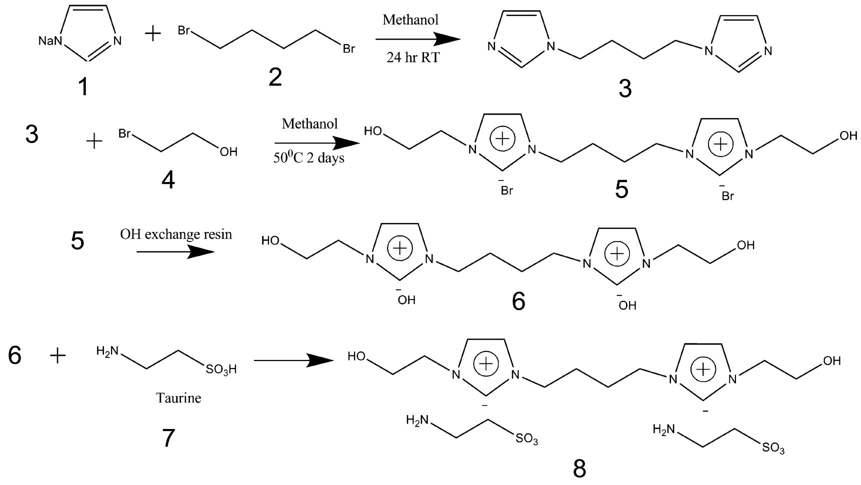

Scheme 2. Synthesis of IL [Taurine]

Functionalization of CNF

Oxidized carbon nanofiber (CNF- OX) was purified by acid treatment prior to each of the functionalization reactions. The acid treatment was performed by dispersing 5 g of CNF-OX in an aqueous HNO_3 solution (2M, 250 ml) and refluxing for 48 hr. The suspension was filtered and washed with deionized water untill the filtrate became neutral. The washed CNF- OX was dried under vacuum. To disperse the acid washed CNF- OX properly in solvent, the solution was sonicated for 15-20 min prior to beginning the reaction.

Functionalization of CNF- OX with [C3-NH$_2$ C3-NH$_2$ Im][Br]

CNF-OX was functionalized via the surface carboxylic acid groups using EDC reaction shown in Scheme 3 (*37*). For this reaction 1 g of CNF-OX was dispersed in 100 ml of DMF or DI water and sonicated for 30 min to obtain uniform dispersion. To this solution under nitrogen atmosphere and constant stirring DMAP (52 mg) and EDC (80 μl) was added and stirred for 5 min. 1,3-di (3-aminopropyl) imidazolium bromide ([$C_{3\text{-}NH2}$ $C_{3\text{-}NH2}$ Im][Br]) (0.3gr) was added to this mixture after 10 min. The reaction was carried out at 80 °C for 16 h. Following the reaction, the mixture was filtered, washed with methanol and extracted with tetrahydofuran (THF) in a Soxhlet extraction column for 24 h to remove any unbound RTIL (*38*). The diamine based IL- functionalized CNF (CNF- IL [NH_2]) was vacuum dried for 24 h at 30 °C.

Functionalization of CNF- OX with ([$C_4[C_2OHim]$][taurine])

CNF-OX was functionalized with IL [Taurine] via the surface carboxylic acid groups using CDI facilitated reaction shown in Scheme 4 (*39*). For this reaction 1 g of CNF-OX was dispersed in 120 ml of anhydrous DMAc or DI water and sonicated for 40 min to obtain a uniform dispersion. CDI (70mg) was added to this solution under nitrogen atmosphere and stirred for one hour at room temperature. Following the reaction, the solution was filtered and washed with anhydrous DMAc several times to remove unreacted CDI. The dried product was dispersed in DI water and sonicated for 20min. The [$C_4[C_2OHim]$][taurine] (0.45g) was added to this mixture and the reaction carried out at room temperature for 20 hours as shown in Scheme 4. The reaction mixture was filtered and washed with water to remove imidazole and unreacted IL. The dihydroxyl based IL functionalized CNF (CNF- IL [Taurine]) was vacuum dried for 24 h at 30^{o}C.

FNN Film Formation

The FNN composites were fabricated using a method modified from the solvent- free two- part cure- condensation silanol system reported in Gelest Reactive Silicone [37] at loadings of 10 and 30 wt %. This range was chosen to ensure that a continuous network of fibers was formed (*37*). The procedure used to form the FNNs was the same for each fiber type and loading. For example for the 30 wt % CNF-OX sheet, 0.3 g of CNF-OX were mixed with 0.63 g (63 wt %) of PDMS-OH (DMS-S21). After mixing uniformly, 0.07 g (7 wt %) of poly(diethoxysiloxane) (PSI-021) were added as a cross-linker. Note that the ratio of PDMS-OH and cross- linker was maintained at 9:1 for all samples. A tin based catalyst (DI-n-Butyldilauryltin or SND3260) in the amount of 0.1 g (10 wt %) was added to the carbon nano-fiber-PDMS mixture, which was pressed between two sheets of wax paper using two-roll mill and kept at room temperature for curing for 12 h to form a flexible CNF sheet. When poly(diethoxysiloxane) was combined with silanol- terminated PDMS and catalyst, a polycondensation reaction occured producing a vulcanized elastomer network.

Characterization

X-ray Photoelectron Spectroscopy (XPS)

XPS was used to qualitatively determine the functional groups bound to the surface of the CNF. The Kratos Axis Ultra XPS at the University of Michigan's Electron Microbeam Analysis Laboratory (EMAL) was used. The CNF samples were mounted on indium foil and kept under vacuum chamber overnight before any analysis. Survey scan were performed using Mono Al source with emission current 8 mA and anode voltage 15 kV. Charge neutralizer was not used for CNF sample as they are conducting. Samples were scanned for 3 times in the binding energy range of 0 eV to 800 eV and the sweep time for each scan was 200 s.

Gas Permeation

The gases used in this study were obtained from Airgas and were used as received. The purity of each gas was at least 99.95%. The permeability of CO_2, CH_4 and H_2 were measured at 35 °C. Argon and helium with a purity of 99.99% were used as the sweep gas and carrier gas, respectively. The penetrants were chosen to allow the determination of permeability and selectivity of several industrially important gas pairs, such as CO_2/CH_4, CO_2/H_2 and H_2/CH_4.

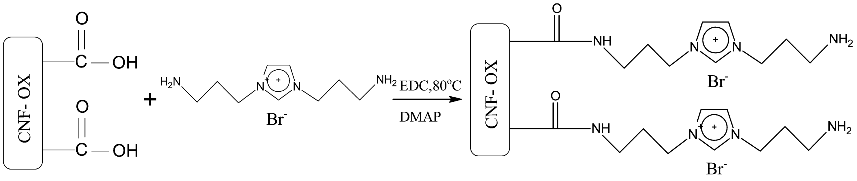
CNF- OX
C—OH
C—OH
O
+
H2N
NH2
N
N
Br-
EDC,80°C
DMAP
NH
NH2
Br-

Scheme 3. IL [Br] functionalized CNF

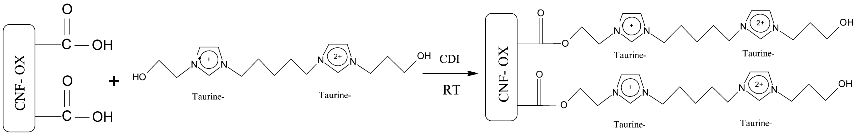
CNF- OX
C—OH
C—OH
+
HO
OH
Taurine-
Taurine-
CDI
RT
2+
OH

Scheme 4. Dihydroxyl based IL functionalized CNF

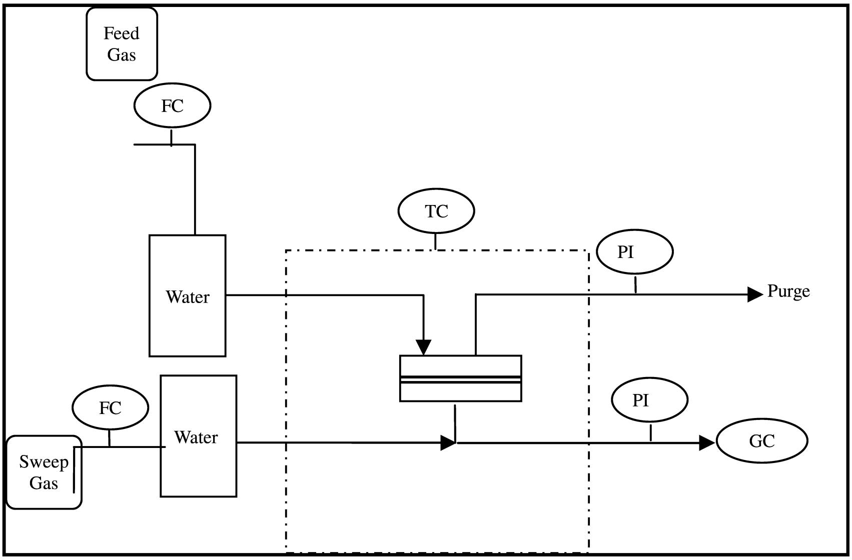
Feed Gas
FC
TC
PI
Water
Purge
FC
Water
PI
GC
Sweep Gas

Figure 2. Permeation cell.

The gas permeation tests were conducted using a permeation cell constructed for this purpose inside an oven (Hewlet Packard 5890, Palo Alto, CA) for the accurate control of temperature. The schematic diagram of the permeation apparatus is shown in Figure 2. A circular stainless steel cell with an active membrane area of 45.60 cm^2 was used for measuring transport properties of the membranes. In this cell, the feed and the sweep gas flows were counter-current. As mentioned earlier, a pure feed gas was used and argon was used as the sweep gas for ease of gas chromatography (GC) analysis. Gas flow rates were controlled by Sierra Instrumens Inc., flowcontrollers (Sierra Instrumens Inc., Montery, CA).

The feed and the sweep gas rates were kept at 60 and 30 cm^3/min, respectively. The pressure of the retentate was controlled by a back-pressure regulator and measured with a pressure gauge. The pressure on the permeate side was set close to atmospheric pressure via a near-ambient pressure regulator and measured with a pressure gauge.

Both the retentate and permeate streams leaving the oven were cooled to ambient temperature and their compositions were analyzed using a Shimadzu GC-2010 gas chromatograph with PDHID detector (Shimadzu, Addison, IL)). Helium was used as a carrier gas for PDHID detector. The GC columns used were ShinCarbon ST micro-packed columns (Restek, Bellefonte, PA).

Results and Discussion

Confirmation of Surface Functionalization with IL

Covalent bonding of RTILs to the surface of the carbon nanofibers was confirmed using XPS analysis. XPS is a sensitive analytical tool that is used to study the surface composition of a sample (*37*, *38*). There is a characteristic binding energy for each element that allows for precise identification of surface elements. In addition these peak shift depending on the local environment, which makes this a very sensitive tool for confirming surface chemistries.

The XPS spectrum for CNF-OX, CNF-IL [Br] and CNF-PDMS [Taurine] is shown in Figure 3. The pristine CNF has a peak at 284 eV that is characteristic for the C 1s of a graphitic carbon nanofiber (*38*). There is an additional peak at 531 eV for O 1s that is due to presence of bound functional groups on surface of CNF-OX (*37*, *38*).

The spectrum of CNF-IL [Taurine] and CNF-IL [Br] fibers have an additional peak at 399 eV corresponding to nitrogen from the amine end group in the cation for CNF- IL [Br] and the in anion for CNF- IL [Taurine]. No peak was seen for bromine in the CNF- IL [Br] because of low concentration of bromine on the surface of CNF. Additional peak at 167 eV for sulfur was observed for CNF- IL [Taurine].

The XPS survey peaks of different functionalized fibers were quantitatively analyzed to determine the atomic % of the various elements present on the surface of the CNF. The fraction of each atom was quantified using CasaXPS software (Casa Software Ltd. UK) based on the area of peak and the relative sensitivity factor (RSF) corresponding to each atom. Table 2 shows the atomic percent of each element present on the surface of the respective functionalized fiber. The

CNF- OX has 10.2% surface oxygen, which is consistent with the results reported in literatures (*38*). Following functionalization with IL [Br] that contains carbon and nitrogen the atomic percent of oxygen decreased and that of nitrogen increased.

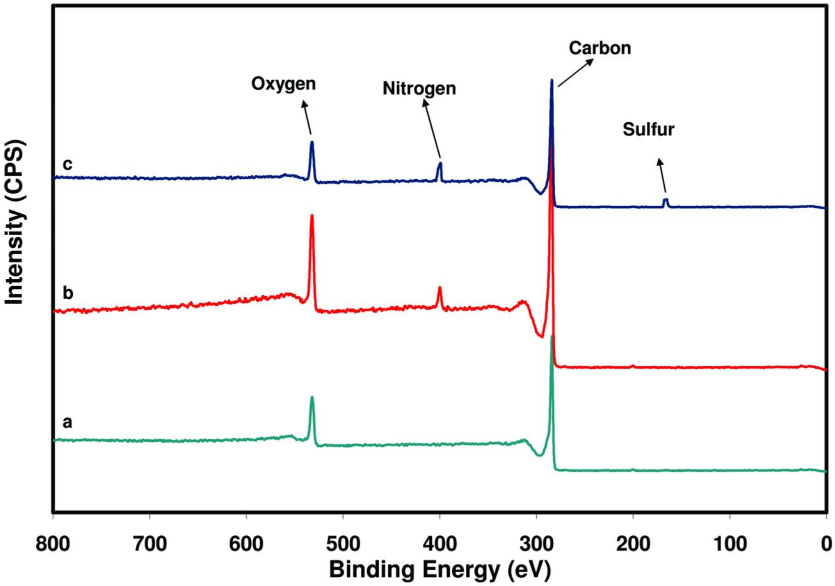

Figure 3. Comparison of XPS spectrum of (a) CNF- OX, (b) CNF- IL [Br] and (c) CNF- IL [Taurine].

Table 2. Atomic percent of elements on the surface of functionalized CNF

CNF Type↓	*Atomic percentage*			
Element→	*% C*	*% O*	*% N*	*% S*
CNF- OX	89.8	10.2	-	-
CNF- IL [Taurine]	84.4	10.5	4.1	1.0
CNF- IL [Br]	87.0	9.7	3.3	-

For CNF- IL [Taurine] an increase in atomic percentage of oxygen and nitrogen was observed due to the three oxygen atoms and two nitrogen atoms in the IL structure bound to the carbon nanofiber surface. In addition, an increase in amount of sulfur was seen. XPS survey spectrum for each type of functionalized fibers indicates that the desired molecules were bounded to the CNF- OX surface following each functionalization step.

Gas Permeation

FNN were produced using CNF- OX, CNF-IL [Br] and CNF-IL [Taurine] at 10 and 30 wt% in PDMS. The CNF-OX are non-porous and do not have functional groups that are expected to result in increase in interaction with CO_2. Therefore, it is expected that all gases will exhibit a decrease in permeability with inclusion of CNF-OX in the PDMS. Note that the CNF-IL [Br] has a Br anion, which was not expected to exhibit any specific CO_2 interactions and a NH_2 group that reacts with CO_2. The CNF- IL [Taurine] has two taurine anions, which have two amine groups and can provide CO_2 interaction.

The impact of surface functionality and loading on the pure gas permeabilities and permselectivities are shown in Figures 4 through 8.

As shown in Figure 4, there was a drop in permeability for CO_2 measured at 35 ^oC and 0.27 MPa following inclusion of CNF in the PDMS at each loading studied. Interestingly, inclusion of 10 wt% CNF- OX in PDMS resulted in larger drop in CO_2 permeability than for the CNF-IL [Br] and CNF- IL [Taurine] based FNNs. The decrease in permeabilities is consistent with the presence of non-porous fillers within the polymer matrix that act as barriers to transport and increased rigidity of polymer matrix. The reduction in permeability for the CNF-OX based FNN is consistent with good adhesion and wetting at the interface, which is consistent with results for tensile properties and SEM analysis reported in an earlier paper (*37*). The FNN produced with the two IL functionalized CNF exhibited similar results for CO_2 permeation. The presence of amine groups in CNF-IL [Br], and CNF- IL [Taurine], which can interact with CO_2, may result in some increase in flux for CO_2 in this annular interfacial region.

Addition of 30 wt % CNF- OX resulted in a further decrease relative to 10 wt % sample. The samples produced with CNF-IL [Br] and CNF-IL [Taurine] exhibited higher permeability for CO_2 relative to the CNF- OX based FNN membrane. These results are consistent with enhancement in permeability in the interfacial region resulting from interactions between amine groups on a surface of nanofiber and the CO_2. It is worth noting that the permeability of CO_2 for in the CNF-IL [Taurine] membrane is similar to the CNF-IL [Br] at low loading (10wt%) but at higher loading (30 wt%) the CNF-IL [Taurine] membrane showed higher CO_2 permeability than the IL [Br] membrane. This is likely due to presence of two taurine anions in the structure of IL [Taurine], which have two amine groups that can result in more interaction with CO_2.

The permeability of H_2 at 35 ^oC and 0.22 MPa as a function of loading of CNF in the FNNM is shown in Figure 5. The samples produced using CNF- OX, CNF- IL [Br] and CNF- IL [Taurine] all showed decreases in permeability of H_2 following inclusion of fiber. All of the samples exhibited similar permeabilities for H_2, which is consistent with lack of functional groups that would interact with H_2.

The decrease in permeability is due to combination of reduction in diffusion pathways due to presence of non-permeable CNFs and the increase in stiffness of the PDMS following inclusion of the rigid nanofillers.

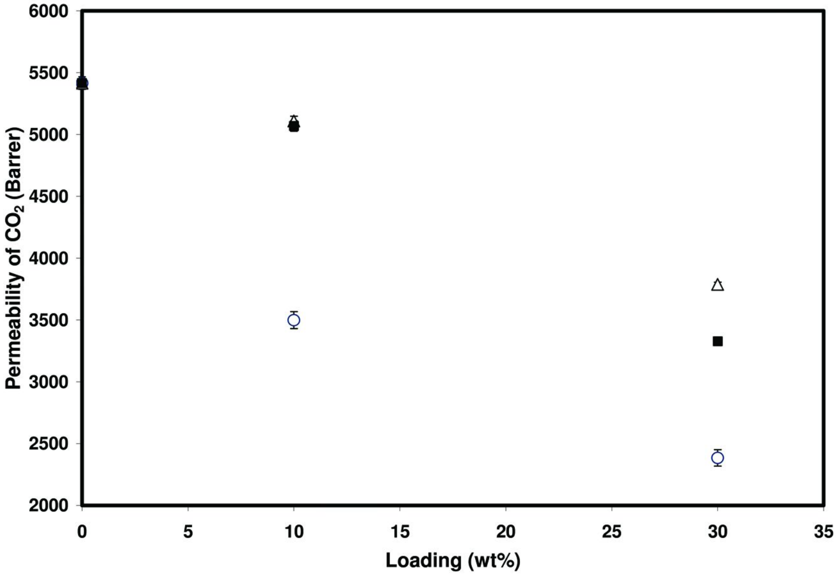

Figure 4. Permeability of CO_2 (△) in CNF- IL [Taurine], (■) in CNF- IL [Br] and (○) in CNF- OX, at 35 °C, 0.27 MPa and dry condition (1 Barrer = 7.6 × 10^{-8} m^3 (STP).m/(m^2.s.Pa)).

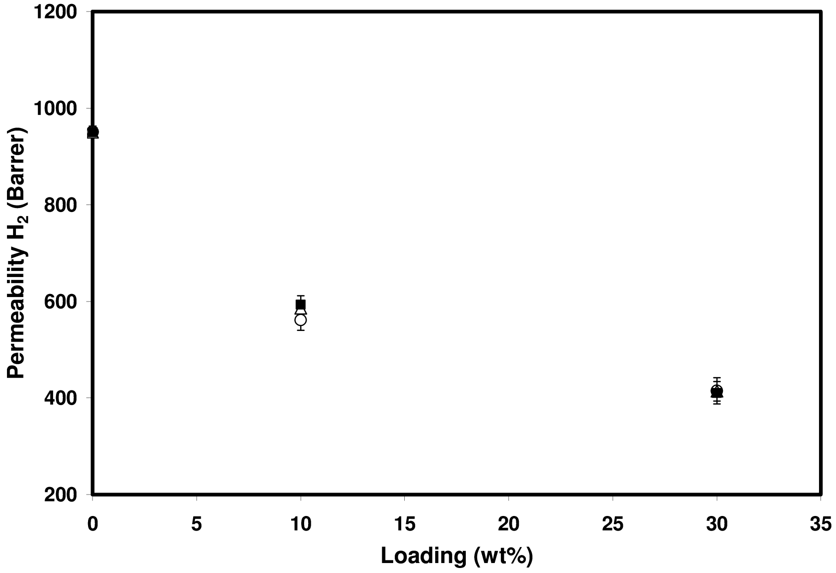

Figure 5. Permeability of H_2 (△) in CNF- IL [Taurine], (■) in CNF- IL [Br] and (○) in CNF- OX, at 35 °C, 0.22 MPa and dry condition (1 Barrer = 7.6 × 10^{-8} m^3 (STP).m/(m^2.s.Pa)).

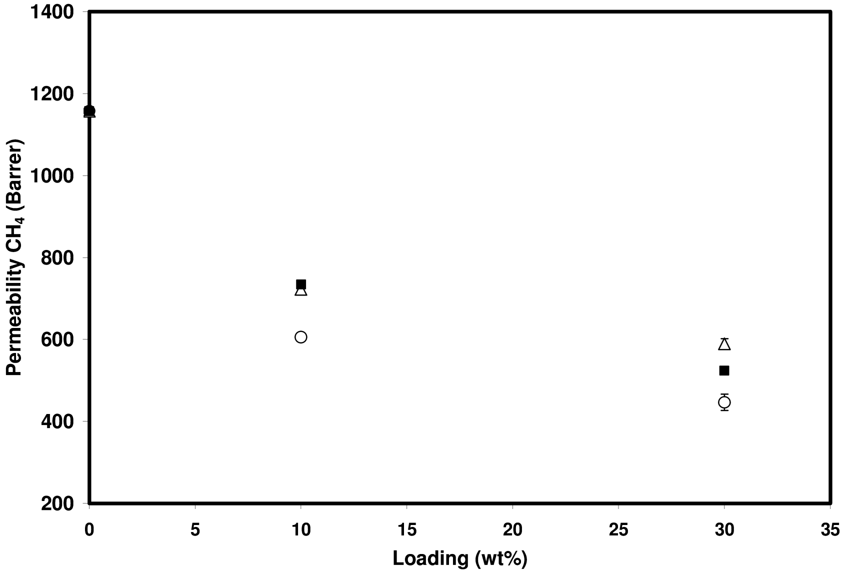

Figure 6. Permeability of CH_4 (△) in CNF- IL [Taurine], (■) in CNF- IL [Br] and (○) in CNF- OX, at 35 °C, 0.26 MPa and dry condition (1 Barrer = 7.6 × 10^{-8} m^3 (STP).m/(m^2.s.Pa)).

Unlike H_2, IL functionalized fibers show higher permeability for CH_4 compared to oxidized fibers (Figure 6). This could be due the fact that these CH_4 can dissolve in IL monomers attached on the surface (*36*).

The selectivity of CO_2/H_2 in the FNN membranes is shown in Figure 7 as a function of nanofiller loading. The samples produced with the CNF- IL showed higher selectivities relative to the samples with CNF- OX due to the interaction of CO_2 with IL groups. Inclusion of 10wt% fibers resulted in increases in the selectivity of CO_2/H_2 in all membranes but adding more fibers (30wt%) results in a reduction in selectivity for both CNF- OX and CNF- IL [Br]. However, the CNF- IL [Br] based FNNM still showed higher selectivity at 30wt% compared to film produced using CNF- OX. Interestingly, CNF- IL [Taurine] based FNNM demonstrated increase in selectivity of CO_2 over H_2 with an increase in loading. This increase corresponds to the higher permeability for CO_2 in CNF- [Taurine] because of higher affinity of IL [Taurine] for CO_2.

The CO_2/CH_4 selectivity in FNNM was measured and shown in Figure 8. The permselectivity of CO_2 to CH_4 increases by adding 10 wt % fibers in all samples but inclusion of 30 wt % fibers results in a decrease in selectivity. It is worth noting that CNF- IL samples show higher selectivity than CNF- OX due to the solubility of CH_4 in those fibers but the CO_2/CH_4 selectivity in both CNF- IL membranes are the same. The standard deviation of selectivity data for all FNN samples in figure 7 and 8 are small, which shows a good accuracy in measuting selectivity.

These results demonstrate the potential of including functionalized carbon nanofibers within a polymer to enhance transport properties because of functional groups bound to the CNF surface with targeted affinity. It also allows for tunable separation properties.

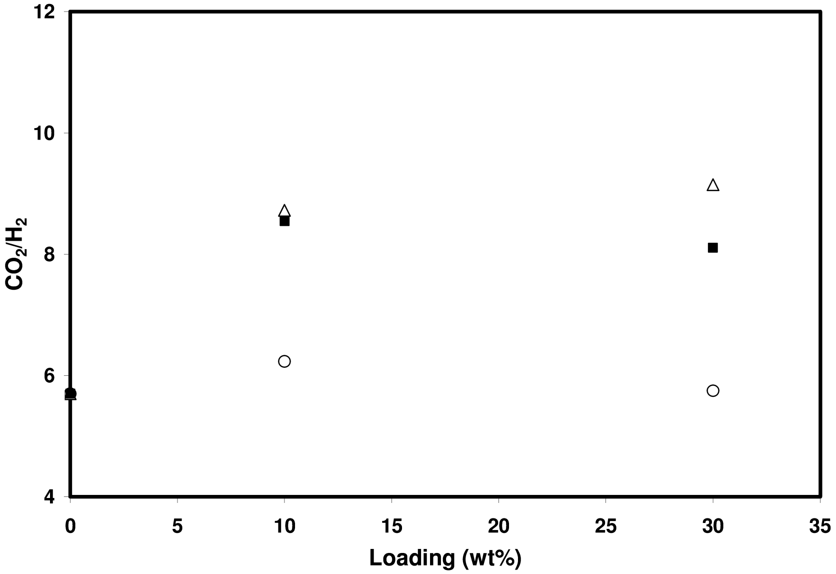

Figure 7. Selectivity of CO_2/H_2 (△) in CNF- IL [Taurine], (■) in CNF- IL [Br] and (○) in CNF- OX.

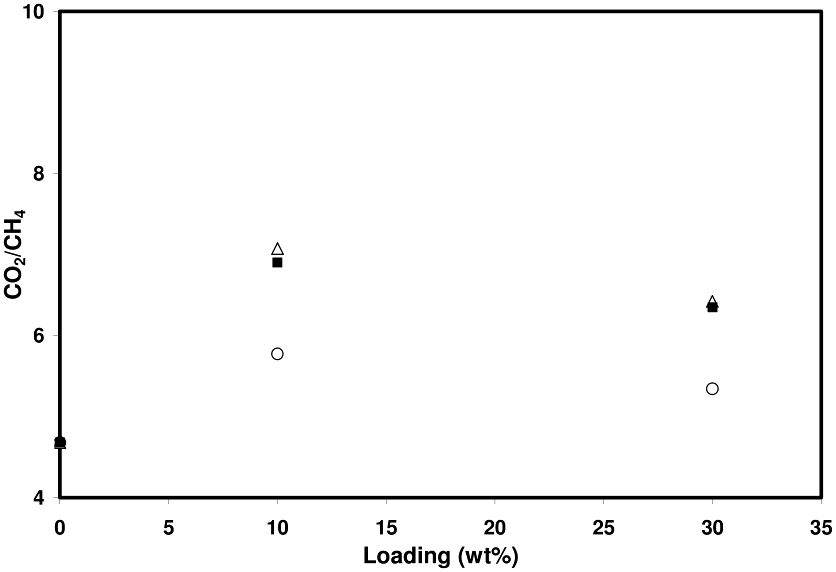

Figure 8. Selectivity of CO_2/CH_4 in (△) in CNF- IL [Taurine], (■) in CNF- IL [Br] and (○) in CNF- OX.

Conclusion

Functional nanofiber network materials were produced using ionic liquid functionalized carbon nanofibers within a PDMS. Oxidized CNF were functionalized with two ionic liquid molecules to provide surface affinity groups that could interact with CO_2 to provide selective transport in the interfacial region. The functionalization was confirmed using XPS analysis.

Inclusion of CNF within PDMS at loadings up to 30 wt% resulted in decreases in permeability for all gases studied. While decreases in H_2 permeability was similar for all systems studied, the decrease for CO_2 was much smaller for FNN produced using IL functionalized CNF. This resulted in increases permselectivity for CO_2/H_2 and CO_2/CH_4 relative to the base PDMS. While this results are interesting, a higher degree of functionalization is needed to realize the potential of this system.

References

1. Anderson, J. L.; Armstrong, D. W. *Anal. Chem.* **2005**, *77*, 6453–6462.
2. Scovazzo, P.; Keift, J.; Finan, D. A.; Koval, C.; Dubois, D.; Noble, R. *J. Membr. Sci.* **2004**, *238*, 57–63.
3. Washiro, S.; Yoshizawa, M.; Nakajima, H.; Ohno, H. *Polymer* **2004**, *45*, 1577–1582.
4. Ohno, H.; Yoshizawa, M.; Ogihara, W. *Electrochim. Acta* **2004**, *50*, 255–261.
5. Ogihara, W.; Washiro, S.; Nakajima, H.; Ohno, H. *Electrochim. Acta* **2006**, *51*, 2614–2619.
6. Nakajima, H.; Ohno, H. *Polymer* **2005**, *46*, 11499–11504.
7. Yoshizawa, M.; Ogihara, W.; Ohno, H. *Polym. Adv. Technol.* **2002**, *13*, 589–594.
8. Bakeeva, R. F.; Oehme, G.; Fuhrmann, H.; Zakirova, G. A.; Sopin, V. F. *Kinet. Catal.* **2006**, *47* (1), 1–4.
9. Wasserscheid, P.; Keim, W. *Angew. Chem. Int.* **2000**, *39*, 3772–3789.
10. Ding, J.; Armstrong, D. W. *Chirality* **2005**, *17*, 281–292.
11. Marcilla, R.; Blazquez, J. A.; Rodriguez, J.; Pomposo, J. A.; Mecerreyes, D. *J. Polym. Sci., Part A: Polym. Chem.* **2004**, *42*, 208–212.
12. Marcilla, R.; Blazquez, J. A.; Fernandez, R.; Grande, H.; Pomposo, J. A.; Mecerreyes, D. *Macromol. Chem. Phys.* **2005**, *206*, 299–304.
13. Gabriel, S.; Weiner, J. *Ber.* **1888**, *21*, 2669–2679.
14. Blancard, L. A.; Hancu, D.; Beckman, E. J.; Brennecke, J. F. *Nature (London)* **1999**, *399*, 28–29.
15. Blanchard, L. A.; Brennecke, J. F. *Ind. Eng. Chem. Res.* **2001**, *40*, 287–292.
16. Gan, Q.; Rooney, D.; Zou, Y. *Desalination* **2006**, *199*, 535–537.
17. Matsumoto, M.; Mikami, M.; Kondo, K. *J. Jpn. Pet. Inst.* **2006**, *49*, 256–261.
18. Ilconich, J.; Myers, C.; Pennline, H.; Luebke, D. *J. Membr. Sci.* **2007**, *298*, 41–47.
19. Bara, J. E.; Gabriel, C. J.; Carlisle, T. K.; Camper, D. E.; Finotello, A.; Gin, D. L.; Noble, R. D. *Chem. Eng. J.* **2009**, *147*, 43–50.

In Modern Applications in Membrane Science and Technology; Escobar, I., et al.;
ACS Symposium Series; American Chemical Society: Washington, DC, 2011.

20. Jindaratsamee, P.; Shimoyama, Y.; Morizaki, H.; Ito, A. *J. Chem. Thermodyn.* **2011**, *43*, 311–314.
21. Kemperman, A. J. B.; Bargeman, D.; Boomgaard, T.; Strathmann, H. *Sep. Sci.Technol.* **1996**, *31*, 2733.
22. Fortunato, R.; Afonso, C.; Benavente, J.; Rodriguez-Castell, E.; Crespo, J. G. *J. Membr. Sci.* **2005**, *256*, 216–223.
23. Tang, J.; Sun, W.; Tang, H.; Radosz, M.; Shen, Y. *Macromolecules* **2005**, *38*, 2037–2039.
24. Tang, J.; Sun, W.; Tang, H.; Radosz, M.; Shen, Y. *J. Polym. Sci., Part A: Polym. Chem.* **2005**, *43*, 5477–5489.
25. Bara, J. E.; Gabriel, C. J.; Hatakeyama, E. S.; Carlisle, T. K.; Lessmann, S.; Noble, R. D.; Gin, D. L. *J. Membr. Sci.* **2008**, *321*, 3–7.
26. Bara, J. E.; Hatakeyama, E. S.; Gabriel, C. J.; Zeng, X.; Lessmann, S.; Gin, D. L.; Noble, R. D. *J. Membr. Sci.* **2008**, *316*, 186–191.
27. Bara, J. E.; Lessmann, S.; Gabriel, C. J.; Evan, S.; Hatakeyama, E. S.; Noble, R. D.; Gin, D. L. *Ind. Eng. Chem. Res.* **2007**, *46*, 5397–5404.
28. Bara, J. E.; Gin, D. L.; Noble, R. D. *Ind. Eng. Chem. Res.* **2008**, *47*, 9919–9924.
29. Bara, J. E.; Noble, R. D.; Gin, D. L. *Ind. Eng. Chem. Res.* **2009**, *48*, 4607–4610.
30. Bara, J. E.; Hatakeyama, E. S.; Gin, D. L.; Noble, R. D. *Polym. Adv. Technol.* **2008**, *19*, 1415–1420.
31. Carlisle, T. K.; Bara, J. E.; Lafrateb, A. L.; Gin, D. L.; Noble, R. D. *J. Membr. Sci.* **2010**, *359*, 37–43.
32. Muldoon, M. J.; Aki, S.; Anderson, J. L.; Dixon, J.; Brennecke, J. F. *J. Phys. Chem. B* **2007**, *111*, 9001–9009.
33. Honga, G.; Jacquemin, J.; Deetlefs, M.; Hardacre, C.; Husson, P.; Costa Gomes, M. F. *Fluid Phase Equilib.* **2007**, *257*, 27–34.
34. Anderson, J. L.; Janeille, K. D.; Brennecke, J. F. *Acc. Chem. Res.* **2007**, *40*, 1208–1216.
35. Camper, D.; Scovazzo, P.; Koval, C.; Noble, R. D. *Ind. Eng. Chem. Res.* **2004**, *43*, 3049–3054.
36. Li , P.; Ph.D. Thesis, University of Toledo, Toledo, OH, 2010.
37. Mapkar, J. A.; Blashi, A.; Berhan, L. M.; Coleman, M. R. Submitted to *Compos. Sci. Technol.* 2010.
38. Li, X.; Coleman, M. R. *Carbon* **2008**, *46*, 1115–1125.
39. Bartling, J. K. *Nature* **1973**, *243*, 342–344.

Chapter 7

Separation of Aromatic/Aliphatic Mixtures by Pervaporation Using *ortho*-Functionalized Polyimide Membranes

Claudio P. Ribeiro Jr.,[1] Benny D. Freeman,*,[1] Douglass S. Kalika,[2] and Sumod Kalakkunnath[3]

[1]Center for Energy and Environmental Research, University of Texas at Austin, 10100 Burnet Road, building 133, Austin, TX, 78759
[2]Department of Chemical and Materials Engineering, University of Kentucky, Lexington, KY, 40506
[3]ConocoPhillips Company, Bartlesville Technology Center, Bartlesville, OK, 74004
***E-mail: freeman@che.utexas.edu**

The performance of a series of soluble aromatic polyimides for the separation of benzene/*n*-heptane and toluene/*n*-heptane mixtures by pervaporation is reported. Homo- and random copolyimides were synthesized by a two-step polycondensation of three aromatic dianhydrides (6FDA, ODPA, BTDA) and five aromatic diamines (APAF, HAB, 3MPD, 4MPD, and FDA). Pervaporation experiments were performed at 80°C with feed streams containing 40 wt% aromatics. All polymers were selective towards the aromatic hydrocarbon, whose permeability could be changed by 4 orders of magnitude depending upon the chemical structure of the diamine. Pure-liquid sorption experiments at 25°C revealed that these large changes in hydrocarbon permeability were mainly caused by changes in the diffusion coefficient. The performance of the synthesized materials was compared with previous results reported for other polymers, as well as with the performance of Matrimid®, a commercial polyimide.

In Modern Applications in Membrane Science and Technology; Escobar, I., et al.;
ACS Symposium Series; American Chemical Society: Washington, DC, 2011.

Introduction

The separation of aromatic and aliphatic hydrocarbons is relevant for various processes in the refining and petrochemical industries, including naphtha reforming, production of cyclohexane, and removal of sulfur from gasoline (*1*, *2*). Many of these mixtures are difficult to separate because they contain close boiling compounds that generally have similar physical and chemical properties. The conventional technologies used to perform these separations, such as extractive distillation, azeotropic distillation and liquid-liquid extraction, are energy intensive and expensive (*3*, *4*) .

In view of the potential energy savings and, more recently, reduction in carbon dioxide emissions, pervaporation has been widely investigated for the separation of aromatic/aliphatic mixtures (*5–8*). One of the major roadblocks to the separation of hydrocarbon mixtures by pervaporation is the development of a membrane material with suitable transport properties that, at the same time, can withstand chemically aggressive feed streams and the harsh operating conditions involved. As a result, most studies in this area have focused on membrane material development. Aromatic polyimides, in particular, have attracted considerable attention for this application due to their high thermal and chemical stability (*9–21*). From the gas separation literature, it is known that an enhancement in permeability for polyimide membranes is obtained by the inclusion of hexafluoropropane moieties, fluorene moieties, and substituents in the ortho position of the diamine relative to the amino group (*22–24*). However, the combination of these three strategies in the development of polyimide pervaporation membranes for the proposed application remains unexplored.

In this chapter, we report a structure/property study of a series of soluble aromatic polyimides for the separation of aromatic/aliphatic mixtures by pervaporation. Homo- and copolyimides were synthesized by the polycondensation of aromatic dianhydrides and diamines. These polymers were then evaluated as pervaporation membranes in experiments at 80^{o}C with either toluene/*n*-heptane or benzene/*n*-heptane mixtures as feed streams. Pure-liquid sorption experiments at 25^{o}C were also conducted to characterize the solubility and the diffusion coefficient of the hydrocarbons in these materials. The long-term chemical stability of the polymers was assessed in exposure tests to benzene in a Soxhlet extractor for at least a week.

Experimental Section

Materials

Three dianhydrides were used for polyimide synthesis: 2,2’-bis-(3,4-dicarboxyphenyl) hexafluoropropane dianhydride (6FDA), 4,4’-oxydiphthalic anhydride (ODPA), and 3,3’,4,4’-benzophenone tetracarboxylic dianhydride (BTDA). 6FDA and ODPA were purchased from Chriskev, while BTDA was purchased from Akros. All dianhydrides were initially dried at 190^{o}C for 6 h under low vacuum (~ 510 torr) and then dried at 120^{o}C overnight under high vacuum (< 1 torr) before use. Figure 1 shows the chemical structure of each dianhydride.

The following diamines were tested for polyimide synthesis: 3,3'-dihydroxy-4,4'-diamino-biphenyl (HAB), 9,9'-bis (4-aminophenyl) fluorene (FDA), 2,2-bis (3-amino-4-hydroxyphenyl)-hexafluoropropane (APAF), 2,3,5,6- tetramethyl-1,4-phenylenediamine (4MPD), and 2,4,6-trimethyl-*m*-phenylenediamine (3MPD). The chemical structure of these diamines can be seen in Figure 2. 3MPD was purchased from TCI America, whereas all other diamines were obtained from Chriskev. Most diamines were dried at 50°C overnight under high vacuum (< 1 torr) before use, with the exception of APAF, for which the drying temperature was set to 95°C. The purity of 3MPD was determined by titration (*25*). All other diamines and dianhydrides were monomer grade.

All solvents used in this work were purchased from Sigma Aldrich. *N*,*N*-dimethylacetamide (DMAc), 1,2-dichlorobenzene (ODB), *n*-heptane, toluene, and benzene were used as received, whereas 1-methyl-2-pyrrolidinone (NMP) was distilled over calcium hydride prior to use.

Matrimid® 5218 from Huntsman Advanced Materials was generously supplied by Air Liquide/Medal, Newport, DE, and used as received. Matrimid®, a polyimide based on BTDA and diaminophenylindane, is commercially used for gas separation membranes (*26*).

Polymer Synthesis

Homopolyimides and random copolyimides were synthesized by the two-step polycondensation method with thermal imidization in solution ((*27–29*)), as shown in Figure 3. For example, to a 500 ml flask purged with nitrogen were added 3.2435 g of HAB (15.00 mmol), 2.4635 g of 4MPD (15.00 mmol) and 50 ml of NMP. The mixture was mechanically stirred to form a clear, brown solution at room temperature. To this solution of diamines were added 13.3262 g of 6FDA (30.00 mmol) and 60 ml of NMP in order to achieve 15% (w/v) solids content. The reaction was carried out at room temperature for 24 h to give a viscous poly(amic acid) solution. ODB (48 ml) and NMP (87 ml) were added to the flask to achieve 8% (w/v) solids content in an ODB/NMP (20/80 v/v) mixed solvent. The poly(amic acid) was thermally cyclized to the corresponding polyimide by heating the mixture to 180°C for 24 h under reflux. Water was removed as the ODB/water azeotrope using a Dean-Stark trap. The cooled polymer solution was precipitated in a blender using a methanol/water solution. The precipitated polyimide was filtered, washed several times with water, allowed to dry at room temperature for 24 h, and then finally dried under vacuum at 200°C for at least 2 days.

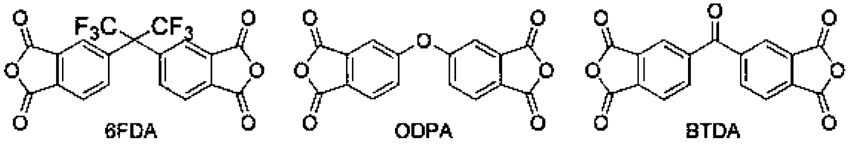

Figure 1. Dianhydrides used for polymer synthesis.

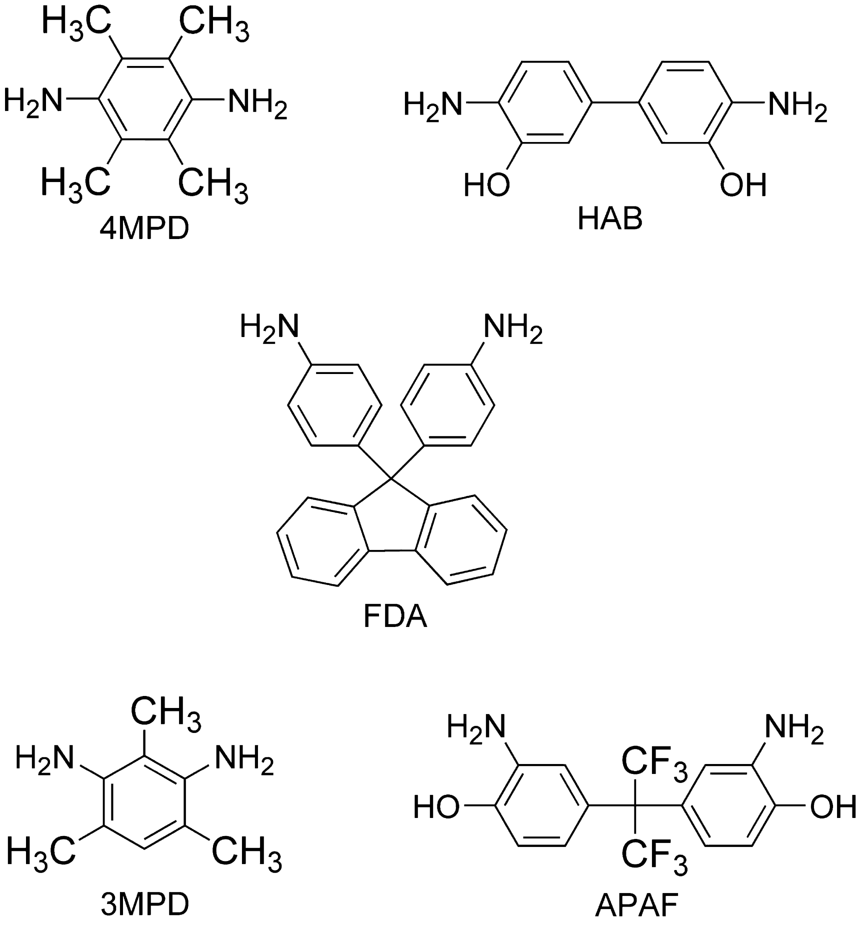

Figure 2. Diamines used for polymer synthesis.

Polymer Characterization

Polymers were characterized by thermogravimetric analysis, infrared spectroscopy, nuclear magnetic resonance spectroscopy, and inherent viscosity measurements.

Thermogravimetric analysis (TGA) scans were obtained in a Q500 thermogravimetric analyzer from TA Instruments, using a heating rate of 5°C/min under nitrogen atmosphere.

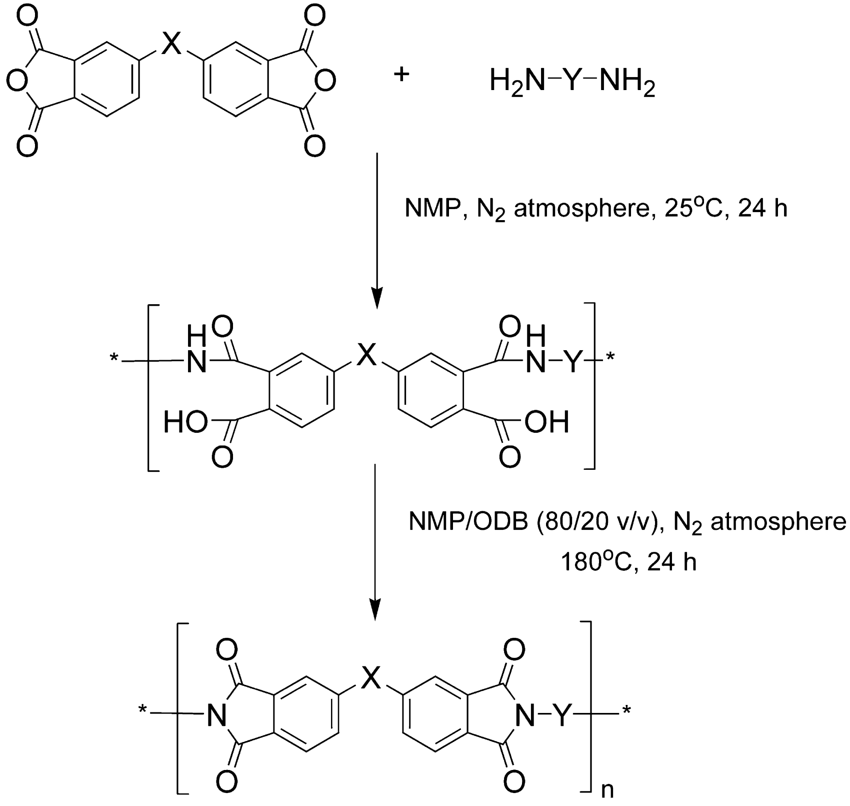
X
+
$H_2N-Y-NH_2$
NMP, N_2 atmosphere, 25°C, 24 h
NMP/ODB (80/20 v/v), N_2 atmosphere
180°C, 24 h
n

Figure 3. Schematic route for polymer synthesis.

Fourier-transform Infrared Spectroscopy (FTIR) studies were completed using the Attenuated Total Reflectance (ATR) technique with a Nexus 470 Fourier-Transform Infrared Spectrometer from Thermo Nicolet. A total of 128 scans were made for each spectrum, with the resolution of the spectrometer set to 2 cm^{-1}.

Proton nuclear magnetic resonance (^1H NMR) spectra were recorded on a Varian INOVA-500 spectrometer operating at 500 MHz. Deuterated chloroform was the standard solvent for sample preparation, while deuterated dimethyl sulfoxide was used for polymers that did not dissolve in chloroform. Trimethylsilane was added as a reference for all samples.

Inherent viscosity of a 0.5 g/dL solution of the polymer in NMP was measured at 25°C using an Ostwald viscometer. The viscometer, immersed in a temperature controlled circulation bath, was washed three times with 15 ml of the polymer solution before measurement. A pipette was used to transfer 10 ml of polymer solution into the viscometer. To ensure that thermal equilibrium had been reached, the polymer solution was held in the viscometer for a minimum of three hours prior to flow time measurement.

Membrane Preparation

Dense polyimide films were prepared by controlled solvent evaporation. A polymer solution approximately 3 wt% in DMAc was filtered through a 5 µm PTFE syringe filter and cast onto a clean glass plate previously leveled inside a vacuum oven. The solvent was slowly evaporated according to the following heat treatment: 4 h at 80°C, 100°C overnight, and 200°C under vacuum for 2 days. The final film thickness, measured with a digital micrometer (Mitutoyo, Model ID-C112E) readable to ± 1 µm, ranged from 15 to 40 µm. For each film sample, thickness was measured at a minimum of 30 different points within the effective permeation area, and the average value was used.

Pervaporation

The dense film to be tested, supported on a sintered stainless steel plate, was mounted in a tailor-made stainless steel permeation cell equipped with a magnetic stirrer. The feed volume in the permeation cell was 400 ml, and either a toluene/*n*-heptane or a benzene/*n*-heptane mixture was used as feed. The pressure on the downstream side was kept below 1 torr with the aid of a vacuum pump. The permeation cell was immersed in a temperature-controlled oil circulation bath whose temperature was set to 80.0°C. Permeate samples were collected in a crystallizer immersed in liquid nitrogen. Once steady-state was achieved, which could take between 2 to 18 h depending on the polymer, the permeate flux (J) was computed based on the mass of permeate (m_P) collected within a given time interval Δt according to Equation 1:

$$J = \frac{m_P}{A\Delta t} \tag{1}$$

where A is the membrane area, whose value, in our permeation cell, was 36.96 cm^2.

Feed and permeate samples were analyzed by gas chromatography, using a flame ionization detector, to determine the concentrations of each hydrocarbon. These concentrations were then used to calculate the separation factor of the membrane for components i and j, βij, according to Equation 2:

$$\beta_{i,j} = \frac{C_i^P / C_j^P}{C_i^F / C_j^F} \tag{2}$$

where C is the hydrocarbon concentration expressed in mass fraction. The superscripts P and F refer to permeate and feed samples, respectively. Each sample was analyzed in triplicate. At a given operating condition, feed samples were collected at the beginning and at the end of each run, while 4-5 permeate samples were collected, and the results were averaged to determine the membrane flux and separation factor.

Traditionally, in the pervaporation literature, different membranes are compared in terms of their flux and separation factor values (*6*, *30*, *31*). However, these parameters depend not only on the membrane material but also on the adopted operating conditions and, in the case of flux, membrane thickness (*32–34*). Therefore, to minimize the influence of the operating conditions, different materials are compared in this work in terms of permeability and permselectivity values. Once the flux and permeate composition are known, the permeability of each hydrocarbon in the membrane can be calculated according to Equation 3 (*32*, *33*):

$$\wp_i = \frac{J C_i^P L}{MW_i x_i^F \gamma_i P_i^{sat}} \tag{3}$$

where L is the membrane thickness, MW_i and P_i^{sat} are the molecular weight and the vapor pressure of component i, respectively, x_i^F is the mole fraction of component i in the feed, and γ_i is the activity coefficient of component i in the feed stream, whose value was computed using the NRTL model with parameters given by Gmehling et al. (*35*). The most common unit of permeability is Barrer (1 Barrer ≡ 1×10^{-10} cm^3_{STP} cm^{-1} s^{-1} $cmHg^{-1}$), and this unit will be used in this work. A variety of IUPAC-type units could also have been used – for example, $m^3_{STP}m^{-1}s^{-1}kPa^{-1}$ ($1\ m^3_{STP}m^{-1}s^{-1}kPa^{-1} = 1.33 \times 10^{14}$ Barrer) or mol $m^{-1}s^{-1}kPa^{-1}$ (1 mol $m^{-1}s^{-1}kPa^{-1} = 2.99 \times 10^{12}$ Barrer). Comparison of materials in terms of permeability coefficients minimizes the effect of operating conditions on the results, but does not completely remove it.

The permselectivity (α_{ij}), in turn, is defined as follows:

$$\alpha_{ij} = \frac{\wp_i}{\wp_j} \tag{4}$$

Benzene Exposure

The chemical stability of the polymers towards aromatics was assessed by exposure to pure benzene in a Sohxlet extractor for at least a week. A film sample of the polymer to be tested was degassed at 50°C under vacuum overnight, weighed, and then placed in the Sohxlet extractor. At the end of the test, if the polymer sample kept its integrity, it was dried at 50°C under vacuum for two days and weighed again. Photographs of the film before and after the benzene exposure were taken to record any visual changes.

Pure-Liquid Sorption

Sorption isotherms for pure benzene, toluene, and *n*-heptane were measured at 25°C for selected polymers to provide information about the solubility and diffusivity of these hydrocarbons in the polymers. A known amount of the polymer film was placed in a sealed glass jar containing the hydrocarbon of interest. The jar was kept in a temperature-controlled circulation water bath. At different times, the film sample was quickly removed from the jar and weighed on an analytical balance after the excess liquid on its surfaces had been wiped off with filter paper. The film sample was placed back into the jar and returned to the water bath. This procedure was repeated until the mass of the film remained constant as a function of time. Before each test, the film samples were degassed overnight at 50°C in a vacuum oven, and the hydrocarbon-containing jars were kept in the water bath overnight.

Results and Discussion

Polymer Characterization

The chemical structure of each polyimide synthesized in this work was confirmed by FTIR and ^{1}H NMR spectra. Examples of FTIR spectra for some of the polyimides are shown in Figure 4. In all cases, the four characteristic peaks traditionally associated with the phthalic imide ring (*28*, *36*, *37*) can be identified: (i) symmetric C=O stretch around 1780 cm^{-1}, (ii) asymmetric C=O stretch around 1720 cm^{-1}, (iii) C-N-C stretch around 1370 cm^{-1}, and (iv) C-N-C ring deformation around 720 cm^{-1}. Polymers prepared using APAF (and HAB as well, though not shown in Figure 4) show a broad peak at 3200-3600 cm^{-1} typical of the O-H stretch from a hydrogen bonded hydroxyl group. Also very clear from FTIR results is the presence of $–CF_3–$ groups in the polymer, evidenced by high intensity peaks in the 1350-1120 cm^{-1} region for materials prepared using either APAF or 6FDA.

For two of the polymers considered in Figure 4, the corresponding ^{1}H NMR spectra are given in Figure 5. With the NMR, the details of the structure are verified, and the lack of additional peaks confirms the absence of byproducts or residual solvent in the polymer. One important aspect is the lack of any features beyond 10.5 ppm, which is the region where one would find the proton peak from a carboxylic acid (*38*). This indicates there is very little residual poly(amic acid) in the polymers prepared in this work. In other words, a high degree of imidization is confirmed.

All polyimides prepared in this work could be cast into self-supporting films, with values of inherent viscosity that ranged from about 0.3 to 1.9. A compilation of inherent viscosity values is given in Table 1.

Table 1. Inherent viscosity (η) of 0.5 g/dL solutions of different polyimides in NMP at 25°C

Polymer	*η (-)*	*Polymer*	*η (-)*
APAF-6FDA	0.66	HAB/4MPD(1:1)-6FDA	0.68
4MPD-6FDA	0.50	HAB/4MPD(1:3)-6FDA	0.65
3MPD-6FDA	0.32	APAF/FDA(1:1)-6FDA	0.66
HAB-6FDA	1.91	FDA-6FDA	0.54
APAF-ODPA	0.98	4MPD-BTDA	0.98

Transport Properties

All polymers were first tested with a toluene/*n*-heptane (40/60 wt%) feed at 80°C, while only those with reasonable transport properties, that is, a toluene permeability higher than 1,000 Barrer and a permselectivity higher than 2.0, were further tested with a benzene/*n*-heptane (40/60 wt%) feed. The reasons for this experimental strategy are twofold. First, such procedure minimizes the number of runs with benzene, a carcinogenic compound. Second, for a fixed concentration of aromatics, the toluene/*n*-heptane mixture is harder to separate by pervaporation, since toluene is less volatile than *n*-heptane, while benzene has a higher vapor pressure than *n*-heptane.

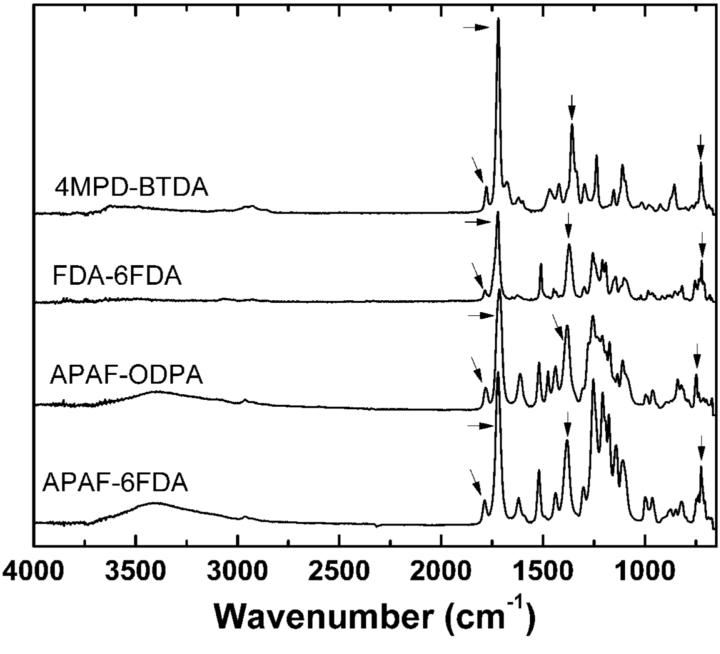

Figure 4. FTIR spectra for some of the polyimides synthesized in this work. Highlighted peaks are characteristic of phthalic imide rings.

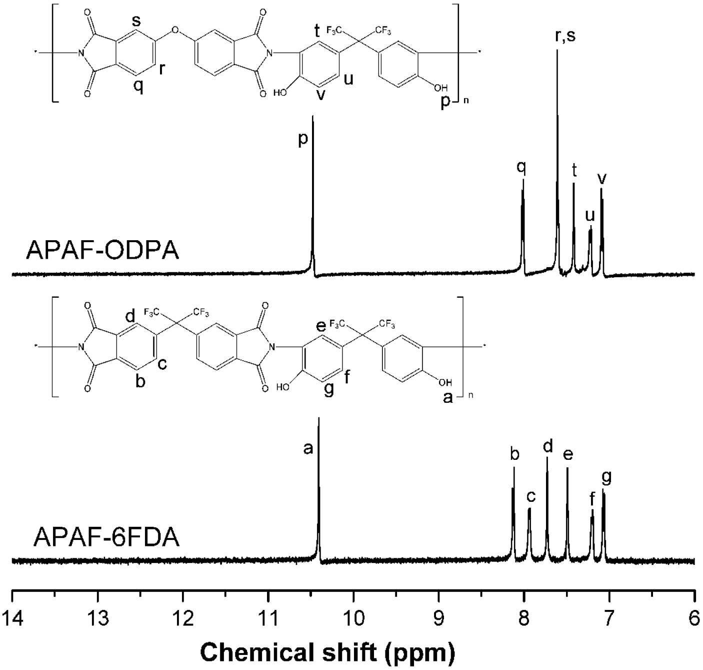

Figure 5. Example of ^1H NMR spectra for two of the polyimides synthesized in this work.

In the following two sections, the effects of the chemical structure of the polymer on the transport properties are illustrated using the pervaporation data for the toluene/*n*-heptane system. In the final section, all transport data obtained in this work are compared with previous literature results.

Effect of Diamine Moiety

With 6FDA as the dianhydride, a homopolyimide was synthesized with each diamine shown in Figure 2. The performance of these polymers as pervaporation membranes for the separation of a toluene (40 wt%) /n-heptane (60 wt%) mixture at 80°C is summarized in Table 2. All fluxes were normalized by the thickness of the dry polymer film.

Table 2. Pervaporation performance of a series of 6FDA-based polyimides for the separation of a toluene/*n*-heptane mixture at 80°C

Diamines	*Toluene conc. (wt%)*		*J × L (kg μm m^{-2} h^{-1})*	*β*	*Permeability (Barrer)*		*α*
	feed	*perm.*			*Toluene*	*n-Heptane*	
HAB	40.6	48.5	0.037	1.38	8.9	4.6	1.93
APAF	40.6	45.6	0.485 ± 0.086	1.23	109	63	1.73
FDA	40.2	71.6	7.48 ± 0.14	3.75	2.63 × 10^3	5.06 × 10^2	5.20
3MPD	40.6	66.2	19.5 ± 1.1	2.87	6.30 × 10^3	1.58 × 10^3	3.99
4MPD	39.8	61.3	53.2 ± 1.7	2.40	1.62 × 10^4	4.88 × 10^3	3.32
4MPD/ HAB (1:1)	41.6	75.2	3.28 ± 0.04	4.26	1.18 × 10^3	1.98 × 10^2	5.96
4MPD/ HAB (3:1)	39.2	67.7	9.89 ± 0.15	3.25	3.36 × 10^3	7.51 × 10^2	4.47
APAF/FDA (1:1)	40.6	64.3	0.031 ± 0.011	2.63	9.8	2.7	3.63
APAF/ 4MPD (1:1)	40.1	76.9	0.017 ± 0.002	4.97	6.5	0.9	7.22

Although all polyimides were selective towards aromatics, the chemical structure of the diamine had a very significant effect on membrane performance. The hydroxyl-containing polyimide based on HAB, the diamine with a biphenyl unit, exhibited the lowest hydrocarbon permeability in this series. When HAB was replaced with APAF, the inclusion of a $-C(CF_3)_2-$ unit between the phenyl groups (and a change from *para* to *meta* connectivity) led to a 12-fold increase in toluene permeability, together with a decrease of about 14% in the separation factor. On the other hand, when FDA was used instead of HAB, which introduced a fluorene unit between the phenyl groups (and kept the *para* connectivity), not only did the toluene permeability increase by almost three orders of magnitude, but also the separation factor was enhanced by more than a factor of 2. Further increases in toluene permeability were achieved by using the methyl-substituted monophenyl diamines 3MPD and 4MPD. Compared to HAB, 4MPD formed a 6FDA-based polyimide whose toluene permeability was almost four orders of magnitude higher. For the polyimides based on these monophenyl diamines, the separation factors were still higher than the values associated with the hydroxyl-containing polyimides (HAB-6FDA and APAF-6FDA).

The diamines 4MPD and FDA led to the homopolyimides with the highest permeability and separation factor in Table 2, respectively. Therefore, these monomers were used together with the *ortho*-functionalized diamines HAB and APAF to form 6FDA-based random copolyimides. The pervaporation performance of these copolyimides is also listed in Table 2. For the copolymers, the numbers given in brackets correspond to the molar ratio of the diamine monomers used in the synthesis. Thus, for instance, the polymer HAB/4MPD(1:1)-6FDA was prepared using an equimolar mixture of HAB and 4MPD.

For the HAB/4MPD copolyimides, hydrocarbon permeability coefficients lay between the values observed for the two homopolyimides, while the separation factors were always higher for the copolyimides. An increase in the 4MPD content resulted in an increase in permeability of both hydrocarbons and a decrease in the aromatic/aliphatic separation factor. On the other hand, copolyimides prepared using APAF and either 4MPD or FDA showed rather low hydrocarbon permeability coefficients. Nevertheless, one of the APAF-based copolyimides is the material with the highest selectivity towards aromatics in Table 2.

Effect of Dianhydride Moiety

Although 6FDA forms soluble polyimides with any diamine, the same does not hold for other dianhydrides. In fact, solubility in common organic solvents is more of an exception than a general rule for polyimides (*29*). As a result, there is considerably less flexibility for varying the dianhydride moiety in the polyimide structure if the final polymer is required to be soluble.

Using APAF and 4MPD as diamines, homopolyimides were synthesized utilizing either ODPA or BTDA as the dianhydride. Table 3 compares these new homopolyimides with their 6FDA equivalents in terms of their performance for the separation of a toluene/*n*-heptane mixture by pervaporation.

Replacement of the $–C(CF_3)_2$ – unit in the dianhydride resulted in a reduction in hydrocarbon permeability, and consequently in the total flux, together with an increase in the separation factor. This behavior is similar to the one observed in gas separation membranes for the CO_2/CH_4 pair (*23*, *24*). With APAF, the use of ODPA instead of 6FDA increased the separation factor by almost 50%, but even this higher value was still lower than 2.0. A more substantial gain in the separation factor, namely 119 %, was achieved by reacting BTDA instead of 6FDA with 4MPD. In fact, among all polyimides prepared in this work, 4MPD-BTDA exhibited the highest separation factor. For both APAF and 4MPD, the total flux decreased by approximately a factor of 10 when 6FDA was replaced as the dianhydride.

Table 3. Effect of dianhydride moiety on the pervaporation performance of polyimides for the separation of a toluene/*n*-heptane mixture at 80°C

Diamine	*Dianhydride*	*Toluene conc. (wt%)*		$J \times L$ (*kg μm m^{-2} h^{-1}*)	*β*
		feed	*perm.*		
APAF	6FDA	40.6	45.6	0.485 ± 0.086	1.23
	ODPA	38.9	53.7	0.053	1.82
4MPD	6FDA	39.8	61.3	53.2 ± 1.7	2.40
	BTDA	38.9	77.0	4.02 ± 0.14	5.26

Comparison with Other Materials and Data for the Benzene/n-Heptane System

Many membrane materials have been tested for aromatic/aliphatic separation by pervaporation (*5–8*, *30*). Nonetheless, most of these previous studies were conducted using only benzene/cyclohexane mixtures as feed streams. For the particular case of toluene/*n*-heptane mixtures, previously investigated materials include fluorinated polyimides (*19*, *20*), cross-linked aliphatic polyurethanes (*39*), and poly(vinyl chloride) nanocomposites (*40*). A comparison between the transport properties of these materials and the polyimides synthesized in this work is shown in Figure 6. Also included in the figure is the result determined in this work for Matrimid®, a commercial polyimide used in gas separation membranes. All permeability coefficients and permselectivity values in Figure 6 were calculated with Equation 3 using either our own experimental data or flux and separation factor data collected from tables and/or graphs given in previous papers.

Unfortunately, the hydroxyl-containing homopolyimides based on HAB and APAF are among the materials with the lowest selectivity in Figure 6. On the other hand, with the other diamines in Figure 2, we were able to prepare polyimides with enhanced transport properties compared to both Matrimid and previous polyimides prepared by Ye at al. (*20*). In fact, our best materials exhibit performance comparable to that reported by Aouinti et al. (*40*) for most of their organic-inorganic composite membranes. The highest combination of selectivity and permeability values reported so far for the toluene/*n*-heptane system is associated with cross-linked aliphatic polyurethanes. One drawback of polyurethanes, however, is their lower thermal stability compared to polyimides (*41*). This topic will be discussed in the next section.

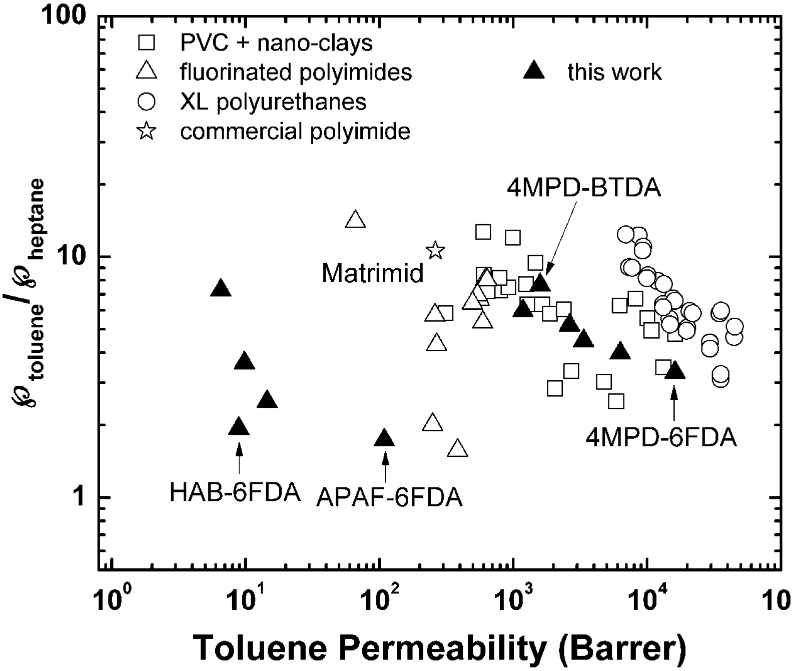

Figure 6. Comparison between the polyimides prepared in this work and other materials used as membranes for the separation of toluene/n-heptane mixtures by pervaporation.

With regard to the benzene/*n*-heptane system, the pervaporation performance for some of the materials prepared in this work is summarized in Table 4. Comparison of the data in Table 4 with the data in Tables 2 and 3 shows that, for a given polymer and similar content of aromatics in the feed, both the separation factors and the total flux are always higher when the benzene/*n*-heptane mixture is used as feed. One could mistakenly conclude from these results that benzene has a much higher permeability in these polymers compared to toluene. However, these differences in total flux and separation factor are a consequence of differences in driving force. In pervaporation, keeping temperature and concentrations fixed is not enough to guarantee equality of driving forces. Due to its higher vapor pressure compared to toluene, at a given temperature, benzene has a higher driving force (the activity coefficients for these two aromatic compounds in binary mixtures with *n*-heptane are similar (*35*)). When the effect of the driving force is accounted for in the calculation of the permeability (Equation 3), it becomes evident that both aromatic compounds have similar permeability coefficients in the polymer. Therefore, although these polymers are selective towards aromatics, they cannot be used to separate benzene from toluene.

Table 4. Pervaporation performance of some polyimides prepared in this work for the separation of a benzene/*n*-heptane mixture at 80°C

Polymer	*Benzene conc. (wt%)*		*J × L (kg μm m^{-2} h^{-1})*	*β*	*Permeability (Barrer)*		*α*
	feed	*perm.*			*Benzene*	*n-Heptane*	
4MPD-6FDA	36.6	61.8	87.6 ± 2.1	2.80	1.14×10^4	7.98×10^3	1.43
FDA-6FDA	35.7	69.1	15.76 ± 0.50	4.03	2.34×10^3	1.14×10^3	2.05
4MPD-BTDA	39.1	79.5	9.18 ± 0.18	6.04	1.47×10^3	4.66×10^2	3.15
4MPD/HAB(1:1)-6FDA	38.1	73.3	9.57 ± 0.17	4.46	1.44×10^3	6.22×10^2	2.32
4MPD/HAB(3:1)-6FDA	39.8	72.7	16.67 ± 0.47	4.03	2.41×10^3	1.14×10^3	2.11

A comparison between our polyimides and other polymers studied in the literature (*19*, *42*) for benzene/*n*-heptane separation by pervaporation is given in Figure 7. Fewer literature data are available for this system compared to toluene/*n*-heptane, and our materials exhibit better performance than other previously tested polyimides.

Thermal Stability

Despite the high importance of the transport properties in the selection of a membrane material, this is not the only factor to be taken into consideration for the target application. The separation of real hydrocarbon streams in refineries will require high operating temperatures (*4*), and therefore the thermal stability of the membrane material should also be taken into account.

Typical TGA results for the materials prepared in this work are shown in Figure 8. None of the polyimides show any significant mass loss before 400°C, which attests to their excellent thermal resistance. In this regard, these materials are much superior to aliphatic polyurethanes. To illustrate this point, a polyurethane was prepared from 1,6-diisocyanatohexane (HDI) and poly(ethylene glycol) 600 (PEG600), following the procedure described by Grabczyk (*43*). These two monomers were used by Roizard et al. (*39*) to prepare the cross-linked polyurethanes exhibiting the highest combination of selectivity and permeability values in Figure 6. Contrary to Roizard et al. (*39*), we did not include 2,2’,2”-nitrilotriethanol in the reacting mixture, and therefore the polyurethane prepared in this work is not cross-linked.

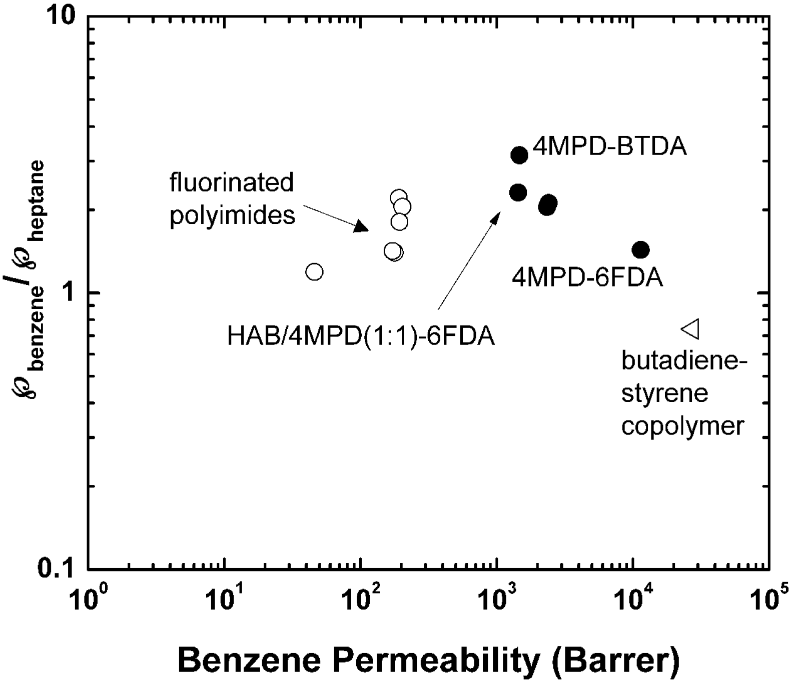

Figure 7. Comparison between the polyimides prepared in this work (filled symbols) and other materials (open symbols) used as membranes for the separation of benzene/n-heptane mixtures by pervaporation.

The thermal stability of the HDI-PEG600 polyurethane, as evidenced by the TGA results in Figure 8, is much lower than that observed for our polyimides. More specifically, the polyurethane began to degrade at around 300°C in nitrogen, and it was completely degraded by 400°C. In an isothermal TGA run, whose results are presented in Figure 9, the same polyurethane displayed slow but continuous degradation at a temperature of 200°C in nitrogen. On the other hand, no significant mass loss was observed for any polyimide from this work in similiar isothermal TGA runs at 200°C, as illustrated by the data presented for the 4MPD-BTDA polyimide in Figure 9.

Chemical Stability

Apart from suitable transport properties and high thermal stability, the membrane material for the target application must also exhibit long-term stability towards aromatics. This requirement was tested in exposure tests to pure benzene in a Sohxlet extractor for at least a week. A summary of the outcome of such exposure tests is given in Table 5. Photographs of some polymer films before and after the exposures tests are shown in Figure 10.

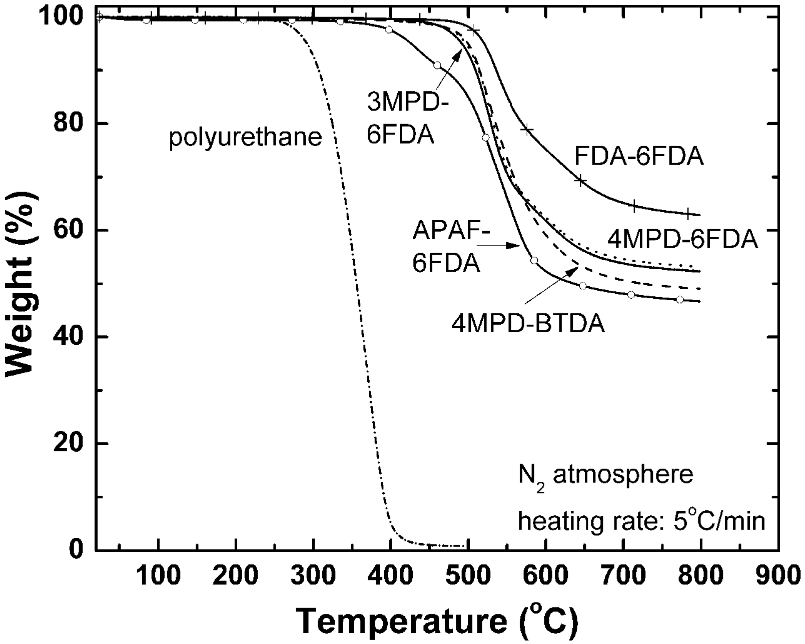

Figure 8. Thermogravimetric analysis (TGA) of different polyimides and a polyurethane (HDI-PEG600) prepared in this work.

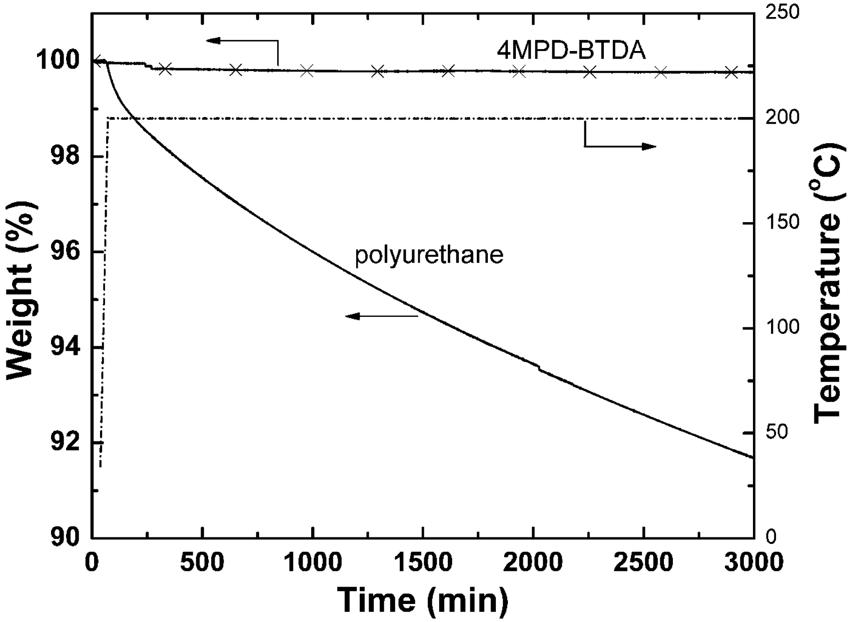

Figure 9. Isothermal TGA of a polyurethane (HDI-PEG600) and an aromatic polyimide (4MPD-BTDA) prepared in this work.

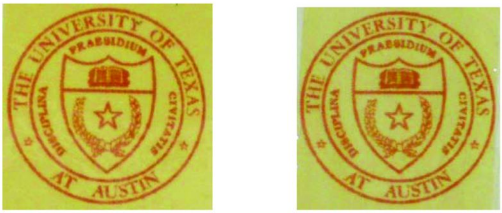

before after

4MPD-BTDA

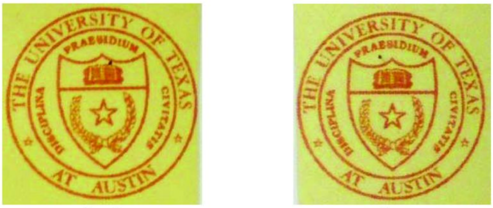

before after

HAB/4MPD(1:1)-6FDA

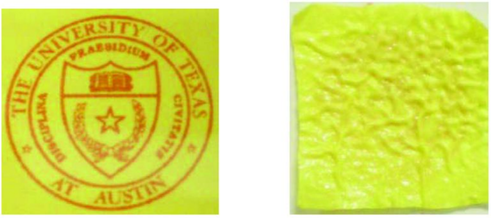

before after

Matrimid®

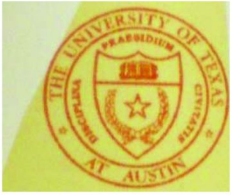

Dissolved
within a few
hours

before after

FDA-6FDA

Figure 10. Photographs of some polymer films before and after benzene exposure in a Sohxlet extractor. Specific exposure times for each material are given in Table 5.

Table 5. Outcome of benzene exposure tests in a Sohxlet extractor for different polyimides

Polymer	*Exposure time (days)*	*Outcome*
HAB-6FDA	7	no visual change or mass loss
APAF-6FDA	7	no visual change or mass loss
Matrimid®	7	film became opaque and brittle
HAB/4MPD(1:1)-6FDA	8	no visual change or mass loss
4MPD-6FDA	13	no visual change or mass loss
FDA-6FDA	1	complete dissolution
APAF/4MPD(1:1)-6FDA	11	no visual change or mass loss
4MPD-BTDA	12	no visual change or mass loss

Although most of the materials did not show any visual changes or mass loss, the long-term stability towards aromatics cannot be taken for granted. Furthermore, based on the results for Matrimid® and the FDA-6FDA polyimide, it is clear that such stability cannot be guaranteed simply based on a successful measurement of pervaporation performance with a toluene/*n*-heptane (40/60 wt%) feed at 80°C. After one week in the Sohxlet extractor, the Matrimid® film, originally transparent and very flexible, became opaque and very brittle (see Figure 10). The FDA-6FDA film, on the other hand, completely dissolved in benzene after a few hours in the Sohxlet extractor.

Pure-Liquid Sorption

Transport in pervaporation membranes occurs by the solution-diffusion mechanism (*6*)(*31*). Therefore, pure-liquid sorption experiments were performed to determine the solubility and the diffusion coefficient of hydrocarbons in some of the polymeric materials considered in this work. This information is important to understand the reasons behind the significant changes in hydrocarbon permeability with the chemical structure of the polymer, and it can be helpful in designing the chemical structure of future polymers for optimal transport properties.

Figure 11 presents the equilibrium uptake of benzene, toluene, and *n*-heptane for some of the polymers tested as membrane materials in this work. In all cases, the solubility of the aromatic hydrocarbons in the polymer is considerably higher than the solubility of *n*-heptane, which is the reason for the selectivity of these materials towards aromatics in pervaporation. Compared to toluene and benzene, *n*-heptane is a smaller molecule, as indicated by its smaller values of minimum cross-section and kinetic diameter (*30*). Therefore, the diffusion step of the separation mechanism always favors *n*-heptane over either toluene or benzene. Although the hydrocarbon solubility is a function of the molecular structure of the polymer, the minimum and maximum uptake values for toluene in this series of polymers differ by less than a factor of two, which is not enough to explain the large differences (approximately 4 orders of magnitude) in toluene permeability seen in Figure 6.

Examples of toluene kinetic sorption curves in some of the polyimides synthesized in this work are given in Figure 12. For some materials, such as 4MPD-6FDA, the sorption curves displayed the characteristics associated with Fickian behavior: (i) the fractional mass uptake is a linear function of square root time in the early stages; (ii) when such linear behavior is no longer valid, the sorption curve becomes concave towards the $t^{1/2}$ axis and steadily approaches the final equilibrium value. These curves can be represented by the solution of the one-dimensional diffusional equation for a plane sheet with uniform initial concentration (C^o) and surfaces kept at a constant concentration (C_1, $C_1 > C_o$), given, for instance, by Crank (*44*):

$$\frac{M(t)}{M_\infty} = 1 - \sum_{n=0}^{\infty} \frac{8}{(2n+1)^2 \pi^2} \exp\left[-\frac{\overline{D}(2n+1)^2 \pi^2 t}{4L^2} \right] \tag{5}$$

where $\overline{D}$ is an effective, concentration-averaged diffusion coefficient, L is the film thickness, and t is time.

Other materials, such as APAF/4MPD (1:1)-6FDA, exhibited non-Fickian behavior, with a sigmoid curve containing an inflexion point. Examples of such non-Fickian behavior are well documented in the literature for organic vapor sorption in glassy polymers (*44*). In this case, the viscoelastic relaxation of the polymer chains to accommodate penetrant can be a rate-controlling step. Often, such sorption kinetics are described using the following empirical model (*45*, *46*)

$$\frac{M(t)}{M_\infty} = 1 - (1 - \sigma_R) \sum_{n=0}^{\infty} \frac{8}{(2n+1)^2 \pi^2} \exp\left[-\frac{\overline{D}(2n+1)^2 \pi^2 t}{4L^2} \right] - \sigma_R \exp\left(-\frac{t}{\tau_R} \right) \tag{6}$$

where σ_R is the fraction of mass uptake occurring after the inflexion point (when the linear relationship between the fractional mass uptake and $t^{1/2}$ is no longer observed) and τ_R is the time constant associated with the long time drift in mass uptake. Both α_R and τ_R have to be fitted based on experimental data.

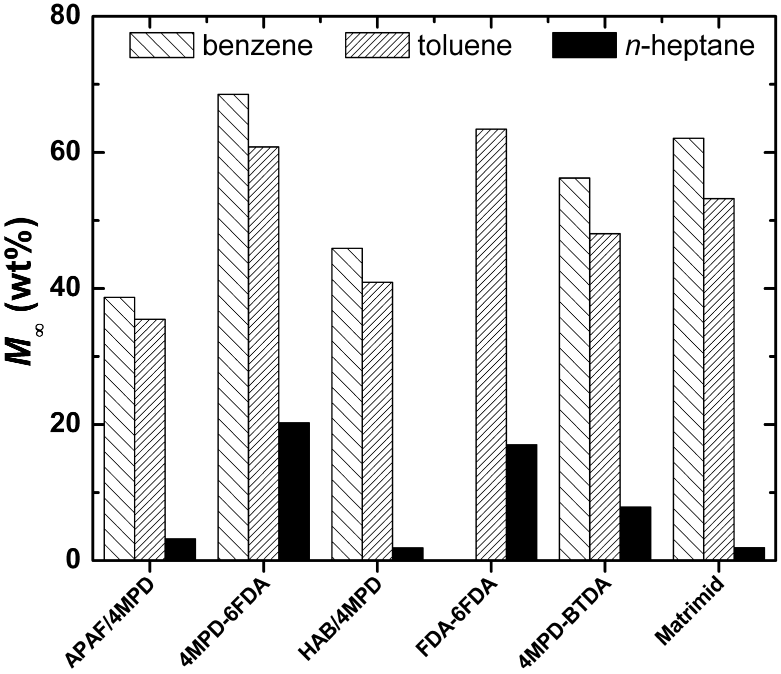

Figure 11. Equilibrium uptake (M_∞) of pure hydrocarbons in different polymers at 25°C. For simplicity, copolymers are specified in the graph only by the name of the diamines, with their full name as follows: APAF/4MPD = APAF/4MPD(1:1)-6FDA; HAB/4MPD = HAB/4MPD(1:1)-6FDA. Benzene uptake for FDA-6FDA could not be measured because the film partially dissolved in this hydrocarbon.

For each polymer, a value of $\overline{D}$ was estimated by fitting either Equation 5 or Equation 6 to the experimental data using the maximum likelihood method (*47*) implemented in the ESTIMA software (*48*). The results obtained for toluene and the polymers in Figure 12 are listed in Table 6, together with permeability values taken from Tables 2 and 3. The values of $\overline{D}$ in Table 6 span four orders of magnitude, which is the same order of magnitude for the variation in toluene permeability. Furthermore, the minimum and maximum values of each parameter ($\overline{D}$ and Ã) occur for the same polymer in Table 6. These results indicate that the large changes in hydrocarbon permeability seen in Figure 6 are mainly caused by differences in the diffusion coefficient. It is worth noting that these effective diffusion coefficients were measured under experimental conditions that were considerably different from those used to determine the permeability coefficients. Nevertheless, the ordering of the diffusion coefficients is coherent with that of the permeability coefficients, suggesting that most of the differences in observed permeability coefficients should be ascribed to differences in diffusion coefficients, likely brought about by changes in the effective free volume of the polymers as a result of varying their chemical structure.

As shown in Figure 11, equilibrium uptake of aromatics in the materials considered in this work is high (> 30 wt%). Therefore, there is significant membrane swelling during aromatic/aliphatic separation by pervaporation, and this factor would be expected to influence the diffusion coefficient as well. One further complication is the fact that the degree of membrane swelling varies across the membrane thickness in pervaporation, since the downstream side is kept under vacuum. The diffusion coefficient values listed in Table 6 are helpful to understand the causes of the large differences in hydrocarbon permeability as a function of polymer structure. However, these values should not be used for a predictive estimation of permeability under pervaporation conditions, even for pure liquids.

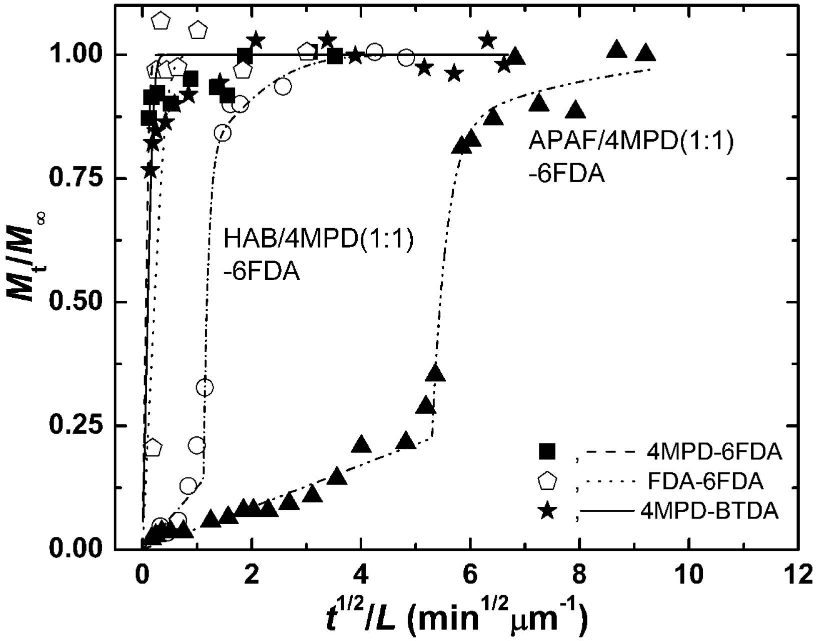

Figure 12. Kinetic sorption curves for pure toluene in different polyimides at 25°C. The lines are fits of either Equation 5 (4MPD-6FDA, FDA-6FDA, 4MPD-BTDA) or Equation 6 to the experimental data.

Table 6. Effective diffusion coefficient ($\overline{D}$) and permeability (Ã) of toluene in different polyimides. Diffusion coefficients were obtained by non-linear parameter estimation using pure-liquid sorption kinetic data at 25°C, while permeability coefficients were measured in pervaporation runs at 80°C with toluene/n-heptane (40/60 wt%) mixtures

Polyimide	$\overline{D}$ *(cm²/s)*	*Ã (Barrer)*
4MPD-6FDA	1.9×10^{-9}	1.62×10^{4}
4MPD-BTDA	8.0×10^{-10}	1.59×10^{3}
FDA-6FDA	1.7×10^{-10}	2.63×10^{3}
HAB/4MPD(1:1)-6FDA	5.0×10^{-12}	1.18×10^{3}
APAF/4MPD(1:1)-6FDA	4.5×10^{-13}	6.5

Conclusions

Soluble, high molecular-weight aromatic polyimides were successfully synthesized and tested as membranes for separation of toluene/*n*-heptane and benzene/*n*-heptane mixtures by pervaporation. All materials were selective towards the aromatic hydrocarbon, whose permeability was highly dependent on the diamine moiety and spanned 4 orders of magnitude for the monomers tested. For a given diamine moiety, the highest permeability coefficients and lowest selectivity values were obtained using 6FDA as the dianhydride. Other dianhydrides, such as BTDA and ODPA, increased the selectivity towards the aromatic hydrocarbon but reduced permeability.

The large variation in hydrocarbon permeability with the chemical structure of the polyimide membranes is mainly caused by changes in the diffusion coefficient, whereas the selectivity towards the aromatic compound is a result of differences in solubility.

Acknowledgments

The authors gratefully acknowledge ConocoPhillips Co. for their financial support.

References

1. Hamid, S. H.; Ali, M. A. *Energy Sources* **1996**, *18*, 65–84.
2. White, L. S.; Wildemuth, C. R. *Ind. Eng. Chem. Res.* **2006**, *45*, 9136–9143.
3. Meindersma, G. W.; Podt, A. J. G.; Haan, A. B. *Fuel Process. Technol.* **2005**, *87*, 59–70.
4. White, L. S. *J. Membr. Sci.* **2006**, *286*, 26–35.
5. Villaluenga, J. P. G.; Mohammadi, A. T. *J. Membr. Sci.* **2000**, *169*, 159–174.
6. Smitha, B.; Suhanya, D.; Sridhar, S.; Ramakrishna, M. *J. Membr. Sci.* **2004**, *241*, 1–21.
7. Lin, L.; Zhang, Y.; Kong, Y. *Fuel Process. Technol.* **2009**, *88*, 1799–1809.
8. Uragami, T. Polymer membranes for separation of organic liquid mixtures. In *Materials Science of Membranes for Gas and Vapor Separation*; Yampolskii, Y., Pinnau, I., Freeman, B. D., Eds.; John Wiley & Sons: West Sussex, 2006; pp 355−372.
9. Tanihara, N.; Tanaka, K.; Kita, H.; Okamoto, K. *J. Membr. Sci.* **1994**, *9*, 161–169.
10. Tanihara, N.; Umeo, N.; Kawabata, T.; Tanaka, K.; Kita, H.; Okamoto, K. *J. Membr. Sci.* **1995**, *104*, 181–192.
11. Hao, J.; Tanaka, K.; Kita, H.; Okamoto, K. *J. Membr. Sci.* **1997**, *132*, 97–108.
12. Okamoto, K.; Wang, H.; Ijyuin, T.; Fujiwara, S.; Tanaka, K.; Kita, H. *J. Membr. Sci.* **1999**, *157*, 97–105.
13. Fang, J.; Tanaka, K.; Kita, H.; Okamoto, K. *Polymer* **1999**, *40*, 3051–3059.
14. Wang, H.; Ugomori, T.; Tanaka, K.; Kita, H.; Okamoto, K.; Suma, Y. *J. Polym. Sci., Part B: Polym. Phys.* **2000**, *38*, 2954–2964.
15. Ren, J.; Staudt-Bickel, C.; Lichtenthaler, R. N. *Sep. Purif. Technol.* **2001**, *22-23*, 31–43.
16. Pithan, F.; Staudt-Bickel, C.; Hess, S.; Lichtenthaler, R. N. *ChemPhysChem* **2002**, *3*, 856–862.
17. Xu, W.; Paul, D. R.; Koros, W. J. *J. Membr. Sci.* **2003**, *219*, 89–102.
18. Wang, L.; Zhao, Z.; Li, J.; Chen, C. *Eur. Polym. J.* **2006**, *42*, 1266–1272.
19. Ye, H.; Li, J.; Lin, Y.; Chen, J.; Chen, C. *J. Macromol. Sci. Pure Appl. Chem.* **2008**, *45*, 172–178.
20. Ye, H.; Li, J.; Lin, Y.; Chen, J.; Chen, C. *Chin. J. Polym. Sci.* **2008**, *26*, 705–712.
21. Katarzynski, D.; Staudt, C. *J. Membr. Sci.* **2010**, *348*, 84–90.
22. Langsam, M.; Burgoyne, W. F. *J. Polym. Sci., Part A: Polym. Chem.* **1993**, *31*, 909–921.
23. Semenova, S. I. Separation Properties of Polyimides. In *Polyimide Membranes - Applications, Fabrication and Properties*; Ohya, H., Kudryavtsev, V. V., Semenova, S. I., Eds.; Gordon and Breach: Tokyo, 1996; pp 103−177.
24. Tanaka, K.; Okamoto, K. Structure and transport properties of polyimides as materials for gas and vapor membrane separation. In *Materials Science of Membranes for Gas and Vapor Separation*; Yampolskii, Y., Pinnau, I., Freeman, B. D., Eds.; John Wiley & Sons: West Sussex, 2006; pp 271−291.
25. Fritz, J. S. *Anal. Chem.* **1950**, *22*, 1028–1029.

26. Comer, A. C.; Kalika, D. S.; Rowe, B. W.; Freeman, B. D.; Paul, D. R. *Polymer* **2009**, *50*, 891–897.
27. Kim, Y. J.; Glass, T. E.; Lyle, G. D.; McGrath, J. E. *Macromolecules* **1993**, *26*, 1344–1358.
28. Takekoshi, T. Synthesis of Polyimides. In *Polyimides: Fundamentals and Applications*; Ghosh, M. K., Mital, K. L., Eds.; Marcel Dekker: New York, 1996; pp 7−45.
29. Kudryavtsev, V. V. Synthesis of polyimides. In *Polyimide Membranes - Applications, Fabrication and Properties*; Ohya, H., Kudryavtsev, V. V., Semenova, S. I., Eds.; Gordon and Breach: Tokyo, 1996; pp 9−82.
30. Semenova, S. I. *J. Membr. Sci.* **2004**, *231*, 189–207.
31. Pereira, C. C.; Ribeiro, C. P.; Nobrega, R.; Borges, C. P. *J. Membr. Sci.* **2006**, *274*, 1–23.
32. Ribeiro, C. P.; Borges, C. P. *Braz. J. Chem. Eng.* **2004**, *21*, 629–640.
33. Baker, R. W.; Wijmans, J. G.; Huang, Y. *J. Membr. Sci.* **2010**, *348*, 346–352.
34. Matsui, S.; Paul, D. R. *J. Membr. Sci.* **2002**, *195*, 229–245.
35. Gmehling, J.; Onken, U.; Arlt, W. *Vapor-liquid Equilibrium Data Collection*; DECHEMA: Frankfurt, 1977.
36. Likhatchev, D.; Gutierrez-Wing, C.; Kardash, I.; Vera-Graziano, R. *J. Appl. Polym. Sci.* **1996**, *59*, 725–735.
37. Farr, I. V.; Kratzner, D.; Glass, T. E.; Dunson, D.; Ji, Q.; McGrath, J. E. *J. Polym. Sci., Part A: Polym. Chem.* **2000**, *38*, 2840–2854.
38. Silverstein, R. M.; Webster, F. X.; Kiemle, D. J. *Spectrometric Identification of Organic Compounds*; John Wiley & Sons: Hoboken, 2005; p 502.
39. Roizard, D.; Nilly, A.; Lochon, P. *Sep. Purif. Technol.* **2001**, *22-23*, 45–52.
40. Aouinti, L.; Roizard, D.; Hu, G. H.; Thomas, F.; Belbachir, M. *Desalination* **2009**, *241*, 174–181.
41. Jonquieres, A.; Clement, R.; Lochon, P. *Prog. Polym. Sci.* **2002**, *27*, 1803–1877.
42. Larchet, C.; Brun, J. P.; Guillou, M. *J. Membr. Sci.* **1983**, *15*, 81–96.
43. Grabczyk, A. W. *Polymer* **2004**, *45*, 4391–4402.
44. Crank, J. *Mathematics of Diffusion*, 2nd ed.; Oxford University Press: Oxford, 1975; p 414.
45. McDowell, C. C.; Freeman, B. D.; McNeely, G. W. *Polymer* **1999**, *40*, 3487–3499.
46. Dhoot, S. N.; Freeman, B. D.; Stewart, M. E.; Hill, A. J. *J. Polym. Sci., Part B: Polym. Phys.* **2001**, *39*, 1160–1172.
47. Anderson, T. F.; Abrams, D. S.; Grens, E. A. *AIChE J.* **1978**, *24*, 20–29.
48. Pinto, J. C.; Lobao, M. W.; Monteiro, J. L. *Chem. Eng. Sci.* **1990**, *45*, 883–892.

Downloaded by UNIV OF GUELPH LIBRARY on June 18, 2012 | http://pubs.acs.org
Publication Date (Web): October 31, 2011 | doi: 10.1021/bk-2011-1078.ch008

Chapter 8

Gas Separation Properties of Triptycene-Based Polyimide Membranes

Yoon Jin Cho and Ho Bum Park*

WCU Department of Energy Engineering, Hanyang University,
Seoul 133-791, Korea
***E-mail: badtzhb@hanyang.ac.kr. Tel: +82-2-2220-2338.**

Tuning of free volume element distributions and sizes in polymers is technologically important because of various applications such as microelectronics (e.g., low dielectric materials), gas storage (e.g., organic adsorbents) and membrane-based gas separation technology (e.g., high permeable, selective polymers). Here we demonstrate that the polymer design via a three-dimensional rigid structure having internal void space can create a number of free volume elements in semi-rigid or rigid glassy polymers, which help improve fast, selective mass transport. To achieve it, we considered an iptycene-based monomer, i.e., triptycene, for polymer material design, as a result, leading to the formation of high fractional free volume with proper cavity size to separate small gas molecules with high selectivity as well as high permeability. Due to rigid structure of triptycene with tiny internal free volume elements, the resultant polyimides show high glass transition temperature of 352 °C and excellent thermal stability as well as solution processibility owing to good solubility in common organic solvents used in chemical industries. We believe that this kind of polymer design will provide keen insight on the development of processable polyimides having fine microporous structures on sub-nanometric scales for high performance glassy polymer applications.

Keywords: polyimide; gas separation; triptycene; free volume

In Modern Applications in Membrane Science and Technology; Escobar, I., et al.;
ACS Symposium Series; American Chemical Society: Washington, DC, 2011.

Downloaded by UNIV OF GUELPH LIBRARY on June 18, 2012 | http://pubs.acs.org
Publication Date (Web): October 31, 2011 | doi: 10.1021/bk-2011-1078.ch008

1. Introduction

Aromatic polyimides, usually obtained from bifunctional carboxylic acid dianhydrides and primary diamines, are widely used in different branches of industry such as electronics, insulators, high-temperature adhesives and photoresist (*1*). The successful applications of such high-performance polyimides are mainly due to excellent physicochemical properties such as high temperature stability, exceptional mechanical strength, low thermal expansion coefficient, dimensional stability, superior insulation properties, and radiation and chemical resistance (*2*, *3*). In the field of membrane science and technology, polyimide membranes have been extensively studied because of their excellent separation performances, particularly for gas separation (*4*–*6*).

To date, there are considerable progresses to be made in developing various polyimide membranes for gas separation since the microstructures (e.g., free volume element sizes and distribution) of polyimides can be tuned for gas separations of interest such as air separation (e.g., oxygen enrichment or nitrogen production), biogas and natural gas purification (e.g., selective CO_2/CH_4 separation) (*7*, *8*) by a number of combinations between dianhydrides and diamines. In many cases, aromatic polyimide membranes act as flexible, organic molecular sieves for gas separation owing to their high selectivity toward small gas pairs. To obtain polyimides having further both high permeability and high selectivity, it is necessary to modify chemical structures with stiff backbone chains and with chain packing efficiency controlled for creating a very narrow free volume distribution (*9*, *10*). Here we report on a new class of polyimide membrane with high internal free volume elements for gas separation.

Our approach to obtain polyimides with high internal free volume elements is to incorporate triptycene moieties into polyimide backbones. In particular, we are interested in the triptycene structure because some polymers including 3-dimensional, rigid triptycene moieties showed elevated glass transition temperature, low dielectric constants, and microporous structures (*11*). Triptycene is the simplest chemical compound of iptycenes. Iptycenes are attractive compounds for polymer building units since they have unique structures with phenyl rings attached to the [2,2,2] bicyclooctatriene bridgehead system (*12*). Triptycene, as shown in Figure 1, has the three phenyl rings joined by together by a single hinge, a paddlewheel configuration with D_{3h} symmetry (*13*). Triptycene has such a rigid framework, and it and its derivatives are incorporated in many organic compounds as a molecular scaffold, for instance, in molecular motors (*14*) or as a ligand (*15*). In addition, triptycene has so high energy barrier to molecular twisting or deformation that the angle between aromatic rings keeps as 120^o (*16*). These unique structural properties make it useful for providing rigidity, regular packing, and creating void spaces in the clefts between the rings – so called as internal free volume (*17*). Recent studies suggest that local cavities can be created owing to the inability for triptycene-based polymeric structures to pack efficiently (*18*).

Downloaded by UNIV OF GUELPH LIBRARY on June 18, 2012 | http://pubs.acs.org
Publication Date (Web): October 31, 2011 | doi: 10.1021/bk-2011-1078.ch008

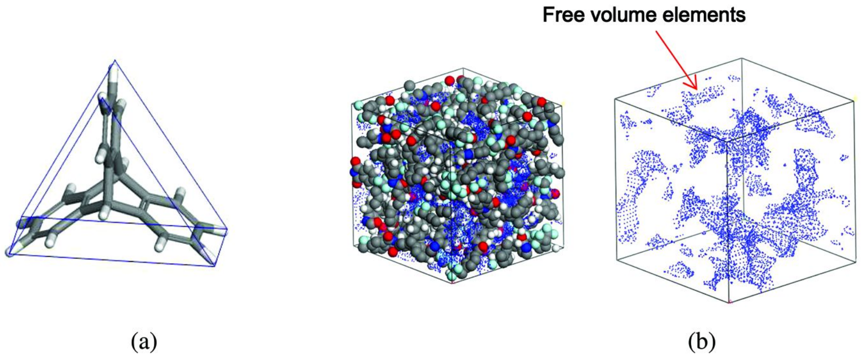

Figure 1. (a) Three-dimensional triptycene structure, and (b) the creation of free volume elements due to triptycene moiety in a polymer structures.

In the late 1960s, a wide variety of triptycene-based polymers (e.g., polyesters, polyamides, polyurethanes and polyoxadizole) were prepared using bifunctional, bridgehead-substituted triptycenes (R-Tr-R (9,10-triptycene), R = CH_2OH, COCl, COOH, NH_2 and NCO) to obtain colorless, thermally stable polymers (*19*) as shown in Figure 2(a). These polymers exhibited high thermal stability but they were too weak or brittle, due to high crystallinity (~80%), to be proper for gas separation owing to low mechanical strength and probable low gas permeability. The most recently, poly(2,6-triptycene) was synthesized via a nickel-mediated Yamamoto-type polycondensation polymerization. This polymer was found to be highly soluble in common organic solvents, which was caused by the high content of rigid triptycene and poor dense packing of polymers (*20*). Analogue to this approach, we intended to synthesize a new class of triptycene-based polyimide including 2,6-triptycene moiety for obtaining probable soluble, thermally stable, and gas permeable polyimides as shown in Figure 2(b). Many reported aromatic rigid polyimides are insoluble in common organic solvents mainly owing to the extremely strong interchain interactions due to dispersion or electrostatic interactions of imide cycles or donor-acceptor interactions together with nonspecific van der Waals interactions. Thereby their membrane applications are relatively limited as compared to other glassy polymers for gas and liquid separations. Generally, poly(amic acid)s, precursor polymers for polyimides, are soluble in common organic solvents of interest in chemical industries. However, poly(amic acid)s are chemically unstable in ambient conditions, which prevent them being used as membrane materials for practical membrane formation (e.g., hollow fibers or flat sheet membranes) with less feasibility and reproducibility. Currently, there are only a few commercially available soluble polyimides (e.g., Ultem and Matrimid) for gas separation membranes. They have quite good separation performances but still low gas permeabilities. In this study, therefore, we aimed at the synthesis of novel polyimides including 2,6-triptycene, the characterization of physiochemical properties (e.g., density, fractional free volume, glass transition temperature, and solubility), and the evaluation of the effect of triptycene structure on the gas permeation behaviors (e.g., gas permeability, solubility and diffusivity). In particular, there are few studies on the mass transport through triptycene-based polymers and thereby this work will provide insight on the gas separation performance of triptycene-based polymer membranes.

2. Experimental Section

2.1. Materials

Triptycene (98%), nitric acid (HNO_3, 70%), acetic anhydride (Ac_2O, ≥98%), hydrazine monohydrate (98%), Raney nickel (slurry in water), tetrahydrofuran (THF, ≥99%), d (6FDA, 99%), 1,2-dichlorobenzene (*o*-DCB, 99%), ethanol (≥99.5%), triethylamine (TEA, ≥99.5%), 1-methyl-2-pyrrolidinone (NMP, 99.5%), chloroform (≥99%), and dimethyl sulfoxide-d_6 (DMSO-d_6, 99.9 atom % D) were purchased from Aldrich (Milwaukee, WI, USA). Silica gel (0.040-0.063 mm) was purchased from Merck (Whitehouse Station, NJ, USA). Methylene chloride (MC, 99.5%), *n*-hexane (95%), ethyl acetate (EA, 99.5%), and methanol (99.5%) were purchased from Duksan reagents (Korea).

2.2. Synthesis of 2,6-Diaminotriptycene (DATri)

A solution of triptycene (10.0 g, 39.4 mmol) in acetic anhydride (190 mL) was cooled in a water-ice bath. A concentrated nitric acid solution (70%, 15 mL) was added to the triptycene solution. Then, the water-ice bath was removed, and the mixture was stirred for 4 h at room temperature. The reaction mixture was poured into water (1 L) and stirred overnight. The precipitate was collected by filtration, and dried in a vacuum oven. The mixture was separated using a column chromatography on silica gel with hexane/methylene chloride (3:1), affording the 2,6-dinitrotriptycene (DNTri) white solid (5.70 g, 42.1%). To a solution of DNTri (2.00 g, 5.81 mmol) in THF (300 mL) was added hydrazine monohydrate (10 mL) and Raney nickel (~1 g). The solution was stirred at 60 ^{o}C under argon for 20 h. After cooling to room temperature, the mixture was filtered and dried in a vacuum oven. The mixture was purified using a column chromatography on silica gel with methylene chloride/ethyl acetate (5:1) and the product, DATri as a light red solid, was obtained in a high yield (1.36 g, 82.4%). The schematic of the synthesis is illustrated in Figure 3(a).

2.3. Synthesis of 6FDA-DATI Polyimide (6FDA-DATri)

6FDA-DATri polyimide was synthesized using an ester-acid chemical imidization method to obtain high molecular weight polyimide. Diamine monomer (DATri) and dianhydride monomer (6FDA) were dried in 150 ^{o}C vacuum oven for 1 day. 6FDA (3.12 g, 7.03 mmol) was reacted with anhydrous ethanol (50 mL) and TEA (3.7 mL) under nitrogen purge with reflux and then ester-acid form of the dianhydride was obtained. During about 1 h, the excess ethanol and TEA were distilled, leaving a viscous ester-acid solution. The equimolar amount of DATri (2.00 g, 7.03 mmol), NMP (37 mL), and *o*-DCB (9.2 mL) were added into the ester-acid solution and then the solution was reacted

Downloaded by UNIV OF GUELPH LIBRARY on June 18, 2012 | http://pubs.acs.org
Publication Date (Web): October 31, 2011 | doi: 10.1021/bk-2011-1078.ch008

at 180 °C for 48 h under nitrogen purge with reflux. The viscous solution was cooled to room temperature and precipitated into stirred methanol, filtered, and washed with methanol several times. The resulting powder was thoroughly dried in 150 °C vacuum oven for 24 h. The schematic of the synthesis is illustrated in Figure 3(b).

2.4. Membrane Preparation

The dried polymer was dissolved in amylene-stabilized chloroform to give 2 wt% solids and the solution was stirred for 12 h. Then the polymer solution was poured into a glass mold and the solvent was slowly evaporated at room temperature. After approximately 2 day, the polymer film was peeled off in water bath, soaked in methanol for 1 h, and dried at room temperature. 6FDA-DATri polyimide film thickness was ca. 130 μm.

2.5. Material Characterizations

Attenuated total reflection Fourier transform infrared (FT-IR/ATR) spectrum of DNTri, DATri, and 6FDA-DATri polyimide film were measured using an IlluminatIR infrared microspectrometer (SensIR Technologies, Danbury, CT, USA) in the range of 4000-1000 cm^{-1}.

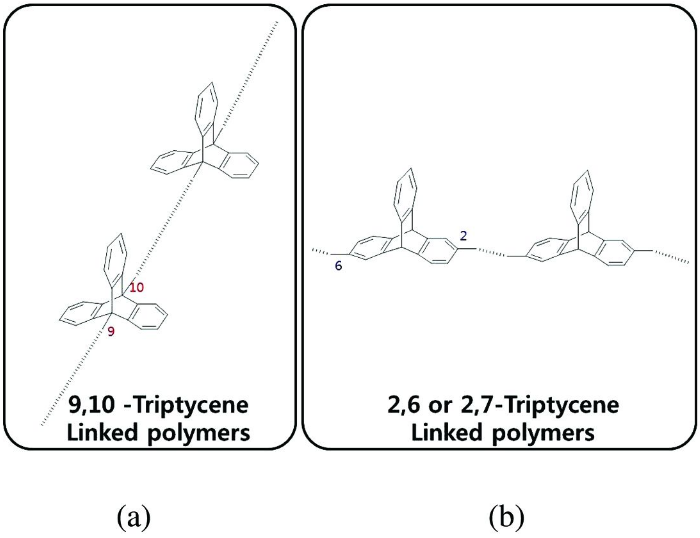

Figure 2. (a) 9,10-triptycene linked polymers (b) 2,6 or 2,7-triptycene linked polymers.

Downloaded by UNIV OF GUELPH LIBRARY on June 18, 2012 | http://pubs.acs.org
Publication Date (Web): October 31, 2011 | doi: 10.1021/bk-2011-1078.ch008

Downloaded by UNIV OF GUELPH LIBRARY on June 18, 2012 | http://pubs.acs.org
Publication Date (Web): October 31, 2011 | doi: 10.1021/bk-2011-1078.ch008

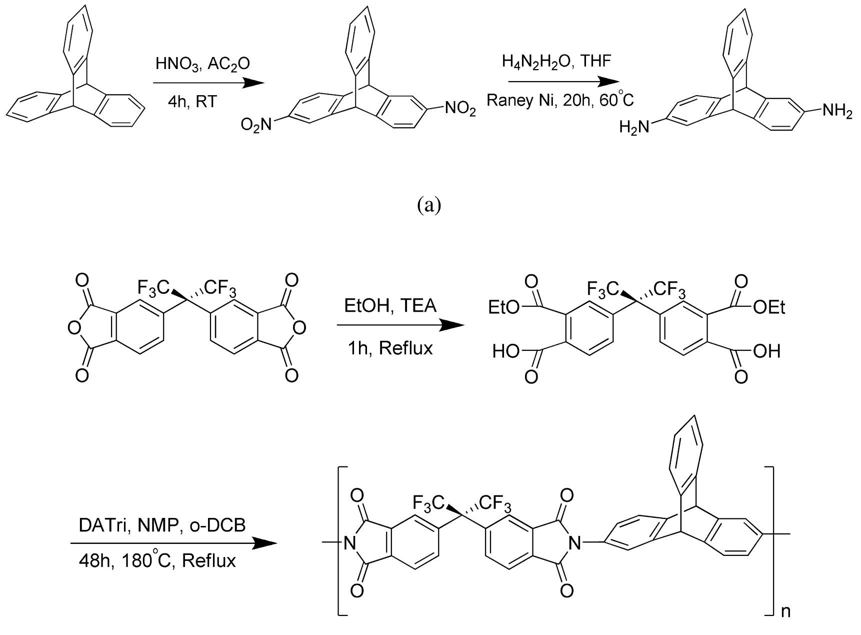

(a)

(b)

Figure 3. The schematic of synthesis of (a) DATri and (b) 6FDA-DATri polyimide.

^{1}H nuclear magnetic resonance (^{1}H-NMR) spectra of DNTri, DATri, and 6FDA-DATri polyimide were obtained with a 300 MHz Varian Model NMR 1000 spectrometer (Varian Inc., CA, USA). All samples were dissolved in DMSO-d_6.

Number and weight average molecular weight of 6FDA-DATri polyimide were determined using a Waters 2690 Gel permeation chromatography (GPC) system (Waters Corp., Milford, MA, USA). THF was used as eluent for 6FDA-DATri polyimide and polystyrene standard was used for calibration.

The glass transition temperature of 6FDA-DATri polyimide was examined with Q20 differential scanning calorimetry (DSC) instrument (TA Instruments, New Castle, DE, USA) under nitrogen atmosphere at the heating rate of 20 ^{o}C/min.

Thermal gravimetric analysis (TGA) was performed in the range of temperature from 100 to 980 ^{o}C under nitrogen by using TGA500 thermogravimetric analyzer (TA Instruments, New Castle, DE, USA) at the heating rate of 10 ^{o}C/min. The polyimide film was annealed at 100 ^{o}C for 1 h in the TGA apparatus to avoid the influence of humidity.

The mechanical properties of 6FDA-DATri polyimide, tensile strength and elongation at break, were measured using a Universal Tester (AGS-J, Shimadzu, Kyoto, Japan). 6FDA-DATri polyimide membrane was cut into 0.5 cm × 2 cm rectangular specimens and stretched at a speed of 5 mm/min. 10 specimens were measured for the polyimide membrane sample.

X-ray diffraction (XRD) was measured to observe the microstructure of polyimide, using an D/MAX-2200 X-ray diffractometer (Rigaku, Japan) which uses CuKα radiation at a wavelength 1.54 Å, operating in a 2θ range of 5-60^o

Downloaded by UNIV OF GUELPH LIBRARY on June 18, 2012 | http://pubs.acs.org
Publication Date (Web): October 31, 2011 | doi: 10.1021/bk-2011-1078.ch008

with a scan rate of 5° min^{-1}. From X-ray scattering data (using of the broad peak maximum), the average *d*-spacing value of the polyimide was calculated using Bragg's law (d = λ/2sinθ).

Fractional free volume (V_f) is calculated using the following equations:

$$V_f = \frac{V - V_0}{V} \tag{1}$$

$$V = \frac{M}{\rho} \tag{2}$$

$$V_0 = 1.3 V_W \tag{3}$$

where V is the total molar volume of the repeating unit (cm^3/mol), M the molar mass (g/mol) of the repeating unit and ρ the density of the film (gcm^{-3}), which was determined by experimentally using a top-loading electronic Mettler Toledo balance (XP205, Mettler-Toledo, Switzerland) coupled with a density kit based on Archimedes' principle. The samples were weighed in air and a known-density liquid, high purity water. The measurement was performed at room temperature by the buoyancy method and the density was calculated as follows,

$$\rho_{polymer} = \frac{w_0}{w_0 - w_1} \rho_{liquid} \tag{4}$$

where w_0 and w_1 are the film weights in air and water, respectively. V_0 is the volume occupied by the polymeric chains (cm^3/mol). V_0 is assumed to be impermeable for diffusing gas molecules. V_w is the Van der Waals volume calculated using the group contribution Bondi method.

Gas permeation measurements were performed using a constant-volume/variable-pressure method at a feed pressure of 1 atm and a feed temperature of 35 °C with different kinetic diameters of gas molecules (e.g., He (0.260 nm), H_2 (0.289 nm), CO_2 (0.330 nm), O_2 (0.346 nm), N_2 (0.364 nm) and CH_4 (0.380 nm)). Before the gas permeation measurements, both the feed and the permeate sides were thoroughly evacuated to below 10^{-5} Torr. The calibrated downstream volume was 77 cm^3, the upstream and downstream pressures were measured using a Baratron transducer (MKS, city, state) with a full scale of 25,000 and 10 Torr, respectively. The pressure rise versus time transient of the permeate side equipped with a pressure transducer was recorded and passed to a desktop computer through an RS-232 cable. The linear slope of the pressure rise versus time provides the permeation rates of penetrating gases. The permeability coefficient for a test gas is determined by multiplying the permeate rate by the membrane thickness and can be expressed by:

$$P = \frac{dp}{dt}\left(\frac{VT_0L}{p_0T\Delta pA}\right) \tag{5}$$

where P is the permeability represented in Barrer; dp/dt is the rate of the pressure rise under the steady state; V (cm^3) is the downstream volume; L (cm) is the membrane thickness; Δp (cmHg) is the pressure difference between the two sides; T(K) is the measurement temperature; A (cm^2) is the effective area of the membrane; p^0 and T^0 are the standard pressure and temperature, respectively. All the gas permeation tests were performed more than three times, and the standard deviation from the mean values of permeabilities was within ca.±3%. Sample-to-sample reproducibility was high and within ca.±2.5%. The effective membrane areas were 2.25 cm2. The ideal separation factor (selectivity) for components 1 and 2 is defined as the ratio of the pure-gas permeabilities of each component:

$$\alpha_{1/2} = \frac{P_1}{P_2} \tag{6}$$

3. Results and Discussion

Triptycene was nitrated via an electrophilic aromatic substitution mechanism using acetic anhydride and nitric acid at room temperature for 4 h, resulting in 2,6-dinitrotriptycene (DNTri) (yield 42.1%). FT-IR and ^{1}H-NMR spectra of DNtri are shown in Figure 4. In the FT-IR spectrum, two N-O stretching bands around 1346 and 1516 cm^{-1} are observed, indicating nitro groups in triptycene structure. In the NMR spectrum, the NMR peaks of six kind protons in DNTI are shown (8.37 (d, 2H), 8.00 (dd, 2H), 7.75 (d, 2H), 7.55 (dd, 2H), 7.10 (dd, 2H), 6.18 ppm (s, 2H)). From these results, FT-IR and ^{1}H-NMR spectra show that two nitro groups are successfully attached to the 2, 6 positions in two phenyl rings in triptycene.

The DNTri was reduced using hydrazine monohydrate in THF solution at 60 ^{o}C under argon atmosphere. After 20 h, 2,6-diaminotriptycene (DATri) was obtained at the yield of 82.4%. Full conversion of nitro groups to amino groups was made as shown in Figure 5. In the FT-IR spectrum of DATri, amine group characteristic bands at 3340, 3413 cm^{-1} (N-H stretching), and 1624 cm^{-1} (N-H bending) appear and two characteristic bands of nitro groups disappear. In the NMR spectrum, seven peaks of protons in DATri are shown (7.30 (dd, 2H), 6.97 (d, 2H), 6.92 (dd, 2H), 6.62 (d, 2H), 6.09 (dd, 2H), 5.11 (s, 2H), 4.81 ppm (s, 4H)). Compared with NMR peaks of DNTri, the DATri peaks are shifted to upfield because of lower electronegative amine groups than nitro groups and a new peak at 4.81 ppm appear. This new peak is indicative of four protons in amine groups.

Downloaded by UNIV OF GUELPH LIBRARY on June 18, 2012 | http://pubs.acs.org
Publication Date (Web): October 31, 2011 | doi: 10.1021/bk-2011-1078.ch008

Downloaded by UNIV OF GUELPH LIBRARY on June 18, 2012 | http://pubs.acs.org
Publication Date (Web): October 31, 2011 | doi: 10.1021/bk-2011-1078.ch008

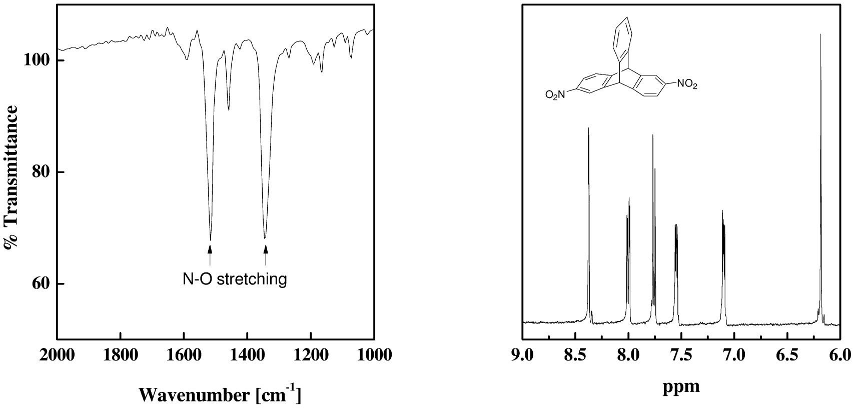

(a) (b)

Figure 4. (a) FT-IR spectrum and (b) ^{1}H-NMR spectrum of DNTri.

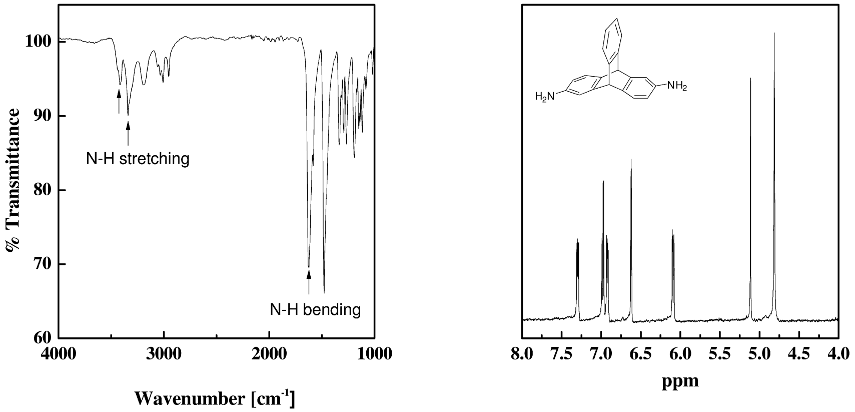

(a) (b)

Figure 5. (a) FT-IR spectrum and (b) ^{1}H-NMR spectrum of DATri.

Downloaded by UNIV OF GUELPH LIBRARY on June 18, 2012 | http://pubs.acs.org
Publication Date (Web): October 31, 2011 | doi: 10.1021/bk-2011-1078.ch008

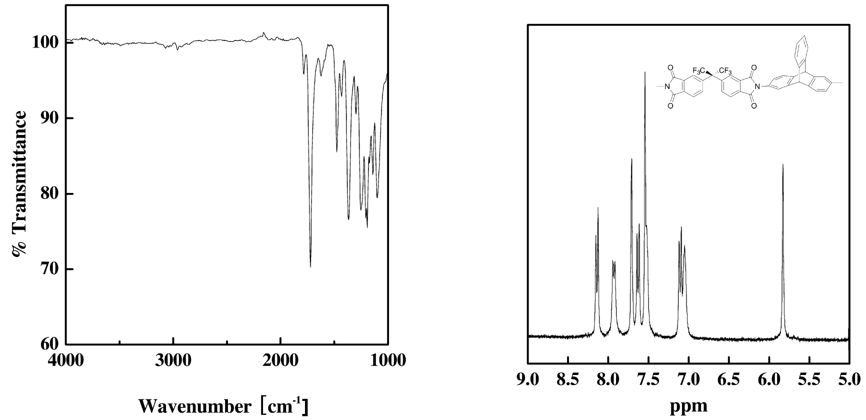

(a) (b)

Figure 6. (a) FT-IR spectrum and (b) ^{1}H-NMR spectrum of 6FDA-DATri polyimide.

A high-molecular-weight-polyimide from 6FDA and DATri was synthesized via an ester-acid chemical imidization method. 6FDA was reacted with anhydrous ethanol and TEA, and then an ester-acid form was obtained. DATri, NMP, and *o*-DCB were added into an ester-acid solution and then reacted at 180 °C for 2 days under nitrogen with reflux. The solution was precipitated in methanol and washed with methanol several times. The 6FDA-DATri polyimide solution was cast on the glass mold and soaked in methanol. Finally we obtained 6FDA-DATri polyimide film whose thickness was ca. 130μm. FTIR/ATR and ^{1}H-NMR spectra, as shown in Figure 6, indicate that 6FDA-DATri polyimide is successfully synthesized. In the IR spectrum, the characteristic absorption bands of imide group appear at 1782, 1720, and 1366 cm^{-1} which corresponds to the imide linkages (C-N=O). The IR characteristic bands of O-H and N-H bonds disappear, meaning that the imidization via an ester-acid method was completely achieved because there are no carboxylic acid groups and amine groups. In the NMR spectrum, the nine peaks of protons in triptycene and 6FDA are obtained and a peak of protons in amine groups disappears.

Table 1. Physical properties of 6FDA-DATRI polyimide

M_n (g/mol)	*M_w (g/mol)*	*PDI**	*Viscosity (dL/g)*	*Tensile strength (MPa)*	*Elongation at break (%)*
21,135	109,862	5.2	0.68	62.2	4.5

* PDI: Polydispersity index

Downloaded by UNIV OF GUELPH LIBRARY on June 18, 2012 | http://pubs.acs.org
Publication Date (Web): October 31, 2011 | doi: 10.1021/bk-2011-1078.ch008

In Tables 1, 2, and 3, the physical properties and gas permeabilities of 6FDA-DATri polyimide studied in this study are summarized with those of other 6FDA-based polyimides. The polymer density at 25°C is 1.297±0.016 g/cm^3, which value is relatively lower than any other 6FDA-based polyimides. From the experimental density, the fractional free volume (V_f) was calculated as 0.226, which is as high as poly(1-phenyl-1-propyne) (0.221), much larger than any other glassy polymers (e.g., polysulfone (0.159) and polycarbonate (0.166)) and any other 6FDA-based polyimides (e.g., 6FDA-*m*TMPD (0.182) and 6FDA-*p*TeMPD (0.182)). Such a high V_f might be caused by an inherent internal free volume due to triptycene structure. We also compared average interspacing distance (*d*-spacing) of current polyimide from a X-ray diffraction pattern data with any other comparable 6FDA-based polyimides, known as high free volume polymers showing fast mass transport (e.g., gas molecules) as shown in Table 4. Interestingly, the *d*-spacing of 6FDA-DATri polyimide film is not greatly higher than those of other 6FDA-based polyimides despite the increasing V_f. This indicates that a number of free volume elements due to internal void space in triptycene structure are created but the size of free volume elements is not as large as expected.

Glass transition temperature (T_g) of 6FDA-DATri polyimide was detected at 352 °C as shown in Figure 7. As compared to other 6FDA-based polyimides, the T_g is fairly high because the phenyl rings of triptycene perpendicular to polymer chain might be able to interlock each other, preventing the thermal motions as the temperature increases. Thermal stability was evaluated using a TGA measurement under an inert atmosphere (nitrogen purge flow). As shown in Figure 8, the 6FDA-DATri polyimide is thermally stable up to 500 °C. 5% weight loss occurs at 540 °C. The final char yield at 980 °C was as high as above 60 wt.%. Owing to this high temperature stability, this polymer can be potentially used for high temperature-gas separation-applications.

In many cases, polyimides have lots of advantages such as excellent chemical and thermal stability as well as strong mechanical properties, but they have limited applications because of their poor solubility in common organic solvents, so leading to less processibility. This is mainly caused by strong charge transfer complex, thermally-induced crosslinking (in the case of thermal imidization from poly(amic acid)s), and close chain packings. In contrast, our polyimide based on triptycene structure show good solubility in useful common organic solvents regardless of any imidization routes (e.g., thermal imidization, solution and chemical imidization) as listed in Table 5. We believe that the excellent solubility of current polyimide comes from the easy accessibility of solvent molecules into internal void spaces around triptycene structures, as shown in high fraction free volume.

Downloaded by UNIV OF GUELPH LIBRARY on June 18, 2012 | http://pubs.acs.org
Publication Date (Web): October 31, 2011 | doi: 10.1021/bk-2011-1078.ch008

Table 2. Physical properties of 6FDA-based polyimides

No.	*Diamine*		*T_g (^oC)*	*Den-sity [g/cm_3]*	*FFV [-]*
1	-DATri*	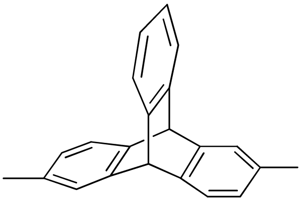	343	1.297	0.226
2	-*m*-TMPD	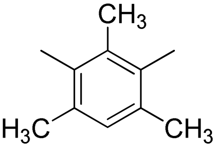	377	1.352	0.182
3	-*p*-TeMPD	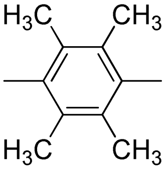	420	1.330	0.182
4	-*p*-PDA	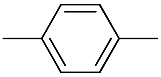	351	1.473	0.161
5	-*m*-PDA	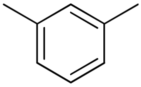	298	1.474	0.160
6	-*2,4*-DAT	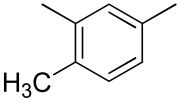	342	1.427	0.169
7	-*2,6*-DAT	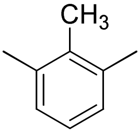	372	1.420	0.173
8	-*3,5*-DBTF	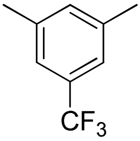	284	1.512	0.175

Continued on next page.

Table 2. (Continued). Physical properties of 6FDA-based polyimides

No.	*Diamine*		*T_g (^{o}C)*	*Density [g/cm$_3$]*	*FFV [-]*
9	-4APF	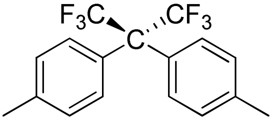	320	1.466	0.190
10	-3APF	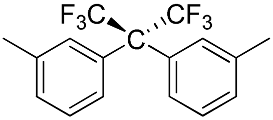	254	1.493	0.175
11	-IPDA	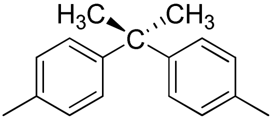	310	1.352	0.168
12	-APAP	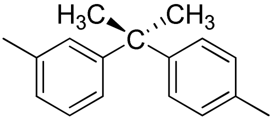	260	1.361	0.163
13	-*p*-ODA	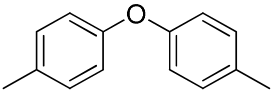	299	1.432	0.165
14	-*m*,*p*-ODA	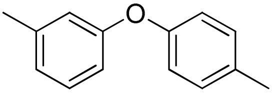	260	1.438	0.162
15	-*m*-ODA	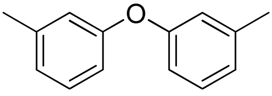	244	1.435	0.163
16	-4APPF	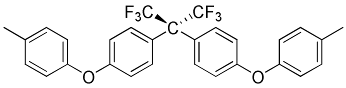	262	1.438	0.176
17	-3APPF	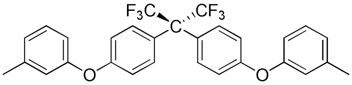	224	1.446	0.171
18	-ATPPF	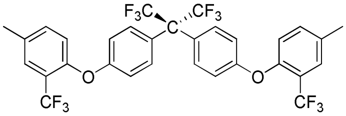	234	1.484	0.190

Downloaded by UNIV OF GUELPH LIBRARY on June 18, 2012 | http://pubs.acs.org
Publication Date (Web): October 31, 2011 | doi: 10.1021/bk-2011-1078.ch008

Downloaded by UNIV OF GUELPH LIBRARY on June 18, 2012 | http://pubs.acs.org
Publication Date (Web): October 31, 2011 | doi: 10.1021/bk-2011-1078.ch008

Table 3. Gas permeabilities of 6FDA-based polyimides

No.	*Permeability (Barrer)*						*Selectivity*	
	He	H_2	CO_2	O_2	N_2	CH_4	O_2/N_2	CO_2/CH_4
1	198	257	189	39	8.1	6.2	4.8	30
2		516	431	109	31.1	25.4	3.5	17
3		549	440	122	35.9	27.5	3.4	16
4		45.5	15.3	4.2	0.79	0.28	5.3	54
5		40.2	9.2	3.0	0.45	0.16	6.7	58
6		87.2	28.6	7.4	1.30	0.72	5.7	40
7		107	42.5	11.0	2.12	0.92	5.2	46
8		58.6	21.6	6.4	1.16	0.45	5.5	48
9		108	51.2	14.2	3.09	1.35	4.6	38
10			5.1	1.8	0.26	0.08	6.9	64
11			30	7.53	1.34	0.70	5.6	43
12		38.2	10.7	2.9	0.48	0.22	6.1	49
13		40.7	16.7	3.9	0.74	0.34	5.3	49
14		23.7	6.1	1.6	0.26	0.12	6.1	49
15		14.0	2.1	0.7	0.10	0.03	6.8	66
16		46.0	19.0	5.4	0.98	0.51	5.5	37
17		21.0	6.3	1.4	0.25	0.13	5.6	49
18			22.8	6.5	1.30	0.71	5.0	32

Table 4. Physical properties (density, FFV, glass transition temperature and d-spacing) of 6FDA-based polyimides

Polymer	*Density* *(g/cm^3)*	*FFV** *(-)*	*Tg* *(^oC)*	*d-Spacing* *(Å)*
6FDA-DATRI PI	1.297	0.226	352	5.7
6FDA-*m*-TMPD	1.352	0.182	377	6.2
6FDA-*p*-TeMPD	1.330	0.182	420	6.1
6FDA-IPDA	1.352	0.168	310	5.7
6FDA-ODA	1.432	0.164	304	5.6

Downloaded by UNIV OF GUELPH LIBRARY on June 18, 2012 | http://pubs.acs.org
Publication Date (Web): October 31, 2011 | doi: 10.1021/bk-2011-1078.ch008

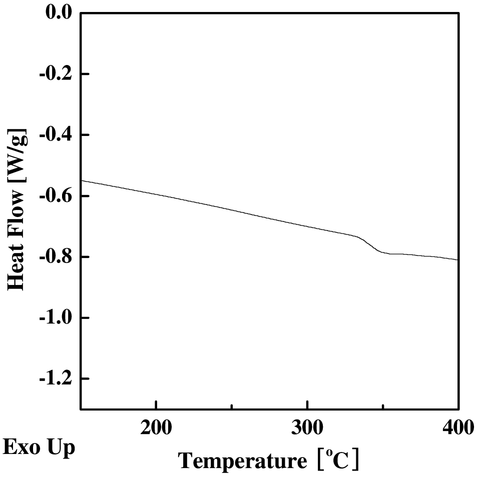

Figure 7. DSC thermogram of 6FDA-DATri polyimide.

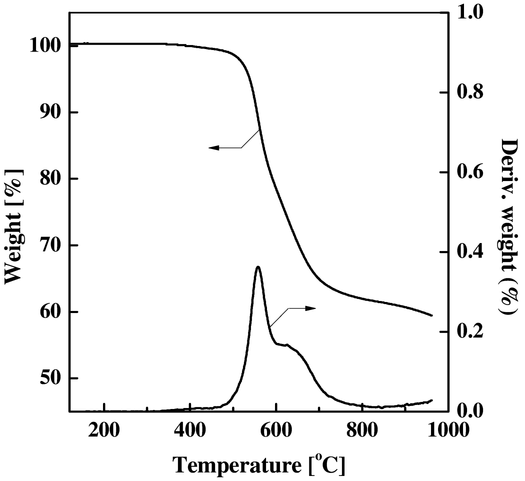

Figure 8. TGA curve of 6FDA-DATri polyimide (nitrogen atmosphere).

Downloaded by UNIV OF GUELPH LIBRARY on June 18, 2012 | http://pubs.acs.org
Publication Date (Web): October 31, 2011 | doi: 10.1021/bk-2011-1078.ch008

Table 5. Solubility of 6FDA-DATRI polyimide in common organic solvents

Solvent	*Solubility Parameter, MPa½*	*Solubility*	*Solvent*	*Solubility Parameter, MPa½*	*Solubility*
Acetone	20.2	O	EA	18.6	O
Chloroform	19.0	O	Benzene	18.8	X
DMAc	22.1	O	Toluene	18.2	X
DMF	24.8	O	Hexane	14.9	X
DMSO	24.5	O	Methanol	29.6	X
NMP	23.0	O	Ethanol	26.0	X
MC	19.0	O	IPA	23.5	X
THF	18.6	O	Water	47.9	X

(O: soluble, X: insoluble)

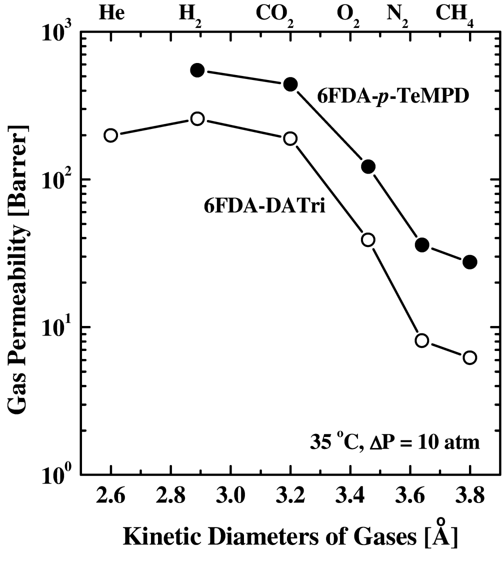

Figure 9. Gas permeability in 6FDA-DATri polyimide membrane at 35°C.

Using a constant volume, pressure-variable gas permeation method, we measured the gas permeability through 6FDA-DATri membrane. The order of gas permeability tested in this study is H_2 > He > CO_2 > O_2 > N_2 > CH_4 as shown in Figure 9. This order coincides well with typical trends observed in the common glassy polymers, showing organic molecular sieving properties, such as aromatic polyimides and polysulfones. The order of gas permeability, except helium, corresponds to the order of kinetic diameter of gas molecules, indicating that the size-sieving effect is a dominant factor for gas separation using this polymeric membrane. The gas permeability of 6FDA-DATri membrane is quite high, definitely which might be caused by high fractional free volumes due to lots of internal void spaces in triptycene-based diamine (DATri), as compared to other polyimides. However, the gas permeability was relatively lower than we originally expected because the fraction free volume is highest of any other polyimides known in the literature. This anomalous result might be caused by differences in distribution of free volume elements and spacing filling by bulky side groups –$C(CF_3)$-. Based on the X-ray data, narrow average *d*-spacing data say that triptycene structure has internal free volume elements but it can also lead to make the interchain distance close, probably due to interlocking of a phenyl ring of triptycene perpendicular along to polymer chain and π-π interactions between phenyl rings, as a result, acting as barriers for gas transport through this polymer microstructure but the gas selectivities toward gas pairs of interest in industries (e.g., air separation and carbon dioxide separation) keep high with high gas permeabilities.

Figure 10 presents the relation between CO_2 permeability and inverse fractional free volume of 6FDA-based polyimide membranes. If except the most permeable 6FDA-based polyimides, i.e., 6FDA-*p*-TeMPD and 6FDA-*m*-TMPD, there is a linear relation between the permeability and inverse fractional free volume. 6FDA-*p*-TeMPD and 6FDA-*m*-TMPD membranes exhibited unusual high gas permeabilities from viewpoint of free volume. This might be due to the fact that the apparent quantities of free volumes in glassy polymers may not always guarantee high gas permeable properties. That is, the size, shape, and connectivity of free volume elements should be deeply taken into account in the case of glassy polymers. Only volumetric factors cannot explain why the gas permeabilities of 6FDA-DATri polymers are lower than those two polyimides in spite of higher fraction free volumes. Generally, the rigidity of polymers hinders the activated diffusion through interchains of polymers, so often leading to low gas permeability, although new classes of rigid polymers, such as polymers of intrinsic microporosity and thermally rearranged polymers, recently show unexpected high gas permeation behavior. Figure 10 shows the relation between glass transition temperatures of 6FDA-based polyimides and CO_2 permeability. Once 6FDA-DATri including 6FDA-*p*-TeMPD and 6FDA-*m*-TMPD exhibits large deviation from the class of other 6FDA-based polyimide membranes. Interestingly, for 6FDA-based polyimides, it tends that the increase in glass transition temperature results in increasing CO_2 permeability. 6F-groups in such polyimide structures are bulky groups that lead to poor packing efficiency and the formation of irregular voids. In addition, such bulky 6F-groups prevent the mobility of interchains, thereby resulting in the increase in the glass transition temperature although the 6FDA-polymer backbone is flexible. This is why 6FDA-based polyimide membranes show higher gas permeability than any other polyimide membranes. This character often leads to very high gas permselectivity (calculated from single gas permeation experiments), particularly in the case of CO_2/CH_4 or CO_2/N_2. However, in the case of mixed gas experiments, the real separation factors dramatically decreases because CO_2 can plasticize the polyimides, which increases the mobility of flexible 6FDA chains. In this study, we did not measure the mixed gas separation performance of 6FDA-DATri membrane but we expect that interlocking and π-π interactions in triptycene units

Downloaded by UNIV OF GUELPH LIBRARY on June 18, 2012 | http://pubs.acs.org
Publication Date (Web): October 31, 2011 | doi: 10.1021/bk-2011-1078.ch008

help prevent severe CO_2 plasticization effect and thereby keep higher CO_2/CH_4 or CO_2/N_2 separation factor.

Figure 11 shows the diffusion coefficient as a function of critical molar volume of gas, and the solubility coefficient as a function of critical temperature. If many penetrants of changing size and shape are considered, estimates of size such as the van der Waals volume or critical volume are often more convenient scaling parameters because these values are available for practically any gas or vapor of interest. As expected, there is a linear relationship between diffusion coefficients of gases and their critical volume. 6FDA-DATri polyimide membrane has stronger linear relations than amorphous PDMS membrane, meaning that they are strongly dependent on molecular size. Therefore, the diffusion selectivity is rather higher than in PDMS, which has weak intermolecular forces and a corresponding broad distribution of inter-segmental gap sizes for responsible for diffusion.

As presented in Figure 12, the solubility coefficients are also higher than those of PDMS, used frequently for membrane materials, indicating that large amount of Langmuir sorption sites exist in the current polymers owing to internal void space. In many cases, gas solubility (S) coefficients over short ranges of penetrant critical temperature are well described by a linear relationship between the logarithm of S and critical temperature, i.e., a measure of penetrant condensability. Such linear dependences are found in 6FDA-DATri polyimide and PDMS membranes. Solubility coefficients increase with increasing forces of intermolecular interaction in the gas. The solubility coefficients in 6FDA-DATri are larger than in PDMS membrane.

Downloaded by UNIV OF GUELPH LIBRARY on June 18, 2012 | http://pubs.acs.org
Publication Date (Web): October 31, 2011 | doi: 10.1021/bk-2011-1078.ch008

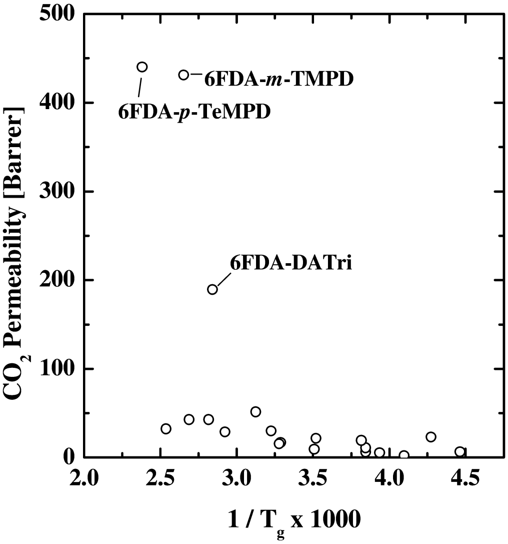

Figure 10. CO_2 permeability as a function of inverse glass transition temperature in 6FDA-based polyimide membranes.

Downloaded by UNIV OF GUELPH LIBRARY on June 18, 2012 | http://pubs.acs.org
Publication Date (Web): October 31, 2011 | doi: 10.1021/bk-2011-1078.ch008

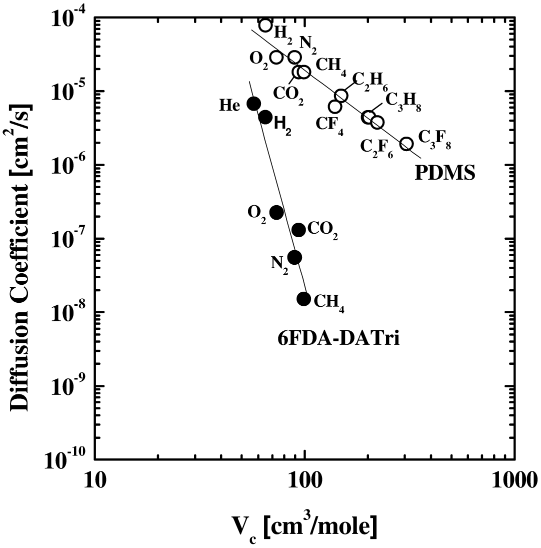

Figure 11. The diffusion coefficient as a function of critical molar volume of gas in 6FDA-DATri polyimide and PDMS membranes.

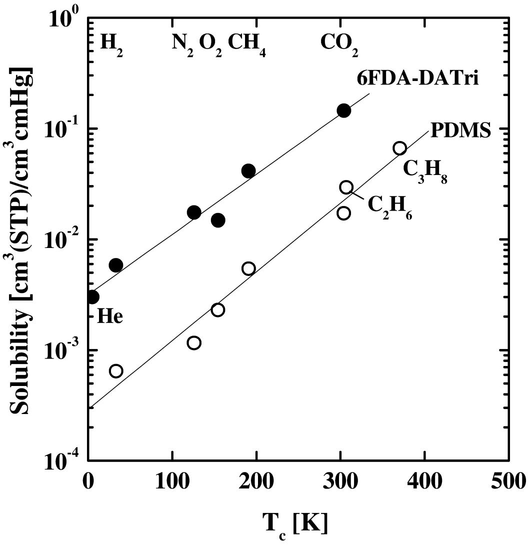

Figure 12. The solubility coefficients of different gases in 6FDA-DATri polyimide and PDMS membranes as a function of critical temperature (T_c) of gases.

Downloaded by UNIV OF GUELPH LIBRARY on June 18, 2012 | http://pubs.acs.org
Publication Date (Web): October 31, 2011 | doi: 10.1021/bk-2011-1078.ch008

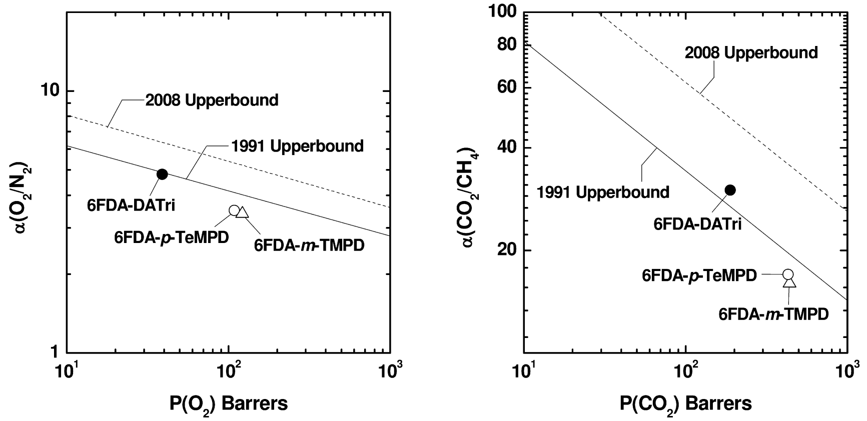

(a) (b)

Figure 13. Gas separation performances of 6FDA-DATri membrane at 35 °C in permeability-selectivity maps of gas pairs of interest (a) O_2/N_2 and (b) CO_2/CH_4.

The dependence of selectivities of polyimides for gaseous mixtures O_2/N_2 and CO_2/CH_4 on gas permeability for O_2 and CO_2 are presented in Figure 13. The line and dot line are upper bounds of permeability-selectivity relations in polymeric membranes, semi-empirically established by Robeson at 1991 and 2008 (*21*)(*22*), respectively. Generally, polyimides have quite high values of both permeability and selectivity, located closely to the upper bounds. As compared to 6FDA-*p*-TeMPD and 6FDA-*m*-TMPD, known as the highest permeability polyimides, the gas permeabilities of 6FDA-DATri membrane are lower than those of them; however, the gas selectivities are much higher. For O_2/N_2 separation, the 6FDA-DATri is located on the line of the upper bound at 1991. In the case of CO_2/CH_4, the separation performance surpasses the upper bound at 2008, meaning that this polyimide would be promising for CO_2 separation applications such as natural gas purification from practical point of view as membrane materials.

4. Conclusions

A polyimide including a three-dimensional, rigid triptycene framework was synthesized with high molecular weight using ester-acid chemical imidization method. The 6FDA-DATRI polyimide has high internal free volume due to triptycene structure in polymer chains. The polyimide has good solubility in many common organic solvents and high thermal stability such as other polyimides. In addition, the triptycene-based polyimide shows high permeability in pure gases and very strong tolerance to CO_2 plasticization in the CO_2/CH_4 mixed gas separation while many glassy polymers having high fractional free volume suffer from a large reduction in mixed gas selectivity. This low CO_2 plasticization may be a physical hindrance effect due to interlocking of a phenyl ring of triptycene perpendicular to polymer backbone, and then π-π interactions between phenyl

Downloaded by UNIV OF GUELPH LIBRARY on June 18, 2012 | http://pubs.acs.org
Publication Date (Web): October 31, 2011 | doi: 10.1021/bk-2011-1078.ch008

rings. Depending on polymer structure and modified triptycene structures, the triptycene-based polyimide membranes can be further tailored for specific separation purposes. That is, many useful physical and chemical properties in this triptycene-based polyimide can be readily tuned by using different dianhydrides, various types of solvents, and different monomer configurations. Further studies are aimed at optimizing polymer design by using other iptycenes monomers, copolymers, and nanoparticles capable of breaking close contact between non-covalent linked phenyl rings in triptycene for other technological applications, such as low-k and organic adsorbants, as well as gas separation.

Acknowledgments

This work was supported by the World Class University (WCU) Program of the Ministry of Education, Science, and Technology (MEST) in Korea.

References

1. Ghosh, M. K.; Mittal, K. L. *Polyimides: fundamentals & applications*; Marcel Dekker: New York, 1996.
2. Mittal, K. L. *Polyimides and other high temperature polymers: synthesis, characterization and applications*; Brill: The Netherlands, 2009; Vol. 5.
3. Feger, C.; Khojasteh, M. M.; Htoo, M. S. *Advances in polyimide science and technology*; Technomic Publishing Company, Inc.: Lancaster, 1993.
4. Ohya, H.; Kudryavsev, V. V.; Semenova, S. I. *Polyimide membranes: applications, fabrications and properties*; Gordon and Breach Publishers: Tokyo, 1996.
5. Langsam, M. Polyimides for gas separation. *Plastics Eng.* **1996**, *36*, 697.
6. Al-Masei, M.; Fritsch, D.; Kricheldorf, H. R. New polyimides for gas separation. 2. Polyimides derived from substituted catechol bis(etherphthalic anhydrides)s. *Macromolecules* **2000**, *33*, 7127.
7. Wind, J. D.; Paul, D. R.; Koros, W. J. Natural gas permeation in polyimide membranes. *J. Membr. Sci.* **2004**, *228*, 227–236.
8. Hillock, A. M. W.; Koros, W. J. Cross-linkable polyimide membrane for natural gas purification and carbon dioxide plasticization reduction. *Macromolecules* **2007**, *40*, 583–587.
9. Stern, S. A.; Mi, Y.; Yamamoto, H.; St. Clair, A. K. Structure/permeability relationships of polyimide membranes. Applications to the separation of gas mixtures. *J. Polym. Sci., Part B: Polym. Phys.* **1989**, *27*, 1887–1909.
10. Heuchel, M.; Hofmann, D.; Pullumbi, P. Molecular modeling of small-molecule permeation in polyimides and its correlation to free-volume distributions. *Macromolecules* **2004**, *37*, 201–214.
11. Long, T. M.; Swager, T. M. Molecular design of free volume as a route to low-k dielectric materials. *J. Am. Chem. Soc.* **2003**, *125*, 14113–14119.
12. Chong, J. H.; Maclachlan, M. J. Iptycenes in supramolecular and materials chemistry. *Chem. Soc. Rev.* **2009**, *38*, 3301–3315.

13. Dahms, K.; Senge, M. O. Triptycene as a rigid, 120° orienting, three-pronged, covalent scaffold for porphyrin arrays. *Tetrahedron Lett.* **2008**, *49*, 5397–5399.
14. Kelly, T. R.; De Silva, H.; Silva, R. A. Unidirectional rotary motion in a molecular system. *Nature* **1999**, *401*, 150–152.
15. Bini, L.; Müller, C.; Wilting, C. J.; Von Chrzanowski, L.; Spek, A. L.; Vogt, D. Highly selective hydrocyanation of butadiene toward 3-pentenenitrile. *J. Am. Chem. Soc.* **2007**, *129*, 12622–12623.
16. Hou, S.; Sagara, T.; Xu, D.; Kelly, T. R.; Ganz, E. Investigation of triptycene-based surface-mounted rotors. *Nanotechnology* **2003**, *14*, 566–570.
17. Tsui, N. T.; Paraskos, A. J.; Torun, L.; Swager, T. M.; Thomas, E. L. Minimization of internal molecular free volume: a mechanism for the simultaneous enhancement of polymer stiffness, strength, and ductility. *Macromolecules* **2006**, *39*, 3350–3358.
18. Long, T. M.; Swager, T. M. Minimization of free volume: alignment of triptycenes in liquid crystals and stretched polymers. *Adv. Mater.* **2001**, *13*, 601–604.
19. Hoffmeister, E.; Kropp, J. E.; McDowell, T. L.; Michel, R. H.; Rippie, W. L. Triptycene polymers. *J. Polym. Sci., Part A-1* **1969**, *7*, 55–72.
20. Chen, Z.; Swager, T. M. Synthesis and characterization of poly(2,6-triptycene). *Macromolecules* **2008**, *41*, 6880–6885.
21. Robeson, L. M. Correlation of separation factor versus permeability for polymeric membranes. *J. Membr. Sci.* **1991**, *62*, 165.
22. Robeson, L. M. The upper bound revisited. *J. Membr. Sci.* **2008**, *320*, 390.

Downloaded by UNIV OF GUELPH LIBRARY on June 18, 2012 | http://pubs.acs.org
Publication Date (Web): October 31, 2011 | doi: 10.1021/bk-2011-1078.ch008

In Modern Applications in Membrane Science and Technology; Escobar, I., et al.;
ACS Symposium Series; American Chemical Society: Washington, DC, 2011.

Downloaded by PENNSYLVANIA STATE UNIV on June 18, 2012 | http://pubs.acs.org
Publication Date (Web): October 31, 2011 | doi: 10.1021/bk-2011-1078.ch010

Chapter 10

Membranes for Water Treatment Applications – An Overview

Tilak Gullinkala[a] and Isabel C. Escobar[*,b]

[a]Hydration Technology Innovations, LLC, Albany, OR 97321
[b]Department of Chemical and Environmental Engineering, The University of Toledo, 2801 W Bancroft St, Toledo, OH 43606, U.S.A.
[*]E-mail: isabel.escobar@utoledo.edu.
Phone: (419) 530-8267. Fax: (419) 530-8086

Water is one of the basic requirements for the survival of life on this planet. However, the total quantity of fresh water on the planet is finite while the world population and its water usage are fast increasing due to industrialization and urbanization (Kirby, A. http://news.bbc.co.uk/2/hi/science/nature/3747724.stm). Only 1% of the water available on earth can be consumed without processing, filtering or melting polar ice caps. The solution to this problem can be achieved by water conservation and guiding research and technology towards sustainable water purification. Although seventy percent of earth's surface is covered with water, ninety seven percent of this water is contained in oceans, making it unsuitable for drinking or any other application due to its high salt content. Of the remaining three percent of fresh water, only 0.3% is found in rivers and lakes and or remains frozen. These numbers clearly indicate the necessity for exploring the waters from other than fresh water sources, i.e. ocean waters and used waters to elude the impending global water crisis. The refinement of these waters through various techniques is a requirement for the survival of life on this planet.

In Modern Applications in Membrane Science and Technology; Escobar, I., et al.;
ACS Symposium Series; American Chemical Society: Washington, DC, 2011.

Downloaded by PENNSYLVANIA STATE UNIV on June 18, 2012 | http://pubs.acs.org
Publication Date (Web): October 31, 2011 | doi: 10.1021/bk-2011-1078.ch010

1. Water Treatment

Water treatment can be defined as the practice of subjecting water to an agent or process with the objective of increasing its quality to meet the specific requirements for different applications, such as human consumption, industrial utilization, domestic operations and irrigation. Water purification can be achieved by thermally-driven process such as distillation, membrane assisted pressure-driven processes such as ultrafiltration (UF), microfiltration (MF) and reverse osmosis (RO), electrically-driven process such as electrodeionization (EDI) and other methods such as activated carbon adsorption and ion exchange, in which appropriate agents are used to adsorb specific impurities present in the water. Of all these processes, membrane-based operations are straightforward, cost effective and versatile (*2*).

1.1. Membrane Separations

Membrane technologies are widely used in separation processes, such as water purification, protein separation, metal recovery and pigment recovery, enabling them to play a pivotal role in major industries, such as food and beverage, biotechnology, chemical and pharmaceuticals and municipal water treatment. A membrane can be defined as a very thin layer or cluster of layers that allows selective components to pass through when mixtures of different kinds of components are driven to its surface. Membranes are considered symmetric and homogeneous if they are made of single layer, or asymmetric and non-homogeneous if they consist of more than one layer (*3*). The flux of the asymmetric membrane is higher than that of symmetric homogeneous membrane because of the thinness of the dense selective layer. This feature of the asymmetric membranes makes them largely applicable in water purification industry so that higher production rates can be achieved.

An integrally-skinned asymmetric membrane was first successfully developed by Loeb and Sourirajan (*20*), which led to the initial breakthrough in the use of membranes and membrane-assisted separation processes. Three general modes of construction are widely observed in polymeric membrane structures. They are homogeneous, asymmetric, and composite. Typical illustrations are shown in Figure 1. Homogeneous membranes constitute of single polymer material and uniform pore size throughout the membrane. In contrast to symmetric membranes, asymmetric membranes usually have a very thin skin layer that determines the membrane selectivity and a relatively thick porous supporting layer (*21*). In a composite membrane, the selective layer is made of a different polymer. Asymmetric and composite membranes can have better performance than the symmetric membranes because the selective layer in an asymmetric membrane is thinner, thereby reducing the membrane resistance relative to a symmetric membrane of similar retentive capability. These membranes consist of a thin, “dense” polymer layer supported by a thick, mechanically strong polymeric substructure. The dense layer, being close-knit in physical structure, provides maximum resistance to the flow through, so it is responsible for the membrane

Downloaded by PENNSYLVANIA STATE UNIV on June 18, 2012 | http://pubs.acs.org
Publication Date (Web): October 31, 2011 | doi: 10.1021/bk-2011-1078.ch010

selectivity. Thus, the dense selective layer provides the filtration properties, while the porous support layer provides mechanical strength to the membrane.

1.1.1. Membrane Materials

Various polymeric materials are used for membrane synthesis. Polymers such as cellulose acetate (CA), cellulose diacetate, cellulose triacetate, polyamide (PA), sulfonated polysulfone and aromatic polyamide are widely used as synthesizing material for water treatment membranes. Combination of these materials is used in casting of the thin film composite (TFC) membranes. The choice of the material makes an enormous difference to the membrane performance (*3*), as the material plays a crucial role in interacting with feed solutions. The material determines various membrane properties, such as hydrophilicity, surface charge, chlorine tolerance limit and allowable pH range. The degree of hydrophilicity is higher for cellulosic materials and some of its ester derivatives such as cellulose acetate. Polyethylene and polypropylene are very hydrophobic in nature. Various polymers with intermediate hydrophilicity, such as the polysulfone (PS)/polyether sulfone (PES) family, polyacrylonitrile (PAN) and polyvinylidene fluoride (PVDF), are also used as selective layers for the membranes (*5*). Cellulose acetate-based membranes are able to tolerate moderate amounts of chlorine (0.3-1.0 mg/L), but are vulnerable to biological attack, hydrolysis, and chemical reaction with feed waters to form cellulose and acetic acid (*3*). Linear polyamide membranes are not tolerant to chlorine, and thus, chlorine levels must be kept below 0.05 mg/L. Linear polyamide membranes typically have allowable pH ranges between 4 and 11 (*22*).

1.2. Modes of Pressure-Driven Separations

Water purification is a rigorous process, which requires removal of a large number of impurities of varying size, shape and solubility depending on the nature of the water source. Membranes of varying pore size distributions and molecular weight cutoffs (MWCO) are used for this purpose. MWCO is defined as the molecular weight in Daltons of the lowest molecular weight solute that is 90% retained by the membrane. Based on these distributions and type of impurities removed, water filtration processes can be classified into particle filtration, microfiltration (MF), ultrafiltration (UF), nanofiltration (NF) and reverse osmosis (RO). A typical pore size distribution and rejection characteristics of the membranes used for these filtration processes are shown in Figure 2. Table 1 summarizes the pore size characteristics of membranes and different application of membranes. These various filtration techniques fall into two broad categories. In the first category, RO and NF are used to remove dissolved components from water or wastewater feeds. RO is dominated by diffusion of matter and NF is characterized by both diffusion through polymer network and convection through membrane pore network. In the second, MF and UF are used for removal of fine particulates as these processes are mainly dominated by feed solution convection through membrane pore network.

Downloaded by PENNSYLVANIA STATE UNIV on June 18, 2012 | http://pubs.acs.org
Publication Date (Web): October 31, 2011 | doi: 10.1021/bk-2011-1078.ch010

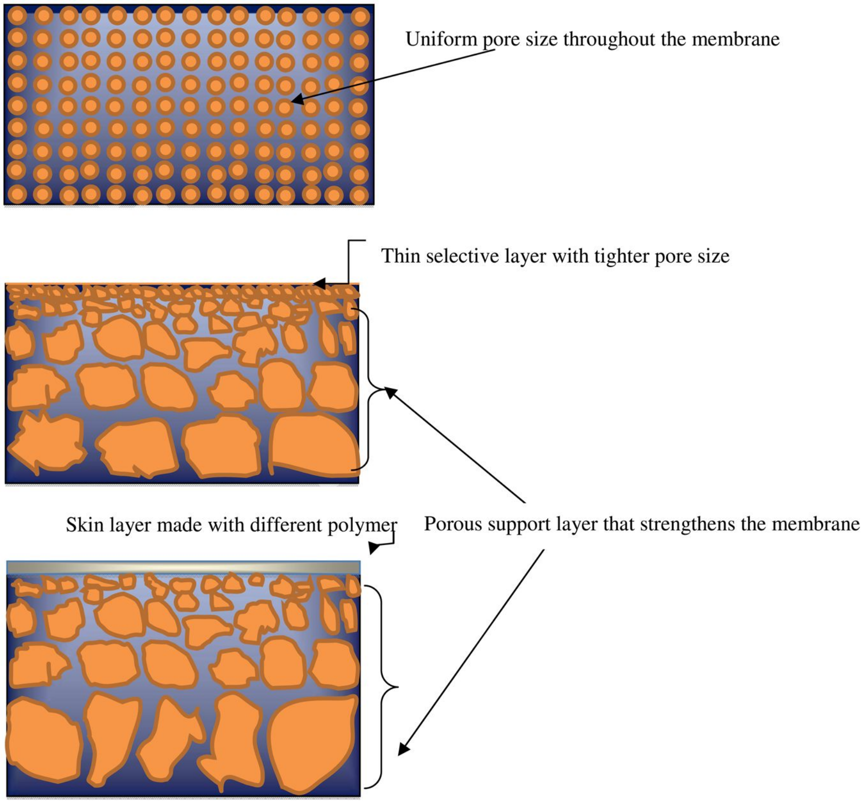
Uniform pore size throughout the membrane
Thin selective layer with tighter pore size
Skin layer made with different polymer
Porous support layer that strengthens the membrane

Figure 1. (A): Homogeneous membrane construction; (B): Asymmetric membrane construction; (C): Thin film composite membrane construction.

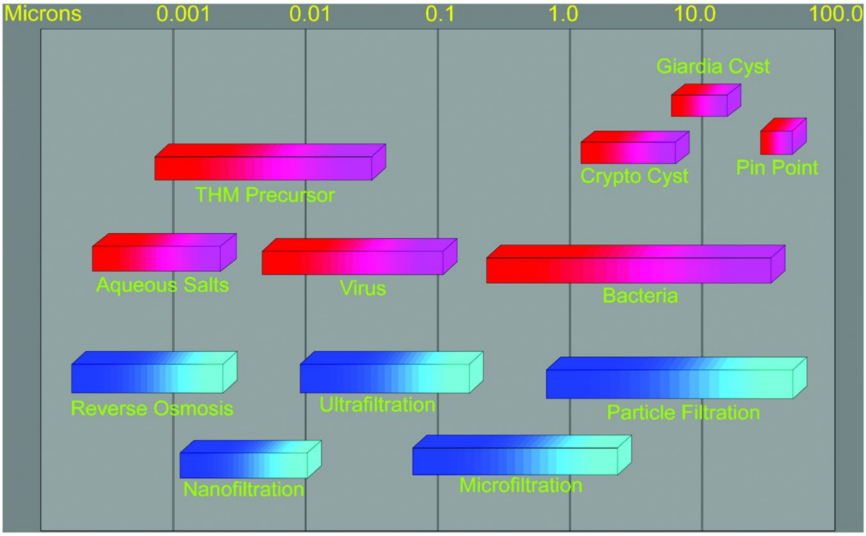

Figure 2. Rejection characteristics of membrane filtration.

Downloaded by PENNSYLVANIA STATE UNIV on June 18, 2012 | http://pubs.acs.org
Publication Date (Web): October 31, 2011 | doi: 10.1021/bk-2011-1078.ch010

Table 1. Membrane pore size characteristics and application

Membrane Type	*Average Pore Size (nm)*	*Application*
MF	200	Suspended solids, turbidity, and pathogens
UF	2-50	Macromolecules, viruses, colloids, and protein
NF	<2	Color, organics, pesticides, and metals
RO	-	Dissolved solids, nitrates, and radionuclides
ED	-	Only removal of ionic contaminants. Ineffective for pathogen and organics

All the membranes have their own application and operational condition:

- RO is a pressure-driven membrane operation that is able to retain salts and low-molecular-weight solutes by applying a high pressure drop (in the range of 1.0 to 8.3 Mpa) to overcome the osmotic pressure difference between the feed water and the permeate. Osmotic pressure is the pressure difference across the membrane that causes water molecules flowing through the membrane from the permeate side (i.e., high water molecule concentration) to the feed water side (i.e., low water molecule concentration).
- NF is used for removal of the organic compounds larger than 100-500 daltons and polyvalent ions. It lies between RO and ultrafiltration in terms of membrane selectivity and is designed for softening processes. Monovalent ions are poorly rejected by NF membranes. The operating pressure used in NF (typically 0.5 - 1.5 Mpa) is much lower than in RO.
- UF is also a pressure-driven membrane process used for the removal of colloids and high-molecular-weight materials (larger than 10,000 daltons). Since the pore size of UF is large, the operating pressure is low (50 -500 kPa).
- MF is used for the elimination of turbidity particles, multicellular parasites and protozoa, some bacteria and some viruses associated with particulate materials (100,000 daltons). Its normal operating pressure range is 30-300 kPa.
- ED is used in the operation by which ions are driven through ion-selective membranes under the influence of an electrical potential. This process also has environmental applications, but it is more limited.

Even though pressure driven membrane processes have many similar aspects (e.g., geometric, flow configuration, etc.), the principles of contaminant rejection by the membranes are different. Rejection of a given material by a membrane commonly refers to the difference between the concentrations in the feed and permeate streams divided by the concentration in the feed stream. The rejection of contaminants by RO membranes is mainly dependent on chemical interactions between membranes and contaminants in feed water, although mechanical sieving is also important for colloidal material rejection. In contrast, rejection by MF

Downloaded by PENNSYLVANIA STATE UNIV on June 18, 2012 | http://pubs.acs.org
Publication Date (Web): October 31, 2011 | doi: 10.1021/bk-2011-1078.ch010

membranes is due almost entirely to physical sieving. NF and UF membranes may reject contaminants to some extent based on combinations of physical sieving and contaminant-membrane chemistries.

Membrane selectivity, permeability, mechanical stability, chemical resistance and thermal stability are highly dependent upon the type of material and the process control variables applied during manufacturing. Among the many raw materials used for membrane manufacturing, most basic types involve various forms of modified natural cellulose acetate materials and a variety of synthetic materials. Synthetic membranes can be made from organic (polymers) or inorganic (metals, ceramics, glasses, etc.) compounds. Because of processing requirements and required membrane lifetime, only a limited number of raw materials are used in practice, such as: cellulose acetate (CA), cellulose diacetate (CDA), cellulose triacetate, polyamide (PA), aromatic polyamides, polyetheramides, polysulphone (PSf), and polyethersulphone (PES). In addition, thin film composite (TFC) membranes may be made from a variety of polymers consisting of several different materials for substrate, the thin film and other functional layers. The membranes made from inorganic materials are rarely used in water industry because they have the disadvantages of being very brittle and more expensive than organic membranes.

1.3. Module Configurations

The single operation unit into which membrane are engineered for use is referred to as a module. This operational unit consists of the membranes, pressure support structures, feed inlet and concentration outlet ports, and permeate draw-off points. Four major types of modules are found on the market: plate and frame, spiral wound, tubular, and hollow fiber.

- Plate and frame modules are made of stacked flat-sheet membranes and support plates. The feed circulates between the membranes of the two adjacent plates. The thickness of the liquid sheet is in the range of 0.5 to 3.0 mm. The packing density of plate and frame units is about 100 to 400 m^2/m^3. Units are easily disassembled to clean or replace the membranes.
- For spiral wound modules, an envelope of two flat-sheet membranes enclosing a flexible porous sheet is sealed on three of its edges. The open edge is connected and rolled up onto a perforated tube which carries the permeate. Several envelopes are fastened and separated from one another by a feed side spacer. This module has lower head loss than the plate-and-frame module. But it is more sensitive to clogging than the plate-and-frame module.
- The tubular module is the simplest configuration in which the membrane is cast on the inside wall of a porous support tube. These tubes have internal diameters from 6 to 40 mm. Individual tubes may be placed inside stainless steel or PVC sleeves or bunched together in a cylindrical housing with appropriate end plates. These modules are easy to clean and particularly well adapted to the treatment of very viscous fluids. Tubular membranes consist of a selective layer supported by fiberglass, perforated

Downloaded by PENNSYLVANIA STATE UNIV on June 18, 2012 | http://pubs.acs.org
Publication Date (Web): October 31, 2011 | doi: 10.1021/bk-2011-1078.ch010

metal, or other suitable porous material. In the tubular configuration, the feed solution is typically on the inside of the tube and the permeate travels through the wall of the tube (membrane) into the shell side of the module. Often, the module contains a collection of tubes (up to 30), known as an array. Both fouling and concentration polarization can be minimized with the tubular configuration by using a high velocity flow of feed water to produce turbulence. Since the inside and outside of the tubes are easily accessible, tubular membranes can be readily cleaned. However, they have a low packing density, thus increasing the capital cost.

- Hollow fiber module is the configuration in which the fibers are gathered in a bundle of several thousand, even several million. Flow of the feed can take place either inside the fiber (inside-out configuration) or outside of the fiber (outside-in configuration). These units are very compact (from 1,000 m^2/m^3 in UF modules, up to 10,000 m^2/m^3 in RO modules). Operation velocities in hollow-fiber modules are normally low, and modules can even be operated without recirculation (dead-end mode). In addition, hollow fiber mode has good back flushing capacity resulted from the fibers being self-supporting. Pressure and feed are at the outside of the fiber. Hollow fibers are sturdy enough to act as their own pressure vessels partially because of their chemical and physical structure. The rigidity of the fibers varies inversely with porosity, thus hollow fibers typically have lower permeabilities than their tubular or flat sheet counterparts. However, they do not need to be as productive on an area basis because their packing density is much higher.

2. Performance Behavior of Clean Membranes

The capital and operating costs of membrane systems are directly related to the membrane permeate flux. Flux refers to mass or volume of product transferred through a unit membrane surface area per unit time. If the permeate flux increases, less membrane area is required to provide for the design flow. This decreases the costs of membrane modules, peripheral piping and pumps, monitoring skids, foundations and buildings. Thus, the permeate flux is an important parameter in membrane system design.

Darcy's law can be employed to describe the flux, J, of clean water across a membrane without fouling:

$$J = \frac{\Delta P}{\mu R_m} \qquad (1)$$

where ΔP is the pressure drop across the membrane (also called the transmembrane pressure, or TMP), μ is the absolute viscosity, and R_m is the hydraulic resistance of the clean membrane.

Darcy expression (1) is similar to the Kedem-Katchalsky equation derived from irreversible thermal dynamics that is shown in Equation 2:

$$J \cong \left(\frac{L_v}{V_w}\right)(\Delta p - \sigma \Delta \Pi) \tag{2}$$

where L_v is a phenomenological coefficient, V_w is the molar volume of water, σ is the reflection coefficient (derived as the ratio of two phenomenological coefficients), and ΔΠ is the difference in osmotic pressure across the membrane.

By analogy, the transmembrane pressure drop in Equation 1 may be modified to account for the reduction in the net transmembrane pressure due to the effect of osmotic pressure:

$$J = \frac{\left(\Delta p - \sigma_k \Delta \Pi\right)}{\mu R_m} \tag{3}$$

Thus, flux of permeate across a clean membrane occurs only when the transmembrane pressure, *Δp*, exceeds the difference in osmotic pressure across the membrane. For UF and MF membranes, the effect of osmotic pressure is small and negligible because the species mainly rejected by those two membranes, such as macromolecules and colloidal materials, have very small osmotic pressure. The osmotic pressure is linearly proportional to the number concentration, and in feed waters, particle number concentration is much smaller than ion number concentration (or molar concentration) so that the solute osmotic pressures in MF and UF are truly negligible. In addition, the permeate flux is affected by the temperature because typically higher temperatures induce a lower viscosity of solution and thus increase the permeate flux.

When membrane filtration is used to treat real raw water, the hydraulic resistance R_m, in Equation 3, will increase because of foulant accumulation on the membrane surface. The hydraulic resistance of fouled membranes is caused not only by the membrane, but also by the fouling layer on the membrane surface. From Equation 3, when fouling occurs, in order to keep a constant permeate flux, higher transmembrane pressure must be supplied to overcome the increased resistance although higher pressure results in higher operating cost. Otherwise, product flux will decrease, and the demand of water quantity cannot be met.

2.1. Mass Transport and Rejection Principals

In all pressure-driven membrane processes, the permeate flow through the membrane causes the transport of materials, especially smaller materials, in the feed water to the vicinity of the membrane. The smaller materials (such as ionic species and small organic compounds) transported to RO/NF membrane by permeate flow can accumulate on the membrane surface to form a concentration boundary layer. This layer also leads to brownian back-diffusion from the membrane because of the formation of the concentration gradient between the boundary layer and the bulk fluid. The combination of the permeate advection and brownian diffusion determines the thickness of the boundary layer.

Downloaded by PENNSYLVANIA STATE UNIV on June 18, 2012 | http://pubs.acs.org
Publication Date (Web): October 31, 2011 | doi: 10.1021/bk-2011-1078.ch010

Colloidal materials transport to membrane surface mainly due to the permeate drag force. In addition, colloidal materials also experience some other forces (i.e., inertial lift induced by wall effect, shear-induced diffusion, and other orthokinetic effects) that tend to increase the backtransport of the particles from the membrane surface. The permeate drag force associated with the backtransport forces determine the transport of the colloidal particles.

The predominate mechanism of particulate material removal by membranes is physical sieving. Physical sieving is also the dominant mechanism for UF and MF membranes. However, rejection of solutes by RO and NF membranes experience complex membrane-solute interactions such as electrostatic interaction, dispersion forces and hydrophobic interaction. Both the membrane composition and the solute characteristics play an important role in the rejection mechanisms of RO and NF membranes.

3. Membrane Fouling

As materials accumulate near, on, and within the membrane, they may reduce the permeability of the membrane by blocking or constricting pores and by forming a layer of additional resistance to flow across the membrane (figure 3). Reductions in permeate flux over time may be substantial and represent a loss in the capacity of a membrane facility (figure 4). The characteristics and location of the deposited materials can play an important role in determining the extent and reversibility of permeate flux decline. Cleaning the membrane, either hydraulically or chemically, may remove some of the accumulated materials and partially restore permeate flux. A reduction in permeate flux that cannot be reversed is referred to as membrane fouling.

Removal of dissolved and fine particulate matter from the feed streams ultimately leads to the formation of a layer of these particles on the membrane surface, which reduces the flux of the membrane. This newly formed layer, sometimes referred to as cake, needs to be removed to regenerate the original flux of the membrane. This layer can be partially removed by employing techniques, such as rinsing, pulsing and backwashing of the membranes (*4*). Fouling of the membrane is caused by the adsorption of feed matter on the membrane surface, which cannot be removed by these techniques and leads to the continual flux decline. The actual mechanism of fouling is not very well understood. This is mainly due to the presence of various kinds of foulants whose properties vary significantly from one another. In a similar way, selective layers of membranes also have properties that vary greatly resulting in numerous permutations and combinations of membrane-foulant interactions. These interactions have to be clearly interpreted for understanding, evaluation, prevention or treatment of membrane fouling. Fouling adversely affects the membrane performance. First of all, it reduces the membrane flux thereby reducing the product rate drastically. Flux loss can be negated partially by increasing transmembrane pressure resulting in higher energy consumption and loss membrane selectivity. Fouling of the membrane gradually leads to increased cleaning operations, reduced production rate and membrane life and increased production cost. Depending on the nature

Downloaded by PENNSYLVANIA STATE UNIV on June 18, 2012 | http://pubs.acs.org
Publication Date (Web): October 31, 2011 | doi: 10.1021/bk-2011-1078.ch010

Downloaded by PENNSYLVANIA STATE UNIV on June 18, 2012 | http://pubs.acs.org
Publication Date (Web): October 31, 2011 | doi: 10.1021/bk-2011-1078.ch010

of the adsorbed matter, fouling can be classified into inorganic, organic and biofouling.

3.1. Inorganic Fouling

Inorganic fouling occurs through the scaling of inorganic salts leading to a loss of membrane flux. It is generally agreed that the causal mechanism is exceeding the solubility of the foulants in water. The solution becomes super saturated with the dissolved salts at the membrane surface as the filtration proceeds and results in the precipitation of salts. Time required for the feed water to reach supersaturation at the membrane surface is known as induction time, and these times are short for filtration systems with high recovery. Membrane recovery is defined as the ratio of permeate flow to feed flow of the membrane. It follows that precipitation is worst in a high recovery membrane system. Among the species commonly encountered in precipitants are Ca^{2+}, Mg^{2+}, CO_3^{2-}, SO_4^{2-}, silicas, and most forms of iron. Scaling is usually prevented by acidifying the feed water to prevent the precipitation of carbonates and by the use of antiscalants to prevent the precipitation of sulfates of Ca^{2+}, Mg^{2+}, Sr^{2+} (*5*). Dosage of antiscalant depends on the feed water analysis but usually is between 2 to 5 ppm. Precipitation of iron on membranes is generally associated with Fe_2O_3 or $Fe(OH)_3$ formed by condensation reactions of hydrolysable Fe^{3+} ions present in the feed solution. Reactions appear to occur in both bulk and concentration polarization regimes. Precipitation of this kind is generally not a problem when concentrations are at about 4 mg/L and recovery is below 80%. When the recovery limit becomes 80 – 90 %, despite the presence of antiscalants, the supersaturation ratio becomes too large (e.g., up to 400% of calcium sulfate). Cases have also been reported in which antiscalants themselves have contributed to the fouling of the membranes. In some cases, reversing the flow before reaching the induction time of the system replaces the supersaturated brine at the exit with unsaturated feed and thus "zeroes the induction clock" (*6*).

3.2. Organic Fouling

Organic fouling occurs significantly due to the adsorption of natural organic matter (NOM) present in the feed water on the membrane surface. Organic fouling constitutes the major portion of the fouling when the water is treated by membrane filtration (*7*). It also serves as precursor for formation of disinfection by-products (DBPs). DBPs are formed when organic or mineral matter present in the feed water reacts with chemical disinfectants used in the water treatment. NOM is comprised of a wide range of compounds in the form of dissolved organic carbon (DOC) and particulate matter. DOC consists of organic matter ranging from low to high molecular weight compounds such as polysaccharides, proteins, amino-sugars, nucleic acids, humic and fulvic acids, organic acids and cell components (*8*). The mechanism of organic fouling is largely characterized by the interactions that exist between organic foulants and membrane surface (*7*, *9*). Researchers have described several mechanisms for NOM fouling that are governed significantly by hydrophobic interactions and also by size exclusion and electrostatic repulsion (*9*).

Downloaded by PENNSYLVANIA STATE UNIV on June 18, 2012 | http://pubs.acs.org
Publication Date (Web): October 31, 2011 | doi: 10.1021/bk-2011-1078.ch010

Apart from causing severe organic fouling on the surface, organic foulants present in the feed solution also facilitate the advent of biofouling as organic layer acts as conditioning film for microbilal deposition on the membrane surface (*10*).

3.3. Biofouling

Biofouling is the unwanted deposition and growth of microorganisms and their microbial products to a surface that is in contact with water. Microbial cells attach firmly to almost any surface exposed to an aquatic environment. Immobilized cells grow, reproduce and produce extra-cellular polymers which frequently extend from the cell, forming a tangled matrix of fibers that provide structure to the assemblage termed a biofilm (*11*). Feed waters containing microorganisms and organic matter have a tremendous potential for causing biofouling as well as organic fouling (*10*). Once the organic matter deposits on the membrane surface, it acts as a conditioning film for microbial attack. Microbial deposition on the conditioned membrane surface usually occurs through various mechanisms such as diffusion, convection or Brownian motion. Sometimes microorganisms in feed waters may be transported towards each other and microbial aggregates can be formed. Subsequently these microbial aggregates or individual microorganisms adhere to the membrane surface. This microbial adhesion is often reversible initially and becomes irreversible in time through excretion exopolymeric substances (EPS) which adsorbs to membrane surface causing biofouling (*12*).

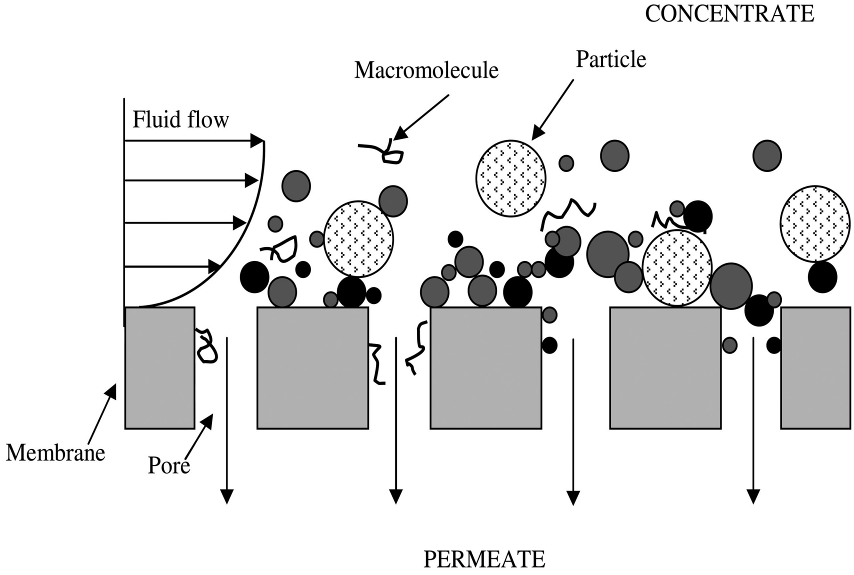

Figure 3. The accumulation of materials on, in, and near a membrane in the presence of a cross-flow. Accumulated materials produce an additional layer of resistance to permeate flux. Some materials are small enough to enter membrane pores where they may be deposited, further reducing the permeate rate.

Downloaded by PENNSYLVANIA STATE UNIV on June 18, 2012 | http://pubs.acs.org
Publication Date (Web): October 31, 2011 | doi: 10.1021/bk-2011-1078.ch010

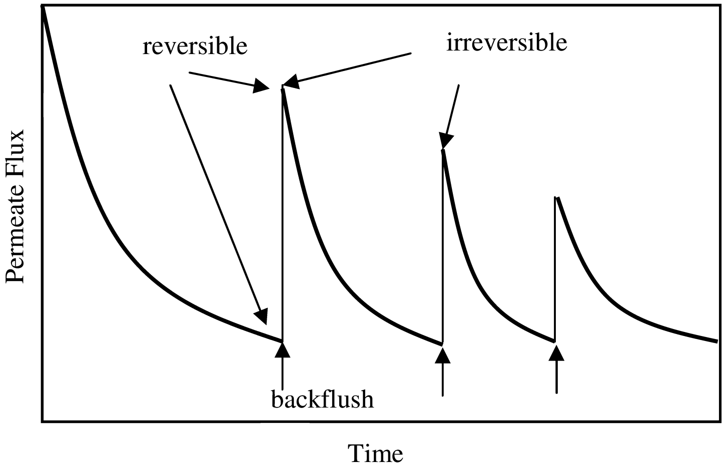

Figure 4. Reduction in permeate flux over time. In this case, periodic cleaning of the membrane by hydraulic backflushing restored a portion of the membrane permeability, but with decreasing efficacy when irreversible fouling occurs. Chemical cleaning may restore a portion of the permeate flux lost to irreversible fouling.

3.4. Fouling Prevention

Various successive approaches such as surface modifications (*13*, *14*), feed water conditioning (*15*) and chemical cleaning (*16*) have been researched to tackle the fouling phenomenon that invariably leads to membrane deterioration. Proper combination of these approaches has been successful in mitigating the fouling process to a modest extent. The study presented here is focused on surface modification of a cellulose acetate ultrafiltration membrane to minimize its fouling. Surface modifications have been widely used in the material- and polymer-based industries over past three decades (*17*). It has the advantage of imparting the desired properties to the surface of interest while keeping the properties of bulk intact. Different innovative physical and chemical surface modification techniques have been introduced by various researchers in the field of polymers (*17*). These techniques include ultraviolet (UV) (*17*), plasma (*13*, *17*), chemical (*14*, *17*) induced free radical graft polymerization, atom transfer radical polymerization (ATRP) (*14*, *18*) and surface irradiation (*19*). These techniques are also frequently used to functionalize wide arrays of commercial polymeric membranes that are available in the market for liquid treatment processes.

3.5. Fouling: Limitations and Functioning

Membrane fouling results in a higher energy use, a higher cleaning frequency and a shorter life span of the membrane. Membrane replacement due to fouling is the single largest source of operating cost when membranes are used in water separation applications (*23*), causing greatest hindrance to the widespread use of membranes. Membrane fouling is mainly attributed to the physiochemical interactions between membrane and contents of the feed solution, resulting in the adsorption of various kinds of organic foulants (*7*, *9*). Some characteristics of the fouling layer data, such as density, thickness and specific resistance could be determined from hydraulic data (*11*), further characterization of the fouling layer generally requires destructive characterization techniques such as atomic force microscopy (AFM) and scanning electron microscopy (SEM). Fouling influences could be felt in industries other than water treatment, such as biotechnology, due to wide spread use of ultrafiltration process in these industries. Ultrafiltration is a kind of membrane-separation, widely used for substance separation, concentration and purification. Due to its wide spread use and application in this project, ultrafiltration membrane fouling is discussed in detail.

Cleaning of the membrane with chemical reagents is a widely used technique to remove the fouling on the membrane surface. K. Kimura et al. (*24*) reported that cleaning agents, such as alkaline (NaOH) and oxidizing reagent (NaoCl), showed good performance in restoring original flux to polysulfone ultrafiltration membranes fouled with polysaccharide-like organic matter with small portions of iron and manganese. S-H. You et al. (*25*) reported reduced flux drop values when a tertiary effluent from industrial park wastewater plant was dosed with ozone likely because of the breakdown of larger organic matter compounds into smaller ones. A. M. M. Sakinah et al. (*26*) reported that alkaline cleaning was 30% more effective compared to acidic cleaning in treating fouling layer caused by various kinds of polysaccharides. St. Pavolva (*27*) reported that cleaning a PAN membrane with 1% formaldehyde solution was more efficient than 0.25% sodium metabisulphite in treating biofouling as well as colloidal fouling of iron and humic acids.

Filtration operating conditions also play major roles in the advent of irreversible fouling on the membrane surface. G. F. Crozes et al. (*28*) reported that irreversible fouling of both hydrophobic and hydrophilic membranes could be controlled by keeping the increase of transmembrane pressure (TMP) below a certain limit. These values were estimated to be 0.85 to 1.0 bar for hydrophilic cellulose derivative membrane and hydrophobic acrylic polymer membrane. They also reported that efficiency of backwashing was decreased with the increase of transmembrane pressure applied in the previous filtration cycle. K. Katsoufidou et al. (*29*) reported the findings of study of evolution of fouling by sodium alginate, a microbial polysaccharide, in ultrafiltration. They reported that irreversible fouling dominated the initial phases of filtration followed by cake formation. With increased calcium addition, reversible cake development became the dominant phenomenon throughout the fouling process. T. Y. Wu et al. (*30*) reported that it was possible to have appropriate control of applied pressure in order to favor fouling that would lead to better rejection of other solutes present in the feed.

The membrane material plays a crucial role in the fouling phenomenon as it governs the physiochemical interactions of the membrane with the foulant matter present in the feed solution. Polymer properties such as hydrophilicity, are very significant in determining the fate of the filtration operation. C. Jonsson et al. (*31*) performed a study in which eight membranes with varying hydrophilicity

Downloaded by PENNSYLVANIA STATE UNIV on June 18, 2012 | http://pubs.acs.org
Publication Date (Web): October 31, 2011 | doi: 10.1021/bk-2011-1078.ch010

In Modern Applications in Membrane Science and Technology; Escobar, I., et al.;
ACS Symposium Series; American Chemical Society: Washington, DC, 2011.

Downloaded by PENNSYLVANIA STATE UNIV on June 18, 2012 | http://pubs.acs.org
Publication Date (Web): October 31, 2011 | doi: 10.1021/bk-2011-1078.ch010

were used to filter octanic acid, a low molecular weight hydrophobic solute. The study showed that octanic acid filtration resulted in marginal reduction in the flux values of hydrophilic membranes, whereas the flux reduction of hydrophobic membranes was very significant. H. Susanto et al. (*32*) reported that hydrophilic and neutral dextrans were able to significantly foul polyether sulfone membranes via adsorption to the surface of the membrane polymer, but not the cellulosic membranes. Likewise, P. J. Evans et al. (*33*) also found that fouling of hydrophilic tea species on more hydrophobic fluoropolymer membrane than on regenerated cellulose membrane. A. W. Zularisam et al. (*34*) described that feed water with relatively hydrophilic NOM exhibited more flux decline than those with higher hydrophobic NOM fractions when filtration occurred using a hydrophobic polysulfone membrane. They also reported that apart from physiochemical interactions, charge interactions between NOM and membrane surfaces also play major roles in membrane fouling. Surface charge of the membrane, ionic strength of the feed solution and hydration radius of the ionic species are the some of the parameters that influence the electrostatic interactions of the membrane.

In a study by I. H. Huisman et al. (*35*), protein-membrane interactions influenced the fouling behavior during the initial stages of filtration but during the later stages, protein-protein interactions dictated the overall performance. Their study also indicated that the structure of the protein fouling layer was strongly dependent on the feed pH values. Open fouling layer structures with high permeability were found below the isoelectric point of the protein. When polyethersulfone membranes were modified with macromolecules, reduction of mean pore size, molecular weight cutoff and humic fouling were observed (*36*). Z-W. Dai et al. (*37*) showed that UV-induced graft polymerization of a ring opening glycomonomer d-gluconamidoethyl methacrylate (GAMA) on a polyacrylonitrile (PAN) membrane resulted in enhanced surface hydrophilicity and inhibition of bovine serum albumin (BSA) adsorption. H. Susanto et al. (*38*) reported synergetic effects between polysaccharide and protein with respect to forming a mixed fouling layer with stronger reduction of flux than for the individual solutes under the same conditions. Lastly, another study described ultrafiltration experiments conducted with hydrophobic, transphobic and hydrophilic fractions to study the membrane fouling (*39*). The results indicated high removal of hydrophobic fractions due to the relatively high molecular weight of organic matter and interactions with membrane surface. Flux decline from hydrophobic fractions was also high compared to transphilic and hydrophilic fractions.

4. Summary

Membrane technology is widely accepted as a means of producing high quality water from surface water, well water, brackish water and seawater for drinking water treatment applications. Membrane technology is also used in industrial processes and in industrial wastewater treatment, and recently membrane technology has moved into the area of treating secondary and tertiary municipal wastewater and oil field produced water. In many cases, one membrane process is followed by another membrane process with the purpose of producing water of increasing purity and quality for various purposes. One type of membrane may thus enhance the function of another to meet goals ranging from disposal of wastewater to production of drinking water from different feed water sources like industrial wastewater, surface water, sea water, brackish water etc. Therefore, membrane technology offers the possibility of managing the total water resources in a region, which is of special interest in geographical areas where the natural water resources are scarce.

References

1. Kirby, A. http://news.bbc.co.uk/2/hi/science/nature/3747724.stm.
2. *Membrane Technology* **2007**, *1*, 9–11.
3. Cheryan, M. *Ultrafiltration Handbook*; Technomic Publishing: Lancaster, PA, 1986.
4. Metzger, U.; Le-Clech, P.; Stuetz, R. M.; Frimmel, F. H.; Chen, V. *J. Membr. Sci.* **2007**, *301*, 180–189.
5. Wilf, M.; Ricklis, J. *Desalination* **1983**, *47*, 209–219.
6. Gilron, J.; Waisman, M.; Daltrophe, N.; Pomerantz, N.; Milman, M.; Ladizhansky, I.; Korin, E. *Desalination* **2006**, *199*, 29–30.
7. Escobar, I. C.; Hoek, E.; Gabelich, C.; DiGiano, F.; Le Gouellec, Y.; Berube, P.; Howe, K.; Allen, J.; Atasi, K.; Benjjamin, M.; Brandhuber, P.; Brant, J.; Chang, Y.; Chapman, M.; Childress, A.; Conlon, W.; Cooke, T.; Crossley, I.; Crozes, G.; Huck, P.; Kommineni, S.; Jacangelo, J.; Karimi, A.; Kim, J.; Lawler, D.; Li, Q.; Schiedeman, L.; Sethi, S.; Tobiason, J.; Tseng, T.; Veerapaneni, S.; Zander, A. *J. - Am. Water Works Assoc.* **2005**, *97* (8), 79–89.
8. Rebhun, M.; Manka, J. *Environ. Sci. Technol.* **1971**, *5*, 606–609.
9. Cho, J.; Amy, G.; Pellegrino, J. *Water Res.* **1999**, *33*, 2517–2526.
10. Gristina, A. G. *Science* **1987**, *237*, 1588–1597.
11. Ye, Y.; Le Clech, P.; Chen, V.; Fane, A. G. *J. Membr. Sci.* **2005**, *264*, 190–199.
12. Bos, R.; Van der Mei, H. C.; Busscher, H. J. *FEMS Microbiol. Rev.* **1999**, *23*, 179–230.
13. Zhou, M.; Liu, H.; Kilduff, J. E.; Langer, R.; Anderson, D. G.; Belfort, G. *Environ. Sci. Technol.* **2009**, *43*, 3865–3871.
14. Li, P-F.; Xie, R.; Jiang, J-C.; Meng, T.; Yang, M.; Ju, X-J.; Yang, L.; Chu, L-Y. *J. Membr. Sci.* **2009**, *337*, 310–317.
15. Shon, H. K.; Kim, S. H.; Vigneswaran, S.; Ben Aim, R.; Lee, S.; Cho, J. *Desalination* **2009**, *238*, 10–21.
16. Maartens, A.; Jacobs, E. P.; Swart, P. *J. Membr. Sci.* **2002**, *209*, 81–92.
17. Kato, K.; Uchida, E.; Kang, E-T.; Uyama, Y.; Ikada, Y. *Progr. Polym. Sci.* **2003**, *28*, 209–259.
18. Gorey, C.; Escobar, I. C.; Gruden, C. L.; Cai, G. *Desalination* **2009**, *248*, 99–105.
19. Chennamsetty, R.; Escobar, I. C. *Langmuir* **2008**, *24*, 5569–5579.

Downloaded by PENNSYLVANIA STATE UNIV on June 18, 2012 | http://pubs.acs.org
Publication Date (Web): October 31, 2011 | doi: 10.1021/bk-2011-1078.ch010

Downloaded by PENNSYLVANIA STATE UNIV on June 18, 2012 | http://pubs.acs.org
Publication Date (Web): October 31, 2011 | doi: 10.1021/bk-2011-1078.ch010

20. Loeb, S.; and Sourirajan, S. (1961). Sea water demineralization by means of a semi permeable membrane. Dept of Engineering, University of California at Los Angeles, Report 60-60.
21. Matsuyama, H.; Teramoto, M.; Uesaka, T. *J. Membr. Sci.* **1997**, *135*, 271–288.
22. Chennamsetty, R. Evolution of two polymeric nanofiltration membranes following ion beam irradiation. Doctoral dissertation. University of Toledo, Toledo, OH, 2007.
23. Glueckstern, P.; Priel, M.; Wilf, M. *Desalination* **2002**, *147*, 55–62.
24. Kimura, K.; Hane, Y.; Watanabe, Y.; Gary, A.; Ohkuma, N. *Water Res.* **2004**, *38*, 3431–3441.
25. You, S-H.; Tseng, D-H.; Hsu, W-C. *Desalination* **2007**, *202*, 224–230.
26. Sakinah, A. M. M.; Ismail, A. F.; Md Illias, R.; Hasan, O. *Desalination* **2007**, *207*, 227–242.
27. Pavlova, St. *Desalination* **2005**, *172*, 267–270.
28. Crozes, G. F.; Jacangelo, J. G.; Anseleme, C.; Laine, J. M. *J. Membr. Sci.* **1997**, *124*, 63–76.
29. Katsoufidou, K.; Yiantsios, S. G.; Karabelas, A. J. *J. Membr. Sci.* **2007**, *300*, 137–146.
30. Wu, T. Y.; Mohammad, A. W.; Jahim, J. Md.; Anuar, N. *Biochem. Eng. J.* **2007**, *35*, 309–317.
31. Jonsson, C.; Jonsson, A-S. *J. Membr. Sci.* **1995**, *108*, 79–87.
32. Susanto, H.; Ulbricht, M. *J. Membr. Sci.* **2005**, *266*, 132–142.
33. Evans, P. J.; Bird, M. R. *Food Bioprod. Process.* **2006**, *84*, 292–301.
34. Zularisam, A. W.; Ismail, A. F.; Salim, M. R.; Sakinah, M.; Hiroaki, O. *J. Membr. Sci.* **2007**, *299*, 97–113.
35. Huisman, I. H.; Pradanos, P.; Hernandez, A. *J. Membr. Sci.* **2000**, *179*, 79–90.
36. Zhang, L.; Chowdhury, G.; Feng, C.; Matsuura, T.; Narbaitz, R. *J. Appl. Polym. Sci.* **2003**, *88*, 3132–3138.
37. Dai, Z-W.; Wan, L-S.; Xu, Z-K. *J. Membr. Sci.* **2008**, *325*, 479–485.
38. Susanto, H.; Arafat, H.; Elisabeth, E. M. L.; Ulbricht, M. *Sep. Purif. Technol.* **2008**, *63*, 558–565.
39. Shon, H. K.; Vigneswaran, S.; Kim, I. S.; Cho, J.; Ngo, H. H. *J. Membr. Sci.* **2006**, *278*, 232–238.

Downloaded by STANFORD UNIV GREEN LIBR on June 19, 2012 | http://pubs.acs.org
Publication Date (Web): October 31, 2011 | doi: 10.1021/bk-2011-1078.ch012

Chapter 12

A Fourier Transform Infrared Spectroscopic Based Biofilm Characterization Technique and Its Use to Show the Effect of Copper-Charged Polypropylene Feed Spacers in Biofouling Control

Richard Hausman* **and Isabel C. Escobar**

Chemical and Environmental Engineering, The University of Toledo,
2801 W. Bancroft Street, Toledo, OH 43606-3390
***E-mail: richard.hausman@utoledo.edu. Phone: 419-367-6540.**

Biofouling of membranes used in high-pressure applications has been and will continue to be a problem that must be addressed in industry as well as academia. Many of these applications use membranes in a spiral wound configuration that contains a feed spacer. When anti-biofouling properties were imparted to these feed spacers, through copper chelation, slower rates of biofouling were observed. This study investigated the effects of this modification on flux decline during filtration of a synthetic feed water that contained a high concentration of *Pseudomonas fluorescens*. Furthermore, some traditional and one novel techniques were implemented to autopsy the membranes after filtration. The novel technique was the use of Fourier Transform Infrared (FTIR) to quantitatively compare the concentration of biofilm components on membranes fouled using both virgin and copper-modified feed spacers.

1. Introduction

Biofouling is the accumulation and growth of microorganisms onto the membrane surface and on the feed spacer. Feed spacers are present between the envelopes in spiral wound reverse osmosis membrane modules. They provide mechanical strength to the membrane, as well as flow channels. This accumulation of microorganisms, along with the presence of nutrients that are common in many membrane applications, forms biofilms. In biofilms, organisms are embedded in a matrix of microbial origin, consisting of extracellular polymeric substances (EPS). Polysaccharides are known to make up the largest portion of EPS, and are related to cell adhesion during initial stages of biofilm formation (*1*). These matrices are often very complex and difficult to remove. For this reason, much effort goes into the prevention of biofilm growth, rather than its removal. This prevention is usually attempted through the use of pretreatments, nutrient removal, maximizing shear forces at the membrane surface, and back-flushing. The problem with pretreatment methods is that even if 99.9% of microorganisms are removed, those left remaining can proliferate and cause irreversible biofouling. Furthermore, biocides, such as free or combine chlorine, can only be used with certain chlorine-resistant membranes, and since biofouling is such a common problem, this has its downfalls.

The fouling of membranes by chemicals and microbes that are rejected continues to demand considerable attention from the research community (*2*). Membrane replacement due to fouling is the single largest operating cost when membranes are used in water separation applications (*2*) and, thus, the greatest hindrance to the widespread use of membranes. Additionally, recent studies have shown that biofouling starts at the membrane/feedspacer interface suggesting that biofouling might be a feedspacer problem (*3*). Because of this, a functionalized feed spacer, containing a spacer arm (GMA) with metal chelating ligands (IDA) to which copper is chelated as described in our previous studies (*4*), was developed. It is believed that the antimicrobial property, as well as the increased hydrophilicity, of the Cu-charged feed spacers aided in hindering cell adhesion and, consequently, biofilm formation and biofouling. Filtration studies in increased biofouling conditions have been performed and resulted in significantly lower flux decline when modified feed spacers were used (*5*). In previous studies, FTIR was used qualitatively to provide information about the nature of the biofilm present on fouled membranes. Further characterization studies have been performed, and the results are presented here. The aim of this study was to develop the FTIR technique further so that quantitative information could be obtained.

Downloaded by STANFORD UNIV GREEN LIBR on June 19, 2012 | http://pubs.acs.org
Publication Date (Web): October 31, 2011 | doi: 10.1021/bk-2011-1078.ch012

2. Experimental Section

2.1. Materials

Polypropylene sheets was obtained from Professional Plastics (Houston, TX). Glycidyl methacrylate (GMA), benzoyl peroxide, toluene, acetone, copper sulfate, were purchased from Fisher Scientific (Waltham, MA) and used as received. Sodium iminodiacetate disbasic (IDA) hydrate 98% was purchased from Aldrich Chemistry (St. Louis, MO) and used as received. PP feed spacers were provided by DelStar Technologies (Middletown, DE).

The membranes used were TFC-S polyamide membranes that are commercially available nanofiltration composite membranes manufactured by Koch Membranes (San Diego, CA). The polyamide membrane, described in greater detail in Chennamsetty and Escobar (*6*), consists of a polysulfone support layer covered by aromatic polyamide selective layer. Its functional groups are carboxylate/carboxylic acid. The film layer is approximately 1,000-2,000 angstroms thick and the molecular weight cutoff is around 200 - 300 Daltons (*7*, *8*). The membrane has a slight negative charge with a contact angle of 55^{o} (*9*). The typical operating pressure is 5.5 bar, with the maximum operating pressure being 24 bar. The maximum operating temperature is 45°C and the allowable pH range is 4-11. Chlorine tolerance is low, with the maximum continuous free chlorine concentration being less than 0.1 mg/l.

Downloaded by STANFORD UNIV GREEN LIBR on June 19, 2012 | http://pubs.acs.org
Publication Date (Web): October 31, 2011 | doi: 10.1021/bk-2011-1078.ch012

2.2. Preparation and Characterization of Cu(II) Charged PP-Graft-GMA-IDA

Polypropylene feedspacers were grafted with poly-GMA. IDA was then covalently attached to the poly-GMA subunits and then charged with Cu(II). A detailed description of the preparation and characterization of the polypropylene feedspacers can be found in previous studies (*4*, *5*).

2.3. Performance of Cu-Charged Feedspacer During Crossflow Filtration

The membrane was housed in a SEPA CF cross-flow filtration unit (Osmonics, Minneatonka, MN). The filtration unit was constructed out of 316 stainless steel and rated for an operating pressure up to 69 bar (1000 psi). The test unit was sealed by applying adequate pressure via a hand pump (P-142, Enerpac, Milwaukee, WI), which actuated a piston on the SEPA CF, sealing the membrane within the membrane cell. The feed stream was delivered by a motor (Baldor Electric Company, Ft. Smith, AR and Dayton Electric Manufacturing Co., Niles, IL) and M-03 Hydracell pump (Wanner Engineering, Inc., Minneapolis, MN) assembly. Flow valves controlled permeate and retenate (also called concentrate) flow and the pressure acting on the membrane in the test unit. A schematic of this filtration setup can be seen in Figure 1.

Cu-charged and unmodified spacers were tested in full recycle mode (where tubes for the pump inlet, permeate outlet, and concentrate outlet are all placed into one reservoir) with the use of identical nanofiltration TFC-S membranes. Filtration experiments were conducted using a 40L reservoir filled with municipal tap water which was dechlorinated with sodium thiosulfate and supplemented with 100mg/L of acetate and 100mg/L of glucose16 hours prior to filtration. Also, at this time (t = -16 hr) *pseudomonas fluorescens* Migula (#49642) cells, which were ordered from American Type Culture Collection (ATCC) and freshly cultured at 34 °C on R2A agar (BD, Franklin Lakes, NJ), were added to the reservoir so that the initial cell concentration was 10^{6} cells/mL. Filtration was carried out at 34°C and 100psi. Since cells were cultured at 34°C and were shown to be viable, this temperature was used as to increase the cellular growth rate, resulting in an environment more prone to biofouling. As shown in previous studies, *pseudomonas fluorescens* cells are viable up to 35°C (*10*). Furthermore, each membrane was subjected to 8 hours of precompaction using DI water before filtration. The fluxes of membranes using both Cu-charged and unmodified feed spacers were measured throughout four filtration runs each: one four-hour run, one 24-hour run and two 48-hour runs.

2.4. Fouled Membrane Autopsies

2.4.1. Live/Dead Cell Counts

Again, samples of each membrane, one used with the unmodified spacer and one used with the Cu-charged spacer, were taken from identical locations on the membrane surface after the filtration period. Cells were detached from the samples using a Stomacher 400 Circulator (Seward Ltd, London, England). Propidium iodide (Roche Diagnostics GmbH, Mannheim, Germany), a red fluorescent integrity stain, was used to indicate cells with damaged membranes that emits red or orange color. Samples were counterstained with PicoGreen®, (PG; P-7859; Molecular Probes, Inc., Eugene, OR) dsDNA, which is a specific stain for assessment cells with intact membranes, that emits green color. They were then imaged and counted using an Olympus BX51 fluorescent microscope and an Olympus DP-70 digital camera. Triplets of each sample were taken, counting ten fields each time.

2.4.2. SEM Imaging of Fouled Membranes

Samples of each membrane, one used with the unmodified/virgin spacer and one used with the Cu-charged spacer, were taken from identical locations on the membrane surface after the filtration period. These membranes were vacuumed dried at ambient temperature to remove all water and were then coated using a gold-palladium target for 30 seconds to aid in electron imaging. Scanning electron microscopy (SEM) imaging (Hitachi S-4800 High Resolution Scanning Electron Microscope) of membrane samples was performed.

2.4.3. FTIR Spectroscopy of Fouled Membranes

FTIR analysis, using an attenuated total reflection Fourier transform infrared spectrometer (ATR-FTIR, Digilab UMA 600 FT-IT microscope with a Pike HATR adapter and an Excalibur FTS 400 spectrometer, Ge crystal with a refractive index of 4.0 and a long wave length cut-off of 780cm^{-1}), was performed on an unfouled membrane, as well as membranes fouled using virgin and modified feed spacers in four locations on each membrane and averaged. The resulting spectra can be seen in Figure 2. To determine the depth of penetration during ATR-FTIR, the following equation was used (*11*), where DP is the depth of penetration of the evanescent IR wave, Ø is the angle of incidence (45°), λ is the wavelength (μm), n_1 is the refractive index (RI) of the Ge Crystal (4.0), and n_2 is the RI of sample being analyzed in this case polyamide with a RI of 1.56 (*12*):

Downloaded by STANFORD UNIV GREEN LIBR on June 19, 2012 | http://pubs.acs.org
Publication Date (Web): October 31, 2011 | doi: 10.1021/bk-2011-1078.ch012

$$\mathbf{DP} = \frac{\lambda}{2\pi n_1\left[\sin^2\emptyset - \left(\frac{n_2}{n_1}\right)^2\right]^{\frac{1}{2}}}$$

(Equation 1)

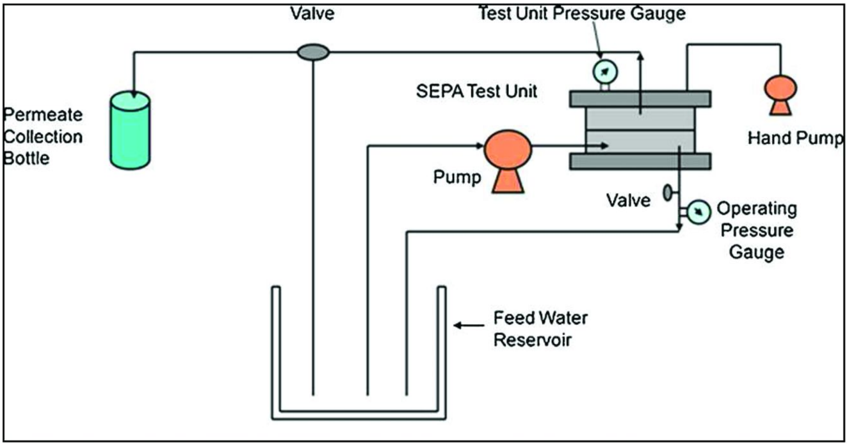
Valve
Test Unit Pressure Gauge
SEPA Test Unit
Permeate Collection Bottle
Hand Pump
Pump
Valve
Operating Pressure Gauge
Feed Water Reservoir

Figure 1. Schematic diagram showing the cross-flow filtration apparatus in full recycle mode.

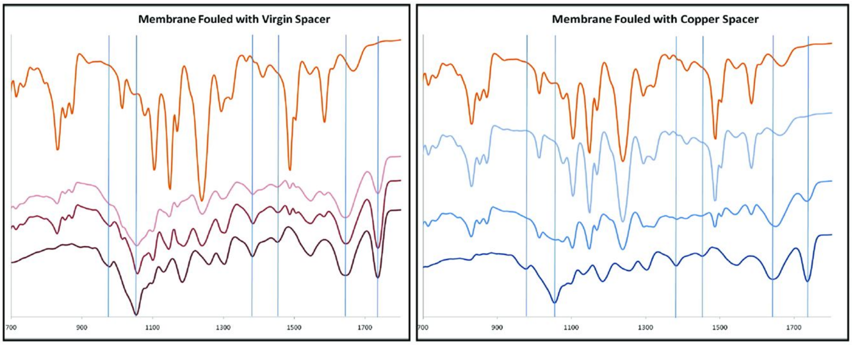

Figure 2. FTIR Spectra, in descending order, of an unfouled membrane, and membranes after 4, 24 and 48 hours of filtration. Spectra from membranes using a virgin spacer appear on the left and those using a modified membrane are on the right. Some notable peaks from the biofilm have been pointed out.

Downloaded by STANFORD UNIV GREEN LIBR on June 19, 2012 | http://pubs.acs.org
Publication Date (Web): October 31, 2011 | doi: 10.1021/bk-2011-1078.ch012

Downloaded by STANFORD UNIV GREEN LIBR on June 19, 2012 | http://pubs.acs.org
Publication Date (Web): October 31, 2011 | doi: 10.1021/bk-2011-1078.ch012

Table I. Relevant Biomolecules Present in *Pseudomonas fluorescens* Biofilms and Their Corresponding Wavenumber Locations

Wavenumber (cm^{-1})	***Associated Biomolecule***	***References***
900-1200	Polysaccharides	(*11*, *14*, *16*, *17*)
1400	Amino acids, fatty acid chains	(*11*)
1468;1455	Lipids/Lipopolysaccharides	(*11*, *13*, *17*)
1627-1693	Proteins (Amide I)	(*11*, *13–15*),
1736	Esters from lipids	(*11*, *13*, *16*, *17*)

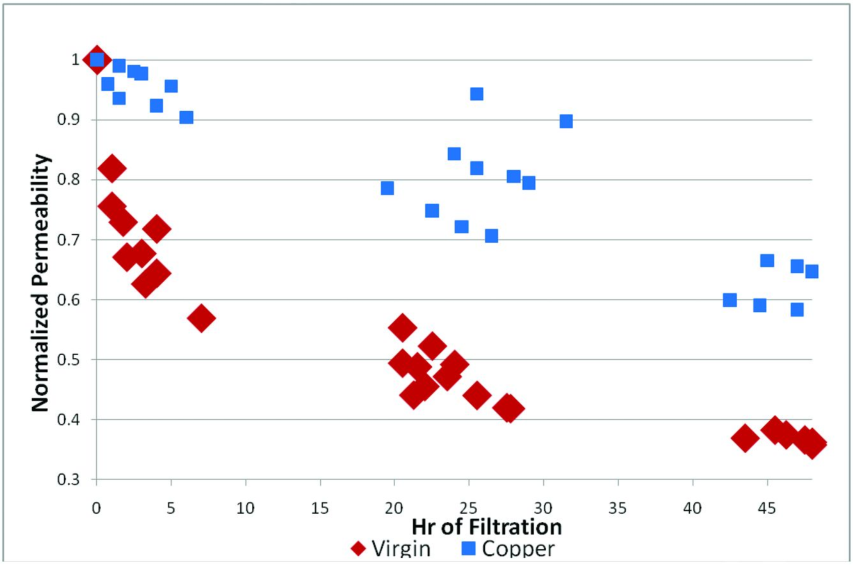

Figure 3. Normalized permeability vs. time of filtration of identical membranes using both virgin and modified feed spacers during cross flow filtration in increased biofouling conditions using Pseudomonas fluorescens cells.

This equation is valid when the refractive index of the sample is uniform throughout the depth of penetration. If one considers a case where there are two layers in the path of the IR penetration, as in the case of a biofouled membrane (biofilm and membrane layers), this equation must be altered to the following, where n_3 is the refractive index of the biofilm layer, t_b is the thickness of the biofilm layer which is seen by the IR, and t_m is the thickness of the membrane, which is seen by the IR.

Downloaded by STANFORD UNIV GREEN LIBR on June 19, 2012 | http://pubs.acs.org
Publication Date (Web): October 31, 2011 | doi: 10.1021/bk-2011-1078.ch012

$$\mathbf{DP} = \frac{\lambda}{2\pi n_1 \left[\sin^2\phi - \left(\frac{n_2\left(\frac{t_m}{\mathbf{DP}}\right) + n_3\left(\frac{t_b}{DP}\right)}{n_1}\right)^2\right]^{\frac{1}{2}}}$$

(Equation 2)

To determine t_m an FTIR spectra of an unfouled membrane must be acquired and a prominent peak that is characteristic of the membrane, but does not appear in the biofilm, is located. The peak at 1238cm^{-1} (8.08μm) was identified as such, and the area under it was determined. Once a biofilm layer of thickness t_b is accumulated on the membrane, the area under this peak decreases. The area under the peak of the fouled membrane is then divided by the area of the initial membrane, and the resulting value is multiplied by the DP calculated using the unfouled membrane to determine t_m. This is summed up in Equation 3, where A_1 is the area under the characteristic membrane peak of the unfouled membrane and A_2 is that of the fouled membrane.

$$t_m = \frac{A_2}{A_1} \times \mathbf{DP}$$

(Equation 3)

DP can simply substituted with (t_b + t_m) in Equation 2, since the depth of penetration through the two-component system is obviously the sum of the thickness of penetration through both. From literature, n_3, the refractive index of the biofilm, is 1.38 (*11*). The values of every variable except tb are now known so it can be determined.

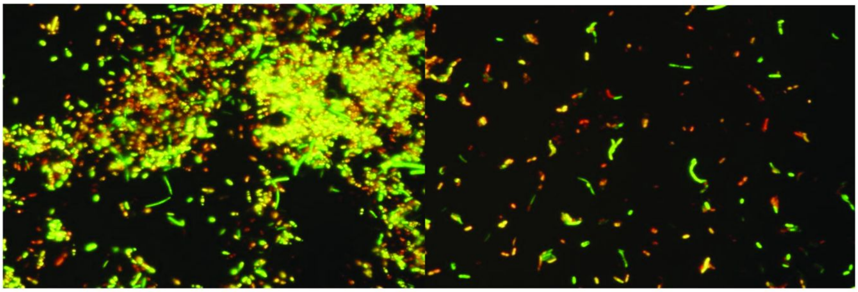

Figure 4. Cells removed from membranes fouled after 48 hours of filtration with a virgin feed spacer (left) and a modified feed spacer (right). The cells were stained with Picogreen and propidium iodide.

Downloaded by STANFORD UNIV GREEN LIBR on June 19, 2012 | http://pubs.acs.org
Publication Date (Web): October 31, 2011 | doi: 10.1021/bk-2011-1078.ch012

Once the thickness of the biofilm has been determined, information about the concentration of components in the biofilms can be investigated. The FTIR spectra of *Pseudomonas fluorescens* biofilms have been studied (*11*), and the locations of peaks for different components are known. A list of these components and their locations are shown in Table I. For the peaks on the biofilm that do not interfere with peaks from the membrane, the area under a peak of interest can be determined by integration. Varian Resolutions Pro Version 4.1.0.101 was used to integrate under the peaks of interest. For both the characteristic membrane as well as the polysaccharide peaks, fixed upper and lower bounds were used in order to insure an accurate comparison between the membrane samples being analyzed. For the characteristic membrane peak, the integration was performed between 1195 cm^{-1} and 1272 cm^{-1}. For the polysaccharide peaks integration was performed between 950 cm^{-1} and 1120 cm^{-1}. This area is then divided by the thickness of the biofilm, t_b, on the membranes to get a concentration with units (amount/μL). The unit in the numerator is not known since extinction coefficients are unknown, and therefore only *relative* quantitative information can currently be gained from this technique; that is, the concentration of a species in a biofilm on a membrane used with a modified spacer versus that fouled with virgin spacer. Since Beer-Lambert's law states that concentration is directly proportional to absorbance, much insight about the difference in biofilm formation when using a copper-charged feed spacer can still be obtained. To determine the area under biofilm component peaks which do overlap peaks coming from the unfouled membrane, the absorption coming from the membrane in the specified region must be subtracted. To do this, the area of this region is determined from the spectrum of the unfouled membrane, multiplied by t_m/DP, and then subtracted from the area integrated under the same region on the fouled membrane.

3. Results and Discussion

3.1. Performance of Cu-Charged Feed Spacer during Cross-Flow Filtration

Permeate flux was measured throughout one four-hour run, one 24-hour run and two 48-hour runs, and normalized to the initial permeability values, which were 4.40 ± 0.40 (L/m^2 hr bar) and 4.68 ± 0.56 (L/m^2 hr bar) for the case of the copper-charged and modified feed spacers, respectively, after precompaction under a pressure of 6.89 bar (Figure 3). As expected, the flux declined significantly less in all cases with the modified feed spacer. This supports trends seen in earlier studies (*5*). Interestingly though, filtration experiments with unmodified spacers exhibited much more instantaneous flux declines in the first four to ten hours, possibly due to cellular attachment coming from EPS secretion. This was investigated further.

Downloaded by STANFORD UNIV GREEN LIBR on June 19, 2012 | http://pubs.acs.org
Publication Date (Web): October 31, 2011 | doi: 10.1021/bk-2011-1078.ch012

3.2. Live/Dead Cell Counts

Following the filtration runs, cells were detached from the membrane, stained with either PI or pico-green and imaged using a fluorescent microscope. An example of the images can be seen in Figure 4. While this method was effective for measuring live and dead cells detached from the membrane fouled with the modified spacers, it was not capable of counting cells detached from the membrane fouled with the virgin spacers because of the high number of cells. Regardless of how diluted the samples to be stained were prepared, clumps of cells always appeared in the images even at early stages in the case of the virgin spacers. As can be seen in Figure 4, it qualitatively appeared that there was a higher concentration of live cells in all images taken of cells attached from the membranes fouled with virgin spacers. These results also pointed to high levels of EPS, resulting in cell "clumps", on the membranes fouled with virgin spacers. It also showed that a different method should be used for a quantitative comparison of the membranes fouled with different spacers.

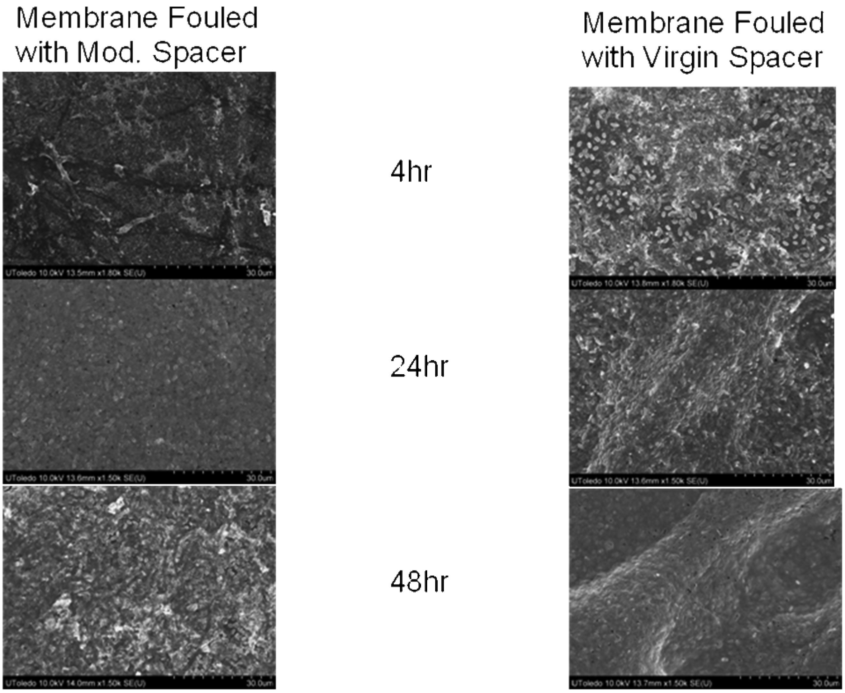
Membrane Fouled with Mod. Spacer
Membrane Fouled with Virgin Spacer
4hr
24hr
48hr
UToledo 10.0kV 13.5mm x1.80k SE(U) 30.0um
UToledo 10.0kV 13.6mm x1.80k SE(U) 30.0um
UToledo 10.0kV 13.6mm x1.50k SE(U) 30.0um
UToledo 10.0kV 13.6mm x1.50k SE(U) 30.0um
UToledo 10.0kV 14.0mm x1.50k SE(U) 30.0um
UToledo 10.0kV 13.7mm x1.50k SE(U) 30.0um

Figure 5. SEM images of membranes fouled using virgin spaces (right) and modified spacers (left) after 4 hr, 24 hr, and 48 hr.

3.3. SEM Imaging of Fouled Membranes

To visualize microbial attachment, SEM images of membranes fouled using both modified and virgin spacers were taken. For this, the membranes, which were fouled during the four-hour, 24-hour and one 48-hour filtration experiments were vacuum dried overnight, coated with gold-palladium and analyzed (Figure 5). Areas that were visually more fouled were chosen since the purpose of the imaging was to understand the mechanisms of fouling rather than any quantitative data collection, as this technique is largely qualitative by nature. The membrane fouled with the virgin spacer after four hours showed significant cell accumulation. After 24 hours, a biofilm covered the surface entirely, and a small amount of contour can see seen in the biofilm. After 48 hours, the biofilm looked similar to what it did at 24 hours but the contour was much greater, indicating that the thickness of the membrane may be greater. The membrane fouled with the modified spacer shows little or no cellular attachment after four hours, slightly more at 24 hours, and, at 48 hours, an image similar to the one taken from the membrane fouled with the virgin spacer after four hours was observed. When the flux from the membrane used with the virgin spacer after four hours is compared to that of the membrane used with the modified spacer at 48 hours, there was agreement. Still, this autopsy is strictly qualitative and the need for something more quantitative remains.

Downloaded by STANFORD UNIV GREEN LIBR on June 19, 2012 | http://pubs.acs.org
Publication Date (Web): October 31, 2011 | doi: 10.1021/bk-2011-1078.ch012

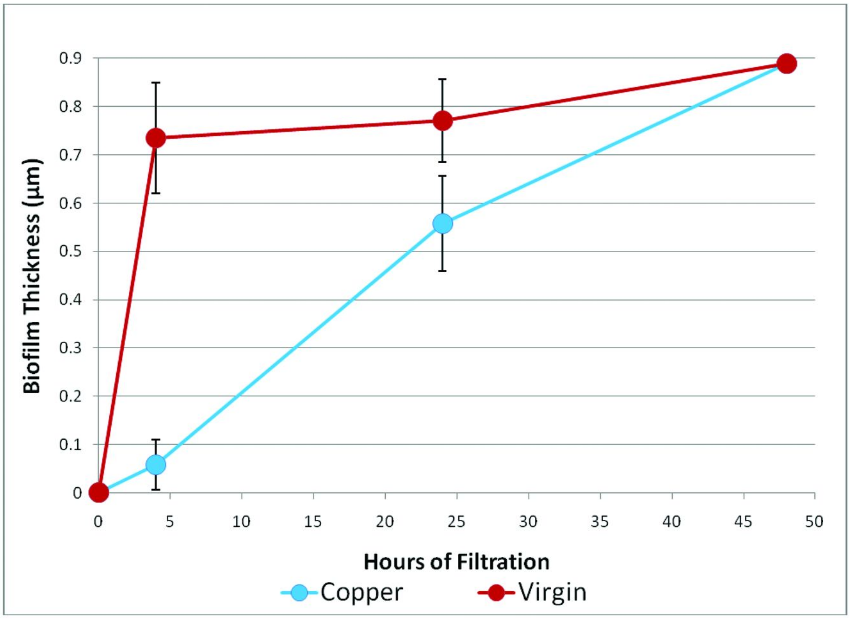

Figure 6. Biofilm thickness was plotted vs. hour of filtration. It should be noted that in both cases, after 48 hours of filtration the biofilm thickness was greater than or equal to the maximum thickness that can be measured with this technique (DP = 0.889 µm).

Downloaded by STANFORD UNIV GREEN LIBR on June 19, 2012 | http://pubs.acs.org
Publication Date (Web): October 31, 2011 | doi: 10.1021/bk-2011-1078.ch012

3.4. FTIR Spectroscopy of Fouled Membranes

This novel method has allowed for monitoring of biofilm thickness versus filtration time and has made it possible to compare biofilm component concentrations on membranes fouled with virgin and modified spacers versus time. As can be seen in Figure 6, the biofilm thickness appeared to grow to the maximum measureable level (that is, when DP = t_b) at a faster rate when the virgin spacers were used. When the polysaccharide (region from 950cm^{-1} to 1120cm^{-1}) concentration was compared between the virgin and modified conditions (Figure 7), a higher concentration after four hours of filtration with the virgin spacer was observed. It appears that the rate of increase in the polysaccharide concentration is increasing with time for the case of the copper-charged feed spacer, and after the initial four hours is even faster than that of the virgin membrane. This may be because the concentration of polysaccharide is significantly higher during the attachment phase of the biofilm formation. Since this phase takes place rapidly in the case of the virgin membrane, the concentration of polysaccharide in this case appears to be increasing very little after the first four hours, if at all. In the case of the copper-charged feed spacer, the attachment phase occurs more slowly and therefore the polysaccharide concentration continues to increase significantly after the first four hours. Previous studies which were conducted for ~300 hours hinted at a similar hypothesis; the copper-charged spacers are delaying the initial attachment of cells which ultimately slows biofilm development (*5*).

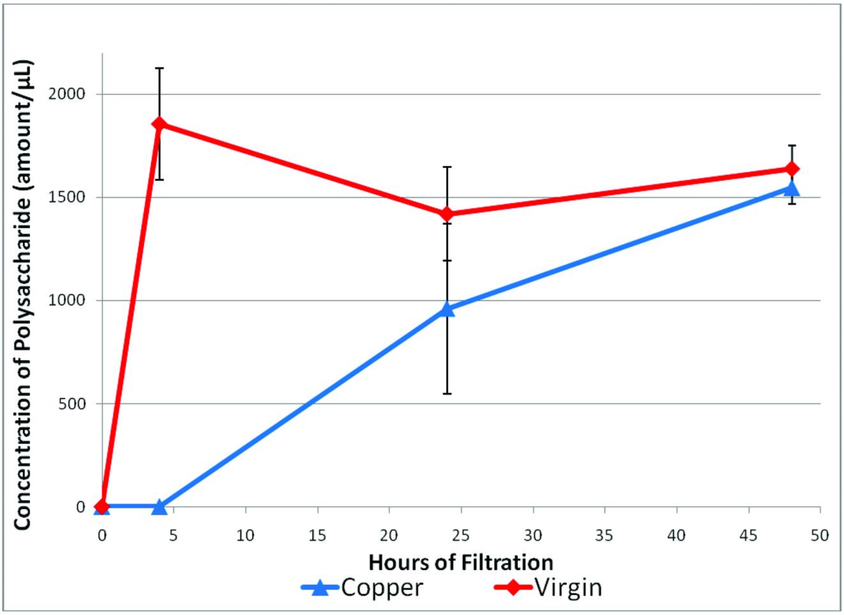

Figure 7. The concentration of polysaccharides in the biofilms was plotted vs. filtration time. It should be noted that since the biofilm thickness was greater than or equal to the DP at 48 hr, the concentration at this time is only that of the top 0.889μm of the biofilm.

This technique allows for a quantitative verification of the qualitative trends observed by the previously described characterization techniques, and it indicates that the copper modified feed spacers affected the cellular attachment of the bacteria by hindering the EPS (polysaccharide) secretion. As our previous studies have mentioned, during the initial attachment, cell activity is higher so more EPS is produced (*5*). While the exact mechanism is not known, it is hypothesized that the copper-charged feed spacers may be inhibiting this production of EPS by the cells which come in contact with the feed spacers through interactions with transmembrane proteins. This decreased cellular attachment ultimately resulted in lower flux decline observed (Figure 3).

4. Conclusions

The goal of this project was to show that copper-charged polypropylene feed spacers could be used to control biofouling and to obtain a better understand behind the mechanism by which the modified feed spacers were able to control biofouling. As expected, the use of the copper-charged feed spacer led to a consistently lower rate of flux decline during filtration. This increased resistance to fouling, and more specifically, biofouling, was hypothesized to be attributed to the hindrance of cell adhesion due to a decrease in the secretion of EPS specifically polysaccharide, since polysaccharides are known to make up the largest portion of EPS, and are related to cell adhesion during initial stages of biofilm formation (*1*). Traditional methods such as live/dead cell counts and SEM imaging pointed to this hypothesis but lacked the ability to quantitatively relate the levels of polysaccharides on the membranes fouled with virgin and modified spacers. Because of this, a novel FTIR based technique was implemented, and while it is limited to only analyzing a biofilm, or layer of biofilm, with a thickness equal to that of the depth of penetration (DP) of the IR evanescent wave, it resulted in a quantitative verification of this hypothesis.

Acknowledgments

The authors would like to acknowledge the source of funding, NSF SGER 0714539 and CBET 0754387, as well as Drs. Amr Zaky and Maria Coleman. Additionally, Del-Star Technologies and Koch Membranes are thanked for providing feed spacers and membranes. The copper-charged polypropylene technology is covered under a United States Patent, WO2009152217-A1 (2009)

References

1. Tsuneda, S.; Aikawa, H.; Hayashi, H.; Yuasa, A.; Hirata, A. *FEMS Microbiol. Lett.* **2003**, *223*, 287–292.
2. Escobar, I.; et al. *J. Am. Water Works Assoc.* **2005**, *97*, 79–89.
3. Cornelissen, E. R.; Vrouwenvelder, J. S.; Heijman, S. G. J.; Viallefont, X. D.; Van der Kooij, D.; Wessels, L. P. *J. Membr. Sci.* **2007**, *287*, 94–101.

Downloaded by STANFORD UNIV GREEN LIBR on June 19, 2012 | http://pubs.acs.org
Publication Date (Web): October 31, 2011 | doi: 10.1021/bk-2011-1078.ch012

4. Hausman, R. T.; Gullinkala, T.; Escobar, I. C. *J. App. Polym. Sci* **2009**, *114*, 3068–3073.
5. Hausman, R.; Gullinkala, T.; Escobar, I. C. *J. Membr. Sci.* **2010**, *358*, 114–121.
6. Chennamsetty, R.; Escobar, I. C *Sep. Sci. Technol.* **2008**, *43*, 4009–4029.
7. Koyuncu, I. *Desalination* **2003**, *155*, 265–275.
8. Liikanen, R.; Miettinen, I.; Laukkanen, R. *Water Res.* **2003**, *37*, 864–872.
9. Norberg, D.; Hong, S.; Taylor, J.; Zhao, Y. *Desalination* **2006**, *202*, 45–52.
10. Lynch, W. *J. Bacteriol.* **1980**, *143* (1), 338–342.
11. Smith-Palmer, T. *Biofilms* **2003**, *1* (3), 157–163.
12. El-Bakary, M. *Opt. Laser Technol.* **2004**, *36* (6), 507–513.
13. Serra, D. *Anal. Bioanal. Chem.* **2007**, *387* (5), 1759–1767.
14. Cheung, H. Y. *J. Appl. Microbiol.* **2007**, *102* (3), 701–710.
15. Parikh, S. J. *Geomicrobiol. J.* **2005**, *22* (5), 207–218.
16. Osiro, D. *FEMS Microbiol. Lett.* **2004**, *236* (2), 313–318.
17. Schmitt, J.; White, D. C.; Flemming, H.-C.; Nivens, D. *Water Sci. Technol.* **1995**, *32* (8), 149–155.

Downloaded by STANFORD UNIV GREEN LIBR on June 19, 2012 | http://pubs.acs.org
Publication Date (Web): October 31, 2011 | doi: 10.1021/bk-2011-1078.ch012

Chapter 13

Comparison of the Permeation of $MgCl_2$ versus NaCl in Highly Charged Sulfonated Polymer Membranes

Geoffrey M. Geise, Benny D. Freeman, and Donald R. Paul[*]

Dept. of Chemical Engineering, The University of Texas at Austin,
1 University Station, Mail Code: C0400, Austin, TX 78712, U.S.A.
[*]E-mail: drp@che.utexas.edu

Downloaded by UNIV OF GUELPH LIBRARY on June 19, 2012 | http://pubs.acs.org
Publication Date (Web): October 31, 2011 | doi: 10.1021/bk-2011-1078.ch013

Sulfonated polymers have been considered for use as chlorine tolerant desalination membrane materials. The hydrophilic nature of these materials results from inclusion of sulfonate moieties on the polymer backbone. These sulfonate groups can dissociate into a fixed and a mobile ion. As such, ion exchange can occur when the polymer is contacted with an electrolyte solution. Different counter-ion forms of the same sulfonated polymer may exhibit very different transport properties. The sodium chloride permeability of a sulfonated pentablock copolymer increases as sodium chloride concentration in the upstream solution increases. However, the magnesium chloride permeability of the material does not show a strong dependence on salt concentration. These observations can be explained by Donnan theory and consideration of the effect of sodium and magnesium ions on the concentration of fixed charge groups in the polymer matrix. Greater association between magnesium ions and the polymer's sulfonate groups reduces the effective fixed charge of the polymer, and Donnan exclusion becomes less effective compared to the sodium ion case.

Introduction

As demand for purified water increases, improved membrane materials will be useful to meet world-wide water purification needs, which include desalination (*1–4*). Sulfonated hydrocarbon polymers are interesting membrane candidates

In Modern Applications in Membrane Science and Technology; Escobar, I., et al.;
ACS Symposium Series; American Chemical Society: Washington, DC, 2011.

Downloaded by UNIV OF GUELPH LIBRARY on June 19, 2012 | http://pubs.acs.org
Publication Date (Web): October 31, 2011 | doi: 10.1021/bk-2011-1078.ch013

for desalination applications. Unlike current state-of-the-art polyamide-based desalination membranes, these sulfonated hydrocarbon materials are often resistant to degradation by the chlorine-based disinfectants used to prevent membrane biofouling in water treatment systems (*1*, *6–8*). These glassy polymers contain sulfonate groups that make the otherwise hydrophobic polymer hydrophilic and, upon exposure to water, dissociate to form a highly-charged swollen polymer. This highly-charged nature is fundamentally different from the situation for other weakly or uncharged materials such as aromatic polyamides and cellulose acetate (*1*, *9*). The presence of fixed charges on the sulfonated polymer backbone results in unique salt sorption and transport behavior (*1*).

Sulfonated polymers have received considerable attention for application in fuel cells (*10*, *11*), ion exchange applications (*9*, *12*, *13*), and electrodialysis (*11*, *13*, *14*). There are few fundamental studies of sulfonated polymers under desalination operating conditions. Most of these studies focus solely on sodium chloride transport. However, there is interest in the fundamental transport properties of other salts (*15*).

The counter-ion associated with the fixed ions on the sulfonated polymer can be altered by an ion exchange process, e.g., soaking an acid form polymer in NaCl solutions can lead to all the protons being exchanged for sodium ions (*9*, *16*, *17*). The nature of the counter-ion alone may influence the nature of the material, e.g., water sorption, owing to the difference in hydration levels of the different counter-ions (*18–20*). Other more complex issues may also be at play when comparing the different counter-ion forms of the same polymer. The nature of the binding between the sulfonate group and the counter-ion will depend on the nature of the counter-ion (*21*). In some cases, the polymer may form ion clusters (*22*). The process of forming the membrane or the ion exchange itself may alter the state of the material and/or the access to the fixed charges; the state of the membrane is usually a non-equilibrium one and depends on prior history (*16*, *17*). These results and ideas also motivate studying sulfonated polymer transport properties using salts other than sodium chloride.

Our previous work has focused on sodium chloride transport in a sulfonated pentablock copolymer (*23*). In the present work, we have extended our study to consider magnesium chloride permeability since divalent ions can influence the separation performance of sulfonated polymers (*7*).

Materials

The material considered in this study is a sulfonated styrenic pentablock copolymer produced by Kraton Performance Polymers Inc. (Houston, TX). The polymer, shown in Figure 1, consists of a hydrophilic middle block that is a random copolymer of styrene and styrene sulfonic acid, and the middle block is surrounded by hydrophobic ethylene-propylene and t-butylstyrene blocks. The sulfonation fractions considered are recorded in Figure I along with each material's corresponding ion exchange capacity (IEC). This sulfonated block copolymer has been described in more detail in the literature (*23–27*).

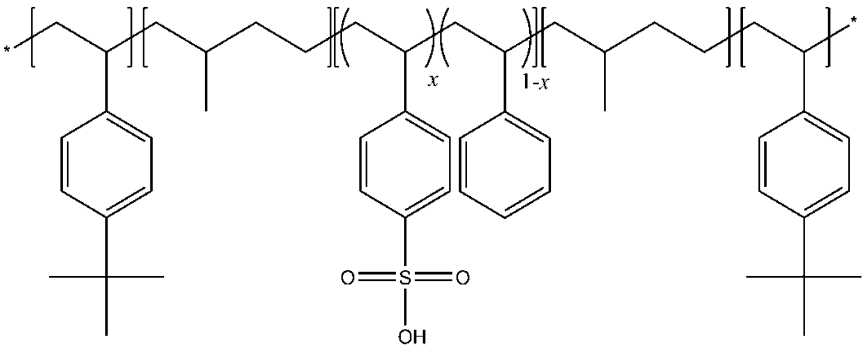

Figure 1. The structure of the sulfonated pentablock copolymer considered in this study. The sulfonation fraction is represented as 'x'.

Table I. Sulfonation fractions, *x*, and ion exchange capacities for the materials considered in this study

Sulfonation Fraction, x	*Ion Exchange Capacity [meq/g(dry polymer)]*
0.30	1.46
0.33	1.6
0.41	2.0

Experimental Methods

Pre-experiment sample preparation followed a previously described procedure whereby polymer film samples were thoroughly washed in de-ionized water to insure that any residual acid or solvent was removed (*23*). The dense polymer films were cast from solution onto a silane-treated glass plate (*26*), and the hydrated thickness of the films increased with increased sulfonation fraction. The hydrated thickness of the films used in these experiments was generally between 30 and 70 μm.

Salt permeability, P_s, was measured using a diffusion cell (custom 35 mL PermeGear Side-bi-Side Diffusion Cell, Hellertown, PA) with an effective membrane area, A, of 1.77 cm^2. These single-salt measurements were conducted at 25°C and atmospheric pressure; salt transport through dense polymer films is not appreciably affected by applied pressure. The details of this salt permeability experiment have been reported previously (*23*). In short, the polymer film separated two equal volumes, V, of solution: the upstream, or donor cell, solution contained the salt of interest and the downstream, or receiver cell, solution was initially de-ionized water. Transport of salt across the membrane was quantified

Downloaded by UNIV OF GUELPH LIBRARY on June 19, 2012 | http://pubs.acs.org
Publication Date (Web): October 31, 2011 | doi: 10.1021/bk-2011-1078.ch013

by tracking the conductivity of the receiver cell solution as a function of time and converting conductivity to salt concentration via a calibration curve. The salt permeability was calculated from

$$\ln\left[1-\frac{2C_{s\ell}^{s}[t]}{C_{s0}^{s}[0]}\right]=-\left(\frac{2AP_s}{V\ell}\right)t$$

where $C_{s\ell}^{s}[t]$ is the salt concentration in the receiver cell at time t, $C_{s0}^{s}[0]$ is the salt concentration in the donor cell at $t = 0$, and ℓ is the thickness of the hydrated polymer film measured immediately following the experiment.

Downloaded by UNIV OF GUELPH LIBRARY on June 19, 2012 | http://pubs.acs.org
Publication Date (Web): October 31, 2011 | doi: 10.1021/bk-2011-1078.ch013

Results and Discussion

Both sodium chloride (NaCl) and magnesium chloride ($MgCl_2$) permeability data are presented as a function of upstream (donor cell) salt concentration in Figure 2. The sulfonated block copolymer's NaCl permeability increases strongly with increasing upstream salt concentration, but the material's $MgCl_2$ permeability increases much more weakly with increasing upstream salt concentration. The NaCl permeability results are qualitatively consistent with Donnan theory; salt sorption and, thus, salt permeability are expected to increase as salt concentration increases (*1*, *9*). The $MgCl_2$ permeability results, however, exhibit a weak dependence on the salt concentration of the feed (i.e., upstream) solution, so when $MgCl_2$ is considered, Donnan exclusion is less significant than when NaCl is considered.

When the external bulk salt concentration is much less than the concentration of fixed-charge groups in the polymer matrix, Donnan theory can be applied to the desalination case to show that the salt permeability is expected to vary as

$$P_s \sim \frac{C_{s0}^{s}}{C_{A}^{m}}$$

where C_{s0}^{s} is the upstream bulk salt concentration, and C_{A}^{m} is the concentration of fixed-charge groups in the hydrated polymer matrix (*1*). In practice, the assumptions associated with Donnan theory may not be strictly realized and $P_s \sim \left(C_{s0}^{s}\right)^{\varphi}$ where $\varphi < 1$ (*28*, *29*). The concentration of fixed-charge groups in the considered materials was much greater than the salt concentrations used in this study. Therefore, it is expected that salt permeability should increase with increasing upstream salt concentration as observed in the NaCl experiments.

Relative to sodium ions, magnesium ions preferentially bind to sulfonate groups (*21*). Therefore, the magnesium ions would not be expected to dissociate from the sulfonate groups as readily as the sodium ions. This decreased dissociation could have two effects. First, magnesium ions could effectively crosslink the polymer matrix by binding to two sulfonate groups on different polymer chains. Second, a low degree of dissociation would render the sulfonated

Downloaded by UNIV OF GUELPH LIBRARY on June 19, 2012 | http://pubs.acs.org
Publication Date (Web): October 31, 2011 | doi: 10.1021/bk-2011-1078.ch013

polymer effectively less highly charged, and the behavior of the material could be expected to approach that of other non-charged materials, such as cellulose acetate, that do not exhibit significant salt permeability dependence upon salt concentration (*1*, *30*).

Polymer films equilibrated in $MgCl_2$ solutions were qualitatively much more rigid than films equilibrated in NaCl solutions. However, cross-linking generally tends to reduce a material's permeability (*31*, *32*). Since the magnesium chloride permeability remains at or above the values measured for sodium chloride it is more likely that another effect, such as neutralization of the fixed charge sites, is dominant. Based upon these observations and the measured permeability data, the more strongly-bound nature of magnesium ions, relative to sodium ions, may reduce the effectiveness of Donnan exclusion in these materials by effectively reducing the concentration of fixed charge groups in the polymer matrix, C_A^m.

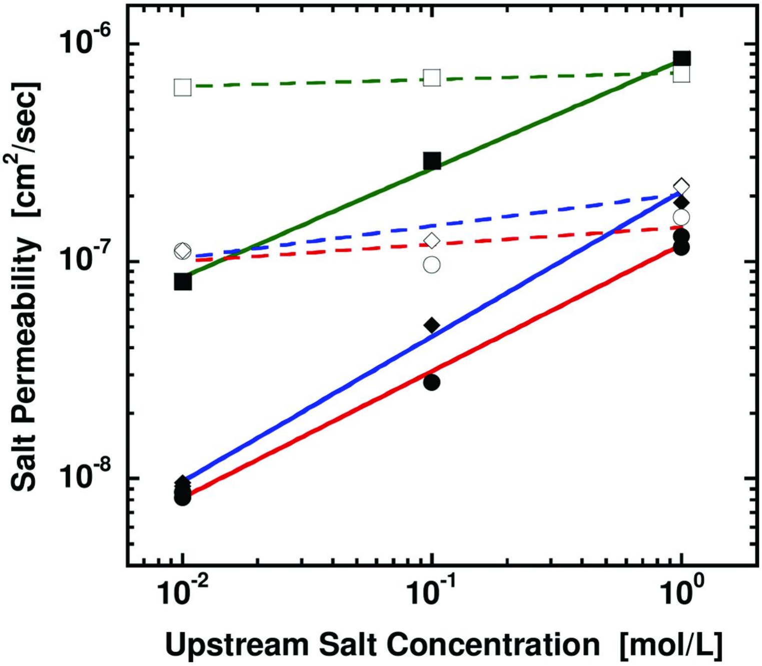

Figure 2. Single-salt permeability data plotted versus upstream salt concentration. Permeability data are shown for NaCl (23) (filled symbols and solid fit lines) and $MgCl_2$ (open symbols and dashed fit lines) using the IEC 1.46 (solid circle, open circle), 1.6 (solid diamond, open diamond), and 2.0 (solid square, open square) meq/g(dry polymer) sulfonated pentablock copolymer materials.

Downloaded by UNIV OF GUELPH LIBRARY on June 19, 2012 | http://pubs.acs.org
Publication Date (Web): October 31, 2011 | doi: 10.1021/bk-2011-1078.ch013

Conclusions

The magnesium chloride permeability of a sulfonated styrenic pentablock copolymer was compared to previously measured sodium chloride permeability data. While the material's sodium chloride permeability strongly depends on upstream salt concentration, the magnesium chloride permeability has a very weak dependence on upstream salt concentration. Since Donnan theory predicts that salt permeability should strongly increase with increasing upstream salt concentration, the magnesium chloride result may indicate that ion exchange to the magnesium counter-ion form effectively decreases the fixed charge concentration within the polymer matrix as a result of greater magnesium ion exchange selectivity and sulfonate group binding relative to sodium ions. Qualitative evidence suggested that magnesium may effectively crosslink the polymer by binding to sulfonate groups on different polymer chains. This potential cross-linking effect, however, did not appear to be the dominant determinant of the material's permeability.

Acknowledgments

The authors thank Carl Willis, John Flood, Donn Dubois, Bob Bening, and Kraton Performance Polymers, Inc. (Houston, TX) for providing valuable scientific discussion, materials, and funding for this study.

References

1. Geise, G. M.; Lee, H.-S.; Miller, D. J.; Freeman, B. D.; McGrath, J. E.; Paul, D. R. *J. Polym. Sci., Part B: Polym. Phys.* **2010**, *48* (15), 1685–1718.
2. Greenlee, L. F.; Lawler, D. F.; Freeman, B. D.; Marrot, B.; Moulin, P. *Water Res.* **2009**, *43*, 2317–2348.
3. Service, R. F. *Science (Washington, D.C.)* **2006**, *313* (5790), 1088–1090.
4. Webber, M. E. *Sci. Am. Sp. Ed.* **2008**, *18* (4), 34–41.
5. Knoell, T. *Ultrapure Water* **2006**, *23*, 24–31.
6. Park, H. B.; Freeman, B. D.; Zhang, Z.-B.; Sankir, M.; McGrath, J. E. *Angew. Chem.* **2008**, *120*, 6108–6113.
7. Parise, P. L.; Allegrezza, A. E. Jr.; Parekh, B. S. *Ultrapure Water* 1987**,** (October), 54-65.
8. Allegrezza, A. E., Jr.; Parekh, B. S.; Parise, P. L.; Swiniarski, E. J.; White, J. L. *Desalination* **1987**, *64*, 285–304.
9. Helfferich, F. *Ion exchange;* Dover Publications: New York, 1995.
10. Smitha, B.; Sridhar, S.; Khan, A. A. *J. Membr. Sci.* **2005**, *259* (1-2), 10–26.
11. Ulbricht, M. *Polymer* **2006**, *47* (7), 2217–2262.
12. Sata, T. *Ion exchange membranes: Preparation, characterization, modification and application;* The Royal Society of Chemistry: Cambridge, United Kingdom, 2004.
13. Xu, T. W. *J. Membr. Sci.* **2005**, *263* (1-2), 1–29.
14. Nagarale, R. K.; Gohil, G. S.; Shahi, V. K. *Adv. Colloid Interface Sci.* **2006**, *119* (2-3), 97–130.

Downloaded by UNIV OF GUELPH LIBRARY on June 19, 2012 | http://pubs.acs.org
Publication Date (Web): October 31, 2011 | doi: 10.1021/bk-2011-1078.ch013

15. Geise, G. M.; Park, H. B.; Sagle, A. C.; Freeman, B. D.; McGrath, J. E. *J. Membr. Sci.* 2010**,** *DOI: 10.1016/j.memsci.2010.11.054*.
16. Xie, W.; Park, H. B.; Cook, J.; Lee, C. H.; Byun, G.; Freeman, B. D.; McGrath, J. E. *Water Sci. Technol.* **2010**, *61* (3), 619–624.
17. Passaniti, L. K. R. M.S. Thesis, The University of Texas, Austin, TX, 2010.
18. Bonner, O. D. *J. Phys. Chem.* **1954**, *58* (4), 318–320.
19. Pushpa, K. K.; Nandan, D.; Iyer, R. M. *J. Chem. Soc., Faraday Trans. 1* **1988**, *84* (6), 2047–2056.
20. Mauritz, K. A.; Moore, R. B. *Chem. Rev. (Washington, DC, U.S.)* **2004**, *104* (10), 4535–4585.
21. Bonner, O. D.; Smith, L. L. *J. Phys. Chem.* **1957**, *61*, 326–329.
22. Sivashinsky, N.; Tanny, G. B. *J. Appl. Polym. Sci.* **1983**, *28*, 3235–3245.
23. Geise, G. M.; Freeman, B. D.; Paul, D. R. *Polymer* **2010**, *51* (24), 5815–5822.
24. Willis, C. L.; Handlin, D. L.; Trenor, S. R.; Mather, B. D. U.S. Patent 7,737,224 B2, 2010.
25. Geise, G. M.; Freeman, B. D.; Paul, D. R. In *ANTEC 2009 ---- Proceedings of the 67th Annual Technical Conference & Exhibition*; Society of Plastics Engineers: Chicago, IL, 2009; pp 97-101.
26. Flood, J.; Dubois, D.; Willis, C. L.; Bening, R. In *ANTEC 2009 ---- Proceedings of the 67th Annual Technical Conference & Exhibition*; Society of Plastics Engineers: Chicago, IL, 2009; pp 107-112.
27. Kota, A. K.; Winey, K. I. In *ANTEC 2009 ---- Proceedings of the 67th Annual Technical Conference & Exhibition*; Society of Plastics Engineers: Chicago, IL, 2009; pp 113-116.
28. Glueckauf, E.; Watts, R. E. *Proc. R. Soc. London, Ser. A* **1962**, *268*, 339–349.
29. Glueckauf, E. *Proc. R. Soc. London, Ser. A* **1962**, *268*, 350–370.
30. Lonsdale, H. K.; Merten, U.; Riley, R. L. *J. Appl. Polym. Sci.* **1965**, *9*, 1341–1362.
31. Ju, H.; Sagle, A. C.; Freeman, B. D.; Mardel, J. I.; Hill, A. J. *J. Membr. Sci.* **2010**, *358*, 131–141.
32. Sagle, A. C.; Ju, H.; Freeman, B. D.; Sharma, M. M. *Polymer* **2009**, *50*, 756–766.

Chapter 14

Studying the Effect of Feed Water Characteristics on the Hydrophobicity of Cellulose Acetate Ultrafiltraion Membranes and Its Correlation to Membrane Morphology: A Chemical Force Microscopy Approach

Amr M. Zaky,*,[a] Isabel C. Escobar,[b] and Cyndee L. Gruden[a]

[a]Department of Civil Engineering and
[b]Department of Chemical and Environmental Engineering, The University of Toledo, 2801 W. Bancroft St., Toledo, OH 43606, U.S.A.
***E-mail: azaky@rockets.utoledo.edu. Phone: (419) 530-8128.**
Fax: (419) 530-8116.

Downloaded by STANFORD UNIV GREEN LIBR on June 18, 2012 | http://pubs.acs.org
Publication Date (Web): October 31, 2011 | doi: 10.1021/bk-2011-1078.ch014

The complexity and variability of solute chemistry which forms the conditioning layer with the membrane surface (i.e., instantaneous fouling) makes it hard to distinguish between abiotic and biotic fouling behaviors. Moreover, the role of membrane chemical heterogeneities and morphology in biofouling and their effect on solute chemistry has received little attention. In this research, the effect of two feed water characteristics (i.e., conductivity and pH) on the membrane-solute interaction forces (i.e., hydrophobic attraction), and its correlation to membrane morphology was assessed. The surface hydrophobicity, and in turn, hydrophobic attraction forces of cellulose acetate ultrafiltration (CAUF, MWCO 20,000 Dalton) membranes were assessed using chemical force microscopy (CFM) to measure surface adhesion. CFM was applied in lateral mode to correlate the difference in the adhesion forces, on the membrane surface, with its topography. Spatially resolved friction images, from CFM scans in lateral mode, were generated on membranes using DI and tap water. Adhesion force analysis showed that as feed water conductivity increased, the range of the adhesion force

In Modern Applications in Membrane Science and Technology; Escobar, I., et al.;
ACS Symposium Series; American Chemical Society: Washington, DC, 2011.

Downloaded by STANFORD UNIV GREEN LIBR on June 18, 2012 | http://pubs.acs.org
Publication Date (Web): October 31, 2011 | doi: 10.1021/bk-2011-1078.ch014

increased. In addition, friction forces increased when adhesion forces increased on the membrane surface.

1. Introduction

Ultrafiltration membranes have been used for a wide range of drinking water and industrial applications. For all applications, membrane hydrophobicity plays a significant role in the transport of water and solute molecules on the membrane surface. Atomic force microscopy (AFM) has been widely used to measure membrane surface roughness (*1–3*). However, membrane surface chemical heterogeneities also play important roles in determining the membrane performance and fouling behavior. Particles with small diameters (< 1 μm) deposit first followed by larger particles (>1 μm) (*4*). Because of the large surface area to volume ratio of small particles, their deposition on the membrane surface is more influenced by thermodynamic forces rather than by hydrodynamic forces. The dominance of thermodynamic forces increases chemical heterogeneity on the membrane, thus increasing its interfacial interaction with particles.

Contact angle measurements have been used extensively to measure membrane hydrophobicity by measuring the membrane surface energy properties (*3–5*). However, contact angle measurements cannot measure hydrophobic attractions at the atomic level. This level of detail may be necessary to adequately characterize membranes to predict their fouling behavior. Modifications of the AFM technique can be used to directly measure the interfacial interactions between a probe and a membrane surface at the nano-scale. CFM, a relatively new technique to characterize membrane surface properties of hydrophobicity and charge density (*4*, *6*), can provide chemically distinct information on the membrane surface, with a nanometer scale resolution, based on the change in friction (i.e., adhesion) between the AFM probe and the membrane surface. Therefore, CFM is a superior method, as compared to contact angle measurements, for correlating nanometer scale membrane surface morphology to chemical heterogeneity.

UF membranes provide a promising technology for purification of macromolecular and colloidal species in solutions (*7–9*). However, membrane fouling still remains a significant challenge. The complexity and variability of solute chemistry which contributes to the formation of the conditioning layer (i.e., instantaneous fouling) makes it hard to distinguish between abiotic and biotic fouling behaviors. Moreover, the role of membrane chemical heterogeneities and morphology on biofouling propensity and its effect on solute chemistry has received less research attention. This is due to the limitations in techniques available to study surface chemical heterogeneities and their correlation to membrane morphology. Thus, this study used CFM to investigate the effect of different feed water characteristics (i.e., conductivity and pH) on the membrane-solute interaction force of hydrophobic attraction and its correlation to membrane morphology.

Downloaded by STANFORD UNIV GREEN LIBR on June 18, 2012 | http://pubs.acs.org
Publication Date (Web): October 31, 2011 | doi: 10.1021/bk-2011-1078.ch014

2. Materials and Methods

2.1. Membranes

CAUF membranes, with a molecular cut-off weight of 20,000 Daltons (General Electric Water and Process Technologies, Minnetonka, MN), were used and stored in deionized water (DI) at 5°C with regular water replacement.

2.2. Crossflow Membrane Filtration Unit

Crossflow experiments were performed on membrane sheets with an area of 138.7 cm^2 at a constant pressure of 172.36 kPa (25 psi) and water temperature of 26°C. The feed water was pumped from the reservoir to the cell membrane (Osmonics Sepa CF, Minnetonka, MN). Both concentrate and permeate were recycled back to the reservoir. Fouling experiments were performed to provide a basic understanding of the influence of physical and chemical operating conditions (i.e., membrane hydrophobicity and morphology) on the fouling behavior of the tested membranes. The final permeate flux (J_f) was reported with respect to initial flux (J_o), and was measured after 24 hours of crossflow filtration using different feed water compositions. Feed water compositions, conductivity (EC), and pH are summarized in Table I. The concentration ratio between carbon source and cell solution was compiled from previous studies (*10–12*). Buffering was in the form of 0.050 mM $NaHCO_3$, 0.010 mM $CaCl_2$, 0.200 mM NaCl, 0.094 mM NH_4Cl, 0.045 mM KH_2PO_4, and 0.060 mM $MgSO_4$. *Pseudomonas fluorescens Migula* (ATCC # 12842) culture was used in this case study, both as active and as inactive cells. To prevent any possible growth in filtration experiments using inactive cells in synthetic DI water (1), sodium azide was added instead of NaCl at the same concentration (*11*).

2.3. AFM Force Curve Analysis

Membrane surface hydrophobicity, and in turn hydrophobic attraction, was assessed by measuring the surface adhesion using chemically modified tips. Chemical force microscopy (CFM) analyses were performed using a liquid cell at room temperature. Force measurements were carried out on membrane sheets using chemically modified silicon nitride pyramidal tips attached to the end of a V-shaped cantilever (spring constant; k = 0.12 N/m and average radius of curvature; R = 40 ± 10 nm). The modified tips were functionalized with self assembled mono-layers (SAM) terminating in methyl (CH_3) end groups (NovaSCAN technologies, Ames, IA). Methyl functionalized tips are used to determine the hydrophobicity of membrane surfaces (*4*, *13*, *14*). The spring constant was used for converting cantilever deflection to interaction force values. Force curves were reported as a function of the separation distance (h). In order to simulate the same feed water conditions during crossflow filtration, clean membranes sheets were incubated for 24 hours at 26°C with feed water concentrations similar to those shown in Table I. However, bacterial cell solutions were not added to the prepared feed water. After incubation, membranes were transferred to AFM and force-distance measurements were conducted in a liquid cell using the same feed water concentration. Prior to force measurements, the liquid cell was cleaned with acetone, rinsed with DI water, and dry blown using a high velocity stream of nitrogen. Under each set of conditions, a minimum of ten curves at different probe-surface separation distances, were randomly collected within an area less than 2 µm.

2.4. Mapping the Hydrophobicity on Membrane Surface

Methyl functionalized tips can also be used to construct hydrophobicity maps on membrane surfaces. The change in friction forces on membrane surfaces and their correlation to membrane morphology was assessed using CFM in lateral mode. It was previously proven that the increase in friction corresponds to an increase in adhesion between the probe and the membrane surface as long as a constant load was applied during CFM imaging (*4*). Immediately after conducting force measurements (section 2.3), CFM images were performed on the same area of the membrane. In this manner, the change in the adhesion forces across the membrane surface could be correlated to its morphology. CFM images were generated by recording traces of cantilever vertical and lateral deflection while the membrane was scanned back and forth in contact mode. In this manner, changes in membrane surface topography and friction (i.e., change in adhesion) were measured simultaneously. CFM operating conditions of temperature and feed water concentration were chosen to match the operating conditions used during crossflow filtration. Thus, in the quartz liquid cell, membrane sheets were tested at 26^{o}C using the feed water concentration shown in Table I. One drawback of simultaneous measurements is their sensitivity to surface roughness, as the measured friction increases with increasing surface roughness. Thus, in order to minimize this drawback, samples were scanned at a slow scan rate (0.5 Hz) and a small scan area (4.0 µm^2). Spatially resolved measurements of membrane adhesion forces can provide valuable insight into membrane fouling to alter membrane-solute interactions.

Downloaded by STANFORD UNIV GREEN LIBR on June 18, 2012 | http://pubs.acs.org
Publication Date (Web): October 31, 2011 | doi: 10.1021/bk-2011-1078.ch014

Table I. Feed water concentrations used in crossflow filtration experiments and the corresponding final normalized flux (J_f/J_o)

Feed water	*Buffering*	*Sodium acetate trihydrate (130.14 ppm)*	*Sodium thiosulfate (65.07 ppm)*	*10^3 cells/mL of active cells*	*Conductivity (ppm TDS)*	*pH*	*(J_f/J_o)*
DI	N/A	N/A	N/A	N/A	3.20	6.80	≤ 0.99
DI synthetic water(1)	Sodium azide was added instead of NaCl at	Added	N/A	Added using inactive cells	93.20	6.51	0.97 ± 0.01

Continued on next page.

Downloaded by STANFORD UNIV GREEN LIBR on June 18, 2012 | http://pubs.acs.org
Publication Date (Web): October 31, 2011 | doi: 10.1021/bk-2011-1078.ch014

Table I. (Continued). Feed water concentrations used in crossflow filtration experiments and the corresponding final normalized flux (J_f/J_o)

Feed water	*Buffering*	*Sodium acetate trihydrate (130.14 ppm)*	*Sodium thiosulfate (65.07 ppm)*	*10^3 cells/mL of active cells*	*Conductivity (ppm TDS)*	*pH*	*(J_f/J_o)*
	the same concentration						
DI synthetic water(2)	Added	Added	N/A	Added using active cells	107.00	6.46	0.93 ± 0.01
Tap water	N/A	N/A	N/A	N/A	135.00	7.38	0.91 ± 0.06
Synthetic tap water	Added	Added	Added	Added	231.00	7.45	0.88 ± 0.09

3. Results and Discussion

3.1. Flux Decline Measurements Based on Feed Water Characteristics

Precompaction was performed by filtering DI water for 24 hours, but results are not shown here as no significant flux decline was observed. The permeate flux (J_f) after 24 hours of filtration of the different feed solutions (Table I) was normalized to initial flux (J_o) for easier comparison. When compared on the basis of final normalized flux for the given filtration time, the membranes flux decline trend ranked in the following order (from lowest flux decline to highest flux decline):

1 Synthetic DI water (1) with conductivity of 93.2 mg/L displayed a final normalized flux of 0.97 ± 0.01;
2 Synthetic DI water (2 with conductivity of 107 mg/L displayed a final normalized flux of 0.95 ± 0.02;
3 Tap water with conductivity of 135 mg/L displayed a final normalized flux of 0.91 ± 0.06; and
4 Synthetic tap water with conductivity of 231 mg/L displayed a final normalized flux of 0.88 ± 0.09.

The decrease in the normalized flux is consistent with the increase in feed water concentration measured as conductivity (Table I) as conductivity can affect electrostatic repulsion associated with membrane surface (*15*, *16*).

3.2. Adhesion Force Analysis

Table II shows the average adhesion forces and the ratio of average adhesion force to the maximum applied force on membranes tested using the different feed water solutions. For each feed water, adhesion forces were calculated from a minimum of ten curves as a function of the detached separation distance. The average adhesion values were also correlated to maximum applied force on the membrane surface. Adhesion forces increased with the following rank:

1 DI water (0.11 ± 0.01 nN);
2 Synthetic DI water (1) (0.20 ± 0.02 nN);
3 Synthetic DI water (2) (0.45 ± 0.30 nN);
4 Tap water (0.63 ± 0.28 nN);
5 Synthetic tap water (1.54 ± 0.63 nN)

This result was also consistent with ratio of average adhesion force to maximum applied force. The maximum applied force encounters adhesion and repulsive forces. Therefore, analysis indicated that as the functionalized tip approached the membrane surface, it encountered long-range repulsive electrostatic interactions between similarly hydrophilic surfaces. As feed water conductivity increased, the range of the repulsive interaction decreased due to compression of the electrical double layer (*17*).

3.3. Relationship between Adhesion Force Analysis and Membrane Surface Roughness

The topographical and corresponding friction images acquired for membranes tested using only DI water and tap water are shown in Figures 1.a and 2.a, respectively. The normal deflection was used to measure changes in surface topography while the lateral deflection provides information regarding changes in the friction (i.e., adhesion). Surface topography was measured in nm and friction due to lateral forces was measured in mV. Replicate 4 μm^2 scans were performed to ensure that the results presented are representative of the membrane surface at each set of conditions. CFM images demonstrated a clear relationship between the surface topography and adhesion, as has been found in similar investigations. In Figures 1.a and 2.a, a random defect (i.e., large peak features; light shades) were observed. Similar CFM investigations concluded that this may be indicative of polymer aggregation during membrane synthesis (*4*, *18*).

Downloaded by STANFORD UNIV GREEN LIBR on June 18, 2012 | http://pubs.acs.org
Publication Date (Web): October 31, 2011 | doi: 10.1021/bk-2011-1078.ch014

Table II. Average adhesion forces and the ratio of average adhesion force to the maximum applied force on membranes tested using different feed water concentrations

Feed water	*Average adhesion force (nN)*	*Ratio of average adhesion force to max applied force*
DI	0.11 ± 0.01	0.47
Synthetic DI water(1)	0.20 ± 0.02	0.92
Synthetic DI water(2)	0.45 ± 0.30	1.78
Tap water	0.63 ± 0.28	2.49
Synthetic tap water	1.54 ± 0.63	9.92

Downloaded by STANFORD UNIV GREEN LIBR on June 18, 2012 | http://pubs.acs.org
Publication Date (Web): October 31, 2011 | doi: 10.1021/bk-2011-1078.ch014

A larger adhesion was measured in the presence of either a surface depression area (dark colors) or in a sudden presence of peak features (light colors). Surface topography height values are a measurement of the cantilever vertical deflection and are correlated to the membrane surface roughness. In Figures 1.a and 2.a, CFM was used to determine the height values of membranes analyzed with DI water, from -20 to 35 nm, which were similar to height values of membranes analyzed with tap water, from -42 to 30 nm. However, lateral deflection values of membranes analyzed with DI water, from -42 to 48 mV, were lower as compared to lateral deflection values of membranes analyzed with tap water, from -280 to 420 mV. Friction forces created as the CFM probe scanned across the membrane surface corresponds directly to the adhesion between the probe and the membrane surface. Thus, the increase in lateral deflection on membranes analyzed using tap water was due to the increase in the measured interactive adhesion forces (Table II), which in turn decreased the permeate flux.

Moreover, for the same set of conditions (i.e., either DI or tap water) the impact of the surface roughness was relevant. For the same set of conditions, an area, highlighted in white box (white boxes are drawn on the right Figures 1.a and 2.a, and are shown in Figures 1.b and 2.b), was selected in which the height values (i.e., membrane surface roughness) were similar and lower in range of -10 to 10 nm. The resulting lateral deflections decreased with membranes analyzed using DI, from -17 to 10 mV, and tap water from -250 to 250 mV. This may explain why rougher membranes tend to foul at higher rates than smooth membranes: rougher regions on the membrane surface tend to encounter higher adhesion (i.e., hydrophobic attraction).

Downloaded by STANFORD UNIV GREEN LIBR on June 18, 2012 | http://pubs.acs.org
Publication Date (Web): October 31, 2011 | doi: 10.1021/bk-2011-1078.ch014

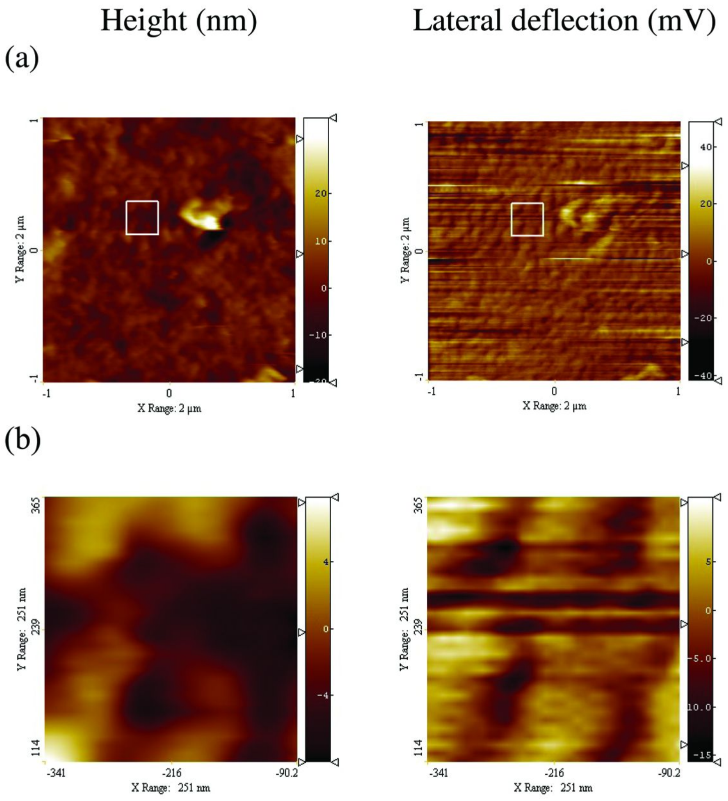

Figure 1. Representative topographical and corresponding CFM images using CH_3-functionalized tip on membrane surfaces using DI water. The images show the surface roughness or height (nm) (left column) and the lateral deflection or adhesion (mV) (right column) for a feed water composed of DI water (a). An area on the membrane with a membrane surface roughness [-10 to 10 nm] was selected for comparison (b).

Chemical force microscopy provided chemically distinct information regarding the correlation between membrane surface roughness and the difference in adhesion generated from hydrophobic interactions. However, the difference in adhesion (i.e., change in friction forces) depends on the area of interaction between the tip and membrane surface, tip radius of curvature, and tip to surface separation distance. Filtration experiments that were performed involved solute as well as cell (i.e., *Pseudomonas fluorescens Migula*) transport. Therefore, future work requires performing CFM analysis by attaching a *Pseudomonas fluorescens Migula* cells to the cantilever (i.e., colloidal probe) and studying the hydrophobic interaction between these cells and the membrane in the presence of the feed water concentration used for filtration. This will help in providing accurate quantitative mapping of the hydrophobic interactions between *Pseudomonas fluorescens Migula* and cellulose acetate ultrafiltraion membranes and in better understanding of membranes' biofouling behavior.

Downloaded by STANFORD UNIV GREEN LIBR on June 18, 2012 | http://pubs.acs.org
Publication Date (Web): October 31, 2011 | doi: 10.1021/bk-2011-1078.ch014

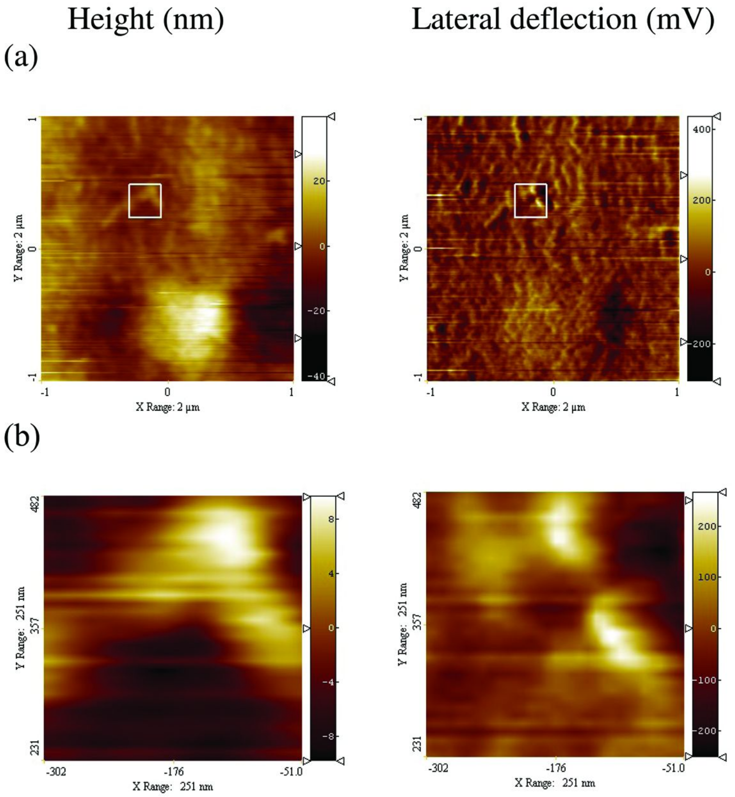

Figure 2. Representative topographical and corresponding CFM images using CH_3-funtionalized tip on membrane surfaces using tap water. The images show the surface roughness or height (nm) (left column) and the lateral deflection or adhesion (mV) (right column) for a feed water composed of tap water (a). An area on the membrane with a membrane surface roughness [-10 to 10 nm] was selected for comparison (b).

4. Conclusions

In conclusion, the effect of feed water conductivity and pH on the membrane-solute interaction forces (i.e., hydrophobic attraction) was investigated, and its correlation to membrane morphology was assessed. Permeate flux decreased with the increase in the feed water conductivity. Adhesion force analysis showed that as the increase in the feed water conductivity lowered the electrostatic repulsion. CFM images demonstrated a clear relationship between surface topography and adhesion. Analysis of membranes using DI and tap water suggested that increasing the adhesion forces on membrane increased the friction forces as well. Moreover, rougher regions on the membrane surface tended to encounter higher adhesion (i.e., hydrophobic attraction) as compared to smoother regions on the membrane. CFM analysis provided chemically distinct information

Downloaded by STANFORD UNIV GREEN LIBR on June 18, 2012 | http://pubs.acs.org
Publication Date (Web): October 31, 2011 | doi: 10.1021/bk-2011-1078.ch014

regarding the correlation between membrane surface roughness and the difference in adhesion generated from hydrophobic interactions. However, the difference in adhesion (i.e., change in friction forces) also depended on the area of interaction between the tip and membrane surface, tip radius of curvature, and tip to surface separation distance. Therefore, future work requires performing CFM analysis by attaching a biological cell to the cantilever (i.e., colloidal probe) to directly study the hydrophobic interaction between the biofoulant and the membrane in the presence of the feed water concentration used for filtration.

Acknowledgments

This work was supported with the grant # 4614 Ohio Water Development Authority: State-of-the-art membrane characterization toward biofouling control and improved membrane performance.

References

1. Boussu, K.; Van der Bruggen, B.; Volodin, A.; Snauwaert, J.; Van Haesendonck, C.; Vandecasteele, C. *J. Colloid Interface Sci.* **2005**, *286*, 632–638.
2. Brant, J.; Johnson, K.; Childress, A. *J. Membr. Sci.* **2006**, *276*, 286–294.
3. Pasmore, M.; Todd, P.; Smith, S.; Baker, B.; Silverstein, J.; Coons, D.; Bowman, C. *J. Membr. Sci.* **2001**, *194*, 15–32.
4. Brant, J.; Johnson, K.; Childress, A. *Colloids Surf., A.* **2006**, *280*, 45–57.
5. Vrjenhoek, E.; Hong, S.; Elimelech, M. *J. Membr. Sci.* **2001**, *188*, 115–128.
6. Brant, J.; Childress, A. *Environ. Eng. Sci.* **2002**, *19*, 413–427.
7. Cai, G.; Gorey, C.; Zaky, A.; Escobar, I.; Gruden, C. *Desalination* **2011**, *270*, 116–123.
8. Goosen, M.; Sablani, S.; Al-Hinai, H; Al-Obeidani, S.; Al-Belushi, R.; Jackson, D. *Sep. Sci. Technol.* **2004**, *39*, 2261–2297.
9. Hilal, N.; Ogunbiyi, O.; Miles, N.; Nigmatullin, R *Sep. Sci. Technol.* **2005**, *40*, 1957–2005.
10. Baker, J.; Dudley, L. *Desalination* **1998**, *118*, 81–90.
11. Herzberg, M.; Elimelech, M. *J. Membr. Sci.* **2007**, *295*, 11–20.
12. Peng, W.; Escobar, I.; White, D. *J. Membr. Sci.* **2004**, *238*, 33–46.
13. Noy, A.; Vezenov, D.; Lieber, C. *Annu. Rev. Mater. Sci.* **1997**, *27*, 381–421.
14. Okabe, Y.; Akiba, U.; Fujihira, M. *Appl. Surf. Sci.* **2000**, *157*, 389–404.
15. Boussu, K.; Belpaire, A.; Volodin, A.; Van Haesendonck, C.; Van der Meeren, P.; Vandecasteele, C.; Van der Bruggen, B. *J. Membr. Sci.* **2007**, *289*, 220–230.
16. Yoon, Y.; Amy, G.; Yoon, J. *Desalination* **2005**, *177*, 217–227.
17. Liang, Y.; Hilal, N.; Langston, P.; Starov, V. *Adv. Colloid Interface Sci.* **2007**, *134-135*, 151–166.
18. Bowen, W.; Hilal, N.; Lovitt, R.; Wright, C. *J. Membr. Sci.* **1998**, *139*, 269–274.

Downloaded by STANFORD UNIV GREEN LIBR on June 19, 2012 | http://pubs.acs.org
Publication Date (Web): October 31, 2011 | doi: 10.1021/bk-2011-1078.ch015

Chapter 15

Carbon Nanotube/Polyethersulfone Composite Membranes for Water Filtration

Evrim Celik[1] and Heechul Choi*

School of Environmental Science and Engineering, Gwangju Institute of Science and Technology (GIST), 261 Cheomdan-gwagiro, Buk-gu, Gwangju 500-712, South Korea
[1]Current Address: Department of Environmental Engineering, Suleyman Demirel University, Isparta 32260, Turkey
***E-mail: hcchoi@gist.ac.kr**

A series of polyethersulfone (PES) - multi-walled carbon nanotube (MWCNT) (C/P) composite membranes with different amounts of MWCNT were prepared using the phase inversion process. The influence of addition of MWCNT on the morphologies, permeation properties and the antifouling performances of C/P composite membranes were investigated through the methods of scanning electron microscopy (SEM), contact angle goniometer, pure water flux test and permeation tests. The results showed that addition of MWCNTs significantly increased the hydrophilicity, pure water flux and solute rejection of the membranes. Antifouling tests showed that the C/P composite membranes have a stronger ability to resist fouling than that of bare PES membrane. The membrane with 2 wt% MWCNT addition displayed ideal permeation properties in pure water flux, solute rejection and antifouling ability.

Introduction

Membrane separation technologies are very promising for the removal of suspended solids including microorganisms and a fraction of dissolved solids (*1*). However, in real applications membrane performance can change with time, and flux decline is observed. The reasons for the flux decline can be concentration

In Modern Applications in Membrane Science and Technology; Escobar, I., et al.;
ACS Symposium Series; American Chemical Society: Washington, DC, 2011.

Downloaded by STANFORD UNIV GREEN LIBR on June 19, 2012 | http://pubs.acs.org
Publication Date (Web): October 31, 2011 | doi: 10.1021/bk-2011-1078.ch015

polarization, adsorptive fouling, gel layer formation, fouling (*2*), change in the membrane properties, and change in feed solution properties. Physical or chemical deterioration results in change in membrane properties (*3*). All these bring on additional resistance to the transport across the membrane (*2*). In the membrane operations fouling is one of the series problems (*4*). Nonspecific adsorption and deposition of the macromolecules on the membrane surface or in the pores increases the hydraulic resistance to the flow, and by that means reduces the permeation flux severely (*5*, *6*). Membrane surface chemistry is very important on the performance of ultrafiltration operations (*7*).

Polymeric membranes are widely used in membrane operations due to their good film forming ability, flexibility, toughness, separation properties and low cost. However, they have low mechanical, chemical and thermal resistance. Moreover, they have poor antifouling ability because of their hydrophobic nature (*8*). Organic-inorganic hybrid membranes prepared by compositing inorganic and organic materials exhibit the properties of both (*9*). There has been a great interest in polymer – inorganic nanocomposites over the last two decades. Addition of inorganic nanoparticles in polymer matrix can provide high performance novel materials which can be used in many industrial fields (*10*). Many studies in organic – inorganic porous membrane preparation and characteristics have reported the advantages of the inorganic fillers such as suppression of macrovoids, enhanced mechanical strength and lifetime, superior permeability with unchanged retention properties (*9*).

Carbon nanotubes (CNTs) have attracted great interest since their discovery in 1991 by Iijima (*11*). CNTs can be defined as tiny cylinders of graphite which are closed at the end by half C_{60}. CNTs usually have a diameter less than 10 nm. In this size range quantum effects become more important. Because of the quantum effect and their unusual symmetries, CNTs have outstanding properties (*12*), such as unique mechanical (extremely high Young's modulus, stiffness and flexibility) and electronic properties (*13*), high electrical and thermal conductivities, low coefficient of thermal expansion and high aspect ratio (*14*). Their unique properties make them attractive candidates for polymer composites. However, CNTs are held together as bundles and ropes because of the intrinsic van der Waals attraction of the CNTs to each other. Hence, homogenous dispersion of the CNTs in polymer solution is not easily obtained. Furthermore, the lack of interfacial bonding due to the atomically smooth non-reactive surfaces of the CNTs, limits the load transfer from the matrix to the CNTs. In this situation, CNTs play a limited reinforcement role because they are typically pulled out from the matrix rather than fractured (*15*).

Functionalization of CNTs can increase their solubility and processibility. Functionalization of the CNTs will allow the combination of unique properties of the CNTs with other materials (*16*). There will be functional groups attached on the nanotube surface after functionalization. CNTs react readily with other chemical agents, with the help of functional groups and form homogenous dispersions or well aligned materials (*17*).

In this study, multi wall carbon nanotubes (MWCNTs) were functionalized and used to improve the ultrafiltration performance of the polyethersulfone (PES) membranes. MWCNT / PES (C/P) composite membranes were prepared via phase inversion method. The morphology, hydrophilicity, permeability and antifouling performance of the C/P composite membranes were examined.

Experimental Section

Membrane Preparation

MWCNTs (Hanwha Nanotech Co Ltd) were functionalized to improve the dispersion in organic solvent following a reported procedure (*18*). MWCNTs were refluxed in a mixture of 3:1 (v/v) HNO_3:H_2SO_4 for 3 h, followed by washing with DI water and drying in room temperature. After drying, the MWCNTs were ultrasonicated in a mixture of 3:1 (v/v) HNO_3:H_2SO_4 for 9 h, followed by washing with DI water until attaining a neutral pH. The final product was isolated and dried in a vacuum oven at 100 °C overnight.

The C/P composite membranes were prepared as described in our previous publication (*19*). Casting solutions were prepared by ultrasonicating the modified MWCNTs in N-methyl-2-pyrrolidinone (NMP, Sigma-Aldrich) and dissolving 20% of PES (Radel H2000, Solvay Korea Co). The amount of MWCNTs varied as 0, 0.5, 2, and 4 wt% by weight of the PES and these samples were labeled as C/P-0, C/P-0.5, C/P-2 and C/P-4, respectively. The casting solutions were stirred at 60°C and ultrasonicated to obtain uniform and homogenous casting suspensions. The suspensions were then cast on a glass plate and immersed into water bath for phase inversion. After complete coagulation, the membranes were washed with and stored in DI water until use.

Membrane Characterization

Scanning electron microscopy (SEM, S-4700, Hitachi, Japan) was used to examine the surface morphologies and cross section structures of the membranes. Cross sections of the membranes were prepared by fracturing in the liquid nitrogen to avoid destroying membrane structure. The top surface and the bottom surface hydrophilicity of the membranes were evaluated by measuring the contact angle between water and the membrane surfaces, using a contact angle goniometer (Model 100, Rame-Hart, USA). The contact angles of both the top and the bottom surfaces of the membranes were measured at least seven times for each membrane and then were averaged to ensure the reliable value was obtained. The zeta potential of the membranes was measured by using an electrophoretic light scattering apparatus (ELS8000, Otsuka, Japan). The zeta potential of the membranes was measured using a 0.001 mol/L KCl solution in the range of pH 2-10 in room temperature. Water content has been used as one of the structural parameters of the membranes. Water content of the membranes is dependent on the porosity of the membranes. It also indicates the hydrophilicity and flux behavior of the membranes (*20*). The wet membranes were weighed after mopping the excess water with a tissue. These wet membranes were dried in a vacuum oven at 60°C for 24 h and the dry weights were determined. The water content of the membranes was calculated as follows:

Downloaded by STANFORD UNIV GREEN LIBR on June 19, 2012 | http://pubs.acs.org
Publication Date (Web): October 31, 2011 | doi: 10.1021/bk-2011-1078.ch015

$$\text{Water content} = \frac{\text{wet membrane weight} - \text{dry membrane weight}}{\text{wet membrane weight}} \times 100 \qquad (1)$$

Membrane Filtration Procedures

Permeation tests were conducted using a cross flow membrane test unit with an effective membrane area of 18.56 cm^2. The temperature in the test unit was maintained at 22 ± 1 °C by a circulator (DTRC-620, Jeio Tech., Korea). The membranes were compacted for 4 h at 0.41 MPa. Then the transmembrane pressure was reduced to 0.35 MPa for pure water flux, fouling, and solute rejection tests. Deinonized (DI) water, polyethylene glycol (PEG) solution (1 g/L), and bovine serum albumin (BSA) solution (1 g/L) were used to test the permeation, solute rejection, and the fouling properties of the membranes. Both the permeate and the retentate streams were circulated to the feed tank for all the experiments. The pure water flux (J_{w1}) and the hydraulic membrane resistance (R_m, m^{-1}) of the membranes were calculated as follows:

$$J_{w1} = \frac{V}{A\Delta t} = \frac{\Delta P}{\mu R_m} \qquad (2)$$

where V is the permeate volume (L), A is the effective membrane area (m^2), Δt is the permeation time (h), ΔP is the transmembrane pressure (Pa), and μ water viscosity at 22 °C (Pa s) (0.0096 Pa s).

The antifouling properties of the membranes were evaluated by protein ultrafiltration tests. The fouling tests were performed with 1 g/L of BSA solution. After 1 h of protein filtration, the protein flux (J_p) was calculated using the following equation:

$$J_p = \frac{V}{A\Delta t} = \frac{\Delta P}{\mu(R_m + R_a + R_c)} \qquad (3)$$

where R_a is the hydraulic resistance of the adsorbed protein layer (m^{-1}), and R_c is the hydraulic resistance of the concentration polarization layer (m^{-1}).

Then the fouled membranes were flushed with DI water for 20 min. After cleaning the fouled membranes, the pure water flux of the fouled membrane (J_{w2}) was calculated suing the following equation:

$$J_{w2} = \frac{V}{A\Delta t} = \frac{\Delta P}{\mu(R_m + R_a)} \qquad (4)$$

Downloaded by STANFORD UNIV GREEN LIBR on June 19, 2012 | http://pubs.acs.org
Publication Date (Web): October 31, 2011 | doi: 10.1021/bk-2011-1078.ch015

Downloaded by STANFORD UNIV GREEN LIBR on June 19, 2012 | http://pubs.acs.org
Publication Date (Web): October 31, 2011 | doi: 10.1021/bk-2011-1078.ch015

In order to evaluate the antifouling property of the membranes, the relative flux of the membranes (J_r) was calculated as follows

$$J_r = \left(\frac{J_{W2}}{J_{W1}}\right) \times 100 . \tag{5}$$

Results and Discussion

Membrane Characterization

The effect of the MWCNT addition on the membrane morphologies were analyzed by SEM. The SEM images of the surfaces and cross sections of the C/P-0, C/P-0.5, and C/P-2 membranes are shown in Figure 1. The surface of the C/P composite membranes show a more porous skin layer compared to the bare PES membrane (C/P-0) due to the MWCNT addition (Figure 1 a, c, and e). Addition of hydrophilic MWCNTs causes a fast exchange of the solvent and the nonsolvent in the phase inversion process (*21*) which results in increased porosity. The cross section images of all membranes display a typical asymmetric membrane structure (Figure 1 b, d, and f). There was not an apparent difference in the cross sections of the bare PES membrane and C/P composite membranes.

The polarity and the surface energy of the polymeric surfaces have been usually characterized by contact angle measurements. Nevertheless, it is difficult to interpret these measurements for porous membranes due to the membrane contraction in the dried state, surface restructuring, heterogeneity, roughness, and the capillary forces within the pores. However, the relative hydrophilicity of each membrane can easily be obtained with these measurements (*22*). The relative hydrophilicity of the membranes was found to be affected by the MWCNTs addition as shown in Figure 2. The hydrophilicity of the membranes increased with increasing the content of the MWCNTs. In addition the hydrophilicity of the top surface of the membranes increased more drastically than that of bottom surfaces. This result suggests that the hydrophilic MWCNTs migrated to the top surface during the phase inversion of the membrane formation. Hydrophilic MWCNTs segregate to the interface between the membrane and water to reduce the interface energy (*23*).

The zeta potentials and water contents of the membranes are shown in Table I. Zeta potential of C/P-0.5 membrane is more negative than the bare PES membrane (C/P-0). Thus, C/P-0.5 membrane is more negatively charged than the bare PES membrane. However, zeta potential values of the C/P-2 and C/P-4 membranes could not be determined probably due to the increased amount of MWCNTs on the surface of the membranes. Water content of the C/P composite membranes was at maximum when the MWCNT content of the membrane was 0.5 wt%; beyond 0.5

Downloaded by STANFORD UNIV GREEN LIBR on June 19, 2012 | http://pubs.acs.org
Publication Date (Web): October 31, 2011 | doi: 10.1021/bk-2011-1078.ch015

wt%, the water content decreased. This is probably due to the increased porosity and pore size up to 0.5 wt% MWCNT addition and reduction of the porosity and pore size beyond 0.5 wt% MWCNT additions. The water contents of the composite membranes are consistent with the SEM images.

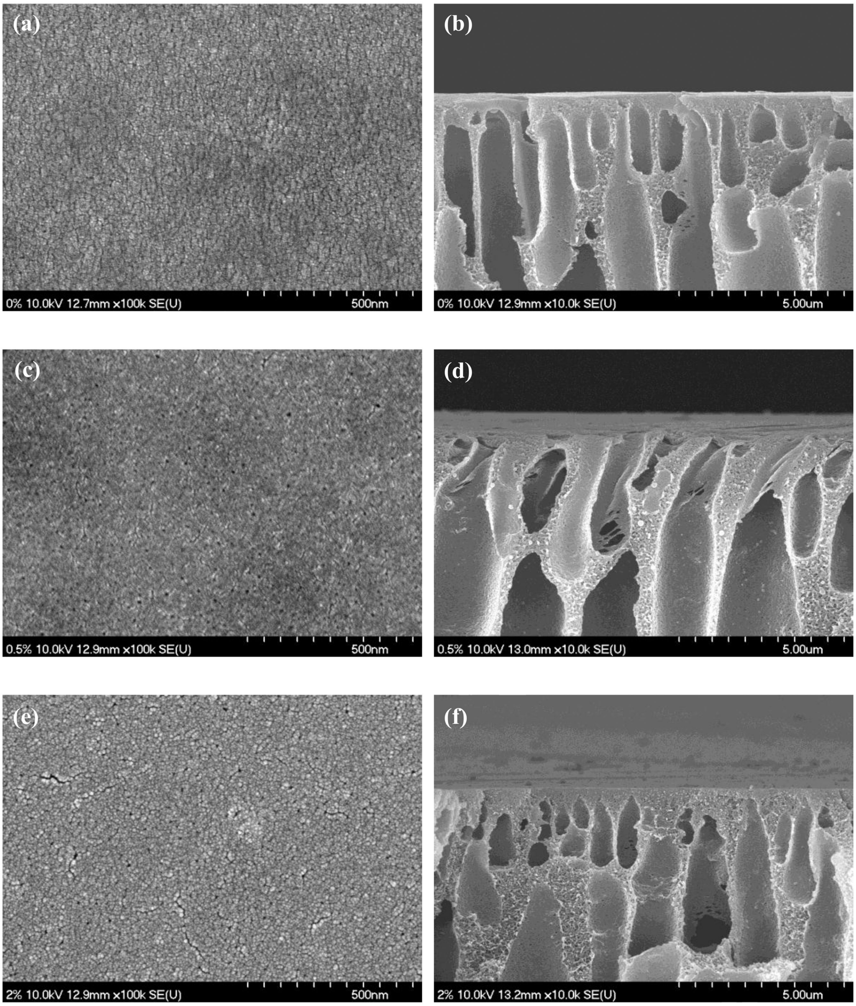
(a)
0% 10.0kV 12.7mm x100k SE(U)
500nm
(b)
0% 10.0kV 12.9mm x10.0k SE(U)
5.00um
(c)
0.5% 10.0kV 12.9mm x100k SE(U)
500nm
(d)
0.5% 10.0kV 13.0mm x10.0k SE(U)
5.00um
(e)
2% 10.0kV 12.9mm x100k SE(U)
500nm
(f)
2% 10.0kV 13.2mm x10.0k SE(U)
5.00um

Figure 1. SEM images of the top surface and the cross section of the C/P-0 (a and b), C/P-0.5 (c and d), and C/P-2 (e and f) membranes.

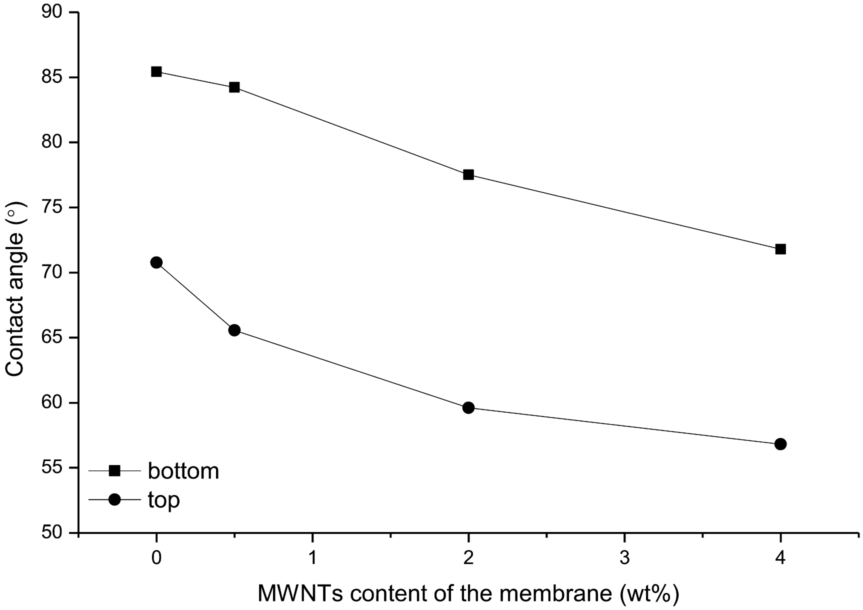

Figure 2. Contact angles of the top and the bottom surfaces of the C/P composite membranes as a function of MWCNTs content.

Permeability and Solute Rejection

It is known that the permeability of the membranes can be enhanced by improving hydrophilicities due to the attraction of the water molecules to the membrane matrix. As presented in Figure 3, 0.5 wt% of MWCNT addition increased the pure water flux drastically. However, when the concentration of MWCNT was more than 0.5 wt%, the pure water flux exhibited a declining trend. The increase in the pure water flux with 0.5 wt% MWCNT addition is presumably due to the fast exchange of the solvent and non solvent during phase inversion process. Addition of hydrophilic MWCNTs result in a higher porosity on the membrane surface. The increased porosity together with the increased hydrophilicity brings a higher pure water flux. On the other hand, the viscosity of the dope solution increases along with the MWCNT amount (*21*, *24*) which results in delay in exchange of the solvent and non solvent (*25*). Hence, the addition of MWCNT more than 0.5 wt% probably resulted in reduced porosity and pore size due to the increased viscosity. Even though the hydrophilicity of the composite membranes increased with increasing MWCNT amount, the lower porosity and pore size bring a lower pure water flux for the membranes with more than 0.5 wt% MWCNT addition. The pure water fluxes of the composite membranes are consistent with the water contents and SEM images of the composite membranes.

Permeation properties of the C/P composite membranes with different amounts of MWCNT were characterized using 1 g/L of PEG solution. The PEG permeation flux and the rejections are shown in Figure 4. The PEG permeability of the C/P composite membranes was followed a similar trend as the pure water

Downloaded by STANFORD UNIV GREEN LIBR on June 19, 2012 | http://pubs.acs.org
Publication Date (Web): October 31, 2011 | doi: 10.1021/bk-2011-1078.ch015

flux of the membranes. The PEG rejections of the C/P-2 and C/P-4 membranes were higher than the bare PES membrane, but the rejection of the C/P-0.5 membrane was lower than the bare PES membrane. Increased flux and lower rejection with C/P-0.5 membrane confirm the higher porosity and pore size due to the hydrophilic MWCNT addition. The rejection for the membrane with MWCNT concentration of 2 wt% was the highest among all the composite membranes. The membrane with 4 wt% MWCNT content showed a slightly less rejection than the membrane with 2 wt% MWCNT content. This might be attributed to the formation of the larger pores or flaws in the membrane structure due to the irregular positioning of the MWCNTs.

Downloaded by STANFORD UNIV GREEN LIBR on June 19, 2012 | http://pubs.acs.org
Publication Date (Web): October 31, 2011 | doi: 10.1021/bk-2011-1078.ch015

Table I. Properties of the C/P composite membranes

Membranes	*Water content (%)*	*Zeta potential at pH 8 (mV)*
C/P-0	69.7	-18.6
C/P-0.5	76.0	-23.4
C/P-2	74.2	NA
C/P-4	70.1	NA

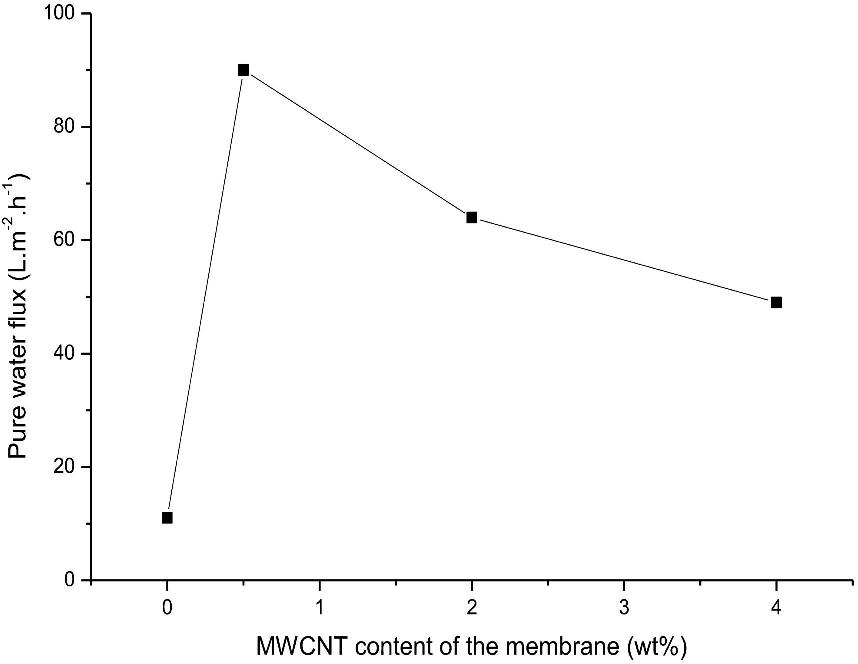

Figure 3. Pure water fluxes of the C/P composite membranes as a function of MWCNTs content.

Downloaded by STANFORD UNIV GREEN LIBR on June 19, 2012 | http://pubs.acs.org
Publication Date (Web): October 31, 2011 | doi: 10.1021/bk-2011-1078.ch015

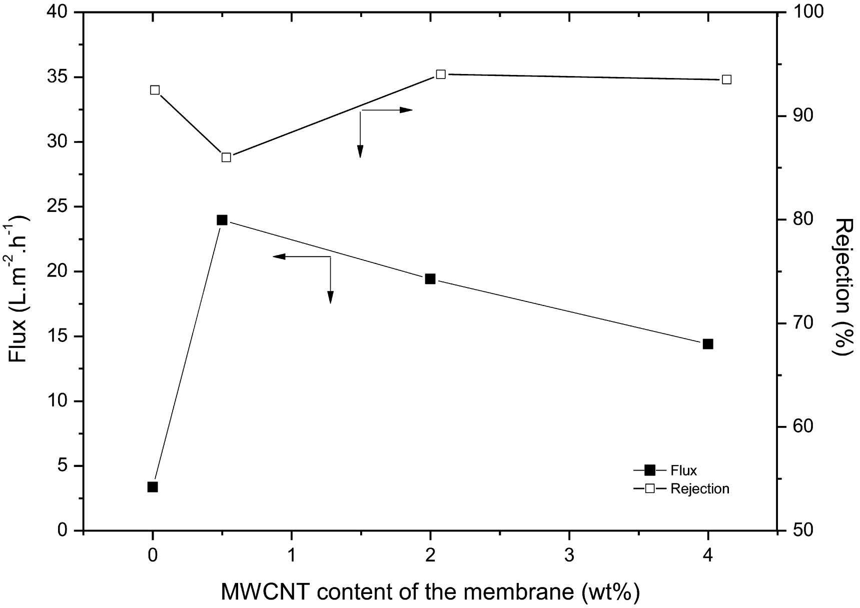

Figure 4. Solute permeation fluxes and rejections of the C/P composite membranes as a function of MWCNTs content.

Antifouling Properties of the Membranes

It is known that the membrane fouling is the main difficulty in membrane operations which could result in a decline in permeability and shorter membrane life. The affinity of the solute and the membrane such as sorption or deposition of solute on the membrane surface or in the membrane pores is the main cause of the membrane fouling. Hence, improving the membrane hydrophilicity is an effective method for fouling control (*8*). The antifouling ability of the composite membranes were investigated in terms of the hydraulic resistances of the membranes and shown in Table II. The hydraulic resistance model can be used to describe the effect of the MWCNT addition on the separation properties of the membranes. Hydraulic membrane resistance (R_m) represents the hydraulic resistance of the virgin membrane due to the differences in the microstructure such as surface porosity, cross-sectional structure, and pore size. Hydraulic resistance of the adsorbed layer (R_a) represents the hydraulic resistance due to the adsorption and the pore plugging. Hydraulic resistance of the concentration polarization layer (R_c) represents the hydraulic resistance due to the concentration polarization of the membranes (*9*). As it was shown in Table II, all 3 hydraulic resistances of the C/P composite membranes are significantly lower than the bare PES (C/P-0) membrane. Hydrophobic interactions of the membrane and the protein determine the fouling behavior in the low fouling regime (*26*). Therefore, increasing hydrophilicity resulted in lower hydraulic resistance of the adsorbed layer up to 2 wt% of MWCNT addition. Hydraulic resistance of the adsorbed layer reduces up to 2 wt% of MWCNT content, and increases beyond

2 wt% MWCNT content. The slight increase of the hydraulic resistance of the adsorbed layer above 2 wt% of MWCNT is presumably due to the irregular positioning of the MWCNT in the membrane structure. The order of the hydraulic membrane resistance according to the contents of the MWCNT of the composite membranes was 0% > 4% > 2% > 0.5%. This order is exactly opposite of the water content of the membranes (Table II). The order of the hydraulic resistance of the concentration polarization layer according to the contents of MWCNT of the composite membranes was 0% > 2% > 4% > 0.5%. This order is following the similar trend with the solute rejection properties of the composite membranes except the bare PES membrane. Concentration polarization occurs when the high flux is combined with high rejection (*27*). Thus, the C/P-2 membrane showed the highest hydraulic resistance of the concentration polarization layer due to the highest rejections and comparatively high flux.

Since the pore size and the pure water flux of membranes are different, the relative flux is generally used to compare the antifouling performances of the membranes. A high relative flux indicates a stronger antifouling ability (*9*). The relative fluxes of the composite membranes are shown in Figure 5. The bare PES membrane (C/P-0) showed the lowest relative flux among the composite membranes. The relative flux of the composite membranes increased up to 2 wt% MWCNT addition. Hydrophobic interaction between the membrane and the protein decreases with increasing hydrophilicity of the membrane which results in a weaker adsorption of proteins on hydrophilic membrane surfaces (*9*). This weak adsorbed protein layer was probably easily washed out during DI water flushing of the composite membranes with MWCNT content of 2 wt%. The lower relative flux of the composite membranes with more than 2 wt% MWCNT content might be due to the irregular positioning of the MWCNTs in the membrane structure.

Downloaded by STANFORD UNIV GREEN LIBR on June 19, 2012 | http://pubs.acs.org
Publication Date (Web): October 31, 2011 | doi: 10.1021/bk-2011-1078.ch015

Table II. Hydraulic resistances of the C/P composite membranes

Membranes	*C/P-0*	*C/P-0.5*	*C/P-2*	*C/P-4*
R_m ($\times 10^9$ m^{-1})	10.20	1.35	1.82	2.11
R_a ($\times 10^9$ m^{-1})	14.60	0.97	0.5	1.09
R_c ($\times 10^9$ m^{-1})	11.67	0.77	1.40	1.29

Downloaded by STANFORD UNIV GREEN LIBR on June 19, 2012 | http://pubs.acs.org
Publication Date (Web): October 31, 2011 | doi: 10.1021/bk-2011-1078.ch015

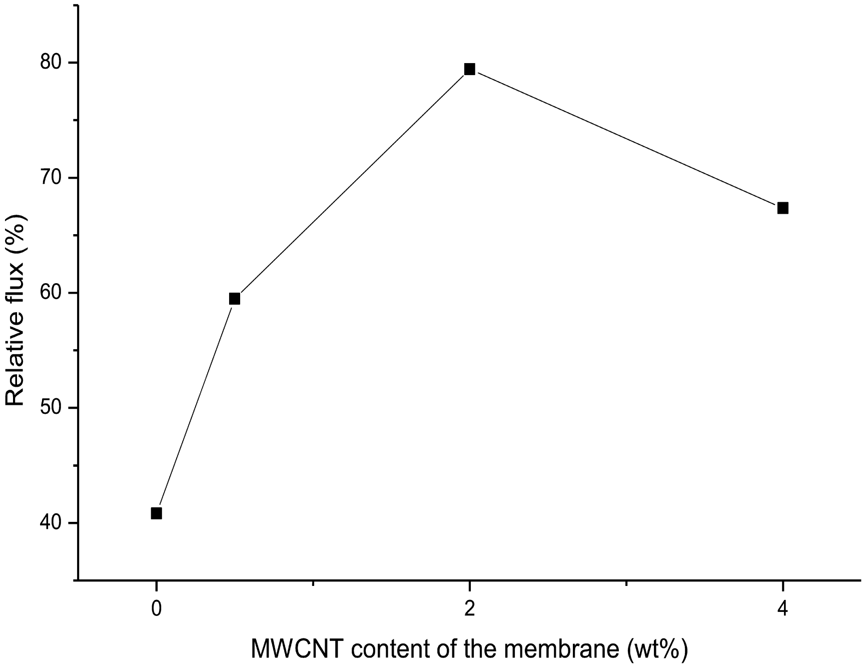

Figure 5. Relative fluxes of the C/P composite membranes as a function of MWCNTs content.

Conclusion

In this paper, C/P composite membranes were prepared via phase inversion method. From the findings of this study the following conclusions can be drawn:

(1) The addition of MWCNT improved the pure water flux, hydrophilicity and permeation properties of the composite membranes.
(2) The hydraulic resistances of the C/P composite membranes were significantly lower than the bare PES membrane. Also, hydraulic resistance of the adsorbed protein layer was decreased by increasing the hydrophilicity of the C/P composite membranes.
(3) The relative flux of the C/P-2 membrane was significantly higher than the bare PES membrane.
(4) The membrane with 2 wt% of MWCNT has ideal permeation properties in terms of pure water flux, rejection and antifouling ability.

Downloaded by STANFORD UNIV GREEN LIBR on June 19, 2012 | http://pubs.acs.org
Publication Date (Web): October 31, 2011 | doi: 10.1021/bk-2011-1078.ch015

Acknowledgments

We acknowledge the support of the Gwangju Institute of Science and Technology (GIST), Korea under the Basic Research Project.

References

1. Choi, H.; Zhang, K.; Dionysiou, D. D.; Oerther, D. B.; Sorial, G. A. Effect of permeate flux and tangential flow on membrane fouling for wastewater treatment. *Sep. Purif. Technol.* **2005**, *45* (1), 68–78.
2. Mulder, M. *Basic principles of membrane technology*, 2nd ed.; Kluwer Academic Publishers: The Netherlands, 1997.
3. Cheryan, M. *Ultrafiltration handbook*; Technomic Publishing Company, Inc.: Lancaster, PA, 1986.
4. Rahimpour, A.; Madaeni, S. S. Polyethersulfone (PES)/cellulose acetate phthalate (CAP) blend ultrafiltration membranes: Preparation, morphology, performance and antifouling properties. *J. Membrane Sci.* **2007**, *305* (1-2), 299–312.
5. Shi, Q.; Su, Y. L.; Zhu, S. P.; Li, C.; Zhao, Y. Y.; Jiang, Z. Y. A facile method for synthesis of pegylated polyethersulfone and its application in fabrication of antifouling ultrafiltration membrane. *J. Membrane Sci.* **2007**, *303* (1-2), 204–212.
6. Chen, J. P.; Mou, H.; Wang, L. K.; Matsuura, T. Membrane filtration. In *Advanced physicochemical treatment processes, handbook of environmental engineering*; Wang, L. K., Hung, Y. T., Shammas, N. K., Eds.; Humana Press Inc.: Totowa, NJ, 2006; Vol. 4, p 203.
7. Reddy, A. V. R.; Patel, H. R. Chemically treated polyethersulfone/polyacrylonitrile blend ultrafiltration membranes for better fouling resistance. *Desalination* **2008**, *221* (1-3), 318–323.
8. Yang, Y. N.; Zhang, H. X.; Wang, P.; Zheng, Q. Z.; Li, J. The influence of nano-sized TiO_2 fillers on the morphologies and properties of PSFUF membrane. *J. Membrane Sci.* **2007**, *288* (1-2), 231–238.
9. Huang, Z. Q.; Chen, K.; Li, S. N.; Yin, X. T.; Zhang, Z.; Xu, H. T. Effect of ferrosoferric oxide content on the performances of polysulfone-ferrosoferric oxide ultrafiltration membranes. *J. Membrane Sci.* **2008**, *315* (1-2), 164–171.
10. Li, S. N.; Lin, M. M.; Toprak, M. S.; Kim, D. K.; Muhammed, M. Nanocomposites of polymer and inorganic nanoparticles for optical and magnetic applications. *Nano Rev.* **2010**, *1*, 5214.
11. Iijima, S. Helical microtubules of graphitic carbon. *Nature* **1991**, *354*, 56–58.
12. Harris, J. F. *Carbon nanotubes and related structures: New materials for the twenty-first century*; Cambridge University Press: U.K., 1999.
13. Santos, C. V.; Hernandez, A. L. M.; Castano, V. M. Carbon nanotube – polymer nanocomposites: Principles and applications. In *Focus on nanotube research*; Martin, D. A., Ed.; Nova Science Publisher: Hauppauge, NY, 2006; p 97.
14. Ash, B. J.; Eitan, A.; Schadler, L. S. Polymer nanocomposites with particle and carbon nanotube fillers. In *Encyclopedia of Nanoscience and*

Nanotechnology; Schwarz, J. A., Contescu, C. I., Putyera, K., Eds.; CRC: Boca Raton, FL, 2004; Vol. 4.

15. Zhu, J.; Kim, J. D.; Peng, H. Q.; Margrave, J. L.; Khabashesku, V. N.; Barrera, E. V. Improving the dispersion and integration of single-walled carbon nanotubes in epoxy composites through functionalization. *Nano Lett.* **2003**, *3* (8), 1107–1113.
16. Hirsch, A.; Vostrowsky, O. Functionalization of carbon nanotubes. In *Topics in Current Chemistry*; Schuster, G. B., Lee, J. K., Angelov, D., Tantillo, D. J., Eds.; Springer: New York, 2005; p 193.
17. Zhang, N. Y.; Me, J.; Varadan, V. K. Functionalization of carbon nanotubes by potassium permanganate assisted with phase transfer catalyst. *Smart Mater. Struct.* **2002**, *11* (6), 962–965.
18. Liu, J.; Rinzler, A. G.; Dai, H.; Hafner, J. H.; Bradley, R. K.; Boul, P. J.; Lu, A.; Iverson, T.; Shelimov, K.; Huffman, C. B.; Rodriguez-Macias, F.; Shon, Y. S.; Lee, T. R.; Colbert, D. T.; Smalley, R. E. Fullerene pipes. *Science* **1998**, *280*, 1253–1256.
19. Celik, E.; Park, H.; Choi, H.; Choi, H. Carbon nanotube blended polyethersulfone membranes for fouling control in water treatment. *Water Res.* **2011**, *45* (1), 274–282.
20. Arthanareeswaran, G.; Latha, C. S.; Mohan, D.; Raajenthiren, M.; Srinivasan, K. Studies on cellulose acetate/low cyclic dimmer polysulfone blend ultrafiltration membranes and their applications. *Sep. Sci. Technol.* **2006**, *41* (13), 2895–2912.
21. Choi, J. H.; Jegal, J.; Kim, W. N. Fabrication and characterization of multi-walled carbon nanotubes/polymer blend membranes. *J. Membrane Sci.* **2006**, *284* (1-2), 406–415.
22. Shim, J. K.; Na, H. S.; Lee, Y. M.; Huh, H.; Nho, Y. C. Surface modification of polypropylene membranes by gamma-ray induced graft copolymerization and their solute permeation characteristics. *J. Membrane Sci.* **2001**, *190* (2), 215–226.
23. Sun, M. P.; Su, Y. L.; Mu, C. X.; Jiang, Z. Y. Improved Antifouling Property of PES Ultrafiltration Membranes Using Additive of Silica-PVP Nanocomposite. *Ind. Eng. Chem. Res* **.2010**, *49* (2), 790–796.
24. Qiu, S.; Wu, L. G.; Pan, X. J.; Zhang, L.; Chen, H. L.; Gao, C. J. Preparation and properties of functionalized carbon nanotube/PSF blend ultrafiltration membranes. *J. Membrane Sci.* **2009**, *342* (1-2), 165–172.
25. Han, M. J.; Nam, S. T. Thermodynamic and rheological variation in polysulfone solution by PVP and its effect in the preparation of phase inversion membrane. *J. Membrane Sci.* **2002**, *202* (1-2), 55–61.
26. Huisman, I. H.; Pradanos, P.; Hernandez, A. The effect of protein-protein and protein-membrane interactions on membrane fouling in ultrafiltration. *J. Membrane Sci.* **2000**, *179*, 79–90.
27. Vankelecom, I. F. J.; Gevers, L. E. M. Membrane processes. In *Green separation processes: Fundamentals and applications*; Afonso, A. M., Crespo, J. G., Eds.; Wiley WCH: Germany, 2005; p 251.

Downloaded by STANFORD UNIV GREEN LIBR on June 19, 2012 | http://pubs.acs.org
Publication Date (Web): October 31, 2011 | doi: 10.1021/bk-2011-1078.ch015

Chapter 16

Investigation of the Effects of Thickness and Presence of Pore Formers on Tailor-Made Ultrafiltration Polysulfone Membranes

Sepideh Hakim Elahi and Isabel C. Escobar[*]

Department of Chemical & Environmental Engineering,
The University of Toledo, 2801 W. Bancroft St.,
MS 305, Toledo, Ohio, 43606
[*]E-mail: isabel.escobar@utoledo.edu

Membranes are capable of separating species as a function of their physical and chemical properties when a driving force is applied, which enables filtration for removal of colloids, cells and molecules. In this work, flat sheet polysulfone ultrafiltration membranes were cast due to polysulfone's high mechanical strength, thermostability and stability against chemicals. The main goal was to investigate the effects of dope concentration, membrane thickness and inorganic additive, lithium chloride (LiCl), on the filtration of different salt concentrations. The results revealed that with increasing dope concentration and membrane thickness, permeability decreased and subsequently salt rejection increased. Furthermore, compared to LiCl-free membranes, LiCl-containing ones were more permeable and displayed higher salt rejection, which was due to more porosity and smaller pore size caused by LiCl additives in membranes.

Introduction

Membrane technology has become an interesting, useful separation method over the past decades due to higher efficiencies and with advances, lower energy requirements for operation. As a result companies have started to utilize them as an alternative for many water purification processes. Membrane properties, such as permeability and rejection, are greatly influenced by the thickness of the membrane (*1–3*), the method of casting the membrane (*4*) and dope solution chemistry (*1*),

In Modern Applications in Membrane Science and Technology; Escobar, I., et al.;
ACS Symposium Series; American Chemical Society: Washington, DC, 2011.

which itself depends on many factors like dope concentration and additives or pore formers. Permeability and rejection are also influenced by the membranes filter solution.

For water purification processes, there are four major kinds of membranes currently used, reverse osmosis, nanofitration, ultrafiltration and microfiltration. Membranes are manufactured from a variety of materials, such as cellulose acetate (CA), cellulose diacetate (CDA), cellulose triacetate, polyamide (PA), other aromatic polyamides, polyetheramides, polyetheramines, polysulfone (PSf), and polyetherurea; also, thin-film composite (TFC) membranes may be made from a variety of polymers consisting of several different materials for the substrate, the thin film and other functional layers. In this work tailor-made flat-sheet PSf membranes were used due to polysulfone's high mechanical strength, thermostability and stability against chemicals.

Ultrafiltration polysulfone (PSf) membranes were chosen to investigate the effects of different casting solution (dope) concentrations, casting thickness, addition of pore-forming additives, and subsequently, the membrane properties of permeability and salt rejection. Therefore, at first, PSf membranes with different concentrations and thicknesses were cast via immersion precipitation (*5*, *6*). They were then precompacted with distilled water followed by the filtration of salt solutions of different concentrations. Then, the exact same membranes were cast with the addition of a pore-forming additive, lithium chloride (LiCl), to determine the significance of the addition of the pore former on the membrane's permeability and salt rejection.

Experimental Section

Materials and Casting Instrument

Chemicals purchased, polysulfone (PSf, Aldrich, Mn: 22000), 1-methyl-2-pyrrolidinone (NMP, Alfa Aesar, 99%) and lithium chloride (LiCl, Sigma-Aldrich, 99%) were used as received. For membrane preparation, a BYK-Gardner film casting knife (Figure 1) was used, and dial gauges were used to measure the thickness in different parts of the membrane to determine the average thickness.

Membrane Preparation

In either the absence or presence of LiCl, casting solutions (i.e. dopes) of different concentrations were made: 10, 12, 13, 15, 16 and 18wt% PSf. These dopes were prepared by adding PSf to NMP and stirring for about 24 hours. Then, by using an adjustable BYK-Gardner film casting knife, the dope was spread on a glass substrate at different thicknesses (optimal thickness range was found to lie between 120-240 micrometers). The formed film on the glass substrate was then put into a coagulation bath filled with deionized water (DI) to separate it from the glass surface. Therefore, flat-sheet membranes (Figure 2) were formed via phase inversion (*5–7*). The reason for using glass instead of Teflon or some other substrates was because of obtaining higher permeability due to less formed shrinkage (*4*).

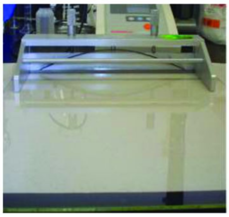

Figure 1. Film casting knife.

Figure 2. Flat sheet PSf membrane.

Precompaction and Filtration

For filtration experiments, dead-end filtration tests, in which applied pressure is a driving force and the only outlet for upstream fluid or feed is through the membrane, were performed using an Amicon 8010 stirred cell (Figure 3) with a rotating speed of about 300 rpm and an applied pressure of 70 psi was used. Small membrane samples of 4.1 cm^2 surface area were cut from similar locations on the cast membranes, and were precompacted by means of using DI water in the filtration cell for six hours. After approximately 6 hours of precompaction upon reaching stable fluxes, filtration of salt solutions of different concentrations was started.

Sodium chloride (NaCl) solutions of different concentrations, also under 70 psi pressure, were filtered for approximately six hours. Flux was measured for every 2 mL permeate volume; that is, time was measured for the filtration of 2 mL, while the filtration cell volume was 10 mL. In detail, the time to filter 2 mL from 6 to 4 mL was measured, which means both precompaction and filtration processes were run for 6 mL solutions separately. After gathering 4 mL DI water from running the test, the time was measured for the next 2 mL. The same was done for salt filtration in order to obtain reliable flux data.

It should be noted that flux data reported (Figures 4−11) do not represent flux measurements evenly every 2 mL; instead, they show flux measurements for 2 mL from each run. That is, if precompaction lasted for 6 hours and 5 runs were needed, for each run the flux was measured for a 2 mL volume. This was done because at the beginning flux was obviously high due to no precompaction, but after 4 mL the flux was more reliable and stable to be measured. This was verified by running different precompaction tests for membranes of same thicknesses.

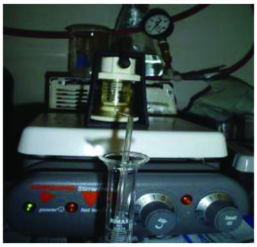

Figure 3. Filtration Instrument (Dead-End Method).

Salt rejection was measured by using the following equation:

$$\text{Rejection: } \frac{[(\text{feed conductivity}) - (\text{permeate conductivity})]}{\text{feed conductivity}}$$

Where the permeate conductivity is the average conductivity of permeate measurements obtained throughout filtration. Conductivity was measured by a portable conductivity meter Accumet® AP75 (Catalog No. 13636 AP75A, Fisher Scientific, PA).

Results and Discussion

Casting Solution Concentration

It was first determined that cast solutions of 10 and 12 wt% PSf led to inconsistent membranes that would tend to tear during filtration. Higher dope concentrations, such as 16 and 18wt%, were then tested. In such cases, casting of membranes was possible, but with resulting very low flux values even at a low thicknesses (for example, a thickness of 100μm led to a precompaction flux of 3 L/m^{2}hr, which was deemed too low for adequate prolonged testing. Therefore, dope solutions of 13 and 15wt% were tested, and were found to be able to lead to consistent (i.e. reproducible) membranes with reasonable flux measurements for testing. Also, precompaction tests were performed at different pressures: 50-60 and 70 psi, and the fact that with increasing the pressure, permeate flux increased, was verified and a pressure of 70 psi was chosen for testing. This is true in this study since the membrane used was ultrafiltration, so concentration polarization did not occur significantly to dominate the flux.

Precompaction and filtration flux data for 13wt% PSf dope solutions in the absence of LiCl for different thicknesses are shown in Figures 4 and 5. Both figures show that as the membrane became thicker, flux decreased due to the increased resistance to filtration, as expected. Furthermore, as the salt concentration increased, flux decreased. With membrane of higher thickness (220 μm), final flux values after filtration of 20 mM NaCl was about 5.3 L/m^{2}hr while the resultant flux obtained from filtration of 100 mM NaCl of a thinner membrane (165 μm) was 16.2 L/m^{2}hr (Table I). In other words, although higher flux values are expected from filtration of lower salt concentrations, this study obtained higher fluxes from higher concentrations due to using membrane of lower thicknesses. Thereby, it can be concluded that membrane thickness displayed a more significant effect on flux than salt concentration.

Figures 6 (6a-6b) and 8 show precompaction and filtration results for 15wt% PSf membranes of different thicknesses. Figures 6a and 6b show the precompaction and filtration, respectively, using 15wt% PSf dopes at lower membrane thicknesses, while Figure 8 at higher thicknesses. To show the reproducibility of the cast membranes, precompaction and filtration for membranes of the same thickness of 155µm were performed three times, and the resultant precompaction flux values were not significantly different (shown in Figure 7). Similar conclusions to the 13wt% membranes were observed with the difference that more concentrated dopes led to lower flux values overall.

As can be seen in all figures, the decrease in precompaction and filtration flux values over time always occurred. Mosqueda-Jimenez et al (*8*) reported, precompaction compresses the membrane, so membranes with more compressible structures, such as polysulfone, experience a reduction in flux during precompaction. The flux reductions are explained by more compaction and by possible concentration polarization during the dead-end filtration of salt solutions, respectively.

Tables I and II show that membrane thickness and the concentrations of both the casting dope and the filtration (NaCl) solutions had a noticeable effect on the permeate flux. Higher thicknesses and casting dope solution concentrations lead to less permeability and subsequently higher rejection (*1*, *2*). Average flux in Tables means the average of fluxes once flux values became consistent, such as during the last 3 hours. That was done bacause precompaction and filtration were done for approximately 6 hrs each, but flux changes were not stable from the beginning.

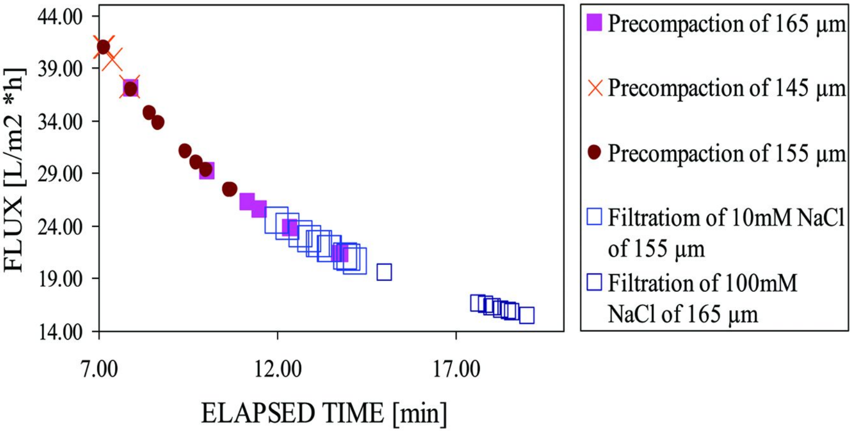

Figure 4. Precompaction and filtration flux data for 13wt%PSf of relatively low thickness (µm).

All flux declines were rather low. It was during precompaction that the majority of the flux decline was observed and that was due to the compression of the PSf membranes. The trends of interest here were not the declines in flux due to the filtration of salt solutions; instead, the focus was the comparison of the effects of dope concentration, presence of LiCl and membrane thickness. The data in Figures 4−8 show that salt solutions had a low effect on flux decline but do provide information on the differences from dope concentration, LiCl and thickness. Based upon the data in Table I, the 13wt% membrane's maximum and minimum flux values for the thickness range of 145-220μm were approximately 40 and 9 L/m^{2}hr, respectively. For 15wt% membranes, Table II shows that for thicknesses in the range of 125-220μm, the maximum and minimum flux values were approximately 27 and 7 L/m^{2}hr, respectively.

Effect of LiCL Additive

Several studies have shown that casting solution properties have a significant influence on asymmetric membrane formation and subsequently its structure (*2*, *9*–*15*). To determine the effects of the addition of a pore-former, lithium chloride (LiCl), the 15wt% PSf dope concentration was chosen since it displayed better behavior in comparsion to 13 Wt.%. Therefore, the ternary solution, PSf, NMP and LiCl (as a pore-former), was prepared to find out the effect of the pore former on membrane performance. In previous published research (*9*, *16*), LiCl changed the membrane morphology and caused changes in permeability and rejection. In this work, the flux after precompaction and filtration was directly measured for the PSf membranes. Solutions of 1, 1.5 and 2 wt% LiCl were added to the solutions containing 15wt% PSf in NMP. In this work, 2wt% LiCl was found too viscous and it was difficult to obtain a smooth, flat-sheet membrane with no excessively large pores. With 2 wt% LiCl, there were noticeably porous on the surface.

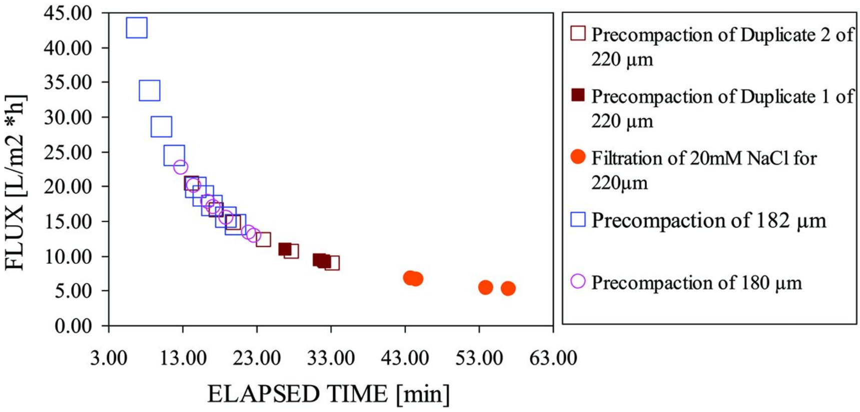

Figure 5. Precompaction and filtration flux data for 13wt%PSf of higher thickness.

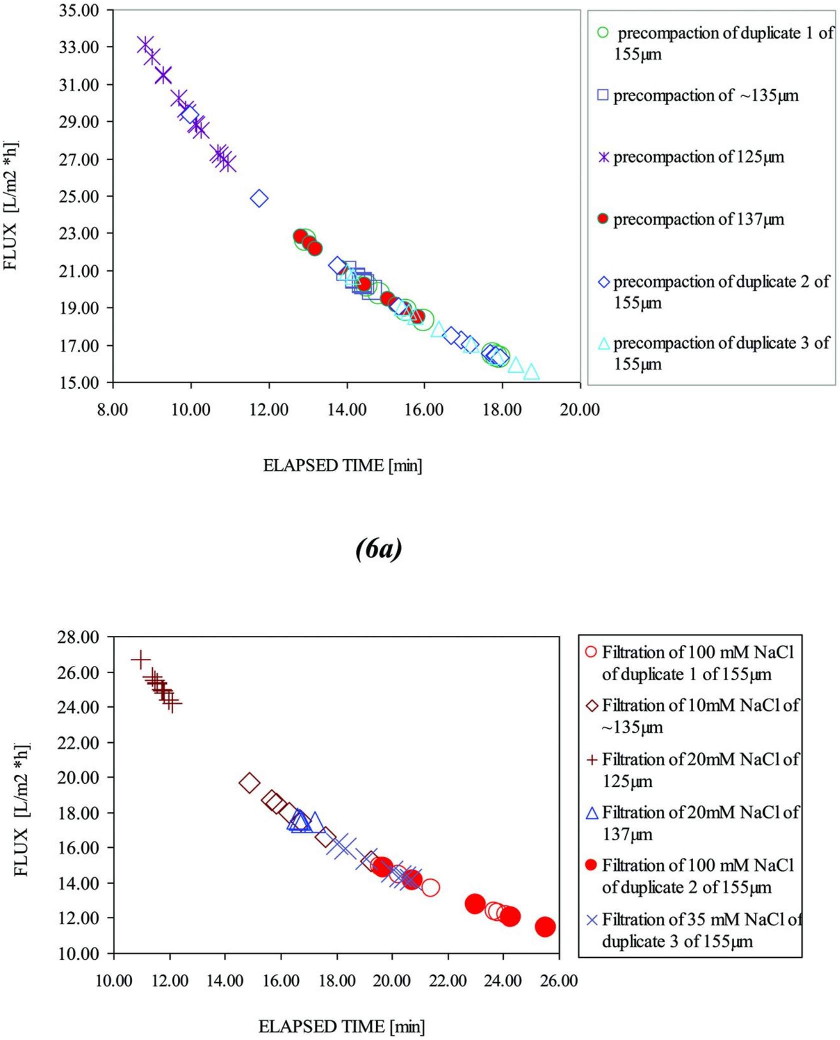

(6a)

(6b)

Figure 6. (6a). Precompaction and (6b). filtration flux data for 15wt%PSf of relatively low thickness.

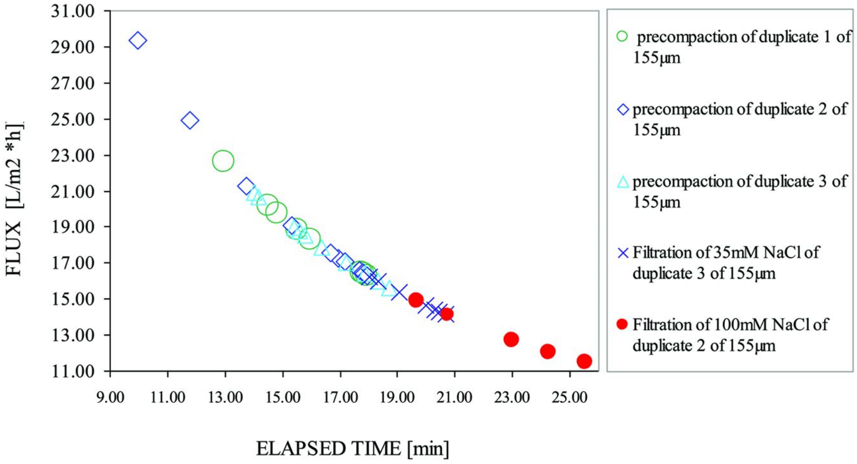

Figure 7. Precompaction and filtration of membranes of 155 µm thickness.

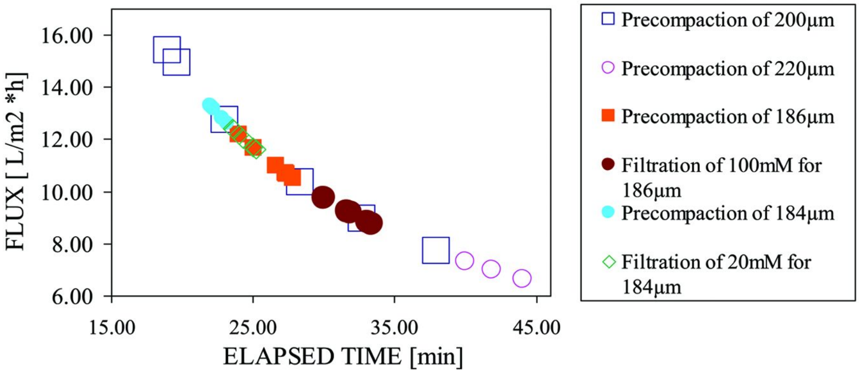

Figure 8. Precompaction and filtration flux data for 15wt%PSf of higher thickness.

Table I. Precompaction and Filtration flux data of 13wt% PSf membrane in the absence of LiCl

Thickness (µm)	145	155	165	180	182	220
Avg. Precompaction Flux (L/m²hr)	40.3	29.0	23.6	13.1	12.2	9.4
NaCl Concentration	_	10 mM	100 mM	_	_	20 mM
Avg. Filtration Flux (L/m²hr)	_	21.5	16.2	_	_	5.3

Note: Any "-" indicates tests were not performed for those thicknesses.

Table II. Precompaction and Filtration flux data of 15wt% PSf membrane in the absence of LiCl

Thickness (µm)	125	135	137	155	184	186	200	220
Avg. Precompaction Flux (L/m²hr)	27.1	20.3	18.9	16.4	12.7	10.7	8.9	6.9
NaCl Concentration	20 mM	10 mM	20 mM	35 mM	20 mM	100 mM	–	–
Avg. Filtration Flux (L/m²hr)	24.7	17.7	17.5	14.4	11.9	8.9	_	_

Note: Any "-" indicates tests were not performed for those thicknesses.

Therefore in this work the maximum appropriate LiCl concentration was found to be 1.5wt% with respect to obtaining higher flux and also being easier to be employed for membrane casting. In Figures 9 through 11, flux measurements for membranes cast using 15wt% PSf dope including 1.5wt% LiCl and with different thicknesses are presented.

It is important to mention that all flat-sheets were cast under the same conditions, and all flux measurements were performed with exact same procedure. Because of these measures to make data obtained reproducible, applicable and reliable, Figures 4−11 presented a smooth and gradual decrease in flux, with flux values falling on a single, characteristic line of flux vs elapsed time. The characteristic line indicated, as expected, that as membrane thickness increased, flux decreased due to increased resistance to flow. Furthermore, since tested membranes were ultrafiltration, the effect of concentration polarization from the filtration of salt solutions was not high, as it would be in the case of reverse osmosis or nanofiltration. Therefore, flux values obtained during the filtration of the salt solutions also fell on the characteristic line albeit at lower fluxes showing minor concentration polarization occurring.

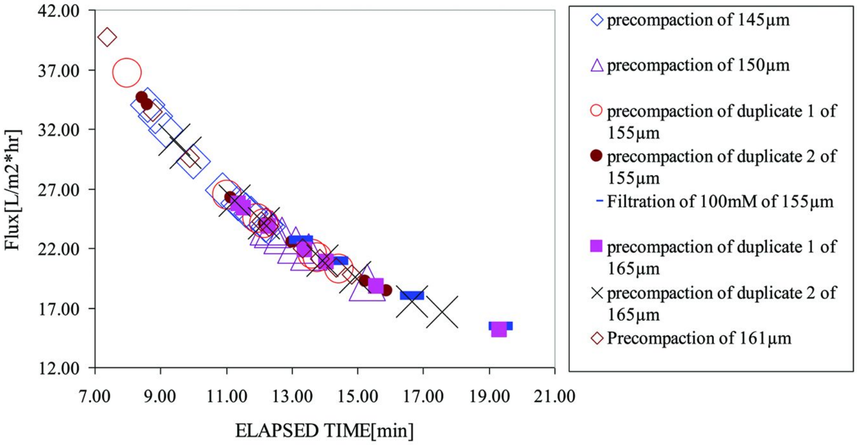

Figure 9. Precompaction flux data for membranes of relatively low thickness cast by 15wt%PSf +1.5% LiCl solution.

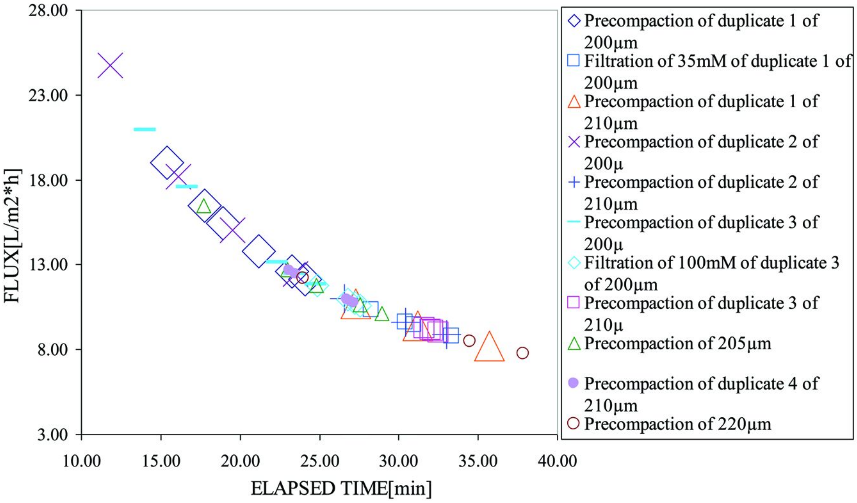

Figure 10. Precompaction flux data for membranes of high thickness cast by 15wt%PSf +1.5% LiCl solution accompanying by two filtration data for 200µm.

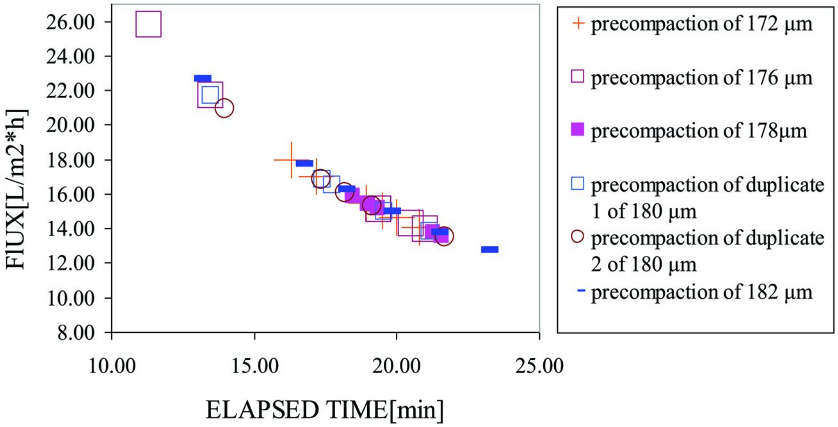

Figure 11. Precompaction flux data for 15wt%PSf +1.5% LiCl.

From Figures 9−11, once more, the effects of thickness and filtration solution concentration on the membrane performance were observed. Flux values after precompaction and filtration (only NaCl solution) for membranes cast with LiCl in the dope are summarized in Table III. When flux values were compared for 15wt% PSf membranes of similar thicknesses with the only difference being the presence of LiCl in the dope (Tables II and III), the effect of LiCl on membrane permeability can be observed. LiCl-free membranes of 155 µm thickness had average precompaction fluxes of 16 L/m^{2}hr, while those containing the pore former (LiCl) in the casting dope and of the same thickness had average fluxes of 22 L/m^{2}hr. As Hyuck et al (*16*) explained, the higher permeability can be elucidated by the interaction between NMP (solvent) and LiCl, which leads to a NMP-LiCl complex. This complex causes a reduction in solvent (NMP) strength that means the polymer (polysulfone) can be less dissolved in the solvent, and consequently, the polymer aggregates in the solution (*16*). Thus, this aggregation reduces macrovoids formation, which means membranes with more porosities and, thus, higher fluxes (*1*, *2*, *10*, *16*).

Rejection Measurements

Rejection of NaCl solutions by 15wt% PSf in the absence of LiCl are presented in Table IV, while those for 15wt% PSf in the presence of 1.5wt% LiCl are shown in Tables V and VI.

Table III. Precompaction and Filtration (only NaCl solution) flux data of 15wt%PSf+1.5%LiCl

Thickness(µm)	**165**	**200**	**145**	**~170**	**200**	**202**
Avg. Precompaction Flux (L/m^{2}hr)	18.7	13	25.4	17.3	12.5	11
NaCl Concentration	**20mM**	**35mM**	**100mM**	**100mM**	**100mM**	**100mM**
Avg. Filtration Flux (L/m^{2}hr)	11.4	9.6	18.8	11.4	10.8	8.5

Table IV. Rejection data for 15wt%PSf solution excluding LiCl

Thickness(µm)	**155**	**155**	**184**
NaCl Concentration	**35mM**	**100mM**	**20mM**
Fraction Rejection	0.036	0.031	0.036

Table V. Rejection data from filtration of 100mM NaCl solution for 15wt%PSf solution including LiCl

Thickness(µm)	**145**	**160**	**170**	**203**
Fraction Rejection	0.05	0.06	0.057	~0.07

Table VI. Rejection data from filtration of 35mM NaCl solution for 15wt%PSf solution including LiCl

Thickness(µm)	**200**	**135**
Fraction Rejection	0.08	0.046

According to the tables above, it was observed that as thickness increased, the resistance to permeability increased and the salt rejection increased. Furthermore, at higher salt concentrations, concentration polarization led to a decrease in filtration flux (*17*).

Based on the presented results, casting membranes using 15wt% PSf dopes including 1.5wt% LiCl showed the highest overall efficiency due to the increase in both permeability and NaCl rejection because of the change in membrane morphology. This trend can be explained as a result of higher porosity with lower pore size as a result of the LiCl additive (*10*). However, since the membrane used was ultrafiltration, rejection of NaCl solutions was low, as expected. Rejection values were therefore not significantly different and just indicate a trend.

Conclusion

For ultrafiltration, it was found that 13 and 15wt% PSf dopes produced membranes that were reproducible and able to be tested in a dead-end mode to exaggerate experimental conditions. Precompaction flux values for membranes cast using 13wt% PSf dopes were higher than those cast using 15wt% PSf dopes. However, by employing 15wt% PSf dopes, membranes of lower thicknesses could be obtained because of the more viscous dope. The 15wt% membranes also displayed higher NaCl rejections, as expected, by denser membranes. It was also determined that membrane thickness affected flux; with higher thicknesses leading to lower fluxes and higher rejections. Moreover, adding LiCl to 15wt% PSf dope decreased the interaction between NMP and polysulfone, which led to polymer aggregation that decreased macrovoids, and as a result, enhanced the membrane porosity and subsequently the permeability. An increase in salt rejection for membranes cast with the addition of LiCl in the dope was also observed.

Acknowledgments

The authors would like to acknowledge the funding source (NSF GRS 1037842), and Drs. Cyndee Gruden and Tilak Gullinkala.

References

1. Mohamed, N. A.; Al-Dossary, A. O. H. *J. Eur. Polym.* **2003**, *39*, 1653–1667.
2. Mohamed, N. A. *J. Polym.* **1997**, *38*, 4705–4713.
3. Mosqueda-Jimenez, D. B.; Narbaitz, R. M.; Matsuura, T.; Chowdhury, G.; Pleizier, G.; Santerre, J. P. *J. Membr. Sci.* **2004**, *231*, 209–224.
4. Aerts, P.; Genn′e, I.; Leysen, R.; Jacobs, P. A.; Vankelecom, I. F. J. *J. Membr. Sci.* **2006**, *283*, 320–327.
5. Zheng, Q. Z.; Wang, P.; Yang, Y. N. *J. Membr. Sci.* **2006**, *279*, 230–237.
6. Zheng, Q.; Wang, P.; Yang, Y.; Cui, D. *J. Membr. Sci.* **2006**, *286*, 7–11.
7. Kim, J.; Lee, K. *J. Membr. Sci.* **1998**, *138*, 153–163.
8. Mosqueda-Jimenez, D. B.; Narbaitz, R. M.; Matsuura, T. *J. Envir. Engr.* **2004**, *130* (1), 90–99.
9. Yeow, M. L.; Liu, Y. T.; Li, K. *J. Polym. Sci.* **2004**, *92*, 1782–1789.
10. Bottino, A.; Capannelli, G.; Munari, S.; Turturro, A. *J. Desalination* **1988**, *68*, 167–177.
11. Kim, S. R.; Lee, K. H.; Jhon, M. S. *J. Membr. Sci.* **1996**, *119*, 59–64.
12. Wang, D.; Li, K.; Teo, W. K. *J. Membr. Sci.* **2000**, *178*, 13–23.
13. Won, J.; Park, H. C.; Kim, U. Y.; Kang, Y. S.; Yoo, S. H.; Young Jh, J. *J.Membr. Sci.* **1999**, *162*, 247–255.
14. Won, J.; Kang, Y. S.; Park, H. C.; Kim, U. Y. *J.Membr. Sci.* **1998**, *145*, 45–52.
15. Idris, A.; Ahmed, I.; Limin, M. A. *J. Desalination* **2010**, *250*, 805–809.
16. Lee, H. J.; Won, J.; Lee, H.; Kang, Y. S. *J. Membr. Sci.* **2002**, *196*, 267–277.
17. Sablani, S.; Goosena, M. F. A.; Al-Belushi, R.; Wilf, M. *J. Desalination* **2001**, *141*, 269–289.

Chapter 17

Reversible Ion Exchange-Membrane (RIX-M) Process for Fouling Free and Energy Efficient Desalination of Seawater

Sudipta Sarkar,* Ryan C. Smith, and Arup K. SenGupta

Fritz Engineering Laboratory, Department of Civil and Environmental Engineering, Lehigh University, Bethlehem, PA 18015
***E-mail: sus9@lehigh.edu**

Reversible ion exchange-membrane (RIX-M) is a hybrid process of desalination in which scale formation potentials of seawater can be eliminated by changing the chemistry of the feed water through the introduction of a reversible cation exchange step before the membrane based desalination step. In this process, scale forming di- or other poly-valent cations like calcium, barium, strontium, etc. are exchanged for equivalent concentrations of magnesium ions when the saline water is passed through a bed of cation exchanger pre-saturated in magnesium form. Near-complete replacement of scale forming cations by non-scale forming magnesium ions allows for obtaining a higher permeate flux compared to the conventional RO process. Addition of anti-scaling agent can be avoided altogether. Also, the exchange of magnesium ions for monovalent sodium ions, either partly or fully, reduces the osmotic pressure of the resultant feed solution to the membrane. Thus, the membrane process can operate with high permeate water recovery and enhanced energy efficiency for natural saline water like sea and brackish water and other industrial saline water effluents. The concentrated return from the membrane process is used as a regenerant for the exhausted ion exchanger. Thus, once started, the process can be sustained without requiring any external addition of regenerant chemicals.

In Modern Applications in Membrane Science and Technology; Escobar, I., et al.;
ACS Symposium Series; American Chemical Society: Washington, DC, 2011.

Introduction

Desalination of sea and brackish water using a membrane is essentially a physical separation of the salt and water phases across a semi-permeable membrane. Separation of the phases takes place under the influence of a chemical potential gradient created either by the application of pressure (reverse osmosis, nanofiltration, etc.), concentration gradient (forward osmosis), electrical potential (electrodialysis), or combinations of them. During the past years, there have been continuous improvements in the reverse osmosis (RO) process in terms of membrane and energy recovery devices making the process the most cost-efficient and popular method of desalination at present. However, despite these advancements, membrane-based desalination processes still suffer from major drawbacks that tend to limit its wide-scale applications for the production of freshwater from brackish or sea water sources. The Desalination and Water Purification Technology Roadmap (DWPTR) from the US Department of Interior reiterates the need to address improvement of the technology to address the following problems (*1*):

- Susceptibility of fouling and lack of durability of RO membranes;
- Low recovery (≤30%) and disposal of reject brine;
- High energy consumption.

In RO processes, the membrane forms the heart of the process and, understandably, current research emphases are directed toward improving the membrane material for robustness, fouling resistance and permeate flux (*2–5*). In this article we present a new process of desalination that can potentially address the above issues related with the process.

From the process point of view, desalination plants are always designed to attain a high water recovery which helps to maximize the energy efficiency of the process. A higher water recovery also means production of a lower volume of concentrate or reject stream from the process. A lower volume concentrate stream is favorable for better concentrate management - especially for those plants located inland or using brackish water. However, any attempt to increase the water recovery from the membrane module is also associated with a corresponding increase in the concentration of ions in the concentrate stream. In addition, all membrane-based desalination processes suffer from an inevitable phenomenon of concentration polarization that causes the saline water in the feed side to get further concentrated inside a boundary layer formed at the surface of the membrane. At elevated concentrations inside the boundary layer, some of the ions present in the seawater tend to form precipitates of their respective salts (scales) when their concentrations exceed the corresponding solubility product constant values. Inorganic fouling or scaling of the membranes caused by these salt-precipitates adversely impacts the process by causing a decrease in the product water flux. Therefore, any attempt to achieve higher product water recovery is limited by the simultaneous increase in the scaling potential at the membrane surfaces. Thus, scaling propensity of the feed water at the membrane surface puts a limit on the attainment of higher energy efficiency in a membrane-based desalination process. Such scaling also necessitates frequent maintenance of the fouled membranes, thereby resulting in a significant reduction in the plant availability.

It is noteworthy that commonly practiced pretreatment of feed water (e.g., microfiltration and acid dosing) cannot prevent membrane fouling caused by salt precipitation. In order to resolve this problem, two measures are practiced in RO based seawater desalination plants:

1. Anti-scaling or sequestering agent is continuously dosed (*6*, *7*) in the feed to inhibit solids precipitation on the membrane surface;
2. Permeate recovery in single-stage RO processes is often, if not always, less than 30% to control sulfate precipitation.

In addition, there have been efforts to develop improved membrane surfaces with grafted polymers to interfere with the process of crystal formation for the precipitating salts (*8*). However, as none of these efforts alter the equilibrium of salt formation, scaling cannot be avoided; the time between two successive membrane cleaning operations can only be increased (*6*). It is also noteworthy that the presence of proprietary organic-based anti-scaling agent (mostly organo-phosphonate and/or polycarboxylate) in the reject stream from RO desalination plants is an emerging environmental issue that needs to be addressed. In one study, increased water recovery with reduced levels of antiscalant was achieved by using reverse flow to periodically switch the seawater feed and concentrate exit ports on the membrane pressure vessel at times less than the induction time for the precipitating salt (*9*). A different approach for control of scaling is to alter the feed water chemistry in such a way that the concentration of scale forming ions is reduced to a level below the critical threshold value for membrane scaling. Many such techniques for pretreatment of feed water have been either proposed or implemented which includes chemical softening, osmotic backwash, nanofiltration softening, ion exchange , intermediate chemical demineralization (*10–13*), etc. Hardness removal using chemicals and ion exchangers requires use of new chemicals and produces high volume of solid waste and liquid brine which pose significant problem for disposal. In the case of softening by nanofiltration, the recovery limitations due to scaling are actually transferred from the RO stage to the nanofiltration stage. Moreover, nanofiltration softening requires extra energy to remove these scale forming cations.

Solubility of Different Sulfate Salts and Scaling Potential

The precipitation potential of a solution containing different scale forming ions is often described by a parameter called the supersaturation index (SI). The SI expresses the level of saturation of a solution with respect to various mineral salts and is given by,

$$SI_i = \frac{IAP}{K_{sp,i}} \qquad (1)$$

Where IAP is the ion activity product and $K_{sp,i}$ is the solubility product for the salt i. A saturation index greater than unity means that the solubility limit for the salt has been exceeded and, therefore, indicates a potential scaling problem.

For a salt i with chemical formula Y_nX_m, the dissociation of the salt and ion activity product is expressed below in equations 2 and 3, respectively:

$$Y_nX_m(s) \Leftrightarrow nY^{m+} + mX^{n+} \tag{2}$$

$$IAP = \{Y^{m+}\}^n\{X^{n-}\}^m = \gamma_Y^n\gamma_X^m[Y^{m+}]^n[X^{n+}]^m \tag{3}$$

where, γ is the activity coefficient of any ion and [ ] denotes the molar concentration of the ion.

Because of the relative abundance of sulfate ions in seawater, insoluble sulfate salts of different cations are common membrane foulants. While the precipitates of other salts, such as carbonate, can be reversed by adjusting the solution pH, the scales formed by sulfate salts cannot be cleaned or controlled by change in pH. Therefore, sulfate salts are of great concern as potential scale-formers that permanently impact the energy efficiency and the economics of the process. Sulfate scaling is also reported to be a major problem in the desalination of brackish groundwater (*14*).

Table I indicates the solubility product constant values of some scale-forming sulfate salts. Table II shows a typical sea water composition collected from the Atlantic Ocean and Figure 1 depicts the theoretically calculated SI values of various sulfate salts as a function of percentage permeate recovery for seawater RO desalination. Even in the absence of concentration polarization effect, it may be noted that the SI is exceeded at 35% permeate recovery for barium, strontium, and calcium sulfate. On the contrary, the SI for $MgSO_4$ is still four orders of magnitude lower than unity i.e., it does not pose any threat with respect to scaling/membrane fouling at higher recovery. Thus, conceptually, replacing calcium, strontium and barium in the feed sea water with magnesium offers a generic solution to the scaling problem associated with higher recovery and concentration polarization. Such an approach is also independent of the specific type of RO membrane used. In fact, even after replacement of all the cations present in the seawater by an equivalent concentration of magnesium ions, the SI still remains two orders of magnitude below unity.

Here we propose a novel reversible ion exchange-membrane (RIX-M) process for desalination which not only eliminates the potential for scale formation by cations without any continuous need of extra chemical or energy, but also has the prospect of achieving energy efficiency by altering the chemistry of the solution subjected to the membrane process.

Table I. Solubility Products of Different Sulfate Salts of Interest. Source: Knovel Critical Tables, 2nd Edition, 2008

Salt	*Solubility product (K_{sp})*
$MgSO_4$	4.67
$CaSO_4$	6.3×10^{-5}
$SrSO_4$	2.82×10^{-7}
$BaSO_4$	1.08×10^{-10}

Table II. Composition of Seawater collected from Atlantic Ocean

Ion	*Valence*	*Concentration*	
(M)	*mg/L*		
Na^+	1	0.448	10300
Cl^-	1	0.545	19330
SO_4^{2-}	2	0.0281	2700
Mg^{2+}	2	0.05327	640
Ca^{2+}	2	0.0124	250
Sr^{2+}	2	9.7×10^{-5}	8.5
Ba^{2+}	2	4.52×10^{-8}	6.02×10^{-3}

Reversible Ion Exchange-Membrane (RIX-M): Underlying Process Concept

The central element of the proposed RIX-M process rests on the premise that by intelligently integrating a self-regenerating ion exchange process with pressure-driven RO process, the sulfate fouling on the membrane can be eliminated for sea or brackish feed water. Concurrently, the osmotic pressure of the feed water is reduced, thus enhancing the energy efficiency and permeate recovery. Three major underlying scientific tenets of the proposed RIX-M process are:

1. Ion exchange processes work on exchange of equivalents of ions while the osmotic pressure of an aqueous solution is governed by molar concentrations of the ions or solutes.
2. Of all the sulfate salts of scale forming metal ions that belong to Group IIA of the periodic table, magnesium has orders of magnitude higher solubility compared to calcium, strontium and barium as shown from the solubility product values in Table I. Magnesium solubility is also much higher for fluoride and carbonate salts.

3. According to the affinity sequence of the widely available strong-acid and weak-acid cation exchangers, barium, strontium and calcium have higher selectivity than magnesium and the selectivity sequence stands as follows : $Ba^{2+} > Sr^{2+} > Ca^{2+} > Mg^{2+}$ (*15*).

Figure 2 shows the concept of the hybrid process where the scale forming cations of barium, calcium and strontium are eliminated and replaced by magnesium ions in the cation exchange step prior to the reverse osmosis process. The dashed lines indicate the regeneration step using the concentrate from the reverse osmosis process.

Figure 3 provides a schematic of RIX-M process which integrates a self-regenerating ion exchange process with RO to avoid membrane fouling caused by sulfate precipitation. Individual steps of the process are:

Step 1. Incoming seawater is passed through a cation exchanger in magnesium form leading to following exchange reactions:

$$\overline{(RSO_3^-)_2 Mg^{2+}} + 2Na^+ \Leftrightarrow 2\overline{(RSO_3^-)Na^+} + Mg^{2+} \qquad (4) \qquad (4)$$

$$\overline{(RSO_3^-)_2 Mg^{2+}} + Ca^{2+}\text{or } Ba^{2+} \Leftrightarrow \overline{(RSO_3^-)_2 Ca^{2+}\text{or } Ba^{2+}} + Mg^{2+} \qquad (5)$$

Overbar denotes the solid exchanger phase while RSO_3^- represents its sulfonic acid functional group.

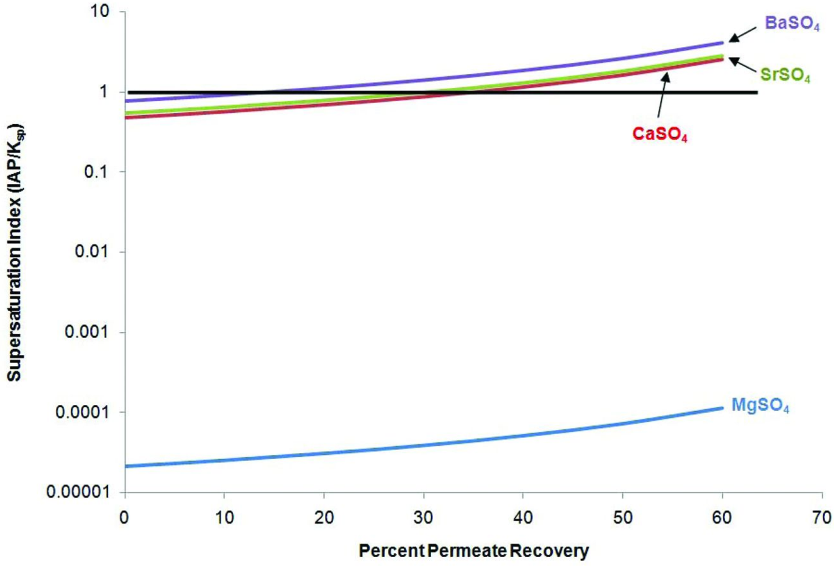

Figure 1. Calculated supersaturation index (SI) values for sulfate salts of different divalent cations at different permeate water recovery for RO membrane desalination of seawater. Note: Construction of Figure 1 takes into consideration the non-ideality effect due to the high ionic strength of sea water.

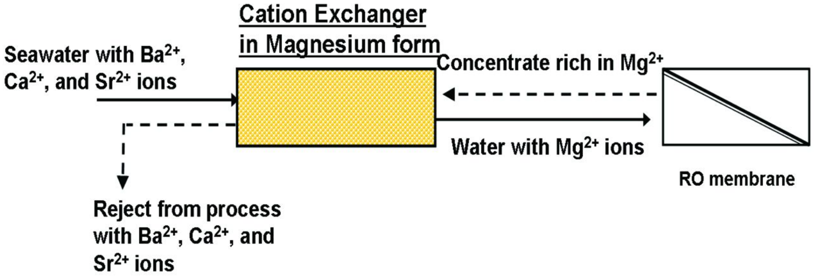
Cation Exchanger in Magnesium form
Seawater with Ba2+, Ca2+, and Sr2+ ions
Concentrate rich in Mg2+
Water with Mg2+ ions
RO membrane
Reject from process with Ba2+, Ca2+, and Sr2+ ions

Figure 2. Replacement of scale forming ions by magnesium ions in an RIX-M process.

Step 2. The resultant solution, mainly containing magnesium and chloride ions, is subjected to reverse osmosis. Since the osmotic pressure of the solution is now lower than the original sea or brackish water and the fouling potential is nearly eliminated, a higher product water recovery is attainable with lower membrane area requirement. Also, as the product water recovery is higher, the energy consumption per unit volume of product water is lower than the conventional RO process.

Step 3. The reject stream from the membrane, rich in magnesium, now passes through the previously exhausted cation exchange column (now mostly in sodium form) from Step 1. The column is transformed back into magnesium form and the resulting effluent mostly contains NaCl (1-1 electrolyte) along with other cations like calcium, magnesium etc, and anions like sulfate, bicarbonate, etc.

$$2\overline{(RSO_3^-)Na^+} + Mg^{2+} \Leftrightarrow \overline{(RSO_3^-)_2Mg^{2+}} + 2Na^+ \tag{6}$$

$$\overline{(RSO_3^-)_2Ca^{2+}\text{or } Ba^{2+}} + Mg^{2+} \Leftrightarrow \overline{(RSO_3^-)_2Mg^{2+}} + Ca^{2+}\text{or } Ba^{2+} \tag{7}$$

No external regenerant is required and the ion exchange unit is now ready for operation in Step 1. In principle, the RIX-M process is self-sustaining i.e., cation exchangers switch back and forth without needing any external regenerant and desalination is accomplished with higher permeate recovery with complete elimination of sulfate precipitation. Obviously, the selectivity sequence of divalent ions toward cation exchange resins (e.g., $Ba^{2+} > Sr^{2+} > Ca^{2+} > Mg^{2+}$) further enhances the efficiency of the proposed process.

Considering Na^+ and Cl^- ions to be the primary constituents in seawater, it is possible that the osmotic pressure of the seawater can be greatly reduced by using a suitably engineered ion exchange process ahead of the membrane desalination step, as illustrated in Figure 4. In an ion exchange process, the exchange of ions takes place in equivalent proportions whereas the osmotic pressure of a solution depends on the summation of molar concentrations of the constituent ions. For a solution containing electrolytes, osmotic pressure (π) is defined as:

$$\pi = \Sigma c_i RT \tag{8}$$

where, c_i is the molar concentration of any constituent ion i, R is the universal gas constant and T is the temperature in Kelvin.

With reference to Figure 4, Na^+ ions in the column influent are exchanged in equivalent concentrations for Mg^{2+} ions. Magnesium, being a divalent ion, has an equivalent concentration is half of its molar concentration. Therefore, as a result of the heterovalent ion exchange there is a corresponding drop in the molar concentration in the resultant solution. According to the relationship in equation 8, heterovalent ion exchange causes a drop in the osmotic pressure of the solution. The resulting solution containing $MgCl_2$ (2-1 electrolyte) from the cation exchange step of the RIX-M process has 30% lower osmotic pressure but the equivalent electrolyte concentration remains the same. This enables the RIX-M process to also achieve greater energy economy compared to the conventional RO process. An experimental validation of such decrease in osmotic pressure due to the replacement of monovalent ions by divalent ones has been performed in the laboratory for chloride-sulfate exchange and the information has been included elsewhere (*16*, *17*).

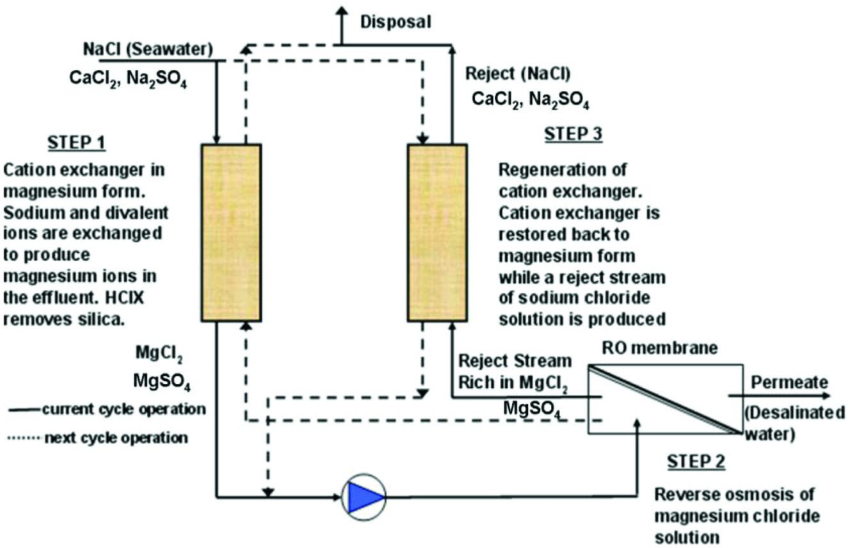
Disposal
NaCl (Seawater)
CaCl2, Na2SO4
Reject (NaCl)
CaCl2, Na2SO4
STEP 1
Cation exchanger in magnesium form. Sodium and divalent ions are exchanged to produce magnesium ions in the effluent. HCIX removes silica.
STEP 3
Regeneration of cation exchanger. Cation exchanger is restored back to magnesium form while a reject stream of sodium chloride solution is produced
MgCl2
MgSO4
Reject Stream Rich in MgCl2
MgSO4
RO membrane
Permeate
(Desalinated water)
—— current cycle operation
······· next cycle operation
STEP 2
Reverse osmosis of magnesium chloride solution

Figure 3. Schematic of the RIX-M desalination process delineating three major operational steps.

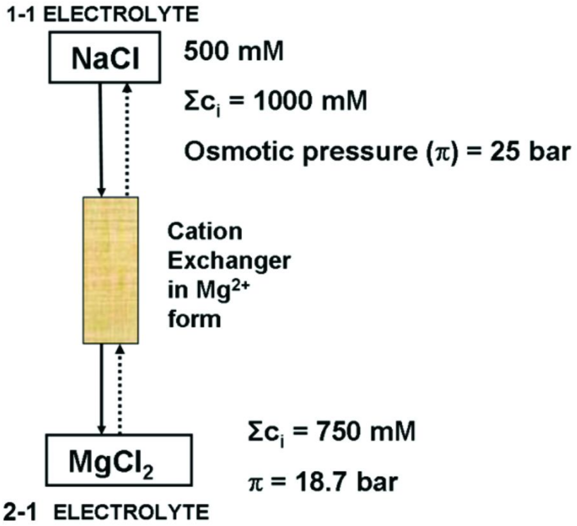

Figure 4. Reduction in theoretical osmotic pressure of sodium chloride following passage through ion exchangers pre-saturated with divalent magnesium ion.

This article focuses on the experimental validation of the general premise of the process. By judicious combination of ion exchange and reverse osmosis, the concentration of scale forming cations originally present in seawater can be significantly reduced before it is contacted with the RO membrane. We also investigated the sustainability of the process over many cycles without needing any external regenerating chemical for ion exchange.

Materials and Methods

A flat-leaf test cell (SEPA CF II, GE-Osmonics) with an effective membrane area of 140 cm^2 was used to perform RO experiments. The unit was operated at different transmembrane pressures ranging from 2 to 60 bar transmembrane pressure using SWHR 30 reverse osmosis membrane (DOW Chemicals Co., Midland, MI). SWHR 30 is a polyamide thin film composite (TFC) membrane with nominal water flux of 38.3 L/m^2-hr at 32,000 ppm NaCl concentration (*18*). A flow sheet and photograph of the closed loop experimental setup is shown in Figure 5. The flat-leaf unit, the high pressure pump and the tubings were all made of SS-316 to avoid corrosion. The membranes were initially conditioned by subjecting them to 30 bar transmembrane pressure for at least 2 h under deionized water. During the test, the system was allowed to stabilize for at least 1 h under a particular pressure before samples were taken and flow rate was recorded. The reservoir of about 30 L capacity was completely mixed during test runs. The temperature was maintained at 22–25 °C during the test runs. For every transmembrane pressure, three samples were collected from the permeate side under steady-state conditions at an interval of 15 min.

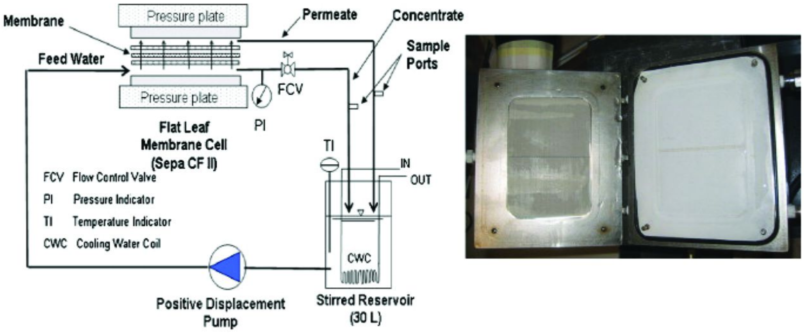
Membrane
Pressure plate
Feed Water
Pressure plate
Permeate
Concentrate
Sample
Ports
FCV
PI
Flat Leaf
Membrane Cell
(Sepa CF II)
TI
IN
OUT
FCV Flow Control Valve
PI Pressure Indicator
TI Temperature Indicator
CWC Cooling Water Coil
CWC
Positive Displacement
Pump
Stirred Reservoir
(30 L)

Figure 5. Schematic of the experimental set up and photograph of flat-leaf test apparatus with RO membrane.

All fixed bed column runs were carried out in a glass column of 2.54 × 10^{-2} m (1 in.) diameter using a strong acid cation exchange resin SST-60 (Purolite Co., Philadelphia, PA). Capacity of the resin is 3.6 eq/kg in Na^+ form. The column was fitted with a peristaltic pump which fed the electrolyte solution at a constant rate and the effluent was collected at an ELDEX fraction collector.

Conductivity of each sample was measured immediately after collection using an ORION (model 120) conductivity meter. Concentrations of the cations magnesium, sodium, and calcium were measured using a flame type atomic absorption spectrometer (AAnalyst 200, Perkin Elmer).

Results

Magnesium Ion Exchange

A synthetic seawater solution containing 460 meq/L Na^+, 30 meq/L Ca^{2+}, and 150 meq/L Mg^{2+} was passed through a column containing cation exchange resins (Purolite SST-60) pre-saturated in magnesium form. Figure 6 represents the breakthrough profile of different cations in the effluent of the column. The increased Mg^{2+} concentration in the effluent is due to its displacement from the bed by other ions. Sodium was the first ion to break through the column; the breakthrough occurred around 2 bed volumes. Calcium ions had a breakthrough much later, at around 12 bed volumes.

Runs with RO Membrane

Solutions containing different molar compositions of sodium chloride and magnesium sulfate but constant equivalent concentrations of electrolyte were subjected to pressure-driven RO process using the flat-leaf type membrane cell test apparatus. Figure 7 shows plots of the permeate fluxes recorded at different transmembrane pressures for different feed solutions. It may be noted that the incremental replacement of sodium and chloride ions in the solution by equivalent concentration of magnesium and sulfate ions respectively, helped achieve higher flux of permeate at same transmembrane pressures. Figure 8 represents the salt rejection characteristics of the reverse osmosis membrane for the same experiment. Higher proportions of magnesium in the feed solution resulted in better salt rejection by the membrane.

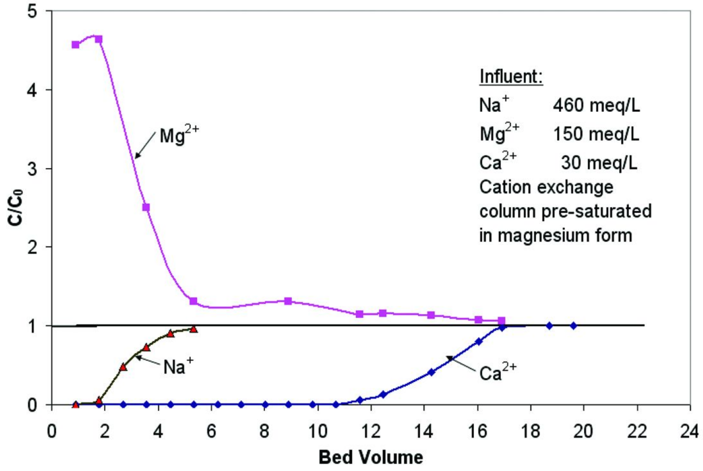

Figure 6. Breakthrough profile of different ions for a synthetic seawater solution passed through cation exchange column pre-saturated in magnesium form. (C_0 and C are the influent and effluent concentration respectively, of a component at any point of operation).

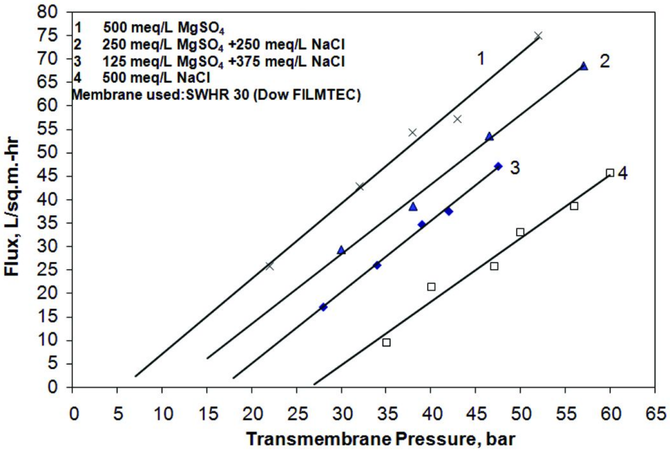

Figure 7. Flux obtained for a RO membrane at different transmembrane pressures for solutions of same equivalent concentrations but different proportions of magnesium and sodium salts.

Reversibility of the RIX-M Process

In order to validate the reversibility of the RIX-M process in the laboratory, cyclical runs were performed according to the schematic in Figure 9(a). The synthetic seawater solution contained 450 meq/L sodium ions, 100 meq/L magnesium, 25 meq/l calcium and 1100 μg/L barium ions. A solution volume equivalent to four bed volumes (BV) was fed to a column filled with cation exchange resin (SST-60, Purolite Co., PA) pre-saturated in magnesium form. The exhausted column was regenerated using a solution of 2BV containing 500 meq/L sodium and 500 meq/L magnesium ions. Figure 9(b) show calcium concentration at the exit of the column during the forward run. Figure 10 shows the barium concentration at the exit of the column in the forward run. The results shown in Figures 9b and 10 indicate that concentrations of both calcium and barium ions approached a steady state with a value much lower than that of the feed seawater. It may be noted that in the RIX-M process, the effluent of the ion exchange column is the feed to the RO membrane.

Discussion

Sustainability of the Process over Multiple Cycles

In order to make the process sustainable over many cycles of operation, it is required that the process continues to run by its own without addition of extraneous chemical during the regeneration step (Step 3 of Figure 3). It is obvious that the affinity of different ions towards the ion exchanger has a significant role to play for determining sustainability of the process. Affinity of different ions towards an ion exchanger depends on many factors that include their valence, hydrated ionic radii, etc. In general for dilute solutions, affinity sequence of the cations for common strong acid cation exchangers (such as SST-60 or C-100 resins) is as follows (*15*): $Ba^{2+} > Sr^{2+} > Ca^{2+} > Mg^{2+} > Na^{+}$

It is apparent that breakthrough of ions from a cation exchange column shall follow the reverse sequence. Breakthrough pattern of different ions as in Figure 6 is in agreement with the above affinity sequence. The general cation exchange reactions as mentioned in equations 4 and 5 take place when synthetic solution of seawater is passed through a column containing cation exchanger in magnesium form. Considering ideality, the equilibrium constant or the selectivity coefficient in equation 4 which represents a heterovalent exchange reaction, can be presented as follows (*19*):

$$K_{Mg/Na} = \frac{y_{Mg} x_{Na}^2}{x_{Mg} y_{Na}^2} * \frac{C_T}{Q} \qquad (9)$$

And for homovalent exchange reaction in equation 5, the selectivity coefficient is defined as follows:

$$K_{Ca/Mg} = \frac{y_{Ca} x_{Mg}}{x_{Ca} y_{Mg}} \tag{10}$$

where x and y represent the fractional concentration of the ions at aqueous and resin phase, respectively while C_T is the total equivalent cation concentration in the aqueous phase and Q is the capacity of the cation exchange resin.

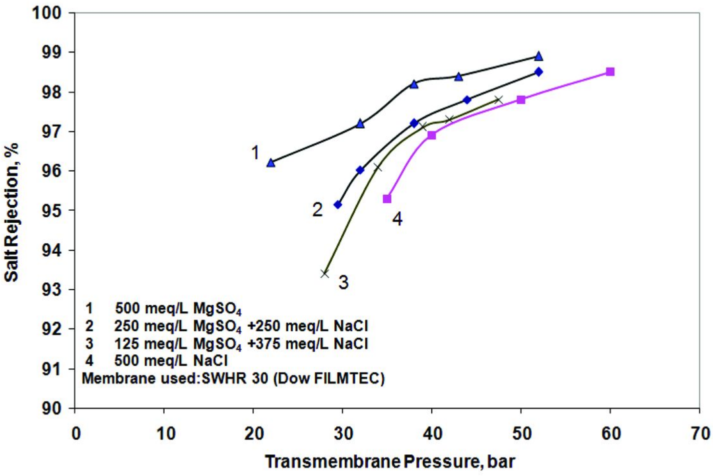

Figure 8. Salt rejection by RO membrane when subjected to different transmembrane pressure for solutions of same equivalent concentrations but different proportions of magnesium and sodium salts.

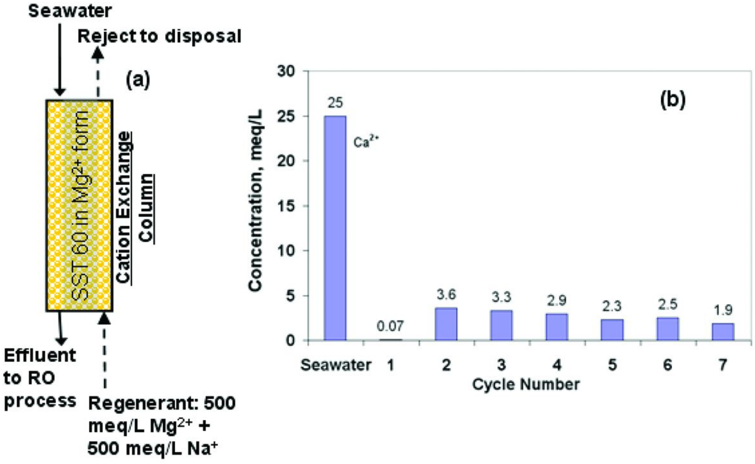

Figure 9. (a)Schematic of experimental column run and (b) calcium concentration in the synthetic seawater and the effluent over number of cycles.

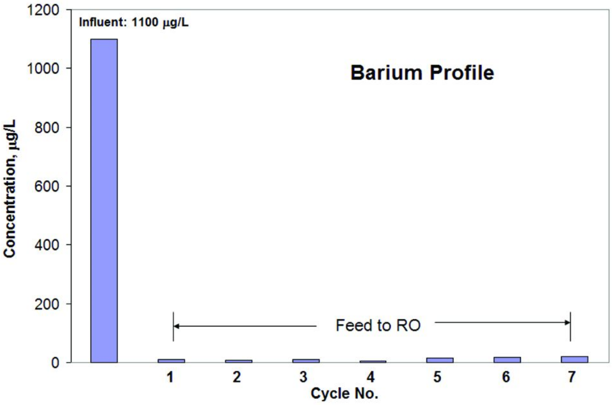

Figure 10. Barium concentration in the synthetic seawater and the effluent over number of cycles.

In an ion exchange column, the breakthrough behaviors of the ions are governed by the separation factor, and not by the selectivity coefficient. Relative preference of one cation over the other for the ion exchange resin is represented by the separation factor. Magnesium/sodium and calcium/magnesium separation factors are represented by $\alpha_{Mg/Na}$ and $\alpha_{Ca/Mg}$, respectively. They are defined as:

$$\alpha_{Mg/Na} = \frac{y_{Mg} x_{Na}}{x_{Mg} y_{Na}} \tag{11}$$

and,

$$\alpha_{Ca/Na} = \frac{y_{Ca} x_{Na}}{x_{Ca} y_{Na}} \tag{12}$$

A closer examination of the equations 9 through 12 reveals that, for heterovalent exchange, such as those involving sodium/calcium or sodium/magnesium exchanges, the separation factor is not a constant. For a given ion-exchange capacity of the resin, the separation factor changes depending on the electrolyte concentration in the aqueous phase. More specifically, the ion exchanger's preference of a divalent ion (e.g. Mg^{2+} ion) over a monovalent ion (e.g. Na^+ ion) rapidly decreases as the electrolyte concentration increases. Beyond a particular electrolyte concentration, the selectivity reverses making monovalent ions preferred over divalent ions. The electrolyte concentration at which this reversal occurs depends on the relative affinities of the exchanging ions. For homovalent exchange, however, there is no effect of aqueous phase electrolyte concentration on the separation factor. Therefore, relative preference of calcium over magnesium remains the same regardless of the electrolyte concentration. According to Figure 6, calcium breakthrough occurs after 10 bed volumes. It is apparent from the selectivity sequence that breakthrough of barium and strontium shall occur much later. In the cyclical run, four BV of influent sea water is used in the forward run. Therefore, the effluent of the column which is actually the feed to RO in RIX-M process should contain a little or no calcium ions. In the RIX-M process, freshwater is recovered in the RO step and the concentrate stream from the RO step is used for the regeneration of exhausted cation exchange column. Thus, the regenerant in the reverse run has higher total electrolyte concentration than the influent seawater in the forward run. The separation factor values change with electrolyte concentration for the heterovalent exchange but not for the homovalent exchange. Based on the above arguments, following points may be inferred:

1) For heterovalent exchange, selectivity decreases with increase in the total electrolyte concentration.

$$\alpha_{Ca/Na,Forward} > \alpha_{Ca/Na,\mathrm{Re}verse} \tag{13}$$

2) For the solution entering the ion exchange column at different cycles during the process are related as,

$$\left(\frac{x_{Mg}}{x_{Ca}}\right)_{\mathrm{Re}verse} > \left(\frac{x_{Mg}}{x_{Ca}}\right)_{Forward} \tag{14}$$

and,

$$\left(\frac{x_{Na}}{x_{Ca}}\right)_{\mathrm{Re}verse} > \left(\frac{x_{Na}}{x_{Ca}}\right)_{Forward} \tag{15}$$

For a multicomponent exchange involving Mg, Ca and Na, the fractional calcium ion concentration in the resin phase is given by the following relationship (*19*),

$$y_{Ca} = \frac{1}{1 + \frac{1}{\alpha_{Ca/Mg}}\frac{x_{Mg}}{x_{Ca}} + \frac{1}{\alpha_{Ca/Na}}\frac{x_{Na}}{x_{Ca}}} \tag{16}$$

Therefore, using relationships 13 through 16 one can conclude that,

$$y_{Ca,Forward} > y_{Ca,\mathrm{Re}verse} \tag{17}$$

Thus, the fractional concentration of calcium in the resin phase after the forward run is greater than that at the end of reverse run. In other words, the overall effect is that the resin does not accumulate calcium ion to a significant extent. Therefore, over many number of cycles the resin phase calcium concentration shall reach a steady state at which there will be a very small leakage of calcium in the ion exchange column effluent solution. Experimental observations in Figures 9 and 10 show that calcium and barium have been sufficiently eliminated from the feed solution going to the RO step of the process. These observations provide a sufficient proof of the concept.

Conclusion

It is validated in the laboratory that an RIX-M process can eliminate scale forming cations from entering the reverse osmosis process. This process has the potential to offer energy-efficient and scaling-free desalination of sea and brackish water. It is also validated that the process does not need any extraneous regenerant or chemical for its sustenance over many number of cycles. However, for better validation of the process concepts and better quantification of process benefits, it is required to run pilot-scale tests where cation exchange columns and a spirally wound reverse osmosis module can be coupled together to run the process continuously over many number cycles. Relative affinity of the ion exchange resin toward the scale causing ions over the other cations and the extent of water recovery are the two parameters which are most likely to dictate the sustainability and energy efficiency of the overall process.

References

1. USBR and SNL (United States Bureau of Reclamation and Sandia National Laboratories). *Desalination and Water Purification Technology Roadmap: A Report of the Executive Committee.* Desalination & Water Purification Research & Development Report #95, United States Department of the Interior, Bureau of Reclamation, Water Treatment and Engineering Group. Denver, CO, 2003.
2. Greenlee, L. F.; Lawler, D. F.; Freeman, B. D.; Marrot, B.; Moulin, P. *Wat. Res.* **2009**, *43* (9), 2317–2348.
3. Cath, T. Y.; Adams, V. D.; Childress, A. E. *J. Membr. Sci.* **2004**, *228*, 5–16.
4. Brusilovsky, M.; Borden, J.; Hasson, D. *Desalination* **1992**, *86* (2), 187–222.
5. Baker, R. W. *Membrane Technology and Applications*, 2nd ed.; John Wiley & Sons, Ltd.: New York, NY, 2004.
6. Hasson, D.; Drak, A.; Semiat, R. *Desalination* **2003**, *157*, 193–207.
7. Greenlee, L. F.; Testa, F.; Lawler, D. F.; Freeman, B. D.; Moulin, P. *Wat. Res.* **2010**, *44* (8), 2672–2684.
8. Kim, M.; Lin, N. H.; Lewis, G. T.; Cohen, Y. *J. Membr. Sci.* **2010**, *354* (1-2), 142–169.
9. Gilron, J.; Korin, E. *Method and system for increasing recovery and preventing precipitation fouling in pressure-driven membrane processes*; No. PCT/IL2004/001110; December 7, 2004.
10. Oren, Y.; Katz, V.; Daltrophe, N. C. *Desalination* **2001**, *139*, 155.
11. Sagiv, A.; Avraham, N.; Dosoretz, C. G.; Semiat, R. *J. Membr. Sci.* **2008**, *322*, 225–233.

12. Hassan, A. M.; Farooque, A. M.; Jamaluddin, A. T. M.; A1-Amoudi, A. S.; A1-Sofi, M. A. K.; A1-Rubaian, A. F.; Kither, N. M.; A1-Tisan, I. A. R.; Rowaili, A. *Desalination* **2000**, *131*, 157.
13. Gabelich, C.; Williams, M.; Rahardianto, A.; Franklin, J.; Cohen, Y. *J. Membr. Sci.* **2007**, *301* (1-2), 131–141.
14. Rahardianto, A.; Mccool, B.; Cohen, Y. *Environ. Sci. Technol.* **2008**, *42* (12), 4292–4297.
15. Helfferich, F. *Ion Exchange*; Dover Publications, NY, 1995.
16. Sarkar, S.; SenGupta, A. K. *J. Membr.Sci.* **2008**, *324* (1-2), 76–84.
17. Sarkar, S; SenGupta, A. K. *Water Sci. Technol.: Water Supply* **2009**, *9* (4), 369–377.
18. Dow Chemicals, Catalogue of Filmtec seawater RO elements for membrane systems, Catalogue no. 609-00377-703.
19. Sarkar, S.; Greenleaf, J. E.; SenGupta, A. K. Ion Exchange Technology. *Encyclopedia Of Polymer Science and Technology*; John Wiley and Sons, Inc.: Hoboken, NJ, 2009.

Chapter 18

Surface Functionalization of Polybenzimidazole Membranes To Increase Hydrophilicity and Charge

Michael Flanagan,[1] Richard Hausman,[1] Brett Digman,[1] Isabel C. Escobar,*,[1] Maria Coleman,[1] and Tai-Shung Chung[2]

[1]Chemical and Environmental Engineering,
The University of Toledo, United States
[2]Department of Chemical and Biomolecular Engineering,
The National University of Singapore, Singapore
***E-mail: isabel.escobar@utoledo.edu. Phone: 419-530-8267.**

Downloaded by UNIV OF DELAWARE MORRIS LIB on June 17, 2012 | http://pubs.acs.org
Publication Date (Web): October 31, 2011 | doi: 10.1021/bk-2011-1078.ch018

Forward osmosis is the movement of water across a selectively permeable membrane. The driving force for water permeation through the membrane is the difference in osmotic pressure between the feed and draw solutions. Polybenzimidazole (PBI) is a material with excellent chemical resistance and high mechanical and thermal stability that is a promising material for forward osmosis separations. Drawbacks associated with the use of PBI as a membrane material include low hydrophilicity and surface charge neutrality. In this study, PBI membranes were cast using the phase-inversion technique in the form of flat sheets, and membrane surfaces were functionalized using different modifying agents with the goal of increasing hydrophilicity and surface charge. The negative charge on the membrane surface was expected to yield an increased rejection of ions and of negatively charged particles in the feed solution, while increased hydrophilicity decreases fouling propensity. The surfaces of the membranes were activated with 4-(chloromethyl) benzoic acid (CMBA). The modifying agents selected for membrane functionalization included: taurine, para-phenylene diamine, and ethylene diamine. These modifying agents were selected for their potential to impart a charge on the PBI membrane when in near neutral pH

In Modern Applications in Membrane Science and Technology; Escobar, I., et al.;
ACS Symposium Series; American Chemical Society: Washington, DC, 2011.

environments. Membranes were characterized using Fourier transform infrared spectroscopy in attenuated reflectance mode (FTIR-ATR), ζ potential, environmental scanning electron microscopy (ESEM), and contact angle measurements. Functionalization, surface charge, and increased hydrophilicity were all verified. Pure water permeability and salt rejection were tested for comparison between both virgin and modified membranes. Monovalent salt rejection was investigated using various sodium chloride feed concentrations, and a range of pH values.

Downloaded by UNIV OF DELAWARE MORRIS LIB on June 17, 2012 | http://pubs.acs.org
Publication Date (Web): October 31, 2011 | doi: 10.1021/bk-2011-1078.ch018

Introduction

Forward osmosis (FO) is an emerging desalination process that is gaining favor as a substitute for currently used desalination methods. Pressure-driven processes, such as reverse osmosis (RO), have been the most common techniques for separating dissolved solutes from feed water for many decades (*1*). Like RO, forward osmosis uses a semi-permeable membrane to allow for water separation. The water flux in a FO system varies from RO, however, in that the driving force for mass transport is the osmotic pressure gradient between the feed and draw solutions (generally a high concentration salt solution), as opposed to hydraulic pressure. The net flow of water through the membrane leads to a dilution of the draw solution and a concentration of the feed stream.

FO is in the early stages of application, and there are still major obstacles that need to be overcome before fully utilizing FO as a widely used water production technology. Such obstacles include a small number of commercially available FO membranes with proper separation performance, and lack of economically viable and user friendly draw solutions. The lack of commercially available FO membrane materials stems from the fact that previously developed membrane materials were developed for pressure-driven applications, there is not a full understanding of transport behavior and fouling, and ideal draw solutions are still being researched.

Ideal FO membranes should have thinner support layers, have very low transport resistance to minimize internal concentration polarization, and enhance membrane permeability. Studies on water transport through FO membranes show that internal concentration polarization within the support layer significantly reduces membrane flux (*2–5*). Therefore, thickness and transport resistance of the support layer plays a critical role in FO membrane performance, although the support layer properties do not affect the performance of RO/NF membranes. Nevertheless, most of the commercially available semi-permeable membranes, such as the widely used polyamide thin-film membranes, have very thick woven fabric supports that would restrict their application as FO membranes. The thickness of successful and commercially available FO membrane support layers as reported by Saren et al. (*6*) is between 40-90 μm for woven fabric supported membranes. This is much thinner than that of conventional thin film composite (TFC) RO membranes (~150 μm). The approach in this study to address these obstacles is by functionalization of existing nanofiltration (NF) membranes to provide more ideal operating conditions. Functionalization involves chemically attaching a charged modifying agent on the surface of a membrane. The added functional group is hoped to result in an increased rejection of monovalent salts (i.e. sodium chloride and potassium chloride).

Researchers in Singapore recently developed a hollow fiber nanofiltration (NF) FO membrane made of polybenzimidazole (PBI) (*7*). PBI is a material with outstanding mechanical and thermal stability and chemical resistance. PBI membranes can generate high flux in FO processes (*7*, *8*) and thus is a very promising material for FO membrane development. The drawback, however, is the salt rejection of this membrane in the virgin stage is relatively low, and the membrane has a high hydrophobicity. If the PBI membrane surfaces can be modified to improve these flaws then PBI has the potential to become an economically viable FO membrane material. A recent study by Hausman et al. (*9*) focused on increasing the negative charge and hydrophilicity of PBI membranes using a very similar approach to the one presented here, with the main difference being that the functionalization of the membrane was achieved after a long and expensive procedure.

This study focused on functionalization of PBI surfaces to impart a surface charge and an increase in hydrophilicity using a less expensive and faster method for the surface modification. The objectives of this research were to cast flat sheet PBI membranes via the phase-inversion technique and to chemically modify the membrane surfaces. PBI membranes were activated using 4-(chloromethyl) benzoic acid (CMBA). N-(3-dimethylaminopropyl)-N'-ethylcarbodiimide hydrochloride (EDCH) and N-hydroxylsuccinimide (NHS) chemistry catalysis was used as an intermediate for reaction of the COOH group added from the CMBA activation with the desired modifying agent. The modifying agents (taurine, ethylene diamine, and para-phenylene diamine) were chosen based on their potential to impart a charge to the membrane surface in near neutral pH environments. It was also expected that the overall hydrophilicity would increase and the increase in surface charge would lead to an increase in salt rejection.

Several analytical techniques were employed to verify that surface modification was successful. Fourier transform infrared spectroscopy in attenuated total reflection mode (FTIR-ATR) was used to detect changes based on specific functional groups associated with each of the modifying agents. ζ potential measurements were taken to detect changes in the membranes surface charge. Environmental scanning electron microscopy (ESEM) was used to detect any changes in morphology of the membranes during and after modification. Determination of changes in hydrophilicity was examined by contact angle measurements using a goniometer.

Transport characteristics were evaluated for unmodified, CMBA surface activated, and all modified membranes. Dead-end flow permeability cells were used in a pressure-driven mode for verification of imparted characteristics. Pure water permeability along with monovalent (sodium chloride) salt rejection was determined for all membranes. In order to detect changes in salinity, the conductance of both the feed and the resulting permeate were tested using a conductivity meter.

Downloaded by UNIV OF DELAWARE MORRIS LIB on June 17, 2012 | http://pubs.acs.org
Publication Date (Web): October 31, 2011 | doi: 10.1021/bk-2011-1078.ch018

Downloaded by UNIV OF DELAWARE MORRIS LIB on June 17, 2012 | http://pubs.acs.org
Publication Date (Web): October 31, 2011 | doi: 10.1021/bk-2011-1078.ch018

Experimental Section

Materials

Polybenzimidazole dope was supplied by PBI Performance Products, Inc. (Charlotte, NC) as a 26 wt% solution. Ethylene diamine, para-phenylene diamine, taurine, dimethylacetamide, 4-(chloromethyl) benzoic acid, N-(3-dimethylaminopropyl)-N′-ethylcarbodiimide hydrochloride, N-hydroxylsuccinimide, and sodium persulfate were purchased from Sigma–Aldrich (U.S.A.). Acetone, glycerol, and sodium chloride were purchased from Fisher Scientific (U.S.A.). All reagents were used as received. DI water was supplied by a continuous distillation apparatus.

PBI Membrane Preparation

All PBI flat sheet membranes were prepared in house. Polybenzimidazole dope was supplied at 26 wt% in a 72 wt% solution of dimethylacetamide (DMAc) with 2.0 wt% lithium chloride. The procedure used to prepare the membranes was adapted from Wang and Chung (*10*). A desired concentration of 20 wt% was achieved by dilution with DMAc. In order to achieve uniform flat sheet membranes, and to prevent air bubbles from being trapped in the dope, the beaker was sealed with parafilm and placed in a sonicator on degas setting for approximately two hours. The dope was then spread in an even line across a well-cleaned mirror. A doctor's blade set at a thickness of 150 µm was used to push the dope across the mirror forming a thin flat sheet. In order to reduce friction between the blade and the mirror, the rails of the doctor's blade were lubricated with motor oil. After the flat sheet was cast, the mirror and sheet were placed in a 12 gallon DI water coagulation bath to remove the solvent by way of the phase-inversion technique. The membrane peeled from the mirror when the phase-inversion process was complete. The membrane was thoroughly washed with DI water and one inch circles were punched for testing and modification. All membranes were stored in a 50/50 mixture of DI water and glycerol until used. The addition of glycerol was to ensure the membranes would stay wet during storage.

Membrane Modification

CMBA Membrane Activation

The initial activation using CMBA (*11*) was performed as follows: in a 50-mL beaker, a 0.5 wt% solution of CMBA was prepared in acetone and stirred until the solute was completely dissolved. A separate 50-mL beaker, with 1.0 wt% sodium persulfate was prepared in DI water and stirred until the solute was completely dissolved. Sodium persulfate acted as a free radical initiator for the CMBA activation. The virgin membrane samples to be modified were added to the sodium persulfate solution. The CMBA/acetone solution was slowly added to the aqueous sodium persulfate solution. The slow addition was necessary to prevent the CMBA from precipitating from solution, since it is insoluble in water. The reaction procedure is given in Figure 1.

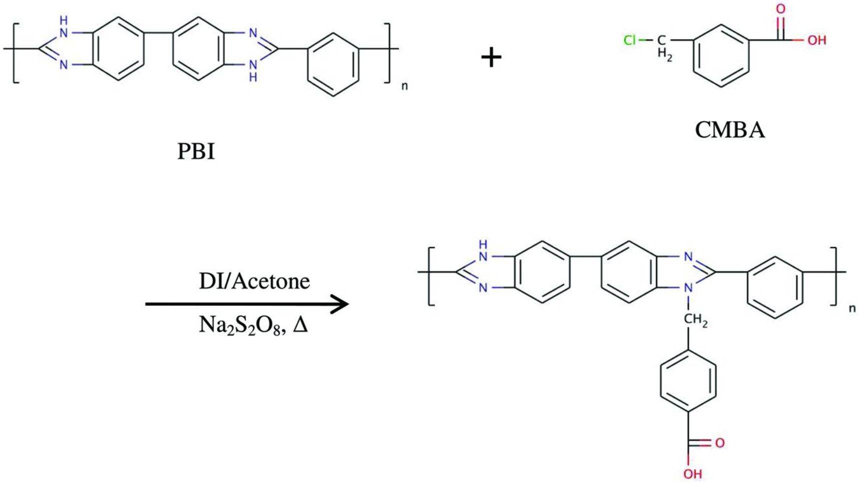

Figure 1. CMBA activation of PBI virgin membrane.

There are two reactive –NH sites on the backbone of the PBI repeat unit. Both of the –NH sites are susceptible to reaction, but for simplification, reaction to one site will be shown throughout the figures in this paper. The final volume was a 50/50 mixture of DI/acetone. The reaction mixture was sealed with parafilm, heated on a hot plate to 40 °C, and reacted for 24 hours. This temperature was selected to help keep the reagents in solution while minimizing acetone evaporation. No agitation was applied. After 24 hours, the sheets were removed and washed with acetone to remove any residual CMBA; then washed with copious amounts of DI water to remove any remaining sodium persulfate and acetone. Once thoroughly cleaned the sheets were stored in 50/50 DI water and glycerol solution.

EDCH and NHS Chemistry

Hausman et al. (*9*) showed an effective technique to functionalize CMBA activated PBI membranes using N-ethyl-N(3-dimethylaminopropyl) carbodiimide (EDC) chemistry. A simpler approach using N-(3-dimethylaminopropyl)-N′-ethylcarbodiimide hydrochloride (EDCH) and N-hydroxylsuccinimide (NHS) (Figure 2) chemistry was the focus of this study. The EDCH/NHS method was favored over the EDC method because it allowed for a reduction in the reaction time and required chemical usage. EDCH facilitates the reaction between –COOH groups bound to the CMBA activated PBI backbone and the amine group of the functional modifying agents (*12*). The EDCH/NHS reaction occurs with the carboxylic acid to form an unstable ester (Figure 3). The modifying agents included ethylene diamine, para-phenylene diamine, and taurine (Figure 4). The amount of reagent necessary for EDCH catalyzed modification depended on the final weight of dried surface activated samples (0.30–0.33 g). Subsequent

Downloaded by UNIV OF DELAWARE MORRIS LIB on June 17, 2012 | http://pubs.acs.org
Publication Date (Web): October 31, 2011 | doi: 10.1021/bk-2011-1078.ch018

modifications were performed in a 2-(N-morpholino) ethanesulfonicacid (MES) buffer solution.

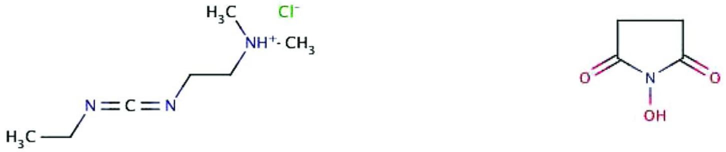
H$_3$C
Cl$^-$
NH$^+$- CH$_3$
N=C=N
H$_3$C
O
N
O
OH

EDCH NHS

Figure 2. EDCH and NHS molecular structures.

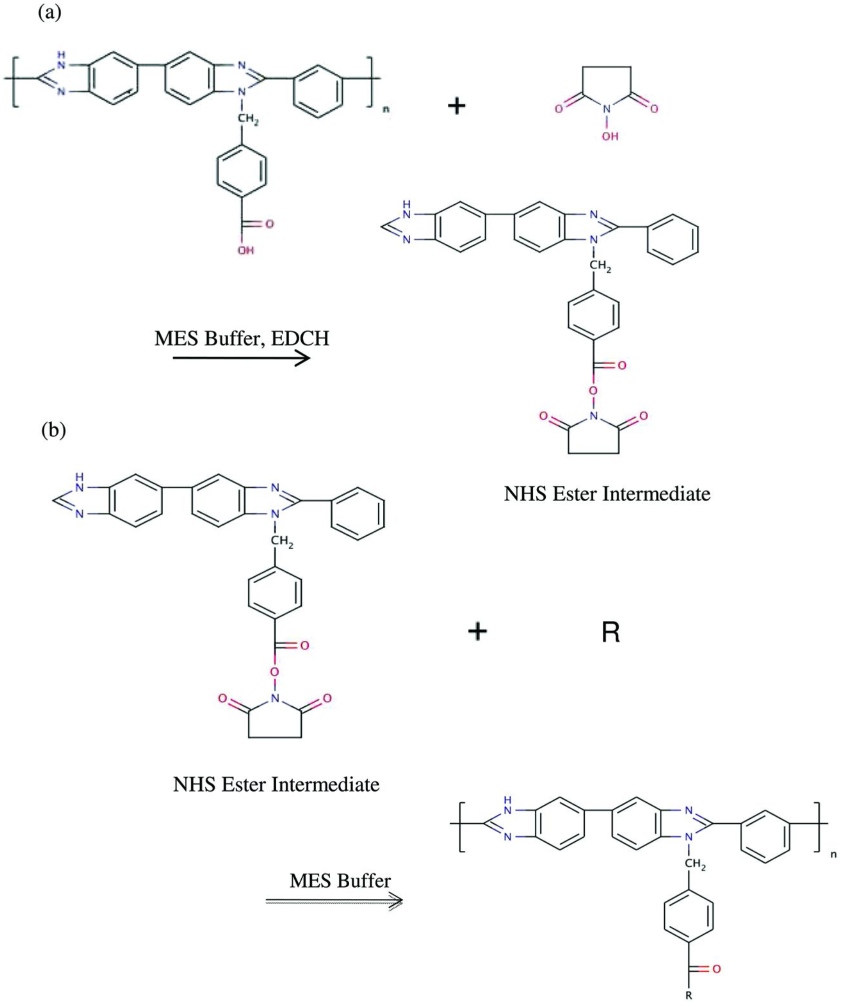
(a)
H
N
N
N
N
CH$_2$
O
OH
n
+
O
N
O
OH
MES Buffer, EDCH
NHS Ester Intermediate
(b)
NHS Ester Intermediate
+
R
MES Buffer
R

Figure 3. (a) EDCH/NHS reaction with CMBA activated PBI to form ester intermediate. (b) NHS ester intermediate reacted with modifying agent to form final functionalized membrane.

Downloaded by UNIV OF DELAWARE MORRIS LIB on June 17, 2012 | http://pubs.acs.org
Publication Date (Web): October 31, 2011 | doi: 10.1021/bk-2011-1078.ch018

A buffer solution composed of 0.1 M MES and 0.5 M NaCl was prepared for all EDCH/NHS reactions. A stock solution was prepared, and titrated with 1 N NaOH to a pH of 6. The pH adjusted MES buffer was used to prepare a 0.002 M EDCH and 0.005 M NHS solution for the final surface modification. After the EDCH/NHS solution was prepared, the membrane sheets were added to the solution and mixed. After 15 minutes, 2-mercaptoethanol was added to the solution to quench the reaction for modifying agent addition. To optimize the conditions for reaction, the pH was adjusted to 7-7.5 with 1N NaOH before the desired modifying agent was added. From the molecular weight of CMBA modified sheets (442 g/mol) and the final weight of the samples to be modified, the weight of the modifying agent was determined. The final step involved an equal-molar addition of modifying agent to that of the CMBA modified samples. Then the reaction was stirred for two hours. Once the reaction was complete, copious amounts of DI water were used to wash the membranes. The final products are shown in Figure 5. It is also important to note that amphoteric compounds, such as taurine, usually require blocking of acid functionality to prevent internal salt formation and free amino-group, which was not done since the reaction proceeded as described. Membranes were stored in a 50/50 DI water and glycerol solution.

Downloaded by UNIV OF DELAWARE MORRIS LIB on June 17, 2012 | http://pubs.acs.org
Publication Date (Web): October 31, 2011 | doi: 10.1021/bk-2011-1078.ch018

Membrane Characterization

Fourier Transform Infrared Spectroscopy (FTIR-ATR)

Evidence that the PBI was successfully modified was obtained using Fourier transform infrared spectroscopy in attenuated total reflectance mode (FTIR-ATR). FTIR uses measurements of vibrational spectra to identify the chemical structure of materials. By monitoring the vibrational spectra changes, molecular conformation can also be observed. FTIR analysis was obtained on a Varian Excalibur Series Fourier Transform Infrared instrument, the FTS-4000 Spectrometer and the UMA-600 Microscope (Randolph, MA).

ζ Potential

Surface charge was analyzed by measuring the zeta potential on the membrane surface. Samples were measured using an electrokinetic analyzer (BI-EKA, Brookhaven Instrument Corp., Holtsville, NY) which was located at Volodymyr Tarabara's laboratories at Michigan State University, East Lansing, MI. Before analysis, membranes were rinsed with copious amounts of DI water to remove any residual glycerol from the storage solution. The KCl electrolyte solution used in these measurements had an ionic strength of 1.0 mM. The pH values for the various readings were adjusted using 0.5 M NaOH and 0.5 M HCl solutions (*13*).

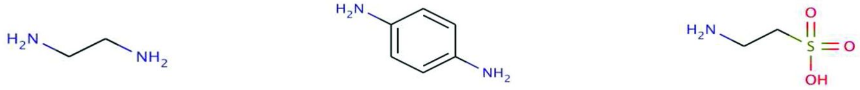
H$_2$N
NH$_2$
H$_2$N
NH$_2$
H$_2$N
O
S
O
OH

Ethylene Diamine

p-Phenylene Diamine

Taurine

Figure 4. Modifying agents.

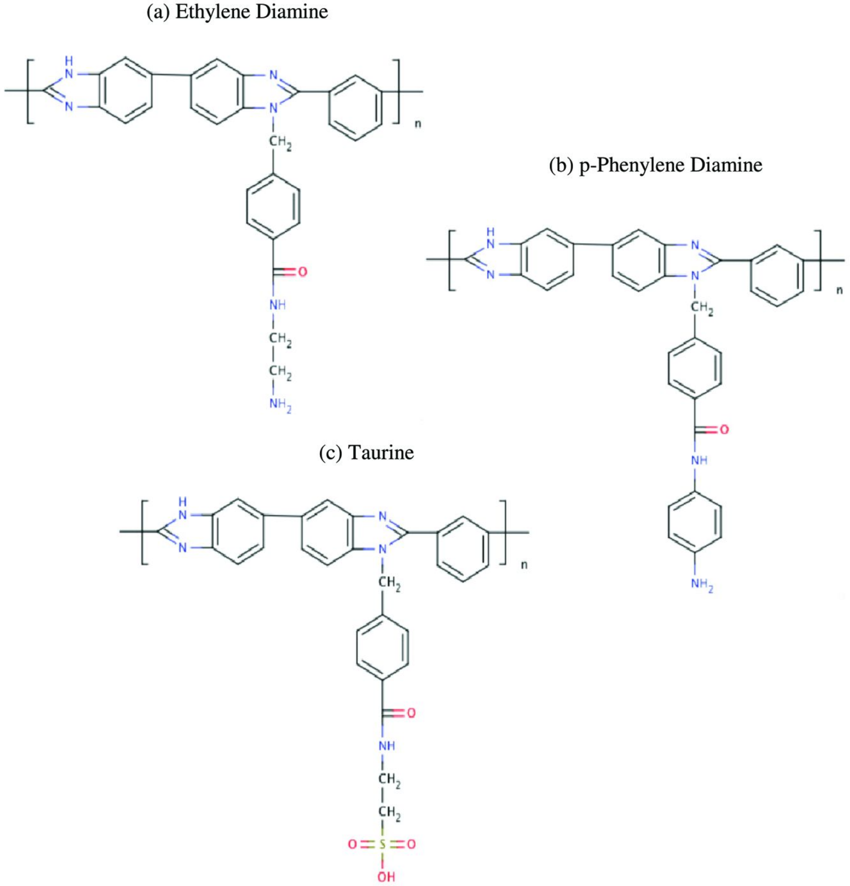
H
N
N
N
N
CH$_2$
O
NH
CH$_2$
CH$_2$
NH$_2$
n
H
N
N
N
N
CH$_2$
O
NH
NH$_2$
n
H
N
N
N
N
CH$_2$
O
NH
CH$_2$
CH$_2$
O
S
O
OH
n

(a) Ethylene Diamine

(b) p-Phenylene Diamine

(c) Taurine

Figure 5. (a) Ethylene diamine modified PBI. (b) p-Phenylene diamine modified PBI. (c) Taurine modified PBI.

Downloaded by UNIV OF DELAWARE MORRIS LIB on June 17, 2012 | http://pubs.acs.org
Publication Date (Web): October 31, 2011 | doi: 10.1021/bk-2011-1078.ch018

Downloaded by UNIV OF DELAWARE MORRIS LIB on June 17, 2012 | http://pubs.acs.org
Publication Date (Web): October 31, 2011 | doi: 10.1021/bk-2011-1078.ch018

Environmental Scanning Electron Microscopy (ESEM)

ESEM was used to detect the impact of surface modification of the membranes, as well as verify thickness of the cast virgin membrane. An FEI Quanta 3D FEG Dual Beam Electron Microscope (FEI, U.S.A.) was used to test the samples. By freezing small samples of the membranes in liquid nitrogen and cracking them, smooth cross-sectional areas could be observed. After the samples were frozen and cracked, they were wet using DI water, and placed vertically in carbon paste. ESEM was advantageous in this case over SEM (scanning electron microscope) because it was important to test wet samples. In aqueous environment, PBI membranes are strong and flexible. When allowed to dry, PBI becomes very brittle and susceptible to breaking.

Contact Angle

A goniometer was used to monitor the changes in the hydrophilicity of the modified membranes over that of the virgin sample. A Tantec Model CAM-MICRO Contact Angle Meter (Tantac, Inc., U.S.A.) was used. By placing a small drop of water onto the surface of the sample, the angle of the resulting water bead can be determined. In samples that are hydrophobic the water droplet beads up and the angle remains high. Successful funtionalization of the membrane surface results in an increase in hydrophilicity, thus a decrease in the water bead contact angle.

Transport Properties

Pure Water Permeability

Pure Water Permeability testing was performed using an Amicon 8010 dead-end flow cell (Millipore, U.S.A.) run as a pressure-driven process, as shown in Figure 6. Testing parameters were as follows: a feed of 10 ml of DI water was used for each test. A Fisher Scientific digital conductivity meter was used to test feed solutions to check if any contamination was present. A constant pressure of 70 psi was used in all tests. Each membrane was supported on a 0.1 μm SH magna nylon filter (Osmonics, Livermore, CA). In order to determine pure water permeability, samples were collected at regular intervals over a period of 10 hours. This process was repeated for the virgin, CMBA activated, and all membrane modifications. In order to obtain a standard deviation for the above-mentioned membranes, three separate membranes were tested for the virgin and modified samples.

Downloaded by UNIV OF DELAWARE MORRIS LIB on June 17, 2012 | http://pubs.acs.org
Publication Date (Web): October 31, 2011 | doi: 10.1021/bk-2011-1078.ch018

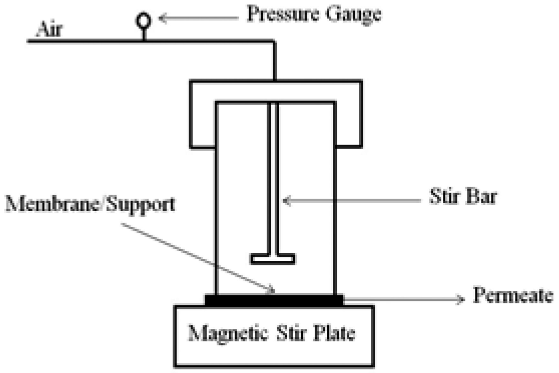

Figure 6. Schematic of dead end cell.

Monovalent Salt Solutions for Testing

Monovalent salt rejection was tested using five solutions of varying sodium chloride concentration. Using a 100 mM stock solution of NaCl in DI water, solutions of 3.4, 10, 20, 35, and 100 mM were prepared as needed. The effects of pH were of interest, and samples of the above mentioned concentrations were tested at both pH 7 and pH 10. In order to obtain samples at pH 10, titrations were performed using 0.5 M sodium hydroxide.

Solutions were run through the dead-end cell (Figure 6) at under the same conditions as used for the pure water permeability testing. Continuous stirring was maintained inside the cell just above the membrane to prevent salt build-up on the membrane surface. 10 mL samples were used for all initial feed volumes. To determine the salt rejection, conductivity readings of each feed solution was tested before sample collection. Two mL samples were collected and the conductivity of these samples measured. As with pure water permeability, three separate membranes for the virgin and each of the modifications was tested. For each membrane-concentration-pH combination, three two-mL samples were collected and tested.

Results and Discussion

Membrane Characterization

Fourier Transform Infrared Spectroscopy (FTIR)

The FTIR-ATR spectrum of PBI is characterized by several typical peaks (Figure 7 and Table 1) as reported by previous researchers (*14–19*). The FTIR spectrum for the virgin PBI samples and all the functionalized membrane samples is described in detail in Hausman et al (*9*). The EDCH/NHS modification technique used in this research yielded the same quality of FTIR data as reported in (*9*), for the EDC chemistry technique used for the membrane modifications.

Therefore, the effectiveness of this technique to modify the surface chemistry of the PBI membranes was verified.

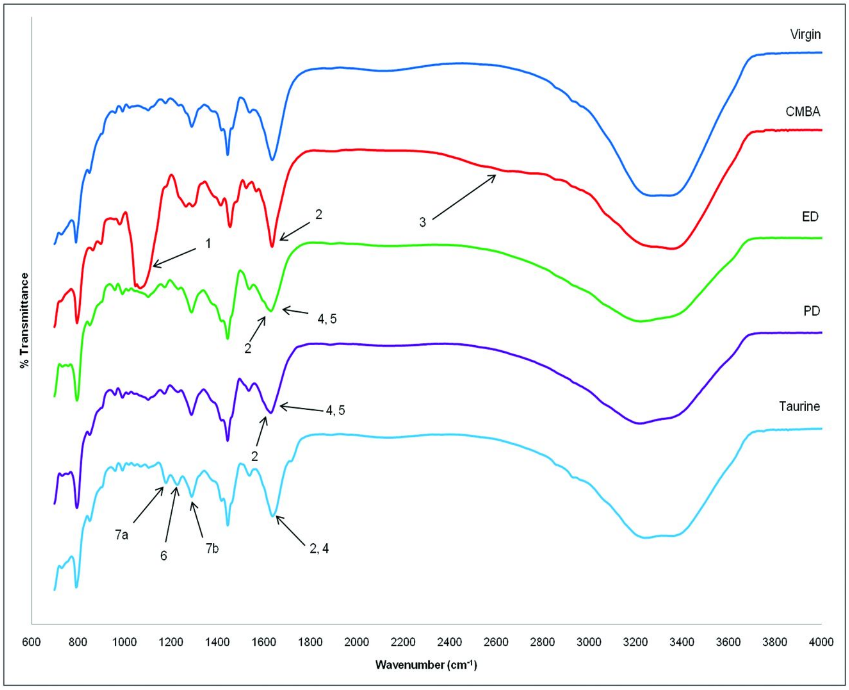

Figure 7. FTIR results for the virgin and all modifications.

Table 1. FTIR functional group location (data obtained from Hausman et al. (*9*))

Number	*Functional group*	*Wave number (cm⁻¹)*
1	C–O	1057
2	C=O	1620–1640
3	OH	~ 2670
4	Secondary amine N–H	1645
5	Primary amine NH_2	1645
6	S=O	1215
7a	SO_2 (symmetrical)	1168
7b	SO_2 (anti-symmetrical)	1285

Downloaded by UNIV OF DELAWARE MORRIS LIB on June 17, 2012 | http://pubs.acs.org
Publication Date (Web): October 31, 2011 | doi: 10.1021/bk-2011-1078.ch018

Downloaded by UNIV OF DELAWARE MORRIS LIB on June 17, 2012 | http://pubs.acs.org
Publication Date (Web): October 31, 2011 | doi: 10.1021/bk-2011-1078.ch018

ζ Potential

The change in surface charge was determined by finding the ζ potential of all the membranes surfaces. The virgin membrane samples were mostly comprised of neutral and slightly positive charges. ζ potential results are plotted against various pH values in Figure 8. All modifying agents used during the final modification step led to an overall increase in the charge of the modified membrane surfaces. These results agree with the research expectations, since all modifying agents were chosen for their ability to impart a charge on the membrane surface.

Environmental Scanning Electron Microscopy (ESEM)

As shown in Figure 9, the cross-sectional SEM image of a fractured PBI membrane shows the overall thickness of the membranes used was actually 170 μm. From the figure, the thin selective layer (the top of the membrane) and thicker support layer were observed. This is characteristic of an asymmetric membrane, and is evidence that the phase-inversion process was successful.

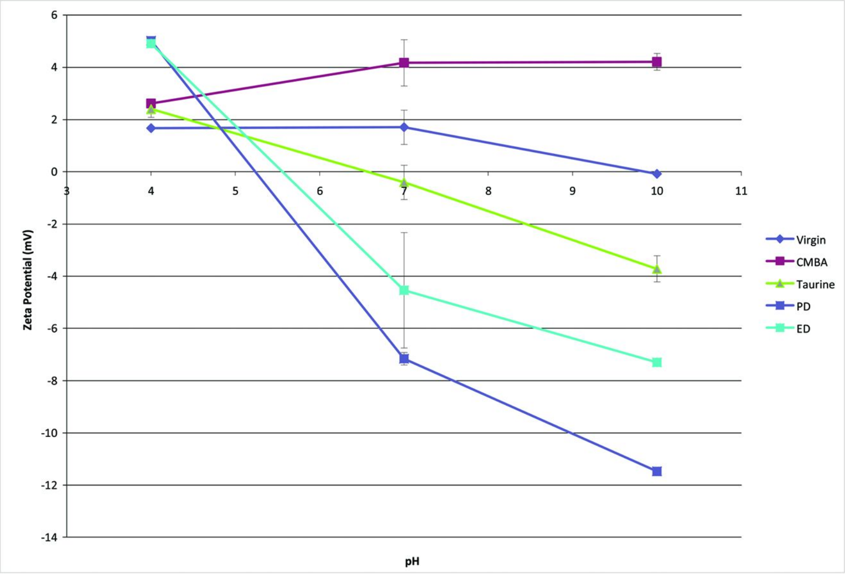

Figure 8. ζ potential vs. pH for virgin, CMBA activated, and all final membrane modifications.

Contact Angle

Contact angle measurements for the virgin, CMBA activated, and all final modifications are shown in Figure 10. The hydrophilicity of the membrane surfaces increased for all the final modifications. The taurine functionalized PBI membranes were shown to have the largest increase in hydrophilicity. This was most likely due to its greater ability to hydrogen bond. The sulfonic acid group associated with taurine contains three oxygen groups, two of which contain two pairs of free electrons and the third with the ability to form salts (i.e. move into an ionic state). The ethylene diamine modification was shown to have the least increase in hydrophilicity. Ethylene diamine is an aliphatic amine, and it offers little in the in the ability to increase hydrogen bonding. The increased hydrophilicity was most likely due to the amine group, which contains one pair of free electrons and also has the ability to hydrogen bond.

Downloaded by UNIV OF DELAWARE MORRIS LIB on June 17, 2012 | http://pubs.acs.org
Publication Date (Web): October 31, 2011 | doi: 10.1021/bk-2011-1078.ch018

Transport Properties

Pure Water Permeability

As shown in Figure 11, the pure water permeability (PWP) decreased following surface modification. After surface activation with CMBA, the average permeability decreased by approximately 33% relative to the virgin membrane samples. For each of the final membrane modifications, the permeability measurements dropped approximately 70% relative to the virgin PBI membranes. The average pure water permeability of the flat sheet virgin, CMBA activated, taurine, ethylene diamine, and p-phenylene diamine samples were 3.67, 2.59, 1.21, 1.20, and 1.16 L m^{-2} bar^{-1} h^{-1} respectively. Lv et al. (*8*) reported PBI nanofiltration FO hollow fiber membranes can produce PWP values of 1.86 L m^{-2} bar^{-1} h^{-1} and other studies have also reported significant loses of membrane permeability after surface modifications with modifying agent additions (*20–27*).

Monovalent Salt Rejection

Figure 12 shows the results for monovalent salt rejection for the virgin, CMBA activated, and all final membrane modifications. Monovalent salt rejection increased for all membrane modifications. Though taurine has a larger negative dipole moment associated with the two pi bonded oxygen groups containing free electrons, in addition to the hydroxyl group, at pH 7 (Figure 12 (a)), para-phenylene diamine had the highest salt rejection for lower concentrations.

Downloaded by UNIV OF DELAWARE MORRIS LIB on June 17, 2012 | http://pubs.acs.org
Publication Date (Web): October 31, 2011 | doi: 10.1021/bk-2011-1078.ch018

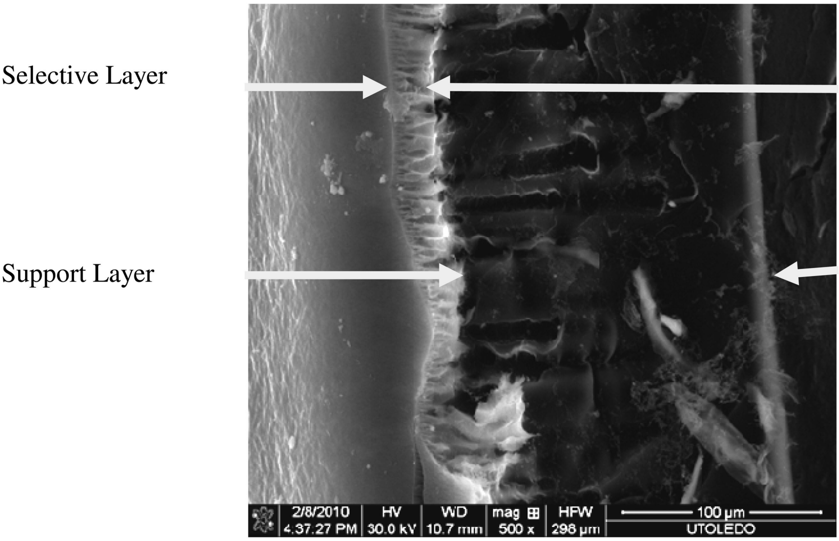
Selective Layer
Support Layer
2/8/2010
4:37:27 PM
HV
30.0 kV
WD
10.7 mm
mag
500 x
HFW
298 µm
100 µm
UTOLEDO

Figure 9. SEM image of virgin membrane.

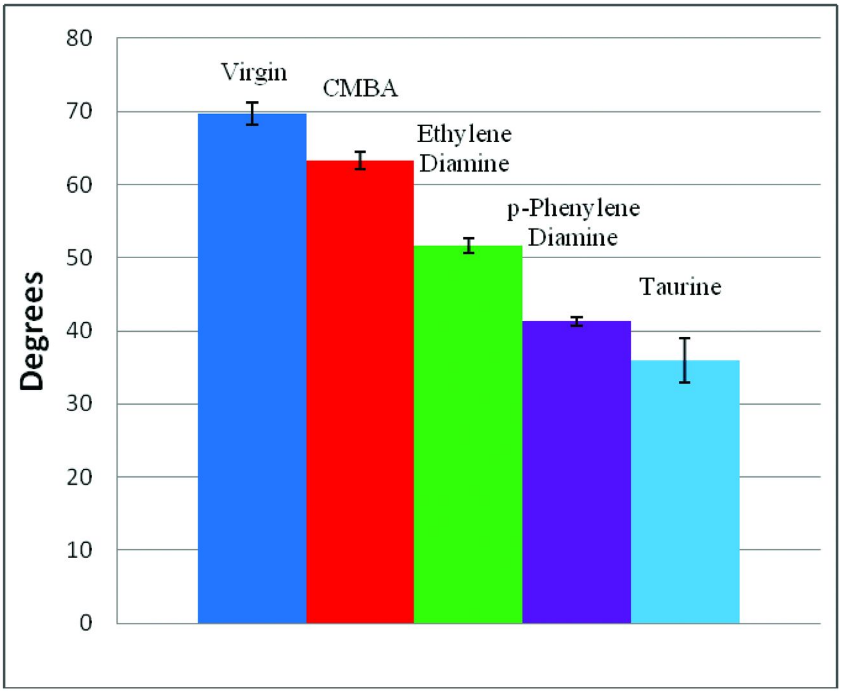

Figure 10. Contact angle measurements for virgin and all modified membranes.

Downloaded by UNIV OF DELAWARE MORRIS LIB on June 17, 2012 | http://pubs.acs.org
Publication Date (Web): October 31, 2011 | doi: 10.1021/bk-2011-1078.ch018

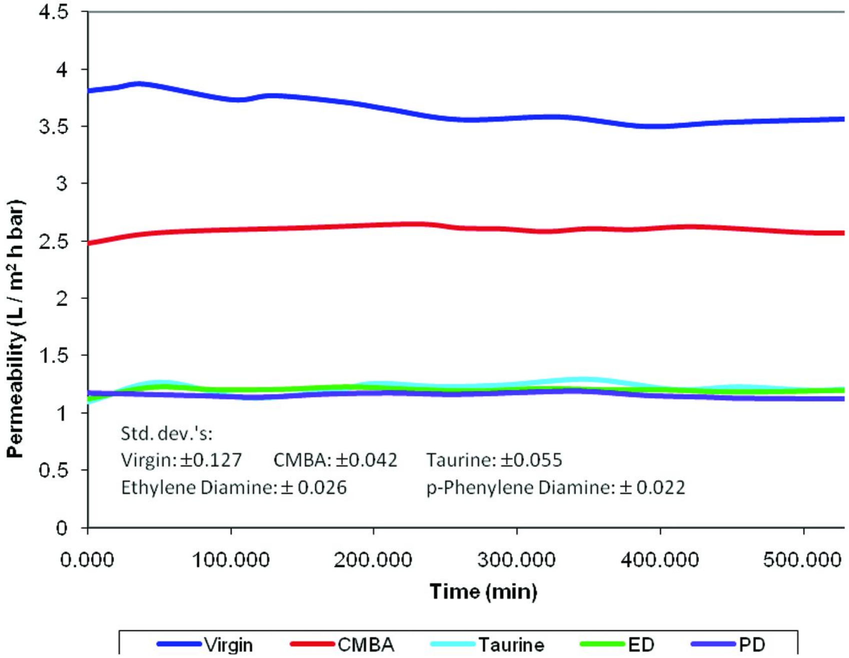

Figure 11. Pure water permeability readings in an Amicon 8010 dead-end flow cell at 70 psi.

As the salt concentration increased, the rejection stabilized, and there was no significant difference in the final percent rejected among the modified membranes. Salt rejection via charge exclusion is only effective at low ionic strengths where monovalent and divalent cations do not screen the negative charge of the membrane surface (*28*). This is consistent with the results presented here. The rejection of the salts drops as a function of increasing ionic strength. Previous studies (*29*) have shown similar results where by increasing hardness, ionic strength, or hydrogen ions (pH), the surface charge of the membrane was masked.

When the pH of the feed stream was increased to 10, the salt rejection for all membranes increased (Figure 12 (b)). The taurine-modified membrane showed the highest rejection values at lower concentration, but the difference from the other modifications was not as significant as that seen at pH 7. Once again, as the concentration increased, the percent rejection stabilized and there was less of a difference. There was only a small increase in the percent rejection of the phenylene diamine from pH 7 to pH 10, but there was a significant increase for taurine functionalized membranes over the same pH range. It is believed that by increasing the pH, taurine was able to form its sodium salt, therefore making the charge higher than at pH 7.

)

Downloaded by UNIV OF DELAWARE MORRIS LIB on June 17, 2012 | http://pubs.acs.org
Publication Date (Web): October 31, 2011 | doi: 10.1021/bk-2011-1078.ch018

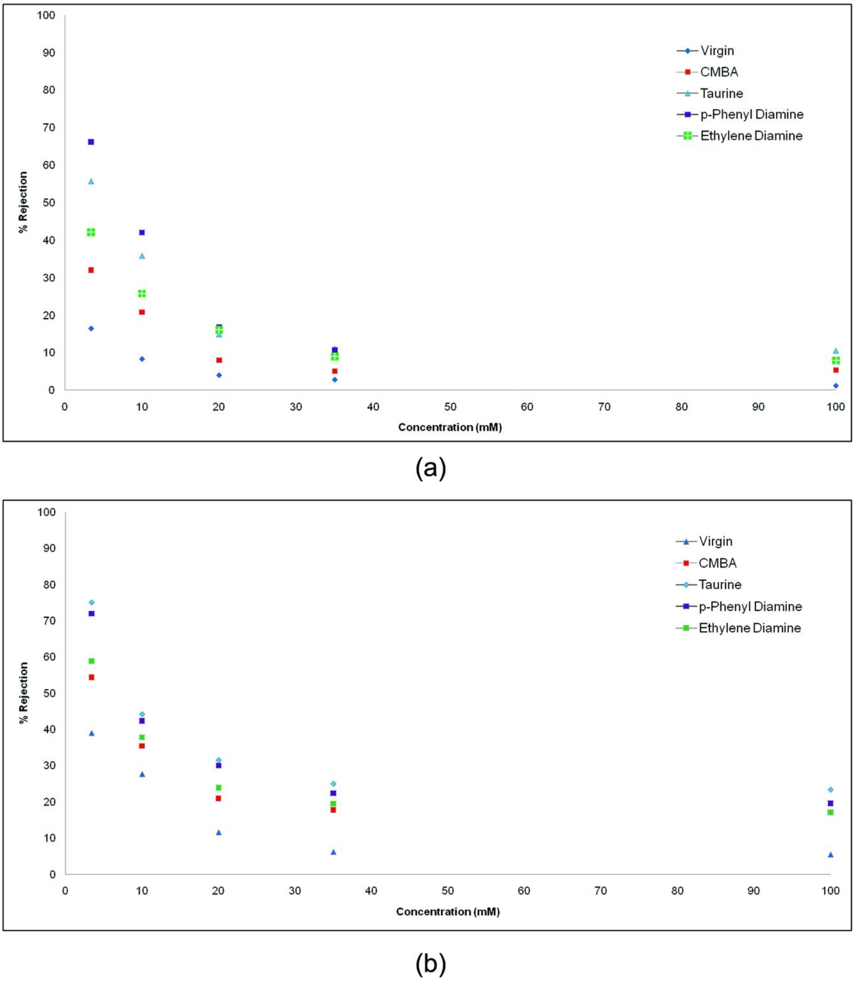

Figure 12. (a) Sodium chloride rejection at pH 7. (b) Sodium chloride rejection at pH 10.

To evaluate the effects of the modifications further, the salt permeability coefficients (B) were determined during 3.4mmol salt rejection studies using equation 1. This technique for calculating the salt permeability coefficient has been reported by previous researchers (*6*, *30*) for a pressure driven process similar to the one used in this study.

$$R = \left(1 + \frac{B}{A(\Delta P - \Delta \pi)}\right)^{-1} \qquad (1)$$

Downloaded by UNIV OF DELAWARE MORRIS LIB on June 17, 2012 | http://pubs.acs.org
Publication Date (Web): October 31, 2011 | doi: 10.1021/bk-2011-1078.ch018

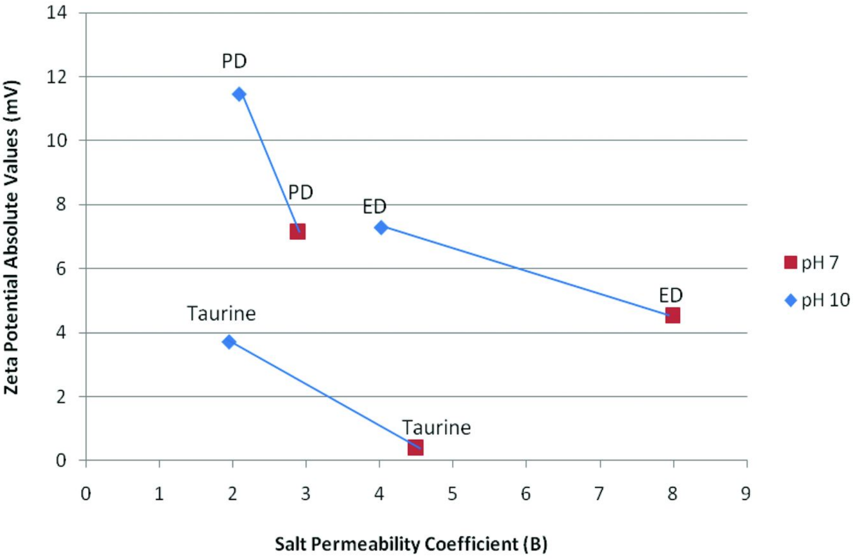

Figure 13. Salt permeability coefficients vs. ζ potential readings for the three final membrane surface modifications.

Where R = salt rejection, A = water permeability, ΔP = pressure difference, and Δπ = osmotic pressure difference. The salt permeability coefficients (B) are plotted against absolute value zeta potentials for the three final membrane modifications in Figure 13. The PWP significantly decreases as the membrane modification process takes place. The average permeability decreased by approximately 33% for the activated membranes, and for each of the final membrane modifications the permeability measurements dropped approximately 70% relative to the virgin PBI membranes. Since all three final surface modifications showed increases in hydrophilicity over the virgin membranes, this PWP decrease is believed to be largely attributed to the change in membrane pore sizes resultant of the larger repeat unit of the PBI backbone for the modified surfaces. Due to the predicted change in pore size, and the significant reductions in PWP readings, comparisons can only be made between the final modifications. The PWP values for all three final modifications were very close to one another so it is believed that the membranes should be similar enough to warrant comparison by way of this technique. The data for each individual membrane can also be compared over different pH values to see the effects of zeta potential on the salt permeability coefficient. As expected, salt permeability coefficients decreased with modifications and with increasing pH.

From the plot of salt permeability coefficient vs. zeta potential it seems that the rejection of NaCl is related more by the decrease in pore size than from the differences in zeta potential. It is important to note however, that for all three surface modifications the values of B decrease as the absolute values of the zeta potentials increase. When the membranes are compared to one other the zeta potential readings don’t seem to be the sole contributor to the increase in salt rejection. The decrease in the salt permeability coefficients from the reduced poor size can be attributed to the size of the aromatic ring in the p-phenylene diamine and the sulfonate group in the taurine molecules versus the much smaller ethylene diamine molecule.

Conclusions

Flat sheet polybenzimidazole membranes were successfully cast, CMBA activated, and modified. ESEM images verified that the membranes were in fact asymmetric with an acceptable overall thickness from the value desired. From the FTIR spectra, there was clear evidence that surface activation and modification took place, which verified that the modification method proposed by this study is effective. An increase in hydrophilicity showed successful completion of one of the research objectives and was a further means of verification of modification. ζ potential analysis showed an overall increase in surface charge. This also verified chemical modification, and the successful achievement of the other research objective, to increase surface charge. Pure water permeability results showed a significant decrease with the CMBA activation and the final modifications. Sodium chloride rejection decreased exponentially as the feed concentration increased for all modifications, as well as the virgin membrane. Modified membranes always showed higher rejections than virgin membranes. This trend was seen at both feeds of pH 7 and pH 10.

The study presented here shows preliminary characterization data on the effectiveness of surface modifications to PBI membranes in rejecting salts. Future research will involve testing the virgin and modified PBI membranes in forward osmosis mode. The rejection of the NaCl at higher ionic strengths by the modified membranes was still low, which would not be effective for FO systems at this time. The study presented here was a proof-of-concept of the ability for functionalization to increase salt rejection. Ongoing and future studies will focus on optimizing the membranes (for instance by increasing dope concentrations to make tighter membranes) and draw solutions for the FO process.

Acknowledgments

The authors would like to acknowledge grant NSF OISE 0832894 that supported the development of the collaboration on PBI FO research between The National University of Singapore and The University of Toledo. PBI Performance Products, Inc. (Charlotte, NC) is thanked for supplying PBI dope for the study. Professor Volodymyr Tarabara (Michigan State University) is also thanked.

References

1. Gray, G. T.; McCutcheon, J. R.; Elimelich, M. *Desalination* **2006**, *197*, 1–8.
2. Ng, H. Y.; Tang, W.; Wong, W. S. *Environ. Sci. Technol.* **2006**, *40*, 2408–2413.
3. Gray, G.; McCutcheon, J.; Elimelech, M. *Desalination* **2006**, *197*, 1–8.

Downloaded by UNIV OF DELAWARE MORRIS LIB on June 17, 2012 | http://pubs.acs.org
Publication Date (Web): October 31, 2011 | doi: 10.1021/bk-2011-1078.ch018

4. McCutcheon, J.; Elimelech, M. *J. Membr. Sci.* **2006**, *284*, 237–247.
5. McCutcheon, J.; Elimelech, M. *J. Membr. Sci.* **2008**, *318*, 458–466.
6. Saren, Q.; Qiu, C. Q.; Tang, C. Y. *Environ. Sci. Technol.* **2011**, *45* (12), 5201–5208.
7. Wang, K. Y.; Chung, T. S.; Qin, J. J. *J. Membr. Sci.* **2007**, *300*, 6–12.
8. Lv, J.; Wang, K. Y.; Chung, T. S. *J. Membr. Sci.* **2008**, *310*, 557–566.
9. Hausman, R.; Digman, B.; Escobar, I.; Coleman, M.; Chung, T. S. *J. Membr. Sci.* **2010**, *363*, 195–203.
10. Wang, K. Y.; Chung, T. S. *AIChE J.* **2006**, *52*, 1363–1377.
11. Sukumar, P. R.; Wu, W.; Markova, D.; Unsal, O.; Klapper, M.; Mullen, K. *Macromol. Chem. Phys.* **2007**, *208*, 2258–2267.
12. Mapkar, J.; Iyer, G.; Coleman, M. *Appl. Surf. Sci.* **2009**, *255*, 4806–4813.
13. Shan, W.; Bacchin, P.; Aimar, P.; Bruening, M.; Tarabara, V. *J. Membr. Sci.* **2010**, *209*, 268–278.
14. Foldes, E.; Fekete, E.; Karasz, F. E.; Pukanszky, B. *Polymer* **2000**, *41*, 975–983.
15. Guerra, G.; Choe, S.; Williams, D. J.; Karasz, F. E.; MacKnight, W. J. *Macromolecules* **1988**, *21*, 231–234.
16. Musto, P.; Karasz, F. E.; MacKnight, W. J. *Macromolecules* **1991**, *24*, 4762–4769.
17. Ahn, T. K.; Kim, M.; Choe, S. *Macromolecules* **1997**, *30*, 3369–3374.
18. Musto, P.; Karasz, F. E.; MacKnight, W. J. *Polymer* **1993**, *34*, 2934–2945.
19. Musto, P.; Karasz, F. E.; MacKnight, W. J. *Polymer* **1989**, *30*, 1012–1021.
20. Freger, V.; Gilron, J.; Belfer, S. *J. Membr. Sci.* **2002**, *209*, 283–292.
21. Gilron, J.; Belfer, S.; Väisänen, P.; Nyström, M. *Desalination* **2001**, *140*, 167–179.
22. Belfer, S.; Gilron, J.; Purinson, Y.; Fainshtain, R.; Daltrophe, N.; Priel, M.; Tenzer, B.; Toma, A. *Desalination* **2001**, *139*, 169–176.
23. Thom, V.; Ulbricht, M.; Kops, V.; Jonsson, G. *Macromol. Chem. Phys.* **1998**, *199*, 2723–2729.
24. Ulbricht, M.; Matuschewski, H.; Oechel, A.; Hicke, H. *J. Membr. Sci.* **1996**, *115*, 31–47.
25. Pieracci, J.; Crivello, J.; Belfort, G. *J. Membr. Sci.* **1999**, *156*, 223–240.
26. Ma, H.; Bowman, C. N.; Davis, R. H. *J. Membr. Sci.* **2000**, *173*, 191–200.
27. Ito, Y.; Inaba, M.; Kono, K.; Imanishi, Y. *Macromolecules* **1992**, *25*, 7313–7316.
28. Skluzacek, J. M.; Tejedor, M. I.; Anderson, M. A. *J. Membr. Sci.* **2007**, *289*, 32–39.
29. Escobar, I. C.; Hong, S. K.; Randall, A. *J. Membr. Sci.* **2000**, *175*, 1–17.
30. Tang, C. Y.; She, Q.; Lay, W. C. L.; Wang, R.; Fane, A. G. *J. Membr. Sci.* **2010**, *354*, 123–133.

Downloaded by UNIV OF DELAWARE MORRIS LIB on June 17, 2012 | http://pubs.acs.org
Publication Date (Web): October 31, 2011 | doi: 10.1021/bk-2011-1078.ch018

Downloaded by UNIV OF DELAWARE MORRIS LIB on June 19, 2012 | http://pubs.acs.org
Publication Date (Web): October 31, 2011 | doi: 10.1021/bk-2011-1078.ot001

Editor's Biographies

Isabel C. Escobar

Isabel C. Escobar is a Professor of Chemical and Environmental Engineering at The University of Toledo, Ohio, USA, and she received a Ph.D. degree from the University of Central Florida, as an U.S. EPA Science To Achieve Results (STAR) Fellow. She has authored one licensed patent on anti-biofouling feed spacers, over 50 publications, over 100 presentations, and a book on sustainable water treatment. She is Associate Editor of *Environmental Progress and Sustainable Energy Journal*. She is the recipient of numerous awards including the 2009 Northwest Ohio YWCA Milestone Award for Education, the 2009 the Northwest Ohio 20 Under 40 Leadership Award, and the 2011 AIChE Kunesh Award.

Bart Van der Bruggen

Bart Van der Bruggen is a chemical engineer by education, with a Ph.D. from K.U.Leuven (Belgium) in 2000. He is currently professor at K.U.Leuven, leading a research group of 20 Ph.D. students active in membrane-related studies. He has authored 130 publications in ISI journals, and 11 book chapters. He is Editor of *Separation and Purification Technology*, and serves as Associate Editor for *Journal of Chemical Technology and Biotechnology*. He actively promotes membrane research as an ambassador for the European Membrane Society, for which he served as a council member (2007-2011) and vice-president, by strengthening collaborations with the America's and Asia/Australia, and developing the membrane community in Africa.

In Modern Applications in Membrane Science and Technology; Escobar, I., et al.;
ACS Symposium Series; American Chemical Society: Washington, DC, 2011.

Subject Index

A

- Aromatic/aliphatic mixtures, separation pervaporation, 82
- Aromatic substitution mechanism nitrated via electrophilic, 114

B

- Benzene exposure tests, 87
  - Sohxlet extractor, 99*t*
- Benzene/n-heptane system
  - materials and data, 93
  - separation, 95*t*
- Biofilm
  - polysaccharides, concentration, 235*f*
  - thickness, filtration hour, 234*f*
- Biofouling, 165, 225
  - biofilm
    - polysaccharides concentration, 235*f*
    - thickness, 234*f*
  - cell removal, membranes fouled, 231*f*
  - cross-flow filtration apparatus, schematic diagram, 229*f*
  - Cu-charged feedspacer
    - performance, 227, 232
  - Cu(II) charged PP-graft-GMA-IDA
    - characterization, 227
    - preparation, 227
  - fouled membranes
    - FTIR spectroscopy, 228, 235
    - live/dead cell counts, 228
    - SEM imaging, 228, 234
  - FTIR spectra, 229*f*
  - live/dead cell counts, 233
  - materials, 226
  - membranes filtration
    - permeability versus time, 230*f*
  - membranes fouling, 225
    - SEM images, 233*f*
  - pseudomonas fluorescens biofilms, 230*t*
- Boundary layer superposition
  - concentration predictions, 142
  - diluent volume fraction, 148*f*
  - FIDAP solution, two-dimensional, 147*f*
  - predicted surface diluent volume fraction, 147*f*
  - radial concentration distribution, schematic diagram, 146*f*
  - variable surface concentration profile, schematic diagram, 144*f*

C

- Carbon nanofiber (CNF)
  - atomic percentage, 73*t*
  - functionalization, 69
    - dihydroxyl based IL, 71*s*
    - IL [Br], 71*s*
- Carbon nanotube/polyethersulfone
  - composite membranes
  - water filtration, 257
- Cellulose acetate ultrafiltration (CAUF)
  - membranes, 247
  - adhesion force analysis, 252
    - membrane surface roughness, 252
  - AFM force curve analysis, 249
  - crossflow membrane filtration unit, 249
  - feed water characteristics, flux decline measurements, 251
  - hydrophobicity, mapping, 250
- Cellulose diacetate (CDA), 272
- Chemical stability, 96
- CH$_3$-functionalized tip
  - CFM images
    - membrane surfaces using DI water, 254*f*
    - membrane surfaces using tap water, 255*f*
- Clean membranes, performance behavior, 161
- CNF- IL [Br]
  - CO$_2$/CH$_4$, selectivity, 77*f*
  - CO$_2$/H$_2$, selectivity, 77*f*
- CNF- IL (Taurine)
  - CH$_4$ (barrer), permeability, 76*f*
  - CO$_2$ (barrer), permeability, 75*f*
  - CO$_2$/CH$_4$, selectivity, 77*f*
  - CO$_2$/H$_2$, selectivity, 77*f*
  - H$_2$ (barrer), permeability, 75*f*
- CO$_2$ capture, membrane, 2
- Cu$_{50}$Pd$_{43.75}$Al$_{6.25}$ alloys
  - DSC plots, 35*f*
- Cu$_{50}$Pd$_{43.75}$M$_{6.25}$ alloys, B2-containing
  - DSC plots, 35*f*
  - EDS/XRD results, 34*t*
  - SEM back-scattered electron images, 33*f*
  - XRD plots, 31*f*

Downloaded by 89.163.35.42 on June 17, 2012 | http://pubs.acs.org
Publication Date (Web): October 31, 2011 | doi: 10.1021/bk-2011-1078.ix002

Downloaded by 89.163.35.42 on June 17, 2012 | http://pubs.acs.org
Publication Date (Web): October 31, 2011 | doi: 10.1021/bk-2011-1078.ix002

D

- Dairy industry, membranes, 171
  - electrodialysis (ED), 202
    - lactose fermentation, removal, 205
    - protein fractions, production, 204
    - whey and milk, 203
  - maintenance and cleaning, 206
  - membranes, uses, 208*f*
  - microfiltration (MF), 172
    - bacteria removal, 173
    - fat and casein removal, 177
    - increased shelf life, 173
    - milk separation, 172*f*
    - milk/cheeses, recombination, 175
    - serum proteins removal, 177*f*
    - spore removal process, 174*f*
  - nanofiltration (NF), 194
    - demineralization, 195
    - lactose, recovery, 200
    - milk UF permeate, 199
    - mineral reductions, 197*t*
    - nutritional benefits made, 198*f*
    - uses, 201
  - reverse osmosis (RO), 189
    - milk concentration, 193*f*
    - versus evaporation, 192
    - waste reduction, 189
    - whey and milk concentration, 190
  - ultrafiltration (UF), 179
    - cheese manufacture, 182*f*
    - cheese production, 180
    - diafiltration (DF), 182
    - farm, 188
    - milk, demineralized, 201*f*
    - protein fractationation processes, 184, 187*f*
    - whey, batch diafiltration, 184*t*
    - whey proteins, properties, 186*t*
- Dead-end method. *See* Filtration instrument
- Density functional theory (DFT) calculations, 28
  - hypothetical B2 $Cu_8Pd_{8-x}M_x$, formation enthalpy, 29*f*
- 1, 3-Di(3-aminopropyl)-imidazolium bromide [C3-NH2 C3-NH2 Im][Br], 67
- 2,6-Diaminotriptycene (DATri)
  - ^{1}H-NMR spectrum, 115*f*
  - synthesis, 110, 112*f*
- 1,4-Di[3-ethanol-imidazolium]butane taurate ([C4 [C2OHim][taurine]) synthesis, 68
- 2,6-Dinitrotriptycene (DNTri), 114
  - FT-IR spectrum, 115*f*
  - ^{1}H-NMR spectrum, 115*f*
- Dry-wet hollow fiber spinning process, schematic drawing, 131*f*

E

- EDCH molecular structures, 308*f*
- Electrodialysis (ED), 202
  - lactose fermentation, removal, 205
  - protein fractions, production, 204
  - whey and milk, 203
- Energy
  - hydrogen, 28
  - membrane, 2

F

- 6FDA-based polyimide membranes
  - CO_2 permeability, 124*f*
  - gas permeabilities, 120*t*
  - physical properties, 118*t*, 120*t*
- 6FDA-DATI polyimide (6FDA-DATri), synthesis, 110
- 6FDA-DATri membrane, gas separation performances, 126*f*
- 6FDA-DATri polyimide membranes
  - diffusion coefficient, 125*f*
  - DSC thermogram, 121*f*
  - FT-IR spectrum, 116*f*
  - gas permeability, 122*f*
  - ^{1}H-NMR spectrum, 116*f*
  - physical properties, 116*t*
  - solubility, 122*t*
    - coefficients, 125*f*
  - synthesis, 112*f*
  - TGA curve, 121*f*
- Feed water concentrations
  - average adhesion forces, 253*t*
  - crossflow filtration experiments, 250*t*
- Film casting knife, 273*f*
- Filtration instrument, 274*f*
- Food industry, membrane contacts, 209*t*
- Functional nanocomposite network material
  - cartoon depicting, 64*f*
- Functional nanofiber network (FNN)
  - materials, 64
  - film formation, 70
  - interfacial region, functional molecules, 65
  - nanofiber network, 65
  - polymer matrices, 66

Downloaded by 89.163.35.42 on June 17, 2012 | http://pubs.acs.org
Publication Date (Web): October 31, 2011 | doi: 10.1021/bk-2011-1078.ix002

G

- Gas permeability, 126*f*
- Gas permeation, 74
  - ionic liquid-functionalized nanocomposite membranes, characterization, 71
  - oxidized carbon nanofiber (CNF- OX), 74
  - permeation cell, 71*f*
- Gas separation
  - membrane, 2
  - *See also* Membrane gas separation

H

- HDI-PEG600 polyurethane
  - isothermal TGA, 97*f*
  - thermal stability, 96
  - thermogravimetric analysis (TGA), 97*f*
- Hollow fiber spinning
  - base spinning conditions, 138*t*
  - bore fluid flow
    - computational domain/boundary conditions, 138*f*
    - recirculation, 137
  - die exit, flow
    - axial velocity contour plot, 140*f*
    - streamline contour plot, 139*f*
  - L_{rec}/L, contour plot, 141*f*
  - outer/inner radii
    - TFA, two-dimensional simulation, 142*f*
  - polyethylene-dodecanol system material properties, 139*t*
  - regions, 132*f*
  - simulation, overview, 129
  - theoretical models, 134
- Homogeneous membrane construction, 158*f*
- Hydrogen separation membranes
  - alloy compositions, 31*t*
  - density functional theory (DFT)
    - calculations, 28
    - hypothetical B2 $Cu_8Pd_{8-x}M_x$, enthalpy, 29*f*
  - experimental procedures, 30
    - chemical analysis, 30
    - DSC, 34
    - SEM/EDS and XRD results, 30
- Hydrophobicity
  - diffusion rate, 46*t*
  - selectivity, variation
    - Mes versus Phl, 47*f*
    - PADPA versus AY, 47*f*
    - versus size, 48
  - by total polar surface area (tPSA), 48*f*
- Hydrophobicity-based diffusion selectivity, 45
- Hydrophobicity-based separations
  - initiated chemical vapor deposition (iCVD)
    - coating characterization, 41
    - diffusion experiments, 42
    - diffusion selectivity, 45
    - electron probe microanalysis (EPMA), 42
    - mechanism selectivity, 48
    - membrane pore size characterization, 41
    - nanopore membranes formation, 41, 42
    - overview, 39
  - nanotube membranes, 39

I

- IL (Taurine), synthesis, 69*s*
- Initiated chemical vapor deposition (iCVD)
  - coating
    - characterization, 41
    - schematic, 43*f*
  - hydrophobicity-based separations
    - diffusion experiments, 42
    - diffusion selectivity, 45
    - electron probe microanalysis (EPMA), 42
    - mechanism selectivity, 48
    - membrane pore size characterization, 41
    - nanopore membranes formation, 41, 42
    - overview, 39
- Ion exchange capacities, 241*t*
- Ionic liquid-functionalized nanocomposite membranes
  - characterization
    - gas permeation, 71
    - X-ray photoelectron spectroscopy (XPS), 70
  - surface functionalization, confirmation, 72

L

- Lactose fermentation, 205
- LiCl

Downloaded by 89.163.35.42 on June 17, 2012 | http://pubs.acs.org
Publication Date (Web): October 31, 2011 | doi: 10.1021/bk-2011-1078.ix002

  filtration flux data, 281*t*
  NaCl solution, 281*t*, 282*t*
  polysulfone (PSf) membranes, 278*t*, 279*t*
  precompaction, 281*t*
  precompaction flux data, 280*f*
  PSf solution, 281*t*
  solution accompanying, 280*f*
Liquid separations, membrane, 3

M

Membrane filtration, rejection characteristics, 158*f*
Membrane fouling, 163
  biofouling, 165
  inorganic, 164
  limitations/functioning, 166
  organic, 164
  prevention, 166
Membrane gas separation
  bibliometric analysis, 16
  challenges, 16
  CO_2 capture, 2, 9
  competing technologies, 8
  gas separation, 8
  history, 10
  overview, 8
  publications, percentages
    articles, 18*t*
    category, 17*f*
    ISI Web, 11*f*
    rank, 18*t*
    search term study, 20*f*
Membrane pore size characteristics, and application, 159*t*
Membranes
  dairy industry, 171
  preparation, 86, 111
  water treatment, 156
Membrane separation technologies, 1, 257
Microfiltration (MF), 172
  bacteria removal, 173
  fat and casein removal, 177
  increased shelf life, 173
  milk separation, 172*f*
  milk/cheeses, recombination, 175
  serum proteins removal, 177*f*
  spore removal process, 174*f*
Milk concentration, reverse osmosis (RO), 193*f*
Milk separation, pressure driven flow, 172*f*
Monomers, chemical structures, 44*f*
Multi-walled carbon nanotube (MWCNT)
  C/P composite membranes
    properties, 264*t*
    pure water fluxes, 264*f*
    solute permeation fluxes, 265*f*
  membrane characterization, 259, 261
  membrane filtration procedures, 260
  membrane preparation, 259
  membranes, contact angles, 263*f*
  permeability and solute rejection, 263
  SEM images, 262*f*

N

NaCl, permeability data, 243*f*
Nanofiltration (NF), 194
  demineralization, 195
  lactose, recovery, 200
  milk UF permeate, 199
  mineral reductions, 197*t*
  nutritional benefits made, 198*f*
  uses, 201
Nanopore membranes formation
  diffusion rate, dependence, 48*f*
  formation, 43*f*
  iCVD coating, 41
    schematic, 43*f*
Nanotube membranes, samples properties, 44*t*
NHS molecular structures, 308*f*
NMP, polyimides, inherent viscosity, 88*t*

O

Oxidized carbon nanofiber (CNF- OX), 66
  confirmed using XPS analysis, 72
  functional groups, 65*t*
  functionalization, 69
    $[C_4[C_2OHim][taurine]$, 70
    [C3-NH2 C3-NH2 Im][Br], 69
  gas permeation, 74
  XPS spectrum, 73*f*

P

PBI virgin membrane
  CMBA activation, 307*f*
  EDCH/NHS reaction, 308*f*
PC membrane
  diffusion rate, 46*t*
  samples properties, 44*t*
Pd composition, high/low, 31*t*
$Pd_{27.75}M_{6.25}Cu_{66}$ alloys

  - XRD plots, 32*t*
- PDMS membranes
  - basic pervaporation performance, 54
  - characterization, 54
  - contact angle measurements, 53
  - diffusion coefficient, 125*f*
  - experiments, ethanol/water, 53
  - fermentation medium, 53
  - solubility coefficients, 125*f*
  - ZSM-5, membrane performance, 55*t*
- Permeability data
  - sulfonated hydrocarbon polymers membrane
    - magnesium chloride ($MgCl_2$), 242
    - single-salt, 243*f*
    - sodium chloride (NaCl), 242
- Pervaporation, 86
  - aromatic/aliphatic mixture separation, 82
  - benzene/n-heptane mixture separation, 96*f*
  - by-product influence, 54
  - carboxylic acid concentration influence, 56*f*
  - dianhydride moiety effect, 93*t*
  - ethanol/water mixtures, 54
    - versus fermentation broth, 55*t*
  - fermentation broth, 53
  - overview, 52
  - polyimides preparation, 95*t*
  - toluene/n-heptane mixture separation, 94*f*
- Polybenzimidazole membranes
  - ethylene diamine, 310*f*
  - FTIR functional group location, 313*t*
  - FTIR results, 313*f*
  - membrane characterization
    - contact angle, 311, 315
    - environmental scanning electron microscopy (ESEM), 314
    - Fourier transform infrared spectroscopy (FTIR-ATR), 309, 312
    - ζ potential, 309, 314
  - membrane modification, 306
    - CMBA membrane activation, 306
    - EDCH/NHS chemistry, 307
  - modifying agents, 310*f*
  - pH 7, sodium chloride rejection, 318*f*
  - preparation, 306
  - pure water permeability, 317*f*
  - salt permeability coefficients versus z potential, 319*f*
  - surface functionalization, 303
  - transport properties
    - monovalent salt solutions, 312, 315
    - pure water permeability, 311, 315
  - virgin membrane
    - contact angle measurements, 316*f*
    - SEM image, 316*f*
  - ζ potential versus pH, 303
- Polyethylene-dodecanol system material properties
  - hollow fiber spinning, 139*t*
- Poly(1H,1H,2H,2H-perfluorodecyl acrylate) (pPFDA)
  - chemical structures, 44*f*
  - membrane samples properties, 44*t*
- Polyimide membranes
  - diffusion coefficient, 103*t*
  - gas separation, 108
  - NMP, 88*t*
    - inherent viscosity, 88*t*
  - toluene
    - kinetic sorption curves, 102*f*
    - permeability, 103*t*
- Polyimide synthesis, 83
  - FTIR spectra, 89*f*
  - ^{1}H NMR spectra, 90*f*
- Polymer characterization, 84, 88
- Polymer films, photographs, 98*f*
- Polymeric ionic liquids (PILs), 63
- Polymers
  - hydrocarbons, equilibrium uptake, 101*f*
  - 2,6/2,7-triptycene linked, 111*f*
  - 9,10-triptycene linked, 111*f*
- Polymer synthesis, 83
  - diamines, 84*f*
  - dianhydrides, 83*f*
  - schematic route, 85*f*
- Polysulfone (PSf) membranes
  - filtration/precompaction flux data, 75*f*, 276*f*, 277*f*, 278*f*, 278*t*, 279*f*
  - flat sheet, 273*f*
  - NaCl solution, 282*t*
- Pore formers, 276
- Pristine, 66
- Pure hydrocarbons, equilibrium uptake, 101*f*
- Pure-liquid sorption, 87, 99

R

- Reverse osmosis (RO), 189
  - milk concentration, 193*f*
  - versus evaporation, 192
  - waste reduction, 189
  - whey and milk concentration, 190
- Reverse osmosis (RO) membrane
  - flat-leaf test apparatus, photograph, 294*f*
  - flux, 295*f*

Downloaded by 89.163.35.42 on June 17, 2012 | http://pubs.acs.org
Publication Date (Web): October 31, 2011 | doi: 10.1021/bk-2011-1078.ix002

Downloaded by 89.163.35.42 on June 17, 2012 | http://pubs.acs.org
Publication Date (Web): October 31, 2011 | doi: 10.1021/bk-2011-1078.ix002

  - milk concentration, 193*f*
  - salt rejection, 297*f*
- Reversible ion exchange-membrane (RIX-M)
  - desalination process, 292*f*
  - different sulfate salts, solubility, 287
  - overview, 285
  - RO membrane
    - flat-leaf test apparatus, photograph, 294*f*
    - flux, 295*f*
    - salt rejection, 297*f*
  - scale forming ions, 291*f*
  - scaling potential, solubility, 287
  - seawater, 289*t*
  - sodium chloride, osmotic pressure, reduction, 293*f*
  - sulfate salts, solubility products, 289*t*
  - supersaturation index (SI) values, sulfate salts, 290*f*
  - synthetic seawater solution
    - barium concentration, 298*f*
    - calcium concentration, 297*f*
    - ions, breakthrough profile, 295*f*
  - underlying process concept, 289
- Room temperature ionic liquids (RTIL), 62
  - synthesis, 67

S

- Serum proteins removal, 177*f*
- Solid fiber spinning, theoretical models, 132
- Solute molecules
  - chemical parameters, 46*t*
  - diffusion rate, 46*t*
- Spinning processes, 130
- Sulfonated hydrocarbon polymers membrane, 239
  - ion exchange capacity (IEC), 240
  - permeability data
    - magnesium chloride ($MgCl_2$), 242
    - single-salt, 243*f*
    - sodium chloride (NaCl), 242
  - polymer film samples, 241
- Sulfonated pentablock copolymer, structure, 241*f*
- Sulfonated styrenic pentablock copolymer, material, 240
- Sulfonation fractions, 241*t*

T

- Tailor-made ultrafiltration polysulfone membranes, 271
  - casting solution concentration, 274
  - LiCL additive effect, 276
  - materials and casting instrument, 272
  - membrane preparation, 272
  - precompaction and filtration, 273
  - rejection measurements, NaCl solutions, 281
- Thermal stability, 95
  - HDI-PEG600 polyurethane, 96
- Thermogravimetric analysis (TGA), 84
- Thin-film composite (TFC) membranes, 272
  - construction, 158*f*
- Transport properties, 89
  - diamine moiety effect, 90
  - dianhydride moiety effect, 92
- Triptycene, 108, 110
  - based polyimide membranes
    - material characterizations, 111
    - membrane preparation, 111
  - nitrated via electrophilic aromatic substitution mechanism, 114
  - polymer structures, 109*f*
  - three-dimensional structure, 109*f*

U

- Ultrafiltration polysulfone (PSf) membranes, 272
- Ultrafiltration (UF), 179
  - cheese manufacture, 182*f*
  - cheese production, 180
  - diafiltration (DF), 182
  - farm, 188
  - milk, demineralized, 201*f*
  - protein fractationation processes, 184, 187*f*
  - whey, batch diafiltration, 184*t*
  - whey proteins, 186*t*
- Ultrafiltration (UF) membranes, 248
  - on farm, 188
  - milk
    - cheese manufacture, 182*f*
    - demineralized, 201*f*
  - protein fractationation processes, 187*f*
  - *See also* Cellulose acetate ultrafiltration (CAUF) membranes

W

Water filtration. *See* Multi-walled carbon nanotube (MWCNT)
  carbon nanotube/polyethersulfone composite membranes, 257
  C/P-0, SEM images, 262*f*
  C/P composite membranes
    contact angles, 263*f*
    hydraulic resistances, 266*t*
    pure water fluxes, 264*f*
    relative fluxes, 267*f*
    solute permeation fluxes and rejections, 265*f*
  membrane characterization, 259, 261
  membrane filtration procedures, 260
  membrane preparation, 259
  membranes, antifouling properties, 265
  multi-walled carbon nanotube (MWCNT)
  permeability, 263
  solute rejection, 263
Water treatment, 156
  asymmetric membrane construction, 158*f*
  clean membranes, performance behavior, 161
    mass transport, 162
    rejection principals, 162
  homogeneous membrane construction, 158*f*
  materials, accumulation, 165*f*
  membrane filtration, rejection characteristics, 158*f*
  membrane fouling, 163
    biofouling, 165
    inorganic, 164
    limitations/functioning, 166
    organic, 164
    prevention, 166
  membrane separations, 156
    materials, 157
  module configurations, 160
  permeate flux over time, reduction, 166*f*
  pressure-driven separations, 157
  thin film composite membrane construction, 158*f*
WDXRF chemical analysis, 32*t*
Whey proteins, properties, 186*t*

Downloaded by 89.163.35.42 on June 17, 2012 | http://pubs.acs.org
Publication Date (Web): October 31, 2011 | doi: 10.1021/bk-2011-1078.ix002